Finanziato dall'Unione europea NextGenerationEU
Ministero dell'Università e della Ricerca
Italiadomani PIANO NAZIONALE DI RIPRESA E RESILIENZA

UNIVERSITÀ DEGLI STUDI DI PALERMO

PhD Course in Chemical, Environmental, Biomedical, Hydraulic and Materials Engineering
Dipartimento di Ingegneria
Settore Scientifico Disciplinare (ICHI-01/B; CHEM-06/A)

Preparation and Characterization of Nanostructured Photocatalysts for Biomass Valorization in Photocatalytic and Photoelectrocatalytic Reactors

PhD Candidate:
Tayyaba Kanwal

Supervisor:
Prof. Vittorio Loddo

Ph.D Course Coordinator:
Prof. Giorgio Domenico Maria Micale

Co-Supervisor:
Prof.ssa Marianna Bellardita

XXXVIII CYCLE

GRADUATION YEAR 2026

CODICE BORSA PNRR PE00000004–DOT204NJ79– CUP B73C22001270006

Dedicated to

my beloved Parents and respected Professors

Dr.

Not just a title, but a lifetime of struggles and dreams!

This achievement was only possible because of them.

ACKNOWLEDGEMENTS

The completion of this thesis marks an important milestone in my academic journey and the conclusion of a significant phase of my life. First and foremost, I express my gratitude to **Allah**, the Creator and Sustainer, for His guidance, strength, and countless blessings.

I would like to sincerely thank my supervisors, **Prof. Vittorio Loddo** and **Prof.ssa Marianna Bellardita**, for their continuous support, guidance, and insightful discussions, which were essential to the development of this work. I am also grateful to **Prof. Leonardo Palmisano** for his valuable suggestions and support. I sincerely acknowledge **Prof.ssa Monica Santamaria** and **Prof. Francesco di Franco** for the opportunity to conduct research in their photoelectrocatalysis laboratory, and **Dr. Claudio Maria Pecoraro** for his valuable guidance and collaboration in **photoelectrocatalysis** and his support, kindness, guidance, helpful discussions and motivation throughout my Ph.D. journey. I am deeply grateful to the Ph.D. Course Coordinator **Prof. Giorgio Domenico Maria Micale** for his constant guidance, encouragement, and valuable support. My appreciation extends to all collaborators, especially **Prof. Giovanni Palmisano** and colleagues from **Research and Innovation Center on CO_2 and Hydrogen, Khalifa University** and **Dr. Khadidja Grissi** from **20 Août 1955 Skikda University, Algeria** for their contributions and assistance during this research. I would like to thank **Prof.ssa Maria José López Muñoz** for the opportunity to carry out part of photocatalysis research at **Rey Juan Carlos University, Spain**.

I am also thankful to my lab-mate **Maya Nobatova** for her constant support, her encouragement and valuable time and all other colleagues for creating a positive working environment.

Finally, I gratefully acknowledge the **Government of Italy**, **MICS** (Made in Italy–Circular and Sustainable) Extended Partnership, for providing funding from the European Union Next-Generation EU that made it possible for me to pursue my Ph.D. at the University of Palermo.

I would like to express my heartfelt gratitude to my Dear Friend **Moazzam Hussain (Moiz)**, whom I met during my Ph.D. journey. He stood by me during some of the most difficult times, offering unwavering moral support and generous financial help when I needed it the most. His constant encouragement, kindness, and presence have been truly invaluable, and I am deeply thankful for having him in my life.

I am profoundly grateful to my beloved father **Lal Hussain** and mother **Nazir Fatima**, my siblings **Shahid Kamran**, **Tahir Kamran**, **Sadia Kanwal, Adeel Kamran**, **Awais Kamran** and Muhammad **Kashif Abdaal** for their unconditional love, endless support, and patience. Their belief in me has been my greatest strength, and their sacrifices have made this achievement possible.

Thank you, everyone, for your valuable contributions.

Tayyaba Kanwal.

JOURNAL PUBLICATION

1. Muhammad Umair, **Tayyaba Kanwal,** Vittorio Loddo, Leonardo Palmisano, Marianna Bellardita. Review on Recent Advances in the Removal of Organic Drugs by Advanced Oxidation Processes. *Catalysts* **2023**, 13(11), 1440. https://doi.org/10.3390/catal13111440.

2. Vittorio Loddo, Muhammad Umair, **Tayyaba Kanwal,** Leonardo Palmisano, Marianna Bellardita. Efficient photocatalytic removal of drugs in aqueous dispersions by using different TiO_2 based semiconductors under UV and simulated solar light irradiation. *Journal of Photochemistry and Photobiology A: Chemistry* **2025**, 468, 116465. https://doi.org/10.1016/j.jphotochem.2025.116465.

3. **Tayyaba Kanwal,** Vittorio Loddo, Claudio Maria Pecoraro, Giovanni Palmisano, Sarah Hamdan, Zhe Wang, Israa Othman, Leonardo Palmisano, Marianna Bellardita. Solar driven photocatalytic glycerol and glucose reforming via noble metals free BiOX (X = Cl, Br, I)-TiO_2 composites. *Sustainable Materials and Technologies* **2025,** e01825. https://doi.org/10.1016/j.susmat.2025.e01825.

4. **Tayyaba Kanwal,** Claudio Maria Pecoraro, Giovanni Palmisano, Sarah Hamdan, Zhe Wang, Leonardo Palmisano, Vittorio Loddo, Marianna Bellardita. Photocatalytic Environmental Remediation by Bismuth Oxyhalides-TiO_2 composites: Pharmaceuticals and pollutants degradation. *Journal of Water Process Engineering* **2025,** 76, 108219. https://doi.org/10.1016/j.jwpe.2025.108219.

5. Khadidja Grissi ,**Tayyaba Kanwal**, Claudio Maria Pecoraro, Hichem Tahraoui, Marianna Bellardita. From Synthesis to Simulation: Data-Driven Optimization of Ce-TiO_2 Photocatalysts for Water Purification. (**under review**).

6. Khadidja Grissi, Hichem Sedrati, Vittorio Loddo, Mohamed Cherif Benachour, **Tayyaba Kanwal**, Hichem Tahraoui, Marianna Bellardita. A first-time EEFO-driven machine learning framework for optimizing Cu-doped TiO_2 photocatalysts toward water purification. (**under review**).

7. **Tayyaba Kanwal**, Vittorio Loddo, Leonardo Palmisano, Maria Jose Lopez Munoz, Marianna Bellardita. Investigating the surface processes addressing the Selective Photocatalytic Oxidation of Aromatic Alcohols by BiOCl/HP-TiO_2 composites. (**In preparation**).

8. **Tayyaba Kanwal**, Marianna Bellardita, Lorenzo Mino, The influence of surface chemistry and structure in Pt-modified polycrystalline anatase and brookite TiO_2 photocatalysts used for glycerol photoreforming: A comparison. **(In preparation).**

9. Maya Nobatova, **Tayyaba Kanwal**, Marianna Bellardita, Photocatalytic environmental decontamination using 2D-BiOCl/TiO_2 heterostructures: Coupled 4-nitrophenol reduction and 4-methoxybenzyl alcohol partial oxidation. (**Submitted**)

10. **Tayyaba Kanwal**, Maya Nobatova**,** Vittorio Loddo, Marianna Bellardita, Kinetics study on the Photocatalytic Diclofenac degradation by BiOCl-P25 composites **(In Preparation)**

CONFERENCE PARTICIPATION

Tayyaba Kanwal, Vittorio Loddo, Claudio Maria Pecoraro, Giovanni Palmisano, Sarah Hamdan, Zhe Wang, Israa Othman, Leonardo Palmisano, Marianna Bellardita. Photoreforming of glucose via noble metals free BiOX (X=Cl, Br, I)-TiO_2 composites. Presented as a poster on III Convegno Nazionale della Divisione di Chimica per le Tecnologie della SCI e XIV Convegno Nazionale dell'Associazione Italiana di Chimica per Ingegneria-AICIng, Milazzo, 1-4 settembre 2025.

LIST OF ABBREVIATIONS

4-NP – 4-Nitrophenol

ABE – Ammonium Borate Electrolyte

AOP – Advanced Oxidation Process

BET – Brunauer-Emmett-Teller

BiOBr – Bismuth Oxybromide

BiOCl – Bismuth Oxychloride

BiOI – Bismuth Oxyiodide

BiOX – Bismuth Oxyhalides

CBZ – Carbamazepine

Ce–TiO_2 – Cerium-Doped Titanium Dioxide

Cu_2O – Copper(I) Oxide

DMPO – 5,5-Dimethyl-1-pyrroline-N-oxide

DRS – Diffuse Reflectance Spectroscopy

EDX – Energy Dispersive X-ray Spectroscopy

EPR – Electron Paramagnetic Resonance

FE – Faradaic Efficiency

FTIR – Fourier Transform Infrared Spectroscopy

HMF – 5-Hydroxymethylfurfural

HP05 – Home-Prepared Titanium Dioxide

HPLC – High-Performance Liquid Chromatography

HRTEM – High-Resolution Transmission Electron Microscopy

ICP-OES – Inductively Coupled Plasma Optical Emission Spectroscopy

MB – Methylene Blue

OCP – Open Circuit Potential

OTC – Oxytetracycline

P25 – Commercial Titanium Dioxide (Degussa/Evonik)

PEC – Photoelectrocatalysis

PL – Photoluminescence

PS – Persulfate

PXRD – Powder X-ray Diffraction

RB – Rose Bengal

ROS – Reactive Oxygen Species

SEM – Scanning Electron Microscopy

TBZ – Thiabendazole

TC – Tetracycline

TEM – Transmission Electron Microscopy

TiO_2 – Titanium Dioxide

TOC – Total Organic Carbon

UV – Ultraviolet

UV–Vis – Ultraviolet–Visible Spectroscopy

WO_3 – Tungsten Trioxide

ABSTRACT

The increasing demand for sustainable energy and the growing concern over environmental pollution have strengthened research into efficient and environmentally friendly technologies capable of simultaneously addressing energy production and water purification. Among the various emerging approaches, semiconductor-based photocatalysis and photoelectrocatalysis have attracted significant attention due to their ability to convert solar energy into chemical fuels and to degrade hazardous organic pollutants under mild reaction conditions.

In this thesis, nanostructured photocatalysts based on titanium dioxide (TiO_2) and bismuth oxyhalides (BiOX, X = Cl, Br, I) were synthesized, characterized, and evaluated for applications in photoreforming (biomass valorization and hydrogen production), selective oxidation of alcohols and environmental remediation. BiOCl, BiOBr, and BiOI materials were synthesized via coprecipitation and subsequently coupled with commercial TiO_2 (P25) and home-prepared TiO_2 (HP05) to form heterostructure photocatalysts containing Y% (3,5,7,9) weight percentages of BiOX with respect to TiO_2, through a ball-milling treatment. The resulting composites were extensively characterized using different techniques such as X-ray diffraction (XRD), Raman spectroscopy, Brunauer-Emmett-Teller (BET) surface area measurements, scanning electron microscopy (SEM), transmission electron microscopy (TEM), X-ray photoelectron spectroscopy (XPS), ultraviolet–visible-light (UV-vis) diffuse reflectance spectroscopy (DRS), photoluminescence (PL) spectroscopy and Fourier transform infrared (FT-IR) spectroscopy.

To explore the versatility of the synthesized catalysts, their photocatalytic activity was evaluated towards different substrates. Firstly, the hydrogen production through photoreforming of biomass-derived compounds, i.e., glycerol and glucose, acting as sacrificial electron donors, was investigated. The results revealed that BiOX-TiO_2 heterojunctions significantly enhanced charge separation and photocatalytic efficiency compared to the bare photocatalysts. 5% BiOCl-TiO_2 composites showed improved hydrogen evolution rates due to the interactions between the two semiconductors in the heterostructures.

Beyond energy applications, photocatalysts were also used for the degradation of pharmaceutical pollutants, mainly tetracycline, oxytetracycline, thiabendazole, carbamazepine and p-nitrophenol in aqueous media. The results demonstrated that BiOX-based composites exhibit stronger oxidative capability under irradiation, which enables efficient removal of persistent organic contaminants. The role of reactive oxygen species on the photocatalytic mechanism was investigated through kinetic studies and mechanistic analysis.

Furthermore, different TiO_2-based composite photocatalysts, including various polymorphs (anatase, rutile, brookite), N-doped TiO_2, and heterojunction materials such as Cu_2O-TiO_2 and WO_3-TiO_2, were investigated for the photocatalytic degradation of pharmaceutical compounds (tetracycline, oxytetracycline) and the dye (Rose Bengal). The photocatalytic activity, performed under UV irradiation, demonstrates that phase composition, doping, and interfacial charge transfer significantly influence degradation efficiency and reaction kinetics. Moreover, data-driven optimization approach was employed for synthesizing Ce-doped TiO_2 photocatalysts, integrating experimental results with advanced analysis to improve pollutant degradation efficiency and mineralization. These studies demonstrated that modification of TiO_2 significantly

improves light absorption, charge separation, and overall photocatalytic activity, highlighting the importance of material design and optimization strategies for efficient water purification applications.

Furthermore, the effectiveness of some of the prepared photocatalysts was studied for selective oxidation reactions leading to the formation of high-value chemicals. In particular, the partial oxidation of aromatic alcohols to the corresponding aldehydes was effectively accomplished, highlighting the potential of photocatalysis for green chemical synthesis in aqueous media.

In addition, TiO_2 nanotube array electrodes were fabricated via electrochemical anodization and applied in photoelectrocatalytic systems to improve charge separation and enhance H_2 generation efficiency. The combination of photocatalytic and electrochemical processes showed higher selectivity values.

In conclusion, this work shows that the synthesis of these photocatalysts and titanium dioxide-based photoelectrodes can provide an effective platform for solar-driven processes that enable simultaneous hydrogen production, biomass valorization, and environmental remediation. The results contribute to the development of sustainable photocatalytic technologies for future clean energy systems and water purification

TABLE OF CONTENTS

LIST OF FIGURES

LIST OF TABLES

CHAPTER 1

Introduction

CHAPTER 1

1. Introduction

1.1 Background

Global energy consumption continues to increase due to population growth, industrial expansion, and rising living standards, placing exceptional pressure on limited fossil-fuel resources. Fossil fuels continue to dominate global energy production, despite sustainable technological advancements in low-carbon energy systems. They lead to consistently high CO_2 emissions and escalating climate instability [1]. These challenges have driven increasing efforts to find environmentally friendly and sustainable energy solutions that can meet future energy demands while lowering greenhouse gas emissions, which has become increasingly important. Clean energy carriers that can be successfully combined with renewable power sources have received a lot of attention among the different approaches that have been investigated. Because of its high energy density and carbon-free combustion, hydrogen has become a sustainable option in this regard. Solar-driven hydrogen production, enabled by semiconductor-based photocatalytic and photoelectrocatalytic processes, offers a direct route to convert abundant solar energy into storable chemical fuels [2]. Continuous advancements in light-harvesting techniques, charge-carrier management, and catalyst design have made these systems much more feasible and established photocatalysis as a crucial technology for sustainable energy conversion [3].

1.2 Energy

Hydrogen has gained importance as a versatile and clean energy vector, particularly when produced from renewable sources like sunlight and wind [4,5]. Based upon the pioneer photoelectrochemical studies on TiO_2 electrodes, subsequent research established solar-driven semiconductor processes as sustainable pathways for renewable hydrogen production [6]. Subsequent milestones, including Turner's work [7] on sustainable hydrogen production, further established sunlight-driven semiconductor processes as feasible pathways for renewable hydrogen generation. Within this framework, photocatalysis and photoelectrocatalysis provide different approaches to transform solar energy into chemical

fuels, while simultaneously offering opportunities for environmental remediation and biomass valorization.

1.3 Renewable Energy Transition: Solar Energy and Solar-to-Fuel Conversion

Solar energy is the most abundant renewable energy available on Earth that delivers more energy to the Earth's surface in one year than total annual global energy consumption. Because of its abundance and high availability solar energy plays a central role in renewable energy transition advancement. Due to advancement in perovskite silicon tandem architectures, photovoltaic efficiency has increased to ~26%. However, conventional photovoltaics system are limited to convert sunlight into electrical energy and they lacked ability of energy storage to address the challenges. Because of this limitation, interest has increased in photocatalytic and photoelectrocatalytic systems that directly convert solar energy into chemical fuels such as hydrogen [8].

The concept of solar-to-fuel conversion originates from early demonstrations of semiconductor-based water splitting, which revealed the possibility of directly converting photon energy into chemical fuels [6,9]. Based upon this concept, different studies demonstrated the possibility of integrated solar hydrogen production systems that highlight the potential of sunlight-driven chemical pathways for sustainable energy storage [7int]. Contemporary research in solar-to-fuel conversion aims to improve photocatalytic efficiency through heterojunction engineering, surface cocatalyst modification, defect control, and band-gap tuning. These strategies enhance charge-carrier separation, extend visible-light absorption, and improve the stability of photocatalysts under operational conditions [10]. Such advancements are necessary for bridging the gap between laboratory-scale demonstrations and scalable solar-fuel technologies that are able to contribute meaningfully to a sustainable global energy transition.

Recent advancements in semiconductor research such as the development of visible-light-responsive materials, heterojunction architectures, and engineered charge-separation pathways have significantly enhanced light utilization and catalytic efficiency under mild reaction conditions [11]. Bismuth-based oxyhalides coupled with TiO_2 have gained more interest in this materials-driven research environment because of their advantageous electronic structures, absorption of visible light, and interfacial charge-transfer

characteristics. These advancements demonstrate the significance of photocatalyst design in the progress of environmental remediation and integrated solar energy conversion technology [12].

Figure 1.1 schematically illustrates the solar-to-hydrogen conversion pathway, highlighting photon absorption by a semiconductor, charge-carrier generation, and subsequent redox reactions leading to hydrogen and oxygen evolution.

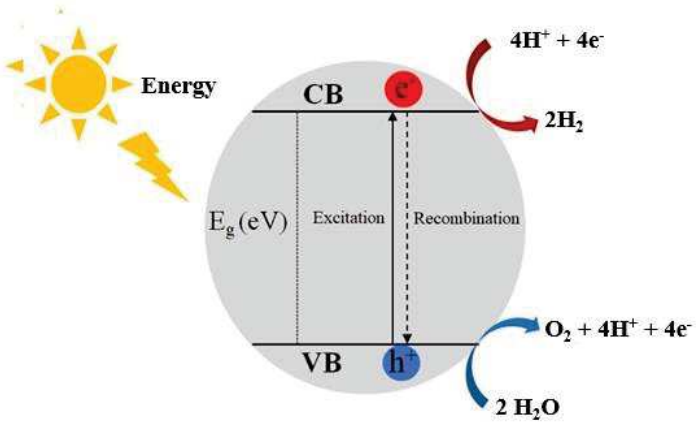

Figure 1.1. Conceptual schematic of solar-to-hydrogen conversion via semiconductor photocatalysis under solar irradiation.

1.4 Biomass as a Renewable Carbon Source

In recent years, many efforts have been made towards the search for renewable and low-carbon energy sources and the valorization of natural biomass, which is often considered waste [13-16]. Biomass reforming, which involves the simultaneous production of valuable chemicals and H_2, represents a promising strategy to counteract the negative effects resulting from excessive consumption of fossil fuels [17-19]. Notably, the partial oxidation of biomass derivatives, such as glycerol, glucose, fructose and other carbohydrates, can allow the obtaining of compounds with high added value to be used as precursors in the pharmaceutical, food, cosmetics and fuel sectors [20,21].

Biomass is the source of renewable carbon that is available on Earth on a larger scale. It takes part in carbon cycle due to its continuous regeneration via photosynthesis. Biomass is part of the short carbon cycle; when sustainably sourced, its net CO_2 impact can be lower than

fossil fuels. Huber et al. [22]. highlighted that biomass is the major source of neutral carbon to synthesize chemicals and fuels by utilizing renewable energy sources that make it a central component of circular and low carbon energy strategies.

In this context, biomass valorization refers to the conversion of biomass derivatives into high value-added chemicals, hydrogen and other solar fuels through different ways like thermal, catalytic, or photochemical processes. Because biomass-derived oxygenates have more favourable oxidation pathways due to their higher chemical reactivity and lower thermodynamic stability than fossil hydrocarbons, this is the most studied pathway.

According to Chen et al. [10], sacrificial agents act as electron donors, improving charge separation by consuming photogenerated holes and suppressing electron-hole recombination. This leads to enhanced photocatalytic hydrogen evolution compared to pure water splitting systems. Puga et al., [23], highlighted that the presence of biomass significantly accelerates hole scavenging, suppresses electron–hole recombination, and enhances hydrogen production efficiency. This synergistic effect represents a key principle in modern photocatalytic systems aimed at maximizing solar-to-fuel conversion efficiency. The fundamental mechanism of photocatalytic biomass reforming is illustrated in Figure 1.2, where photogenerated electrons drive proton reduction to produce H_2, while holes promote the oxidation of biomass into value-added compounds.

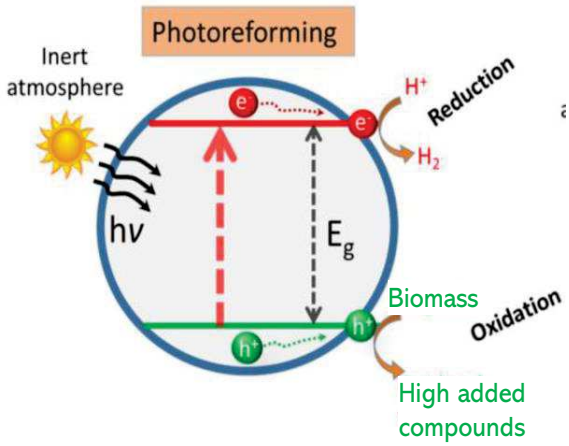

Figure 1.2. Biomass derivatives photoreforming process under light irradiation for simultaneous hydrogen production and value-added products formation

1.5 Biomass model molecules and context

1.5.1 Glycerol as Biomass Model Molecule

A wide range of biomass-derived model molecules has been explored for photocatalytic reforming, each offering distinct advantages. Glycerol is obtained as a by-product of biodiesel production from biomass, accounting for 10% of biodiesel formation, but its quantity largely exceeds demand. This molecule has great versatility in transforming more easily than other substrates into useful compounds such as 1,3-dihydroxyacetone and glycolic acid, and in the formation of H_2 under anaerobic conditions [24-27]. Particularly desirable is the production of glycolic acid, an alpha hydroxy acid that has antibacterial, antioxidant, keratolytic and anti-inflammatory properties used in pharmaceutical and cosmetic fields [28,29].

1.5.2 Glucose as Biomass Model Molecule

Glucose is an abundant carbohydrate derived from cellulose that can be converted into valuable platform chemicals such as gluconic, levulinic and formic acids and 5-hydroxymethylfurfural [30-32]. Meanwhile, short-chain hydrocarbons such as methanol and ethanol, and benzyl alcohols, are commonly employed because their favourable redox properties allow efficient hole scavenging and high hydrogen yields. Together, these substrates provide a versatile toolkit for understanding the photocatalytic upgrading of biomass-derived molecules and form the foundation of the photoreforming systems investigated in this thesis. Biomass valorization via heterogeneous photocatalysis is emerging as an efficient and promising alternative technology to convert solar energy into chemical energy under economical and environmentally friendly conditions [25,33-37].

1.5.3 Limitations of conventional biomass conversion

Conventional approaches for biomass conversion include high-temperature catalytic and biological processes, which are often energy-intensive, expensive, and require the use of organic solvents or hazardous oxidizing agents [38]. Although TiO_2 is the most employed and active photocatalyst [39-41], it presents some drawbacks such as high hole-electron recombination rate, activation by ultraviolet light and indiscriminate oxidizing capacity which generally results in low selectivity in chemical syntheses. These problems can be overcome either by using alternative photocatalysts [42-45] or by coupling TiO_2 with suitable

semiconductors [25, 46-48]. The coupling of TiO_2 with appropriate semiconductors, including metal sulfides, metal oxides, and modified oxides such as bismuth oxyhalides (BiOX, where X = Cl, Br, or I) [49], has been demonstrated to be advantageous as the distinct electronic and surface properties of both solids, improving charge separation efficiency and enabling, effective utilization of sunlight for practical applications [50-53]. Notably, by choosing semiconductors with adequate energy values of the edges of valence and conduction bands, an efficient production of H_2 is possible following the formation of a direct Z-scheme [25,48,54].

Bi-based oxyhalides (BiOX) have emerged as promising photocatalysts due to their chemical stability, non-toxicity, ability to exhibit activity under visible light, as well as desirable optical and electrical properties [44,55-58]. Although they found applications in the photocatalytic removal of harmful compounds from effluents, water splitting, disinfection applications [59,60]. BiOXs' photoactivity in real applications is limited due to the rapid electron-hole recombination and their band structures. Consequently, different strategies such as doping with metal and non-metal species, structure engineering, and heterojunction design, have been explored to overcome these limitations. Layered BiOCl nanoplates revealed higher stability and photocatalytic activity towards methyl orange (MO) degradation than TiO_2 under UV light irradiation [61]. Li et al. [62], synthesized flower-like BiOX (X = Cl, Br, I) microspheres containing oxygen vacancies to remove volatile organic sulfur compounds (VOCs) under simulated solar light irradiation. Among the BiOX materials investigated in literature, BiOI exhibited the highest activity toward pollutant removal under specific experimental conditions, achieving up to 75% degradation within 3 h. BiOBr-RGO (Reduced Graphene Oxide) composites were active under visible light irradiation towards the degradation of nitrobenzene [63]. The samples containing 0.6 wt% RGO afforded a nitrobenzene degradation rate about 2.16 times that of bare BiOBr due to the reduced electron-hole recombination rate and higher light absorption. g-C_3N_4/BiOCl heterostructures exhibited high photoactivity for methyl orange and phenol degradation thanks to an effective migration of the photogenerated charges [64]. Li et al., [65] used BiOCl/TiO_2 heterojunctions for the degradation of Rhodamine B under visible light irradiation. The composite samples showed superior photocatalytic activity than both the individual photocatalysts and the commercial TiO_2 (P25).

1.6 Hydrogen as a Clean Energy Vector

In the context of biomass valorization as a renewable and carbon-neutral carbon source, the generation of clean energy carriers becomes a central objective of sustainable energy systems. Hydrogen has been the most attractive energy vector among the various options because of its high energy density and ecologically friendly combustion. Hydrogen has gained global importance as a clean and versatile energy carrier capable of supporting the transition away from fossil-based systems. Its high gravimetric energy density, adaptability in storage, and suitability for a wide range of uses, including steel production, ammonia production, fuel cells, and long-duration energy storage, are what make it interesting. Hydrogen plays a crucial role in stabilizing renewable-dominant energy networks and decarbonizing hard-to-electrify industrial sectors, according to Chu and Majumdar [4]. Combustion of hydrogen produces just water and no CO_2 or particle emissions, making it particularly compatible with climate mitigation techniques.

Hydrogen's clean oxidation reaction is represented by equation 1.1.

$$2H_2 + O_2 \rightarrow 2H_2O \quad (1.1)$$

The reaction is highly exothermic, highlighting how H_2 is considered as an environmentally friendly carrier for future energy. Moreover, it demonstrates that H_2 is a carbon-free fuel. Turner's pioneering work [7], established renewable H_2 production as a practicable long-term solution, demonstrating the potential of photoelectrochemical and solar-driven systems to deliver sustainable hydrogen with drastically lower emissions than fossil-derived routes. As shown in Figure 1.3, renewable electricity derived from photovoltaic (PV) systems can be effectively coupled with water electrolysis to produce hydrogen, which can be stored and later utilized as a carbon-free energy carrier, thereby contributing to sustainable energy systems and decarbonization strategies.

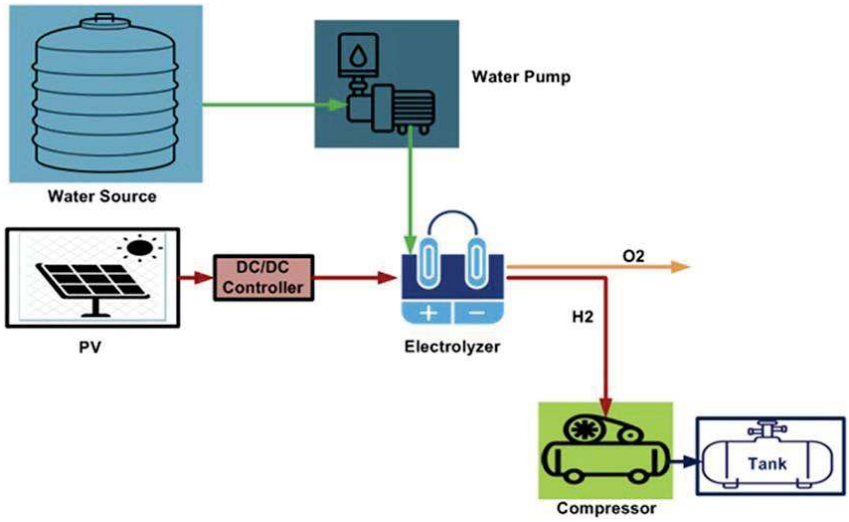

Figure 1.3. Conceptual representation inspired by the hydrogen economy pathway.

Currently, steam methane reforming (SMR), a fossil-based process that releases significant CO_2 amounts, is used to produce over 95% of H_2 in the world [66]. Bhandari et al. [67] measured SMR's lifecycle emissions and discovered it as the most carbon-intensive source of hydrogen**.** To moderate these emissions, blue hydrogen pathways combine SMR with carbon capture and storage (CCS). However, Voldsund et al. [68], demonstrated that CCS efficiency varies widely, and upstream methane leakage can undermine the environmental benefit.

Green hydrogen, produced via electrolysis powered by renewable energy, offers the most sustainable solution. Glenk and Reichelstein et al. [69], showed that dropping solar and wind costs are steadily reducing the price of renewable hydrogen, strengthening its competitive position relative to fossil-derived pathways. Furthermore, the Global Carbon Budget analysis confirms that large-scale adoption of green hydrogen is critical for achieving global decarbonization targets [70].

A comparison of major hydrogen production pathways is presented in Table 1.1.

Table 1.1 Comparison of Major Hydrogen Production Pathways

Hydrogen Type	Source & Method	CO_2 Emissions	Advantages	Limitations	Reference
Grey H_2	Natural gas via steam methane reforming (SMR)	Very high	Cheapest; mature technology	Largest CO_2 emissions; methane leakage; fossil-dependent	[67].
Blue H_2	SMR + carbon capture & storage (CCS)	Medium	Uses existing infrastructure; lower emissions	CCS efficiency uncertain; methane leakage risk	[68].
Green H_2	Water electrolysis using solar/wind electricity	Near zero	Carbon-neutral; aligns with renewables; future scalable	Higher cost; relies on renewable availability	[71].

Thus, hydrogen enables decarbonization in a variety of sectors and acts as an energy carrier. Its compatibility with renewable electricity and promising photocatalytic and photoelectrocatalytic systems makes it a central component of next-generation energy infrastructures. The scientific foundations of H_2 production technologies, including photocatalysis and semiconductor-driven water splitting, are explored in successive sections to establish the basis for the materials and methodologies employed in this research.

1.7 Photocatalytic Water Splitting

Photocatalytic water splitting is a solar-driven process in which semiconductor materials absorb light and convert photon energy into chemical energy by converting water molecules into hydrogen and oxygen (Figure 1.1). This concept originates from early photoelectrochemical studies that demonstrated the feasibility of using semiconductor electrodes to drive water splitting under illumination, thereby establishing the scientific basis for solar hydrogen production [72-74]. Because water is an abundant and carbon-free feedstock, this approach represents an environmentally friendly pathway for producing hydrogen directly from renewable solar energy.

From an energy-conversion perspective, photocatalytic water splitting differs from conventional photovoltaic-electrolysis routes by integrating light absorption, charge separation, and surface redox reactions within a single material system. Although its practical efficiency remains limited, photocatalytic water splitting serves as a fundamental reference reaction for evaluating semiconductor performance and understanding charge-transfer phenomena in solar-driven hydrogen generation. Consequently, this process provides a conceptual framework for the development of advanced photocatalytic and photoelectrocatalytic systems aimed at sustainable hydrogen production [75].

1.8 Photocatalysis and Photocatalytic H_2 production principles

Photocatalysis is a branch of chemistry in which the reaction rate is increased in the presence of light and a photocatalyst. There are three types of photocatalysis: heterogeneous, homogeneous, and plasmonic antenna-reactor catalysis. Here we discuss heterogeneous photocatalysis.

To recognize H_2 as a truly sustainable energy carrier, it is essential to develop environmentally friendly production routes capable of utilizing renewable energy sources. In this regard, semiconductor-based photocatalysis has emerged as a promising approach for solar-driven H_2 generation. Since previous photoelectrochemical studies on TiO_2 electrodes demonstrated the feasibility of solar-driven water splitting, laying the foundation for modern heterogeneous photocatalysis [6], given that the original setup was a biased photoelectrochemical cell rather than a suspended photocatalyst system. Since then, a very large number of papers have been published, ranging from environmental clean-up [76-80]. to the synthesis of high value-added products [20, 81-83] to hydrogen production [25,84-87].

A photocatalytic process carried out by using solar light could be an economical way to produce H_2 on an industrial scale since often the synthesis of the photocatalyst and the design of the photoreactor present no difficulties [88]. The band gap of a semiconductor (SC) is defined as the energy difference between the valence band (VB) and the conduction band (CB) and determines its photo response under solar irradiation. When photons with energy equal to or greater than that of the band gap are absorbed as shown in Figure 1.4, electrons are promoted from the VB to the CB, generating electron-hole pairs. These photogenerated charge carriers may either recombine or migrate to the semiconductor surface, where they can participate in redox reactions with adsorbed species. In aqueous systems containing

oxygen and organic compounds, such processes lead to the formation of reactive oxygen species, which play a key role in photocatalytic oxidation pathways and hydrogen-related reactions (Equations 1.2–1.9) [60].

$$SC + hv \rightarrow SC\ (e^{-}_{(CB)} + h^{+}_{(VB)}) \quad (1.2)$$

$$H_2O + h^{+}_{(VB)} \rightarrow {}^{\cdot}OH + H^{+} \quad (1.3)$$

$$OH^{-} + h^{+}_{(VB)} \rightarrow {}^{\cdot}OH \quad (1.4)$$

$$O^2 + e^{-}_{(CB)} \rightarrow {}^{\cdot}O_2{}^{-} \quad (1.5)$$

$${}^{\cdot}O_2{}^{-} + H^{+} \rightarrow {}^{\cdot}HO_2 \quad (1.6)$$

$$2\,{}^{\cdot}HO_2 \rightarrow O_2 + H^2O^2 \quad (1.7)$$

$$H_2O_2 + {}^{\cdot}O_2{}^{-} \rightarrow OH^{\cdot} + {}^{\cdot}OH + O_2 \quad (1.8)$$

$${}^{\cdot}OH + organic\ compounds \rightarrow CO_2 + H_2O\ or\ partial\ oxidation\ derivatives \quad (1.9)$$

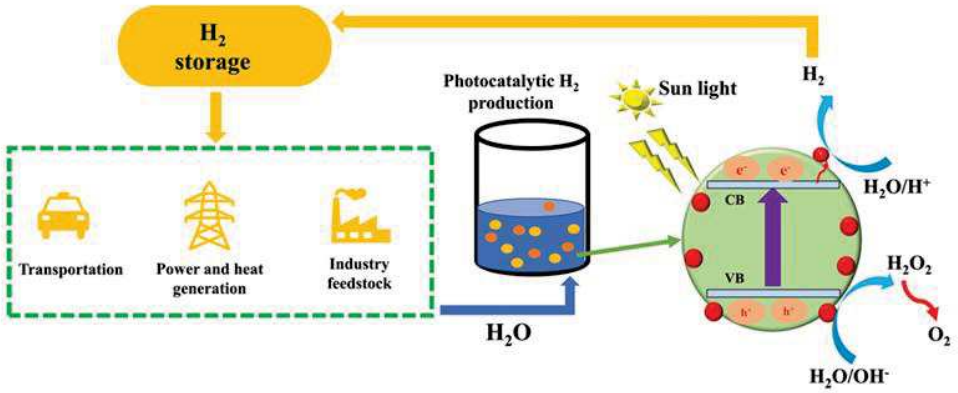

Figure 1.4. H_2 production in water system [89].

Photocatalytic H_2 production involves three key steps (Figure 1.5): (i) activation of the photocatalyst upon light absorption, leading to the generation of electron-hole (e^{-}/h^{+}) pairs; (ii) migration of the photogenerated charge carriers to the surface of the photocatalyst; and (iii) surface redox reactions driven by these charges. A fraction of the generated charge carriers undergoes recombination, which reduces the number of electrons and holes available

for productive reactions. Consequently, the recombination rate is a critical parameter governing the efficiency of heterogeneous photocatalytic processes [90]. In addition, effective hydrogen evolution requires suitable alignment of the conduction- and valence-band edge energies with the redox potentials of the targeted reactions [25,10,89].

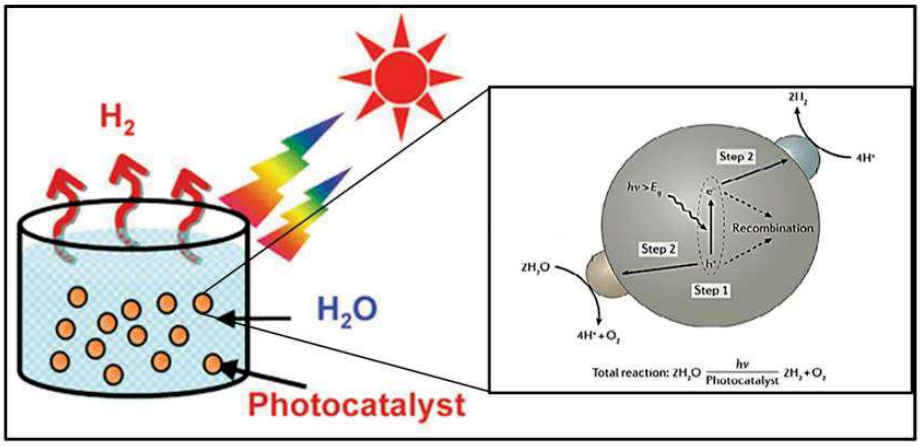

Figure 1.5. Schematic photocatalytic H_2 production on the surface of a semiconductor.

The feasibility of a given photocatalytic reaction is determined by the energetic positions of the conduction band (CB) and valence band (VB) of the photocatalyst, which govern the reduction and oxidation capacity of photogenerated electrons (e^-) and holes (h^+), respectively. In pure water systems, these charge carriers can induce hydrogen and oxygen evolution through the water-splitting mechanism. For efficient H_2 production, the CB edge must be more negative than the H^+/H_2 redox potential (0 V vs. NHE, pH 0), while the VB edge must be more positive than the O_2/H_2O oxidation potential (1.23 V vs. NHE, pH 0) (Figure 1.6) [91].Therefore, the semiconductor band gap (E_g) must exceed 1.23 eV, although practical kinetic overpotentials require wider band gaps in the range of 2.0-2.4 eV. At the same time, visible-light activation imposes an upper limit of approximately 3.0 eV ($\lambda > 400$ nm) [10,92,86].

1.8.1 Titanium Dioxide as a Benchmark Semiconductor in Photocatalysis

Among the wide variety of semiconductor materials investigated for photocatalytic applications, titanium dioxide (TiO_2) has been most extensively studied and is widely regarded as a benchmark photocatalyst in heterogeneous photocatalysis, mainly due to its low cost, chemical stability, non-toxicity, and strong oxidative power. Because of these

characteristics, TiO_2 is widely adopted as a benchmark material for understanding fundamental photocatalytic principles and reaction mechanisms [93,94].

TiO_2 exists in three main polymorphic forms: anatase, rutile, and brookite, which differ in crystal structure and photocatalytic behavior. Among them, anatase is the most commonly employed phase for photocatalytic hydrogen production, as it generally exhibits higher photostability, more efficient separation of photogenerated electron-hole pairs, and favorable electronic properties compared to the other polymorphs [94]. Rutile, although primarily used as a white pigment, is also frequently applied in photocatalytic and photoelectrocatalytic systems, while brookite is less explored due to its structural complexity and synthesis challenges [93].

Regardless of its advantages, TiO_2 presents fundamental limitations. Its wide band gap restricts photoactivation mainly to the ultraviolet region, and the rapid recombination of photogenerated charge carriers significantly limits its quantum efficiency. To overcome these drawbacks, various strategies have been suggested, including metal and non-metal doping, coupling with other semiconductors, surface modification, and morphological or crystal structure control [39,95-97].

One of the most effective approaches involves the doping of TiO_2 with metallic elements (Fe, Cu, Ag…) or non-metallic ones (N, C, S) [98], which introduce intermediate energy levels within the band gap of TiO_2, allowing for the absorption of lower-energy photons and the generation of charge carriers under visible light. In this field, rare earth elements, particularly lanthanides like cerium (Ce), show strong potential. Due to their unique electronic properties, notably cerium's ability to exist in two stable oxidation states ($Ce^{3+}$and Ce^{4+}), they play an important role in reducing the recombination of electrons and holes, which improves photocatalytic efficiency [52]. Doping TiO_2 with Ce not only reduces the band gap but also increases visible light absorption, stabilizes the anatase phase at high temperatures and increases the specific surface area of the material, all factors being favorable for enhanced photocatalytic activity [99].

In particular, the formation of semiconductor heterojunctions has proven to be efficient in enhancing solar light utilization, overcoming charge recombination, and improving the overall photocatalytic performance [30, 100]. In addition to the semiconductor coupling strategy for Cu_2O-TiO_2 [101] and Ce-TiO_2 heterojunction formation, the non-metal doping

strategy such as nitrogen doping have been widely employed to enhance photocatalytic performance. The N-doped TiO_2 system showed an improved activity under UV irradiation. These strategies lead to efficient degradation and high mineralization of pharmaceutical pollutants.

1.9 Heterojunctions

Despite its promising properties, the photocatalytic performance of TiO_2 is severely limited by fast charge-carrier recombination and its restriction to visible-light response. To overcome these intrinsic drawbacks, the formation of semiconductor heterojunctions has appeared as an effective strategy to enhance charge separation and solar-energy utilization. It is challenging for a single-phase photocatalyst to simultaneously exhibit strong redox capability and broad solar-light absorption. In addition, rapid recombination of photogenerated electron–hole pairs in single-component photocatalysts significantly limits their overall efficiency [102,103]. Because of these limitations, a lot of research has been done to create modified photocatalytic systems that can improve charge separation and increase the use of solar energy [104-108].

One of the most effective strategies to overcome these limitations is the synthesis of semiconductor heterojunctions. When two semiconductors with different band structures are brought into close contact, an interfacial region is formed that promotes directional charge transfer and suppresses electron–hole recombination. Depending on the relative alignment of the conduction and valence band edges, heterojunctions are commonly classified as Type-I, Type-II, Z-scheme, and S-scheme systems. Among these, Z-scheme and S-scheme heterojunctions are particularly attractive for photocatalytic hydrogen production because they preserve strong redox ability while maintaining efficient charge separation [105].

1.9.1 Z-scheme heterojunction

In a Z-scheme heterojunction system (Figure 1.6), both semiconductors are photoexcited under light irradiation. The photogenerated electrons in the conduction band of one semiconductor recombine with the holes in the valence band of the second semiconductor at the interface. Therefore, electrons with strong reducing ability and holes with strong oxidizing power are retained in the different semiconductors, enabling highly efficient redox reactions [109].

Compared with conventional Type-I and Type-II heterojunctions, where charge migration often results in a loss of redox potential, Z-scheme systems sustain the fundamental redox strength of the photogenerated charge carriers [103]. This characteristic makes Z-scheme heterojunctions particularly suitable for reactions requiring high redox power, such as photocatalytic hydrogen evolution and selective oxidation processes.

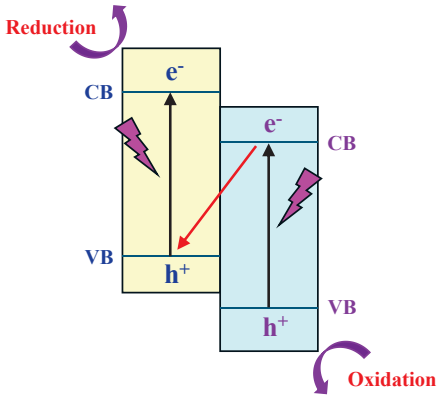

Figure 1.6. Mechanism of Z-scheme heterojunction.

Nevertheless, Z-scheme heterojunctions may experience charge accumulation and partial light-induced recombination under prolonged irradiation, which can affect photocatalytic stability and efficiency. Despite these limitations, Z-scheme architecture remains highly attractive [104]. Z-scheme systems are effective for hydrogen production when the conduction band edge of the reduction photocatalyst is more negative than the H^+/H_2 redox potential [105-108].

1.9.2 S-scheme heterojunction

The S-scheme (step-scheme) heterojunction represents a refined charge-transfer model that further improves photocatalytic efficiency (Figure 1.7). In this configuration, the two coupled semiconductors can be classified as an oxidation photocatalyst (OP) and a reduction one (RP), according to their band positions and Fermi energy levels [110-112]. Typically, the OP exhibits lower conduction and valence band edges and a higher work function compared to the RP.

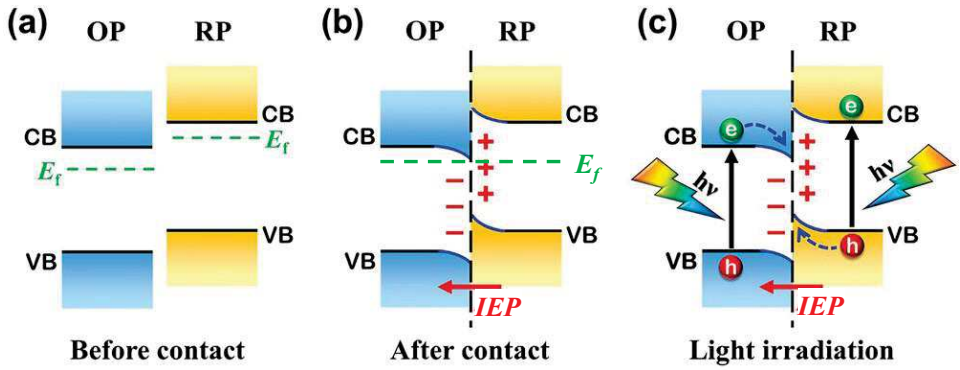

Figure 1.7. S-scheme heterojunction charge-transfer mechanism illustrating (a) energy band alignment before contact, (b) band bending and internal electric field formation after contact in the dark, and (c) directional migration and separation of photogenerated charge carriers under light irradiation. [113]

Compared to Z-scheme systems, S-scheme heterojunctions depend on band bending and internal electric fields to drive selective charge recombination, rather than interfacial recombination mediators [115,117]. Upon contact between the two semiconductors, electrons spontaneously migrate from the RP to the OP until Fermi level equilibrium is achieved. This charge redistribution leads to the formation of an internal electric field at the interface. Under light irradiation, the internal electric field, together with band bending effects, selectively promotes the recombination of low-energy electrons and holes at the interface, while preserving high-energy electrons in the RP and high-energy holes in the OP. As a result, the S-scheme heterojunction maintains strong redox capability while simultaneously achieving efficient charge separation [110-112]. Due to this synergistic charge-transfer mechanism, S-scheme heterojunctions display enhanced photocatalytic activity and stability, making them particularly suitable for noble-metal-free hydrogen production and solar-driven redox reactions involving biomass-derived substrates [105].

1.10 Cocatalysts and Their Function in Photocatalytic Hydrogen Production

In photocatalytic H_2 generation, the semiconductor primarily determines light harvesting and charge-carrier formation, but the overall activity is frequently limited by two practical bottlenecks: rapid electron-hole recombination and sluggish surface proton-reduction kinetics. For this reason, many photocatalysts remain inactive toward H_2 production unless an appropriate cocatalyst is introduced. Cocatalysts are therefore crucial

components that upon deposition on catalyst surface activate the hydrogen evolution reaction by facilitating the interfacial charge transfer and decreasing the kinetic barriers associated with proton reduction. This means that cocatalysts address both limitations by acting as electron sinks and by supplying catalytically competent surface sites for the H_2 evolution reaction.

A common strategy to enhance hydrogen production involves the deposition of cocatalyst nanoparticles on the surface of the semiconductor photocatalyst. When noble metals are employed, the mismatch between the Fermi level of the semiconductor and that of the metal leads to the formation of a Schottky junction at the interface. This junction drives photogenerated electrons from the semiconductor conduction band toward the metal nanoparticles, where they are efficiently trapped and consumed in proton reduction reactions, thereby suppressing charge recombination and enhancing hydrogen evolution efficiency [114]. As a result, noble metals such as Pt, Pd, and Ru have long been regarded as benchmark cocatalysts due to their favourable work functions and fast hydrogen evolution kinetics [115]. Figure 1.8 shows a schematic illustration of the photocatalytic water-splitting mechanism, depicting the promotion of electrons from the valence band to the conduction band, the charge transfer and recombination pathways, and the surface redox reactions for hydrogen and oxygen evolution in the presence of oxidation and reduction co-catalysts.

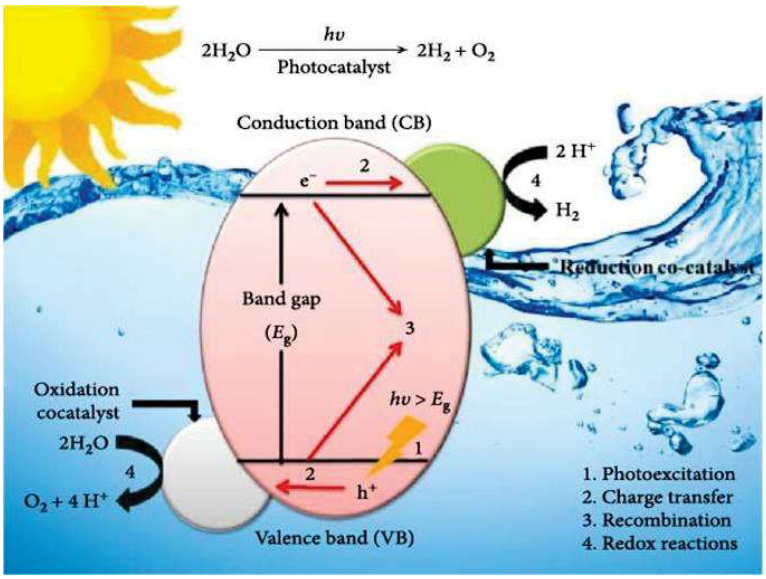

Figure 1.8. Schematic illustration of the photocatalysis for hydrogen and oxygen evolution in the presence of oxidation and reduction co-catalysts.

The photocatalytic performance is strongly dependent on the amount and dispersion of the cocatalyst. An increase in cocatalyst loading typically improves H_2 formation by increasing the number of active reduction sites; however, beyond an optimal threshold, activity often declines. This decrease has been attributed to cocatalyst particle agglomeration, growth in nanoparticle size, poor surface dispersion, and partial shielding of the photocatalyst surface from incident light, which collectively reduce effective charge transfer and accessible active sites [86]. These observations highlight that cocatalyst optimization is governed not only by chemical composition but also by surface architecture.

To overcome the economic and sustainability limitations associated with noble metals, significant effort has been devoted to the development of alternative cocatalyst systems based on earth-abundant materials. Metal phosphides, such as Cu_3P supported on g-C_3N_4, have demonstrated enhanced hydrogen evolution due to their semi-metallic conductivity and efficient electron transfer properties [116]. Similarly, metal borides and carbides have attracted attention as low-cost cocatalysts owing to their favourable electronic structures and catalytic activity toward proton reduction [117]. Metal sulfides, including NiS and CuS, have also been reported to play a crucial role in activating hydrogen evolution, particularly in g-C_3N_4-based photocatalytic systems, where they facilitate electron trapping and surface reduction reactions [115].

Further improvements in H_2 production have been achieved through the co-loading of reduction and oxidation cocatalysts. This approach promotes spatial separation of photogenerated electrons and holes, enhances directional charge migration, and reduces recombination losses, ultimately leading to a superior photocatalytic efficiency [119]. Such strategies demonstrate that cocatalysts operate not merely as auxiliary additives but as key elements governing charge dynamics and reaction pathways.

Overall, the integration of suitable cocatalysts is indispensable for activating photocatalytic hydrogen evolution, optimizing interfacial charge transfer, and achieving efficient solar-driven hydrogen production. These principles provide the conceptual foundation for the design of noble-metal-free photocatalytic and Photoelectrocatalytic systems explored in this thesis.

1.11 Organic electron donors (hole scavengers)

Organic electron donors (also referred to as hole scavengers) are commonly employed in photocatalytic hydrogen production systems to enhance charge separation efficiency and suppress the recombination of photogenerated electron-hole pairs. These organic compounds preferentially react with photogenerated holes, thereby prolonging the lifetime of conduction-band electrons available for proton reduction and hydrogen evolution. Typical organic electron donors include alcohols (such as methanol and ethanol) [120,121]. as well as biomass-derived molecules like glycerol and glucose [119], which can act as renewable and sustainable sacrificial substrates. In addition to improving hydrogen generation rates, the oxidation of these organic donors may lead to the formation of partially oxidized intermediates, providing an added benefit in terms of chemical valorization. For this reason, the use of organic electron donors coming from biological substrates represents an effective strategy to boost photocatalytic hydrogen production while simultaneously linking solar energy conversion with biomass utilization [23].

1.12 High value-added products from photocatalytic reforming

In photocatalytic H_2 production systems employing organic electron donors, the oxidation half-reaction does not necessarily lead to complete mineralization of the organic substrate. Instead, partial and selective oxidation of biomass-derived molecules can occur, resulting in the formation of high value-added chemicals alongside H_2 evolution. Such products include aldehydes, organic acids, polyols, and furan-based compounds, which are widely used as intermediates in chemical, pharmaceutical, and polymer industries. Therefore, photocatalytic reforming represents a dual-benefit approach, where solar energy is simultaneously converted into clean hydrogen fuel and value-added chemicals, improving the overall economic and sustainability profile of the process [23,123].

Photocatalytic partial oxidation of aromatic alcohol represents an attractive strategy for coupling solar energy utilization with the sustainable production of value-added chemicals. Unlike complete mineralization pathways, alcohol oxidation can proceed selectively under mild conditions, enabling the formation of aldehydes and related intermediates of industrial relevance. The use of semiconductor-based photocatalytic systems allows these transformations to be carried out in aqueous media and under solar irradiation, avoiding harsh reaction conditions and hazardous oxidants. As a result, alcohol

is widely adopted as model substrates to evaluate selectivity and efficiency in solar-driven redox processes [25,46-48,124].

1.13 Photoelectrocatalysis: Principles and Key Advantages

In addition to conventional photocatalytic systems, photoelectrocatalysis (PEC) represents an emerging extension of semiconductor-based processes, where an external bias is employed to further suppress charge recombination and enhance redox efficiency. A brief overview is provided here, while detailed applications and performance discussions are addressed in subsequent sections of this thesis.

Heterogeneous photocatalysis literature has long highlighted that the practical efficiency of light-driven redox chemistry is often limited by charge-carrier recombination and slow interfacial kinetics, even when band positions are thermodynamically favourable. Foundational reviews by Fox and Dulay [125] and by Mills and Le Hunte [90] emphasize these intrinsic constraints and the need for strategies that improve charge separation and surface reaction rates in semiconductor systems. Photoelectrocatalysis addresses this limitation by combining semiconductor photoexcitation with electrochemical control, enabling more directional charge transport and better utilization of photogenerated carriers than the conventional slurry photocatalysis in many cases [126-127].

In a PEC configuration, the photocatalyst is immobilized as a photoelectrode within an electrochemical cell. Upon illumination, electron–hole pairs are generated in the semiconductor; an external circuit and applied bias then promote vectorial (directional) charge flow, extracting one carrier type through the electrode while driving the complementary redox reaction at the interface. Classic photoelectrochemical concepts and device physics describe how the electric field at the semiconductor/electrolyte junction, together with the applied bias, suppresses bulk and surface recombination and improves interfacial charge transfer. This framework established through the evolution of photoelectrochemical cells and semiconductor photo electrochemistry forms the mechanistic basis for PEC performance improvements [128,129].

Beyond its role in water splitting, PEC has expanded rapidly into broader energy and chemical transformations. Modern overviews emphasize that PEC can operate “beyond water oxidation,” enabling selective organic conversions and coupled reaction schemes by tuning bias, electrode architecture, and catalyst/electrolyte interfaces to steer charge use

toward targeted pathways. Recent trend analyses further underline that PEC is increasingly applied as a platform technology spanning hydrogen generation, environmental remediation, and value-added synthesis precisely because it couples photochemistry with electrochemical selectivity control [130-131].

For solar water splitting specifically, materials design remains central, with emphasis on band energetics, junction engineering, and stability under operating conditions [132]. In parallel, PEC is widely recognized as an efficient approach for pollutant removal and environmental applications, where bias-assisted charge extraction can enhance oxidative performance and mitigate the recombination losses [133].

Importantly for biomass-linked energy systems, PEC also enables selective photoelectrochemical synthesis of valuable chemicals, providing a controlled route to pair oxidation chemistry with reductive hydrogen formation. Recent literature highlights PEC as a versatile method for green production of building-block chemicals and for selective transformations in aqueous media, aligning well with sustainable process goals [127,134,135]. Overall, PEC offers a rational pathway to overcome recombination-limited photocatalysis by integrating illumination with electrical driving force and interfacial control, thereby strengthening the conceptual bridge from fundamental photocatalysis to the Photoelectrocatalytic systems investigated in this thesis [131].

1.14 Organic drugs removal

Due to population growth, increase in industrial activities and urbanization water resources, especially rivers, lakes, and groundwater are increasingly subjected to contamination that result in a constant deterioration of water quality worldwide [136]. Growing attention has been given to emerging organic pollutants that are not effectively removed by traditional treatment technologies, with pharmaceutical compounds being of particular concern owing to their persistent nature and continuous introduction into aquatic systems.

The wide use of pharmaceutical products for human and veterinary applications has led to the widespread use of drugs and related pharmacological substances in aquatic environments [137,138]. Therefore, pharmaceutical residues have been detected in surface water, groundwater, wastewater, and even drinking water at concentrations ranging from ng to μg L^{-1} [139-141]. The presence of pharmaceuticals in water systems is particularly problematic because they often occur as complex mixtures, where synergistic interactions

can significantly enhance overall ecotoxicity [142]. Furthermore, incomplete removal of parent compounds and their metabolites during wastewater treatment processes contributes to the continuous discharge of biologically active substances into natural water bodies [143].

Pharmaceutical compounds are hard to eliminate from water systems using conventional wastewater treatment technologies due to their low degradation rates, stable chemical structures, and high hydrophilicity [144,145]. Traditional treatment methods, including biological treatment [146], adsorption [147], nanofiltration [148], and membrane bioreactors [149], have been widely directed for drug removal from wastewater; however, these approaches are often inefficient and fail to achieve complete mineralization [144]. Consequently, the development of efficient and environmentally sustainable technologies for the removal of pharmaceutical contaminants from aquatic systems has become a pressing research priority [137].

1.14.1 Advanced oxidation processes

Among the available treatment strategies for pharmaceutical-contaminated water, advanced oxidation processes (AOPs) are considered cost-effective, flexible, and highly efficient methods for degrading persistent organic molecules [150,151]. AOPs are characterized by the in-situ generation of highly reactive oxidizing species with limited selectivity, such as hydroxyl radicals ($^{\bullet}OH$), ozone (O_3), hydrogen peroxide (H_2O_2), and superoxide radicals ($O_2^{\bullet-}$). These species enable the non-selective oxidation and mineralization of complex organic contaminants into CO_2, H_2O, and inorganic compounds. Under appropriate operating conditions, AOPs are regarded as environmentally favourable for water treatment applications [152].

AOPs have demonstrated excellent effectiveness in producing clean drinking water free from organic, inorganic, and microbial contaminants [153]. One of the major advantages of AOPs over conventional treatment methods is that they do not simply transfer pollutants from one phase to another but instead promote their chemical transformation without generating large quantities of secondary waste [154-155]. Depending on the characteristics of the contaminated water and treatment objectives, AOPs can be applied either as standalone processes or in combination with biological and physicochemical treatments, where process coupling often enhances overall removal efficiency [156].

Heterogenous photocatalysis is a type of advanced oxidation processes that was widely studied in past as non-toxic and economic process based on the activation of semiconductors able to mineralize a large variety of toxic organic molecules [157]. The photogenerated electrons reduce O_2 to reactive oxygen species (e.g., O_2^-), while holes oxidize H_2O/OH^- to •OH radicals. These reactive species drive oxidation of organic pollutants, ultimately leading to mineralization into CO_2 and H_2O [158].

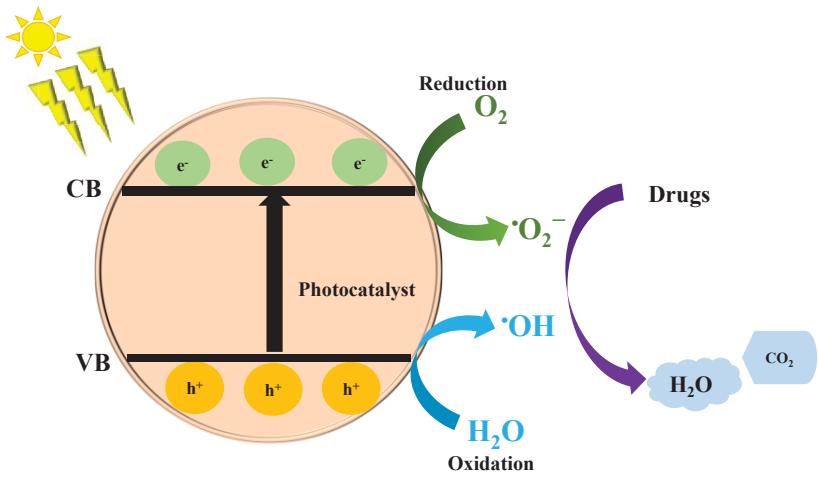

Figure 1.9. Photocatalytic mechanism of drugs degradation.

1.14.2 Thiabendazole (TBZ) as a persistent fungicide pollutant

Thiabendazole (TBZ) is a benzimidazole derived fungicide, which is extensively used in preservation mainly after the harvesting of the fruits and in veterinary medicine. Because of its intensive application and high chemical stability, TBZ deposits are frequently detected in surface water, groundwater, and wastewater streams, where they demonstrate strong resistance to conventional treatment processes. Moreover, TBZ and its transformation products present ecotoxicological risks, classifying it as an emerging contaminant of environmental concern [159-161].

1.14.3 Persulfate-based advanced oxidation processes for TBZ removal

To overcome the difficulty of degrading TBZ by traditional removal methods, persulfate based advance oxidation process has gained higher attention. Persulfate activation process generates sulfate radicals ($SO_4^{\bullet -}$) that show higher oxidation potential and enhanced lifetime as compared to hydroxyl radicals which lead to efficient degradation of recalcitrant compounds like TBZ. Recent studies revealed that the photocatalytic activation of persulfate

can substantially improve TBZ degradation efficiency through synergistic radical pathways [162,163].

1.14.4 Carbamazepine (CBZ)

Carbamazepine is an antiepileptic pharmaceutical that is widely detected in aquatic environments due to its extensive use and high chemical stability. Conventional wastewater treatment plants show very low removal efficiency for CBZ, often below 10%, leading to its continuous release into water bodies. Therefore, the development of efficient treatment technologies for CBZ removal has become an important environmental research topic [164].

1.14.5 Antibiotics as pharmaceutical pollutants representatives

Antibiotics are recognized as one of the most critical groups of pharmaceutical contaminants frequently detected in aquatic environments. Owing to their extensive consumption in human healthcare, veterinary medicine, and agricultural activities, antibiotics such as tetracycline, oxytetracycline, and lincomycin are routinely reported in wastewater streams and surface water bodies [139-141,165-168]. The environmental persistence of these compounds is largely associated with their stable molecular structures and limited biodegradability, which substantially restricts their removal efficiency in conventional wastewater treatment systems [144,145].

1.14.6 Tetracycline (TC)

TC is an antibiotic used to treat infectious diseases in humans and animals, and it is commonly retained in the medicine, farming, animal, and aquatic sectors [169]. The chemical structure of TC contains different functional groups, such as acylamino, phenolic hydroxyl, dimethylamino, and ketone enol conjugated double bond structure. Together with sewage, it is directly released into the environment as it cannot be completely absorbed by organisms [170,171]. So, it is important to develop suitable technologies that can degrade TC at an affordable cost.

1.14.7 Oxytetracycline (OTC)

OTC belongs to the family of tetracycline, and it is a widely used antibiotic for human beings and animals [172]. OTC is used to treat several diseases, including urethritis, pneumonia, and chronic bronchitis, as well as for boosting animal growth. OTC has been found within the range of mg L^{-1} to μg L^{-1} in soil, fresh water and wastewater treatments plants [173].

OTC is harmful to aquatic organisms and ecosystems when it is released into water supplies. It can harm the natural cycle of the ecosystem and environment [174].

1.14.8 Lincomycin (LMC)

LMC is one of the generally used antibiotics that has been found in natural water and wastewater treatment plants. It is resistant to degradation owing to its stable structure and physicochemical characteristics [175]. In aquatic ecosystems, the use of LMC may lead to bacterial resistance and the dissemination of resistance genes [176]. It was found that these genes can be transferred from animals to humans through food chains [177]. Figures 1.9 A, B and C state TC, OTC and LCM structural forms, respectively.

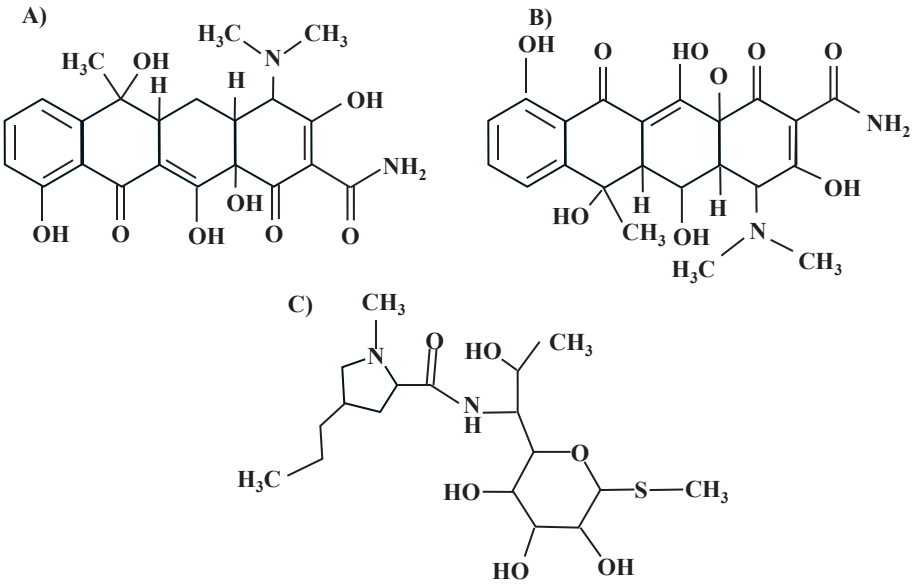

Figure 1.10. A): Chemical structure of TC; B): Chemical structure of OTC; C): Chemical structure of LMC.

Among these compounds, tetracycline and oxytetracycline are widely adopted as representative model antibiotics in photocatalytic studies due to their high environmental persistence, complex molecular structures, and resistance to conventional biological treatment processes [178-180].

1.14.9 Para-nitrophenol

In addition to pharmaceutical contaminants, phenolic compounds such as p-nitrophenol are widely recognized as toxic and persistent organic pollutants originating from industrial activities, including pesticide production, dye manufacturing, and chemical processing [181]. Due to their high chemical stability and resistance to conventional wastewater treatment processes, p-nitrophenol is frequently employed as a model pollutant for evaluating the efficiency of advanced oxidation and photocatalytic systems [182, 183].
In addition to antibiotics and nitro-aromatic pollutants, phenolic compounds are also considered environmentally relevant contaminants due to their toxicity and persistence in aquatic systems.

Advanced oxidation processes rely on the generation of highly reactive species that initiate radical-driven oxidation reactions, leading to structural modification and degradation of antibiotic molecules. The overall removal efficiency is strongly influenced by factors such as the chemical structure of the target antibiotic, the type of reactive species involved, and the operational parameters of the applied AOP [156]. This is directly relevant to the present thesis, where semiconductor-based photocatalytic materials developed for solar-driven energy applications are also evaluated for their capability to remediate antibiotic-contaminated water.
Photoreactor design is as important as the intrinsic properties of the photocatalyst because it determines photon delivery, mixing, and mass/heat transfer under the operative conditions. Parameters such as irradiance, reactor geometry, hydrodynamics (stirring intensity and catalyst suspension), temperature control, and gas-liquid contact strongly influence reaction kinetics, apparent quantum efficiency, and reproducibility. A well-controlled reactor configuration is therefore essential to ensure that observed activity trends reflect catalyst behaviour rather than artefacts arising from non-uniform irradiation, catalyst settling, or uncontrolled heating.

1.15 Photocatalytic Reactor

Photocatalyst reactor design plays a crucial role in photocatalysis, the same as intrinsic properties of the photocatalyst. The photoreactor helps to control how well light hits the catalyst, in mixing the suspension, to prevent problems with heat and mass transfer. Parameters such as light distribution (irradiance and geometry), mixing intensity,

temperature control, and gas–liquid contact can significantly affect reaction kinetics, efficiency, and reproducibility. Therefore, a reactor configuration is necessary to make it reliable, and that activity trends truly reflect catalyst behaviour rather than experimental products caused by non-uniform irradiation, catalyst settling, or uncontrolled heating.

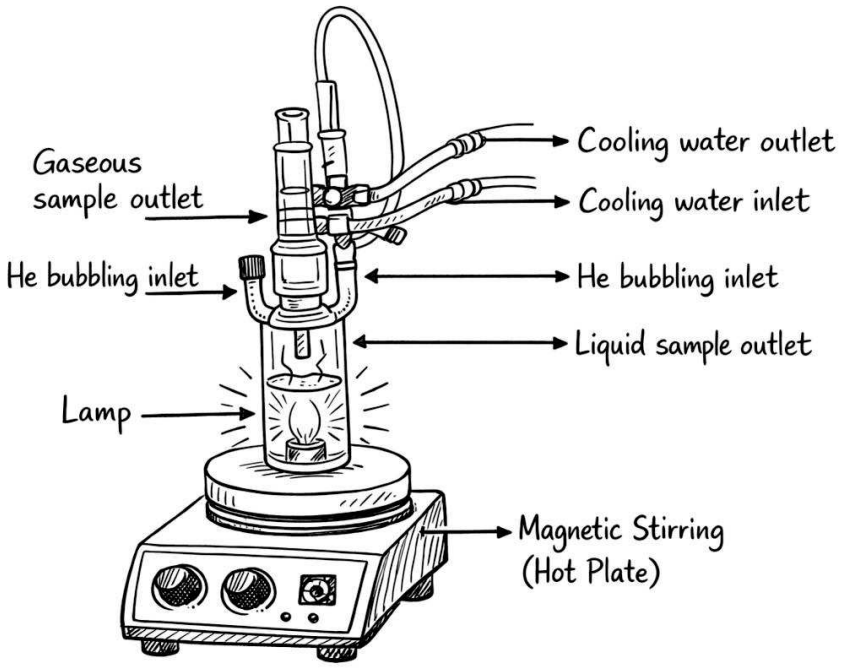

Figure 1.11. Reactor design for photocatalysis.

1.16 Scope, Objectives and Structure of the Thesis

This thesis focuses on the development and application of semiconductor-based photocatalytic and photoelectrocatalytic systems for solar-driven hydrogen generation, biomass valorization, and organic pollutant removal. Particular attention is devoted to TiO_2-based materials modified with bismuth oxyhalides (BiOCl, BiOBr, and BiOI), owing to their favourable band structures, interfacial charge-transfer properties, and potential to improve photocatalytic performance through heterojunction formation.

The primary objective of this work is to investigate the role of BiOX-TiO_2 heterostructured photocatalysts in improving charge separation efficiency and directing

photogenerated carriers toward productive redox reactions. These systems are explored for H_2 production via photocatalytic reforming of biomass-derived substrates (such as glycerol, glucose, and related alcohols), selective oxidation of aromatic alcohols to value-added chemicals, and the degradation of environmentally relevant pharmaceutical pollutants, including antibiotics. In addition, photoelectrocatalytic approaches based on TiO_2 nanotube arrays are examined as an advanced strategy to further suppress charge recombination and enhance reaction efficiency under applied bias.

The structure of the thesis is organized as follows.

Chapter 1 introduces the global energy demand and environmental challenges that motivate this research. It also presents the fundamental concepts of photocatalysis, photoreforming, photoelectrocatalysis, biomass valorization, and the removal of pharmaceutical pollutants, establishing the scientific framework of the study.

Chapter 2 provides a comprehensive state-of-the-art review, covering photocatalytic hydrogen production, biomass-derived substrate conversion, selective oxidation processes, advanced oxidation processes, and recent developments in BiOX- and TiO_2-based materials.

Chapter 3 describes the materials, synthesis procedures, characterization techniques, and experimental methodologies employed throughout the work.

Chapter 4 focuses on the preparation and characterization of BiOX (X = Cl, Br, I) and TiO_2 (P25) composite photocatalysts, including structural, optical, and electronic analyses, as well as insights into charge transfer behaviour.

Chapter 5 is divided into V sections; s**ection 5-I** investigates photocatalytic applications of BiOX for glycerol and glucose photoreforming that includes biomass valorization for hydrogen production; **section 5-II** investigates environmental remediation i.e., degradation of pharmaceutical pollutants and organic drug contaminants using TiO_2-based and BiOX-TiO_2 photocatalysts; **section 5-III** is based thiabendazole and carbamazepine degradation with BiOCl-P25 photocatalyst using persulfate assisted system; **section 5-IV** investigates TiO_2 based photocatalyst for environmental remediation for drugs degradation with detailed kinetics and mechanistic analysis; **section 5-V** highlights the drugs and dyes degradation using Ce-TiO_2 doped photocatalyst.

Chapter 6 is dedicated to the Selective Photocatalytic Partial Oxidation of Biomass-derived substrates and Aromatic alcohols, highlighting the formation of value-added chemicals under mild and sustainable conditions.

Chapter 7 explores Photoelectrocatalytic (PEC) systems based on TiO_2 nanotube arrays. This chapter discusses the synthesis and modification of nanotube electrodes with Ni and W species, and their application in biomass oxidation and H_2 production. The role of applied bias, charge separation, and Faradaic efficiency is critically analysed to evaluate system performance and limitations.

The central objective of this dissertation was the development of TiO_2-based and BiOX-modified photocatalytic systems capable of improving charge separation and solar energy utilization for sustainable applications. The same material-design strategy was applied to biomass valorization, hydrogen production, environmental remediation, selective oxidation and photoelectrocatalysis, demonstrating the versatility of engineered heterojunction photocatalysts.

Although the applications investigated in this dissertation include biomass photoreforming, environmental remediation, selective oxidation and photoelectrocatalysis, all chapters are connected through a common scientific strategy: the development of TiO_2-based heterostructures with improved charge separation and solar-energy utilization. Similar photocatalytic principles govern hydrogen production, pollutant degradation and selective oxidation reactions, demonstrating the versatility of the developed photocatalytic materials. Furthermore, previous studies have highlighted that photocatalytic technologies can be applied across wastewater treatment, solar fuel production and chemical synthesis using similar reactor concepts and scale-up approaches.

Finally, the main conclusions and perspectives for future research are presented in the concluding section.

CHAPTER 2

State of the art

CHAPTER 2

2. State of the art

This chapter reviews the pertinent literature on semiconductor photocatalysis focusing on the aims of this thesis, with emphasis on solar-driven hydrogen generation, biomass valorization and environmental remediation. In the first part, valorization of biomass-derived substrates with main emphasis on glycerol and glucose photoreforming into high value-added products are highlighted with their selectivity and challenges associated with bare TiO_2. The key limitations of TiO_2 such as UV-activation only, fast charge recombination and over oxidation tendencies are discussed to induce material synthesis strategies that can improve charge separation and control surface redox chemistry.

Building on these concepts, the chapter discusses and analyses semiconductor-coupling approaches and heterojunction engineering, with particular attention to BiOX-TiO_2 systems reported in the literature and their typical synthesis routes and applications. A comparative overview is then provided through literature tables that summarize representative BiOX-TiO_2 heterojunctions and photocatalytic systems for the degradation of persistent pharmaceutical pollutants (e.g., tetracycline, oxytetracycline, and ciprofloxacin), enabling evaluation across different catalysts and operating conditions. This literature context identifies the limited exploration of noble-metal-free, scalable BiOX-TiO_2 platforms for biomass photo reforming and supports the approach adopted in the present work, where simple ball-milled heterostructures are evaluated across both energy-related and environmental applications.

2.1 Photocatalytic valorization of biomass-derived substrates

2.1.1 Glycerol as biomass model molecule

Glycerol is an emerging biomass-derived substrate used in photocatalytic reforming because of its abundance as a by-product of biodiesel production and its multiple hydroxyl groups that make it readily oxidizable. Seadira et al. reported that glycerol is particularly attractive for solar-driven hydrogen production because it can act as an efficient hole scavenger, thereby lowering the kinetic barrier associated with water oxidation and enhancing hydrogen evolution efficiency [184]. Unlike conventional alcohols such as methanol or ethanol, glycerol is cheap, non-toxic, and abundantly available, making it a realistic model molecule for biomass valorization studies under photocatalytic conditions.

2.1.2 Photocatalytic glycerol reforming - mechanism & products

Glycerol photoreforming does not follow a single, straightforward oxidation route; instead, it typically evolves through a series of competing and consecutive steps. Oxidation can begin with dehydrogenation at either primary or secondary hydroxyl groups, generating soluble intermediates before progressing under certain conditions to C-C bond cleavage and the formation of smaller oxygenated species and, eventually, CO_2. In a TiO_2-based system, Sanwald et al. [185] identified glyceraldehyde and dihydroxyacetone as the main early-stage products associated with selective oxidation of glycerol, whereas more extensive oxidation led to fragmentation of products and mineralization pathways. Overall, these observations show that the product distribution depends strongly on surface photocatalyst adsorption, charge-carrier availability, and interfacial charge-transfer.

Beyond polyols such as glycerol, the selective photocatalytic oxidation of other biomass-derived alcohols has also attracted significant attention as a promising route toward the production of high-value-added chemicals under mild and sustainable conditions.

2.1.3 Photocatalytic Selective Oxidation of Aromatic Alcohols

Many aromatic alcohols, such as benzyl alcohol and its derivatives, can be obtained from lignin depolymerization or biomass-derived intermediates, making their selective oxidation highly relevant in the context of biomass valorization.

Palmisano et al. [186] showed that TiO_2-based photocatalysts can promote the selective oxidation of aromatic alcohols to the corresponding aldehydes in aqueous media under mild irradiation conditions; however, high conversion is often accompanied by decreased selectivity due to TiO_2's strong oxidative nature, particularly in water. Their work further highlighted that surface chemistry and reaction environment strongly influence oxidation pathways and aldehyde selectivity. Despite extensive studies on TiO_2-based systems for alcohol oxidation, reports addressing noble-metal-free BiOX-TiO_2 heterojunctions for the selective oxidation of biomass-derived alcohols remain scarce.

2.1.4 Role of catalyst-substrate interaction

Yurdakal et al. [187] systematically studied the aqueous photocatalytic oxidation of salicyl alcohol over TiO_2 catalysts and demonstrated that catalyst-substrate interactions play a decisive

role in determining selectivity toward salicylaldehyde. They showed that adsorption of reaction intermediates on surface active sites can either preserve partial oxidation products or promote further oxidation, depending on the catalyst surface features. Similar conclusions were reported by Bui et al. [188], who observed progressive deactivation of TiO_2 during oxidative reactions due to strong adsorption of intermediates, leading to reduced catalytic efficiency over time.

2.1.5 TiO_2 limitations explicitly reported in literature

Fujishima et al. [189], provided an early comprehensive analysis of TiO_2 photocatalysis, emphasizing its high oxidative power and chemical stability, but also pointing out its intrinsic limitation related to UV-light activation. Tomita et al. [190] further reported that, although TiO_2-based systems can achieve high alcohol conversion, the selectivity toward aldehydes often decreases at prolonged irradiation times due to over-oxidation processes. These findings indicate that improving selectivity remains a key challenge for TiO_2-based photocatalytic oxidation systems.

2.1.6 Semiconductor coupling strategies for selective oxidation and biomass valorization

Qi et al. [191] reported that coupling TiO_2 with a second semiconductor can significantly improve charge separation and enhance selective oxidation performance by tuning the redox properties of the photocatalyst. Wolde et al reported that coupling oxidation and reduction reactions in photocatalytic systems can significantly improve charge separation and enhance overall photocatalytic efficiency [192]. Previous studies demonstrated that BiOCl-based and noble metal modified heterostructures exhibit enhanced activity toward selective alcohol oxidation; however, they also noted that the use of noble metals increases material cost and limits large-scale applicability [49,193]. Consequently, the development of noble-metal-free BiOX-based heterojunction photocatalysts remains an open research challenge. While these semiconductor coupling strategies have been widely explored for selective oxidation reactions, their specific application to glycerol photoreforming is more commonly associated with noble-metal-loaded TiO_2 systems, as discussed in the following section.

2.1.7 Noble-metal-loaded TiO_2 systems for glycerol photoreforming and the need for noble-metal-free catalysts

Numerous studies have reported that TiO_2 photocatalysts loaded with noble metals, particularly platinum, exhibit significantly enhanced activity toward glycerol photoreforming owing to improved charge separation and accelerated hydrogen evolution kinetics. For instance, Carozo et al. [194], systematically investigated Pt/TiO_2 systems prepared by photodeposition and demonstrated that the incorporation of low Pt loadings (0.15–0.60 wt.%) markedly increases H_2 production compared to bare TiO_2 under UV irradiation. Their results showed that Pt acts as an efficient electron sink, reducing electron-hole recombination and facilitating proton reduction at the metal sites. However, they also observed that excessive Pt loading can negatively affect performance due to the formation of recombination centers, indicating the existence of an optimal noble metal content. Despite their high efficiency, the reliance on noble metals such as Pt raises concerns related to cost, resource scarcity, and large-scale applicability, thereby motivating the development of noble-metal-free photocatalytic systems for sustainable glycerol valorization.

Despite extensive research on noble-metal-loaded TiO_2 systems, studies focusing on noble-metal-free heterojunction photocatalysts for glycerol photoreforming remain comparatively limited. In particular, BiOX-TiO_2 heterostructures have been predominantly investigated for pollutant degradation, while their potential for glycerol valorization and simultaneous H_2 production under solar irradiation has not been systematically explored. This gap in the literature motivates the investigation of simple and scalable BiOX-TiO_2 photocatalysts for integrated biomass valorization and energy production.

Literature reports that BiOX-TiO_2 heterojunctions are mainly synthesized via hydrothermal or solvothermal methods, often requiring high temperatures, long reaction times, and complex multi-step procedures involving surfactants or templates. Such energy-intensive synthesis routes may limit scalability and practical implementation.

On this basis, Table 2.1 summarizes representative BiOX-TiO_2 heterojunctions reported in the literature, highlighting their synthesis routes, coupling strategies, and main photocatalytic applications.

Table 2.1 Overview of reported BiOX-TiO_2 heterojunctions, their synthesis routes, coupling strategies, and photocatalytic applications reported in the literature.

Photocatalyst	Synthesis method	Conditions	Coupling method	Reaction	Light source	Ref.
BiOBr/TiO_2	Solvothermal method in ethylene glycol solution	120 °C, 12 h	Addition of TiO_2 during the solvothermal synthesis	Glycerol partial oxidation in aqueous H_2O_2 solution	120 W UV high-pressure mercury lamp	[195]
BiOCl/TiO_2–Zeolite	Hydrolysis–precipitation in nitric acid solution (aqueous, multi-step, pH control)	400–700 °C, 2 h	Sequential: TiO_2 loaded on zeolite, then BiOCl precipitated; heterojunction formed on zeolite support	Rhodamine B and formaldehyde degradation	500 W Xenon lamp	[196]
BiOCl/TiO_2 hierarchical composites	One-pot solvothermal method in ethylene glycol solution containing polyvinyl pyrrolidone (PVP)	180 °C, 8 h in Teflon-lined autoclave; PVP (0–1 g) controls morphology	Co-precipitation solvothermal method	Rhodamine B degradation	500 W Xenon lamp	[65]
BiOCl/TiO_2	Two-step hydrothermal in the presence of *n*-butyl alcohol + sol–gel + template-assisted	- Hydrothermal step 1: 80 °C, 4 h - Hydrothermal step 2: 100 °C, 20 h - Calcination: 450 °C, 4 h	In-situ stacking of BiOCl nanoplates on porous TiO_2 obtained from tetrabutyl orthotitanate	Rhodamine B degradation	220 W UV mercury lamp	[197]
BiOX (X = Cl, Br and I)/TiO_2	Hydrothermal method in	120 °C, 12 h	Addition of TiO_2 during the hydrothermal synthesis	Decomposition of perfluorooctanoic acid	30 W 254 nm UV light and 300 W	[198]

	ethylene glycol solution				Xenon lamp	
BiOCl/TiO_2	Hydrothermal method in ethylene glycol solution	160 °C, 8 h	Addition of TiO_2 during the hydrothermal synthesis	H_2O_2 production	300 W Xe lamp	[199]
BiOX (X = Cl, Br and I)/TiO_2	Solvothermal method in ethylene glycol and water mixture (volume ratio is 20:1) containing CTAB	160 ℃, 12 h	Coprecipitation in the presence of tetrabutyl titanate	Rhodamine B degradation	1000 W tungsten halogen lamp	[200]
BiOCl/TiO_2	Modified sol-gel method, drying at 105 °C for 8 h	600 °C 2h	Coprecipitation in the presence of tetrabutyl titanate	Rhodamine B and formaldehyde degradation	500 W Xenon lamp	[201]
BiOBr/TiO_2(P25)	Hydrothermal method in NaOH solution	200 °C, 24 h	TiO_2 treated in autoclave at 120 ◦C for 6 h in the presence of cetyltrimethylammonium bromide. BiOBr and TiO_2 were added to in 1:1 water and ethanol solution. This mixture was then heated to 120 °C, 1h.	Ciprofloxacin degradation	300 W metal halide lamp	[202]
BiOCl/TiO_2	Precipitation at room temperature in aqueous-ethylene glycol solution	140 °C, 5 h	TiO_2 was prepared hydrothermally by mixing tetrabutyl tita nate , ethanol and hydrofluoric acid. The mixture was stirred at 180 °C for 12 h	Hydrogen production from aqueous triethanolamine solutions	300 W xenon lamp	[203]

Unlike most literature reports summarized in Table 2.1, which mainly discuss hydrothermal or solvothermal synthesis routes involving high temperatures, long reaction times, surfactants, or multi-step procedures, the present work implements a simple, scalable, and noble-metal-free ball-milling strategy to prepare BiOX-TiO_2 heterojunctions. This approach avoids complex synthesis conditions and facilitates contact between the photocatalyst components while preserving structural simplicity, making it more suitable for practical applications. While the reported BiOX-TiO_2 systems have been investigated also for pollutant degradation, several studies indicate that both biomass valorization and pharmaceutical pollutant degradation are governed by comparable photocatalytic principles, particularly charge separation efficiency, interfacial charge transfer, and hole-driven surface oxidation pathways. As a result, photocatalyst systems synthesized for one application are frequently explored for the other, especially in the case of BiOX-based and TiO_2-based heterostructures. On this basis, the same photocatalyst platform in this thesis is systematically evaluated for multiple solar-driven applications, including biomass photoreforming for H_2 production, selective oxidation of biomass-derived molecules, pharmaceutical pollutant degradation, and photoelectrocatalytic processes, enabling a direct comparison of energy-related and environmental performances within a single material framework.

2.2 Photocatalytic degradation of pharmaceutical pollutants

To verify the versatility of the prepared BiOX-TiO_2 heterojunctions, we investigated the degradation of some pollutants like 4-nitrophenol and persistent pharmaceutical contaminants such as TC and OTC.

2.2.1 Tetracycline degradation

Photocatalytic degradation of tetracycline (TC) has been widely investigated due to its extensive use and persistence in aquatic environments. Recent studies have demonstrated that semiconductor-based photocatalysts operating under UV and visible irradiation can effectively remove TC from water. Phakathi et al. [204], reported that porous graphitic carbon nitride nanosheets achieved significant TC degradation under visible light, highlighting the role of extended light absorption and improved charge separation.

Gaffar et al. [205] further enhanced TC removal by employing $CuFe_2O_4$ and PANI/$CuFe_2O_4$ nanohybrids, demonstrating that heterojunction formation and surface modification can markedly improve photocatalytic activity. In addition to carbon-based systems,

MOF-derived and oxide-based heterostructures have attracted increasing attention. Jia et al. showed that the regulation strategies applied to UiO-66 significantly improved photocatalytic TC degradation efficiency, while maintaining structural stability [206]. Similarly, Li et al. [207], developed a $Bi_2Sn_2O_7/Bi_2MoO_6$ S-scheme heterojunction that exhibited high TC degradation efficiency and reduced toxicity of the transformation products. Despite these promising results, direct comparison among reported systems remains challenging due to differences in catalyst loading, irradiation sources, and initial TC concentrations, and many studies primarily emphasize degradation efficiency rather than mineralization and catalyst durability.

2.2.2 Oxytetracycline degradation

Oxytetracycline (OTC) is another widely used antibiotic frequently detected in wastewater and surface waters. Advanced oxidation processes coupled with photocatalysis have been extensively explored to enhance OTC degradation efficiency. Zhang et al. [208] reported that magnetic MOF-based photocatalysts activated persulfate under visible light, leading to efficient OTC degradation with good catalyst stability and recyclability. Ma et al. [209], demonstrated that MWCNTs-$CuNiFe_2O_4$ composites effectively activated persulfate, achieving high OTC removal even at elevated initial concentrations. Besides photocatalytic routes, conventional oxidation techniques such as ozonation have also been investigated. Li et al. [210] studied the ozonation of oxytetracycline and reported improved biodegradability and reduced toxicity of the treated effluents, suggesting that ozonation can serve as a useful pretreatment step in integrated treatment systems. Although high OTC degradation efficiencies have been reported, many systems rely on additional oxidants or complex catalyst synthesis, which may limit their practical applicability.

2.2.3 Ciprofloxacin degradation

Ciprofloxacin (CIP), a fluoroquinolone antibiotic, has raised considerable environmental concern due to its toxicity and contribution to antimicrobial resistance. Photocatalytic degradation of CIP was initially demonstrated using ZnO-based photocatalysts under UV irradiation, achieving moderate degradation efficiencies following pseudo-first-order kinetics [211]. Wen et al. [212], to enhance visible-light activity, developed a Z-scheme CeO_2-Ag/AgBr heterojunction, which significantly improved CIP degradation through enhanced charge separation and interfacial electron transfer. More recent studies have focused on photo-Fenton and photo-thermal synergistic approaches. Yang et al. [213], reported that rGO-$ZnFe_2O_4$ photocatalysts benefited from photo-

thermal effects, leading to accelerated CIP degradation under visible light. Similarly, Ge et al. [214], demonstrated that $LaFe_3$-based photo-Fenton catalysts achieved degradation efficiencies exceeding 98% under mild conditions. Despite these advances, the complexity of catalyst preparation and the need for auxiliary oxidants remain key challenges for large-scale applications.

To provide a more detailed benchmark specifically for TC, Table 2.2 compiles degradation efficiencies reported for a wider range of photocatalysts under different irradiation conditions.

Table 2.2 Tetracycline (TC) degradation efficiency reported for different photocatalysts.

Photocatalyst	**Irradiation**	**TC Concentration (mg L^{-1})**	**Catalyst quantity (g L^{-1})**	**TC degradation**	**References**
α-Fe_2O_3/TiO_2	500 W Halogen	30	0.614	97.5%	[215]
Cu_2O–TiO_2 Cu_2O coupled with TiO_2 nanotubes	Visible light	100	1.5	100%, 60 min	[216]
MWCNT/TiO_2 nano-composite	UVC irradiation	10	0.2	100% 100 min 37.3% mineralization	[217]
TiO_2@g-C_3N_4	Xenon Lamp	20	0.1	100%	[218]
Graphitic carbon nitride	Visible Light	10	1	77% 120 min	[204]
5-PANI/$CuFe_2O_4$	UV-Vis	50	0.1	86% 120 min 95% mineralization	[205]
$Bi_2Ti_2O_7$ (BTO)	Visible light	25	0.1	88.2% 150 min	[219]
CuO/Fe_2O_3	UV	20	0.05	88% 50 min	[220]
ZnO/γ-Fe_2O_3	UV-visible light	30	0.01	88.52% 150 min	[221]
Black graphitic carbon nitride (CN-B)	UV-Vis	30	0.05	92% 120 min	[222]
$AgI/BiVO_4$	300 W Xenon lamp	20	0.03	94.91% 60 min 90.5% mineralization	[223]
UiO-66-NDC/P–C_3N_4	UV Visible light	30	1	95% 120 min	[206]

				49 % mineralization	
3% SnO_2/g-C_3N_4	Visible Light	30	0.5	95.90% 120 min	[224]
[(L1(Ag_4I_7)]CH_3CN	Visible light	20	0.01	97.91% 180 min	[225]
ZnO/$NiFe_2O_4$/Co_3O_4	Natural solar Light	30	0.02	98% 20 min 90 % mineralization	[226]
$Bi_2Sn_2O_7$/Bi_2MoO_6	300 W-Xenon lamp	20	0.035	98.7% 100 min 56.4 % mineralization	[207]
MIL-88A	Visible light	200	0.25	99.8%	[227]
UiO-66-NH_2@WO_3/CC	Visible Light	20	0.02	100% 60 min	[228]

As summarized in Table 2.2, a wide range of photocatalysts have been explored for tetracycline degradation, often achieving high removal efficiencies under UV, visible, or solar irradiation.

2.2.4. Para nitrophenol

In addition to antibiotic contaminants, other organic pollutants such as nitrophenols have also been widely investigated as model compounds to study photocatalytic performance and oxidation mechanisms. Nawaz et al. [181] demonstrated that catalytic ozonation over mesoporous α-MnO_2 enhances the degradation efficiency of 4-nitrophenol while maintaining good resistance to catalyst leaching. Dieckmann and Gray [182] compared direct and sensitized photocatalysis in TiO_2 systems, highlighting the role of light absorption pathways in influencing degradation rates. Similarly, Di Paola et al. [183] reported that TiO_2 -based heterogeneous photocatalysis effectively degrades nitrophenols via hydroxyl radical-driven oxidation mechanisms.

CHAPTER 3

Materials and Methods

CHAPTER 3

3. Materials and Methods

3.1. Chemicals

Bismuth nitrate pentahydrate ($Bi(NO_3)_3 \cdot 5H_2O$), titanium tetrachloride ($TiCl_4$), sodium chloride (NaCl), potassium bromide (KBr), potassium iodide (KI), niobium(V) chloride ($NbCl_5$), platinum chloride, sodium tungstate dihydrate ($Na_2WO_4 \cdot 2H_2O$), glacial acetic acid (CH_3COOH), ethanol (CH_3CH_2OH), ethylene glycol, and nitric acid (HNO_3) were purchased from Sigma-Aldrich and used without further purification. Commercial TiO_2 P25 (Aeroxide) was employed as the reference photocatalyst. Tetracycline and oxytetracycline, thiabendazole and carbamazepine (Sigma-Aldrich), as well as 4-nitrophenol (Fluka Chemika), were used as model organic pollutants.

Biomass-derived substrates and reaction standards, including glycerol, glucose, fructose, arabinose, erythrose, gluconic acid, formic acid, and citric acid, were obtained from Sigma-Aldrich.

Aromatic alcohols, aldehydes, and corresponding carboxylic acids used as reference compounds, namely 4-methoxybenzyl alcohol, 4-methoxybenzaldehyde, 4-methoxybenzoic acid, 2-hydroxybenzyl alcohol, 2-hydroxybenzyl aldehyde, 2-hydroxybenzoic acid, furfuryl alcohol, furfural, 2-furoic acid, piperonyl alcohol, piperonal, piperonylic acid, vanillyl alcohol, vanillin, and vanillic acid, were also purchased from Sigma-Aldrich.

Tert-Butanol, silver nitrate ($AgNO_3$), benzoquinone, and sodium oxalate ($Na_2C_2O_4$) were employed as scavenging agents for hydroxyl radicals, electrons, superoxide radicals, and photogenerated holes, respectively.

5,5-Dimethyl-1-pyrroline-N-oxide (DMPO) and hydrogen peroxide (H_2O_2) were used as spin-trapping agents and radical promoters, respectively, for electron paramagnetic resonance (EPR) measurements.

Ammonium pentaborate was used as the supporting electrolyte for photoelectrochemical measurements.

Helium was employed to establish anaerobic conditions during photocatalytic experiments. Sulfuric acid was used for the preparation of the aqueous mobile phase employed in high-performance liquid chromatography (HPLC) analyses.

For high-performance liquid chromatography (HPLC) analysis of thiabendazole, acetonitrile was used as the organic component of the mobile phase. The aqueous mobile phase consisted of a phosphate buffer prepared from sodium dihydrogen phosphate (NaH_2PO_4, 5 mM) and disodium hydrogen phosphate (Na_2HPO_4, 12.5 mM) (obtained from sigma Aldrich).

Deionized water was used throughout all synthesis, characterization, and photocatalytic experiments.

2-Propanol (isopropanol) was employed for the dispersion of photocatalyst powders during scanning and transmission electron microscopy (SEM and TEM) sample preparation. Hydrochloric acid (HCl), together with nitric acid and sulfuric acid, was used for microwave-assisted digestion of photocatalyst samples prior to inductively coupled plasma–optical emission spectroscopy (ICP–OES) analysis.

Platinum wire and Ag/AgCl (saturated KCl) electrodes were used as counter and reference electrodes, respectively, in photoelectrochemical measurements.

Ultrapure deionized water was used throughout the study. For Thiabendazole study Milli-Q water was used.

3.2 Analytical determinations

3.2.1 Photons' absorption intensity of solar radiation

Solar irradiance was continuously monitored and recorded in units of $W \cdot m^{-2}$ at one-minute intervals using a UV radiometer (Kipp & Zonen CUV3, spectral range 280–400 nm). The sensor was mounted on a dedicated platform and oriented at the same inclination angle as the compound parabolic collector (CPC), corresponding to the local latitude (37°), to ensure accurate measurement of the incident radiation during the experiments.

3.2.2 HPLC-1

HPLC-I analyses were carried out for the identification and quantification of high-value products formed during photocatalytic reactions involving glucose, fructose, glycerol, furfuryl alcohol, and 5-hydroxymethylfurfural (HMF) as sacrificial agents. A Thermo Scientific Dionex Ultimate 3000 HPLC system, equipped with both diode array (DAD) and refractive index (RI) detectors, was employed for the quantitative determination of glucose and fructose as well as for the detection of their reaction products. Separation was achieved using a Phenomenex Rezex ROA-Organic Acid H^+ column, with 2.5 mM aqueous H_2SO_4 as the mobile phase at a flow rate of 0.6 $mL \cdot min^{-1}$.

3.2.3 HPLC-II

HPLC-II was used to investigate the oxidation of aromatic alcohols into their corresponding aldehydes and to monitor the degradation of organic pharmaceutical compounds. Analyses were performed using a Beckman Coulter HPLC system equipped with a diode array detector. A Phenomenex Kinetex C18 column (5 μm) was utilized for chromatographic separation. The mobile phase consisted of a mixture of acetonitrile and 13 mM trifluoroacetic acid (20:80, v:v), delivered at a flow rate of 0.8 $mL \cdot min^{-1}$. Identification and quantification of substrates and intermediates were carried out using external standards, which were also employed to construct calibration curves.

3.2.4. GC

The gaseous products generated during photocatalytic reactions were analysed using an HP 6890 Series gas chromatograph equipped with a thermal conductivity detector (TCD) and a Supelco packed column (GC 60/80 Carboxen™-1000). This system was used to determine the concentrations of hydrogen (H_2) and carbon dioxide (CO_2).

3.2.5 pH

The solution pH values were measured using a CRISON GLP22 multimeter throughout the experimental runs.

3.2.6 Total Organic Carbon (TOC) Analyzer

The degree of mineralization of organic pollutants was evaluated by measuring the total organic carbon (TOC) using a Shimadzu TOC-5000A analyser equipped with an automatic sample injector (ASI-5000A).

3.2.7 UV-Vis Spectrophotometry

UV-visible absorption spectra of reaction samples were recorded using a Shimadzu UV-2401 PC spectrophotometer.

3.3. Materials characterizations

3.3.1 Brunauer-Emmett-Teller (BET)

The determination of the specific surface area of the photocatalysts (SSA) was performed by the single-point BET method using a Flow Sorb 2300 device (Micromeritics).

3.3.2 UV-Visible Diffuse Reflectance Spectroscopy (DRS)

The optical characteristics of the powders were analyzed by UV-visible diffuse reflectance spectroscopy (DRS) by means of a a Shimadzu UV-2401 PC.

3.3.3 Photoelectrochemical Photocurrent Spectroscopy (PEC-PS)

The photoelectrochemical characterization was carried out by irradiating the samples (through a quartz cell window) with a 450 W xenon lamp coupled to a monochromator. A lock-in amplifier extracted the photocurrent from the overall cell current, a potentiostat adjusted the electrode potential, and a mechanical chopper operating at 13 Hz allowed intermittent irradiation. For these measurements, The photocatalysts were deposited on carbon paper (Toray 40% wet Proofed-E-Tek) and immersed in a 0.1 M ammonium pentaborate (ABE) solution (pH ~ 9) inside a three-electrode cell where a platinum wire served as the counter electrode and a silver/silver chloride (Ag/AgCl/sat. KCl) electrode as the reference electrode (0 V vs Ag/AgCl = 0.197 V vs SHE).

3.3.4 X-ray Diffraction (XRD)

The crystalline structure of the samples, was determined by an XRD Panalytical Empyrean diffractometer in 2Q range 20°-80° angle with Cu Kα radiation (1.5406 Å) in 0.02 step size using the program reflection transmission spinner (RTS). X-ray tension was 45 kV and current 40 mA.

3.3.5 Raman Spectroscopy

Raman analyses were carried out in a confocal Witec Alpha 300R Raman spectroscope. Samples were excited with a 532 nm laser having a single mode output power of 52 mW and the scattered light was collected in a back scattering configuration with the aid of a 50× objective lens. All Raman analyses were carried out at room temperature, with an integration time of 0.5 s and 100 accumulations. The signals were registered in the range 50–700 cm^{-1}.

3.3.6 Scanning Electron Microscopy (SEM) and Transmission Electron Microscopy (TEM)

A Nova NanoSEM was used to observe the morphology and dimensions of samples. The sample was prepared by suspending the powder in 2-propanol, treating with ultrasound, and finally depositing 2 μL of the suspension on carbon tape attached to a stainless-steel stub. The solvent was then evaporated at room temperature. An energy dispersive spectrometer (EDS) was used for elemental analysis purposes.

Tecnai G2 transmission electron microscope operating at 200 kV was employed for transmission electron microscopy (TEM) analysis. Samples were prepared by suspending the

powder in 2-propanol, ultrasonicating it, and then dropping 3 µL of the suspension twice on a 300 mesh Cu grid supplied by Tedpella. Finally, the solvent was evaporated at room temperature. The electron beam was focused to a fine point and scanned over the sample in a raster illumination system.

3.3.7 Photoluminescence Spectroscopy (PL)

Photoluminescence spectra (PL) were recorded in emission mode with an excitation at 300 nm by using a Perkin Elmer LS 55 spectrometer between 320 and 580 nm (100 nm/min scan rate).

3.3.8 Inductively Coupled Plasma-Optical Emission Spectroscopy (ICP-OES)

Inductively coupled plasma-optical emission spectroscopy (ICP-OES) was performed using an Agilent T 5100 inductively coupled plasma optical emission spectrometer to determine the concentration of bismuth in the BiOCl-TiO_2 and BiOBr-TiO_2 composites at a wavelength of 306.77 nm. Prior to the analysis, 15 mg of the sample is first digested using a CEM Mars 6 microwave digestion system at a temperature of 210 $^{\circ}$C for 30 mins in a 10 mL mixture of concentrated HNO_3, HCl, and H_2SO_4 with a volumetric ratio of 1:3:12, respectively. After cooling, the digestate (complete digestion was observed with clear colourless digestate) was diluted with deionized water to a final acid concentration of 2% to abide by the ICP- OES equipment limitation.

3.3.9 Electron Paramagnetic Resonance (EPR) Spectroscopy

For the identification of free hydroxyl radical species ($^{\bullet}OH$) formed after irradiation of the photocatalysts, electron paramagnetic resonance (EPR) was carried out by a Bruker EMX-nano spectrometer equipped with a lamp emitting high intensity UV radiation. 1 mg of catalyst was dispersed in 25 mL of deionized water using ultrasonication. Subsequently, to 100 µL of the resultant suspension, 90 mM of the trapping agent 5,5 Dmethyl-1-pyrroline N-oxide (DMPO) and 1mM of H_2O_2 were mixed. After stirring, the mixture was placed in a capillary tube and transferred to the EPR test chamber for analysis. The sample was irradiated for 10 minutes using a UV lamp and data were recorded. The Centre Field was fixed at 3480 G with 100 G Sweep Width. The Modulation Amplitude, Attenuation, and Receiver Gain were fixed at 1G, 10 dB, and 40 dB, respectively. The Scan Number and Modulation Frequency were settled at 1 time and 100 kHz, respectively.

3.4 Photocatalytic activity

The photocatalytic activity of the synthesized materials was evaluated under different conditions using various organic substrates, including glycerol and glucose, at room temperature and atmospheric pressure. For hydrogen production experiments, reactions were performed under anaerobic conditions, and the evolution of H_2 and CO_2 in the gas phase was monitored by gas-chromatography, while the formation of reaction intermediates was analysed in the liquid phase by HPLC. Photocatalytic degradation experiments involving pharmaceutical compounds, namely tetracycline and oxytetracycline, as well as p-nitrophenol, were carried out under aerobic conditions in reactors open to the atmosphere. In the case of tetracycline and oxytetracycline degradation, a continuous flow of oxygen was bubbled through the reaction suspension throughout the entire irradiation period to ensure sufficient dissolved oxygen availability.

Different cylindrical Pyrex batch reactors with working volumes of 150 and 500 mL were employed, depending on the specific reaction system. For experiments carried out under anaerobic conditions, helium gas was bubbled through the aqueous suspension for 30 minutes before irradiation in order to remove the dissolved oxygen and to establish adsorption–desorption equilibrium between the substrate and the catalyst surface. After this pretreatment, the reactor was sealed and irradiated using either a near-UV lamp (125 W medium-pressure mercury lamp) or a halogen lamp with a nominal power of 150 W or 50 W, depending on the experimental requirements.

The initial concentrations of the substrates were fixed at 0.5 mM for glucose and alcohols and 2 mM for glycerol while for drugs was 100 ppm and 20 ppm for PNP. All reactions were performed at the natural pH of the aqueous suspension, which was measured after the addition of the photocatalyst. The catalyst loading was adjusted according to the specific material under investigation. To evaluate the substrate adsorption in the absence of light, control experiments were carried out by stirring the catalyst–substrate suspension in the dark for 30 minutes, after which the residual substrate concentration was determined. The duration of the photocatalytic reactions was 5 hours for glycerol and glucose, 4 hours for pharmaceutical compounds, and 2 hours for p-nitrophenol. Liquid samples were collected at fixed time intervals during irradiation and filtered through 0.2 μm membrane filters (HA, Millipore) prior to analysis.

For the selective oxidation of alcohols, an analogous experimental protocol was followed under aerobic conditions, using halogen lamp irradiation. These reactions were carried out for a

total duration of 4 hours. A schematic representation of the experimental setup is presented in Figure 3.1.

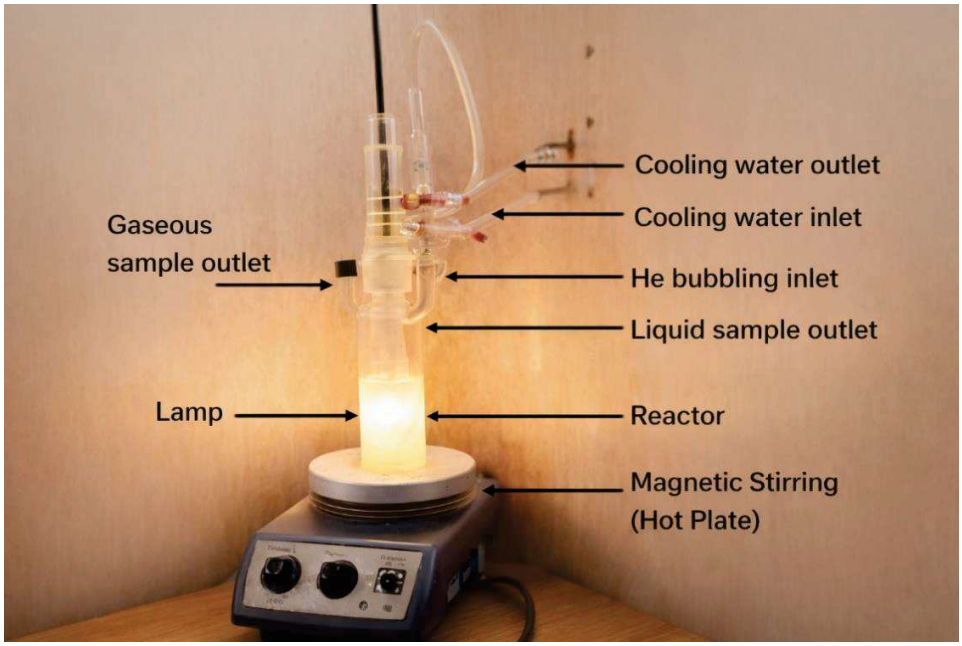

Figure 3.1. Experimental setup used for photocatalytic activities.

3.4.1 Investigation of adsorption behaviour and scavenging species

The extent of adsorption of the substrate and its intermediates on the catalyst surface was determined in the dark after 2 h of stirring the aqueous mixture. To investigate the contribution of the active species formed under irradiation on partial and selective oxidation, trapping experiments were carried out in the presence of selected scavengers such as tert-butanol, $AgNO_3$, and benzoquinone, $Na_2C_2O_4$. (concentration 1mM), used as $^{\bullet}OH$, e^-, $^{\bullet}O_2^-$, and h^+ scavengers, respectively.

3.4.2 Data analysis and calculation of conversion and selectivity

Conversion and the selectivity towards the formed products were calculated as follows:

$$\text{Conv \%} = \frac{\text{initial moles of the substrate} - \text{moles of substrate after fixed time}}{\text{initial moles of the substrate}} \times 100 \quad \text{Eq. 1}$$

$$\text{Selectivity \%} = \frac{\text{moles of a specific product}}{\text{moles of substrate converted}} \times 100 \quad \text{Eq. 2}$$

3.4.2. Solar box

The reactor was placed inside a solar simulator (Solar box 1500 standard, CO.FO.ME.GRA, Italy) provided with a 1500 W Xenon Lamp and a cutoff filter for $\lambda < 300$ nm. The total irradiance between 300 and 800 nm was estimated to be 328.7 W m^{-2}.

CHAPTER 4

Preparation and Characterization of Bismuth Oxyhalides and P25 Composites Photocatalysts

CHAPTER 4

4. Preparation and characterization of BiOX (X=Cl, Br, I) and BiOX-P25 Composites

4.1 Preparation of Photocatalysts

4.1.1 Methodology

Bismuth oxyhalides BiOX (X= Br, Cl, I) photocatalysts were synthesized by using a co-precipitation method as reported in the literature [229]. 9 mmol of Bi $(NO_3)_3 \cdot 5H_2O$ (Sigma Aldrich) were dissolved it in 30 mL of glacial acetic acid and then 90 mL of distilled water was added in solution which was stirred for 1 hour and marked as Solution A. Solution B was prepared by adding 9 mmol KBr (for BiOBr) and 9 mmol NaCl in 90 mL of distilled water and stirred for 1 hour. Finally, solution B was added drop by drop into solution A, and a white precipitate was formed. After uniform mixing, the mixture was stirred constantly for 12 h by means of a magnetic stirrer. After washing, filtration, and drying, it was calcined at 150°C for 12 hours in an oven. The optimum BiOX concentration was determined by means of transmitted photonic flow measurements using a Quantum Photo radiometer. It was 0.15 g/150 mL, corresponding to 1 g/L.

4.1.2 Composites Synthesis by Ball Milling

The two semiconductors, i.e. BIOX (BiOBr, BiOCl, BiOI) and TiO_2 (P25) (Aeroxide) were mixed in different weight ratios (3, 4, 5 and 7%) and named X%BiOX-TiO_2 (where X % indicates the BiOX weight percentage). The powders were kept inside a chrome steel jar coated with zirconium oxide and filled with 6 zirconium oxide balls, and ground in the open air at room temperature for 2 h by using a planetary ball mill (PM 100, Retsch-Allee 1–5, 42,781 Haan, Germany). At a rotation speed of 150 rpm [46]. After the treatment, the mixtures were hand-ground.

4.1.3 Photodeposition Synthesis

Some photocatalysts were loaded with 0.5 wt% Pt by a photo-deposition method. Distilled water (400 mL), ethanol (100 mL), $PtCl_4$ (0.0172g) and photocatalyst (2g) were added to the photoreactor. The resulting dispersion was stirred in the dark for 0.5 h by bubbling N_2 and then irradiated for 7 h. The resulting mixture was filtered, washed with distilled water, and then dried in an oven for 6 h.

4.1.4 Photocatalytic activity

The photocatalytic activity was studied both in anaerobic and aerobic conditions by using different substrates at room temperature and atmospheric pressure. The reactions were carried out in a 150 mL reactor for photoreforming and 500 ml for photo remediation and selective oxidation of alcohols by stirring at 400 rpm at natural pH. Typically, 2 mM glycerol, 0.5mM Glucose, 100 ppm drugs, 0.5mM alcohols solution and a certain amount of catalyst (0.15g for BiOX and 0.45g for P25) were charged into the reactor and irradiated by 125 W medium-pressure mercury lamp (aerobic conditions) or 150 W Halogen lamps (in both aerobic and anaerobic conditions). The experiments had a duration of 5 hours at room temperature, and samples were collected every 1 hour. The liquid products were analysed by High Performance Liquid Chromatography (HPLC) while the gaseous ones by Gas Chromatography (GC).

The amount of photocatalyst employed in all experiments was optimized in order to ensure absorption of approximately 90% of the incident photons, as determined by transmitted photonic flow measurements. This criterion allowed a reliable comparison of intrinsic photocatalytic activity among different materials, minimizing optical artefacts related to light scattering or shielding.

4.2 Characterization Techniques for BiOX (X=Cl, Br, I) Study

4.2.1 Powder X-ray diffraction (PXRD)

Powder X-ray diffraction (PXRD) is a versatile tool to characterize the structural properties (phase purity, crystallinity, crystallite size, lattice parameters, etc.) of the solid material. The powder XRD patterns of bare TiO_2 and BiOX (X=Cl, Br)-TiO_2 composite samples are shown in Figure 4.1 (a and b). For convenience purposes, the XRD diffractograms are stacked one above the other. The predominant phase for all the composites matches precisely with anatase TiO_2 (JCPDS#84-1285) [230]. TiO_2 is further confirmed to be present in the composite samples as confirmed by EDX analysis; this will be addressed in more detail in the following section. XRD pattern of bare BiOCl indicates the formation of tetragonal crystalline BiOCl (JCPDS#73-2060) [231], whose main peaks are distinguishable even in composite samples, confirming the formation of a heterostructure in all samples prepared. In the pattern of BiOCl-TiO_2 composites (Figure 4.1a), the peaks at 32.5°, 33.3° and 47.2° besides the ones from TiO_2, were denoted. Furthermore, the prepared BiOBr NPs (Figure 4.1b) are in the tetragonal structure in accordance with JCPDS#25-0390 [232]. The BiOBr-TiO_2 NPs possess the feature peaks of both P25 and BiOBr, indicating that the BiOBr NPs have

been successfully coupled with P25 through the ball milling method. The BiOCl structure consists of Cl-Bi-O-Bi-Cl layers in the XY plane, stacked along the z-axis. The increase of BiOCl content (e.g., 3%, 5%, and 7%), promotes its growth along the z-axis, diminishing the relative influence of TiO_2 intergrowth and increasing the (101) reflection intensities [233]. A similar effect was observed in the samples containing BiOBr.

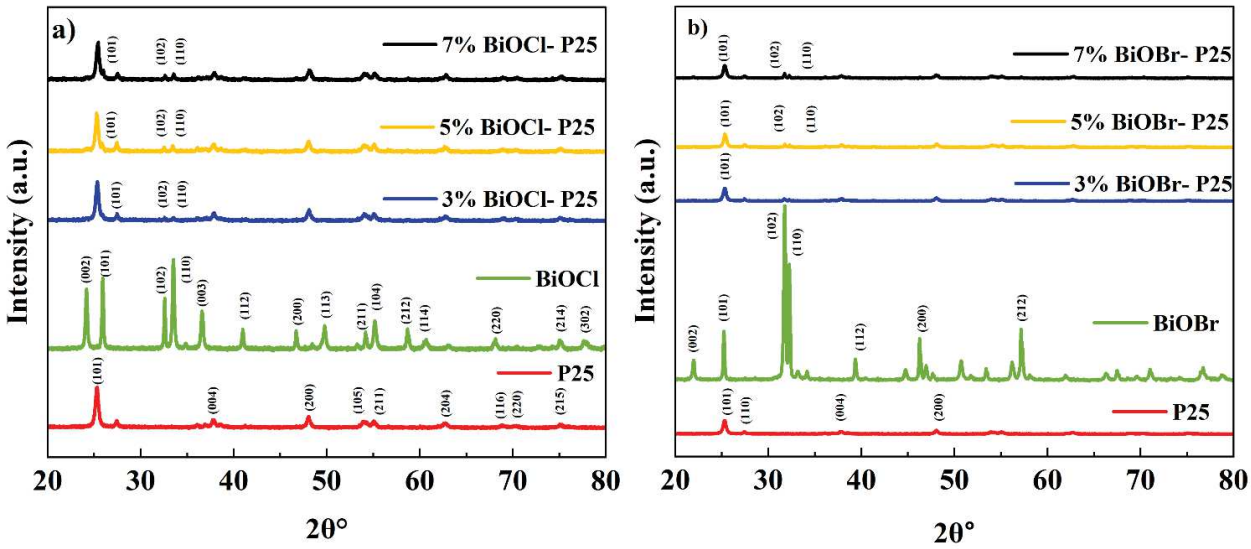

Figure 4.1. XRD patterns of (a) Bare P25, BiOCl and Y%BiOCl-P25 composites (Y=3,5,7 w/w%), (b) Bare P25, BiOBr and Y%BiOBr-P25 composites (Y=3,5,7 w/w%).

4.2.2 Raman Spectroscopy

Figure 4.2 (a-b) shows the Raman spectra of the composite photocatalysts, which confirms the successful formation of P25/BiOX heterostructured samples. The Raman spectrum of P25 exhibits several peaks at 144 cm^{-1}, 197 cm^{-1}, 395 cm^{-1}, and 640 cm^{-1}, corresponding to the optical phonos of anatase TiO_2. These peaks can be ascribed to five Raman-active modes with the symmetries of E_g, E_g, A_{1g}, B_{1g}, and E_g, respectively [234]. For BiOCl, the signal at 139 cm^{-1} corresponds to the A_{1g} vibration mode, associated with Bi-Cl A_{1g} internal stretching, while the peak at 202 cm^{-1}, is attributed to the E_g internal Bi-Cl stretching mode. Three distinct peaks at 144 cm^{-1}, 201 cm^{-1}, and 398.5 cm^{-1} can be assigned to three different Raman modes of BiOCl. A significant reduction in the intensity of BiOCl Raman bands is observed after introducing P25 species. This reduction is likely due to the well-dispersed BiOX (X=Cl, Br) within P25, which absorbs or scatters the laser

light during Raman surface analysis. The introduction of BiOX in P25 probably also leads to the formation of defects, such as oxygen vacancies, reducing the crystal quality of P25, as also confirmed by the peaks intensity decreases after coupling [235]. According to Wang et al. [236], the formation of oxygen vacancies can result in a shift of the E_g mode. In addition, structural distortions in BiOX (X=Cl, Br) due to the integration with P25 can alter the Raman spectrum. The observed shift of the E_g peaks towards the lower wavenumber indicates an increase in oxygen vacancy defect caused by the substitution of P25 with BiOX (X= Cl, Br) .

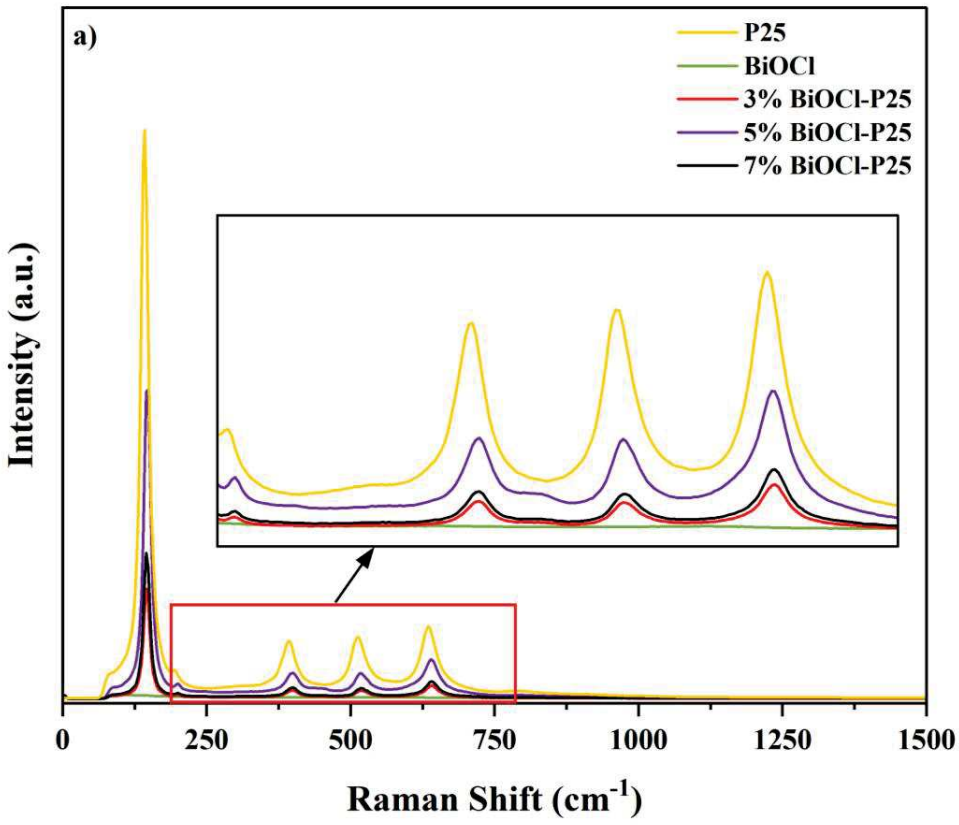

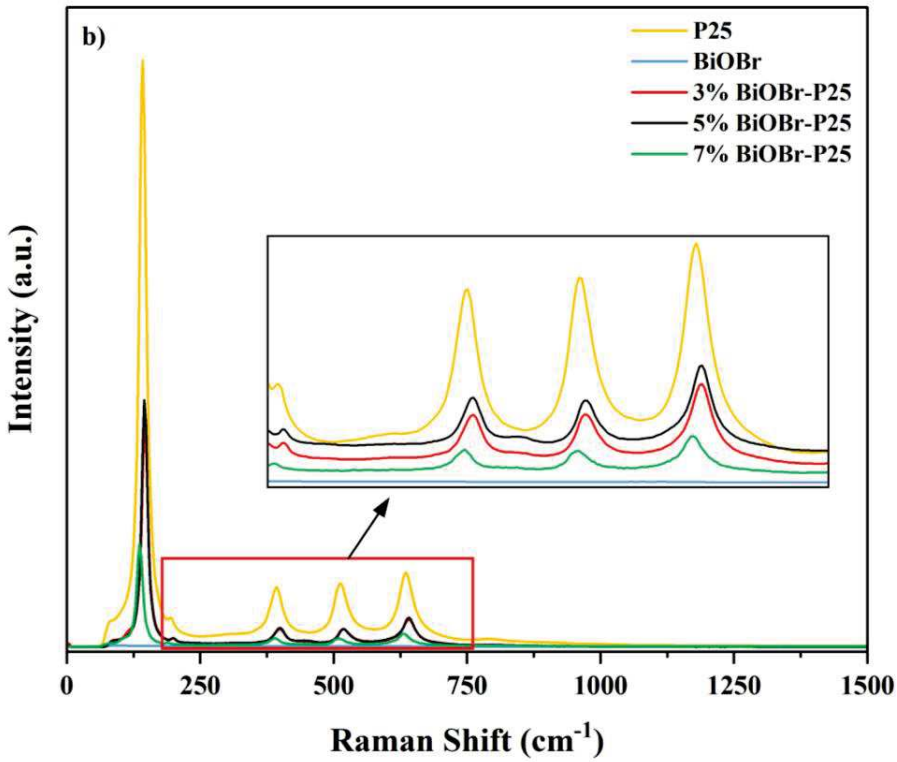

Figure 4.2. Raman Spectra of (a) Bare P25, BiOCl and Y%BiOCl-P25 composites (Y=3,5,7 w/w%), (b) Bare P25, BiOBr and Y%BiOBr-P25 composites (Y=3,5,7 w/w%).

4.2.3 UV-visible Spectroscopy

The UV-vis spectra of the used samples are reported in Figures 4.3a and b. Band gap values of all the samples, determined by plotting the modified Kubelka-Munk function, $F(R'_{\infty})hv]^{½}$, versus the energy of the incident light [46,65] are shown in Table 4.1. It can be noted that all the powders absorb light in the UV-Visible region, and the spectrum of the bare commercial P25 is typical of anatase TiO_2. In fact, although the sample is made of a mixture of anatase and rutile, the latter phase is present in a smaller quantity. At around 380 nm, corresponding to a band gap of 3.10 eV, an onset of absorption can be observed.

4.2.4 Photoluminescence Spectroscopy

The BiOCl sample absorbs at lower wavelengths and the BiOCl-P25 composites have spectra very similar to that of P25; BiOBr and the mixed BiOBr-P25 composites (Figure 4.3d, c) resemble P25, the latter being the main component, as can also be seen by analysing the corresponding band gaps. The photoluminescence (PL) spectra for TiO_2 (P25) and its composites with BiOCl (Figure

4.3c) and BiOBr (Figure 4.) reveal the effect of hosted oxide concentration on charge carriers' recombination rate in TiO_2. The peak at ca. 418 nm derives from the direct band-to-band transition on TiO_2, whilst the peak at ca. 460 nm visible in bare BiOX samples can be ascribed to the indirect oxygen vacancies-valence band electron–hole recombination [237].

Pure materials, namely BiOBr and BiOCl, exhibit lower PL intensities compared to P25, indicating a lower rate of radiative recombination [238]. Upon forming composites of BiOCl with TiO_2, the order of the PL intensities, as depicted in Figure 4.3c is: 5% BiOCl-P25 > 7% BiOCl-P25 > P25 > 3% BiOCl-P25 > BiOCl. The observed PL trend for BiOCl/TiO_2 composites suggests that the interaction between BiOCl and TiO_2 influences charge carrier dynamics in a non-linear manner, probably due to the simultaneous occurrence of two phenomena: The decrease in the recombination rate of the charges (which corresponds to a decrease in photoluminescence) and the formation of oxygen vacancies (which corresponds to an increase in photoluminescence) [239].

At 3% BiOCl-P25, the PL intensity is lower than at 5%, suggesting that insufficient BiOCl loading might not create enough interaction sites for efficient charge separation [231]. This trend implies that there is an optimal BiOCl loading (around 5%) where the balance between charge transfer and recombination is most favourable, and higher or lower loadings disrupt this balance.

In the composites BiOBr-TiO_2 samples the order of the PL intensities as depicted in Figure 2d is: 3% BiOBr-P25 > 5% BiOBr-P25 > P25 ~ 7% BiOBr-P25> BiOBr. The photoluminescence of 7% BiOBr-P25 is very similar to that of P25 and increases by decreasing the BiOBr amount, probably ascribable to a higher defect concentration and/or an increase in the charge recombination rate.

The data reported in Table 4.1 indicate a decrease in the band gap for the BiOX samples with increasing atomic number of the halogen, and this agrees with the literature [195].

Pristine BiOX present (Table 4.1) a small surface area (< 4 $m^2 g^{-1}$), but it increases significantly in composite samples since TiO_2 P25, which is their major component, has an area of 50 $m^2 g^{-1}$.

Table 4.1 Specific surface area and band gap of the used photocatalysts.

Catalyst	S.S.A. (m^2 g^{-1})	Band gap (eV)
BiOCl	3.3	3.48
3%BiOCl-P25	39.1	3.10
5%BiOCl-P25	32.5	3.08
7%BiOCl-P25	37.8	3.10
BiOBr	3.6	2.88
3%BiOBr-P25	38.5	3.10
5%BiOBr-P25	37.3	3.10
7%BiOBr-P25	38.2	3.10
P25	50.0	3.10

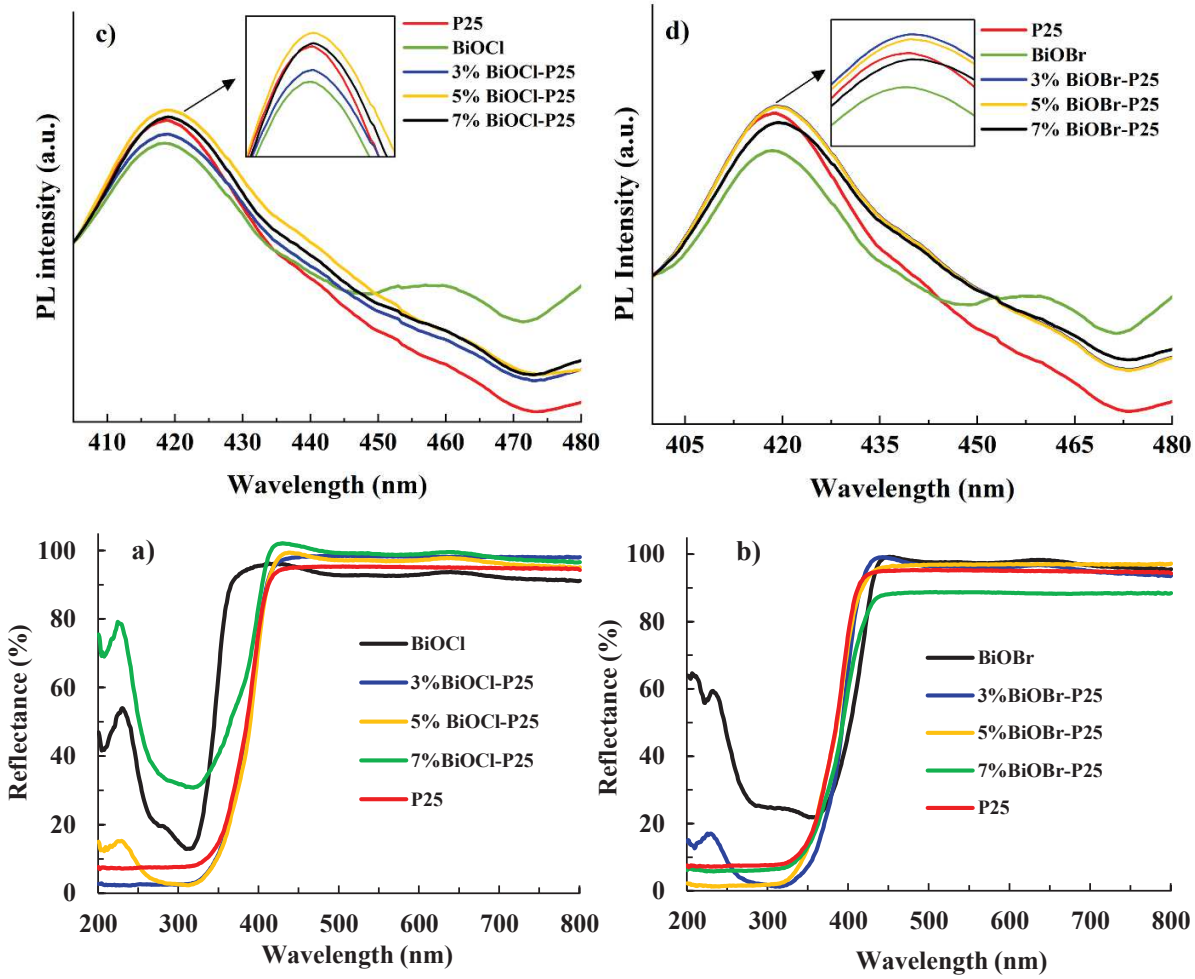

Figure 4.3. UV-Vis reflectance and photoluminescence spectra of (a-c) Bare P25, BiOCl and Y%BiOCl-P25 composites (Y=3,5,7 w/w%), (b-d) Bare P25, BiOBr and Y%BiOBr-P25 composites (Y=3,5,7 w/w%).

4.2.5 Scanning electron microscopy (SEM)

Scanning electron microscopy (SEM) can be utilized to observe the morphology of the samples. BiOCl exhibits a tightly stacked sheet-like structure, as shown in Figure 4.4a. Upon the coupling with P25, the morphology is practically coincident with that of P25 [240] due to its higher amount (Figure 4.4b). Moreover, during the ball milling process an aggregation of BiOCl into an irregular structure can occur. The same trend can be found in BiOBr (Figure 4.4c) and BiOBr-P25 (Figure 4.4d) samples. In Figures 4.4 e-f, the elemental mapping illustrates the distribution of Bi,

O, Cl, Br, and Ti, showing that all elements are uniformly dispersed and confirming an intimate contact among P25 and BiOCl or BiOBr. It is worth noting that the Bi signal in the EDX analysis was relatively weak, likely due to the heterogeneous distribution of BiOCl/BiOBr within the composite. Since EDX primarily provides information from the surface top layers, it may not fully capture the overall Bi content of the material. To achieve a more accurate and representative measurement of the Bi concentration throughout the entire sample, ICP-OES analysis was performed, offering a more reliable and bulk-sensitive quantification of the elemental composition.

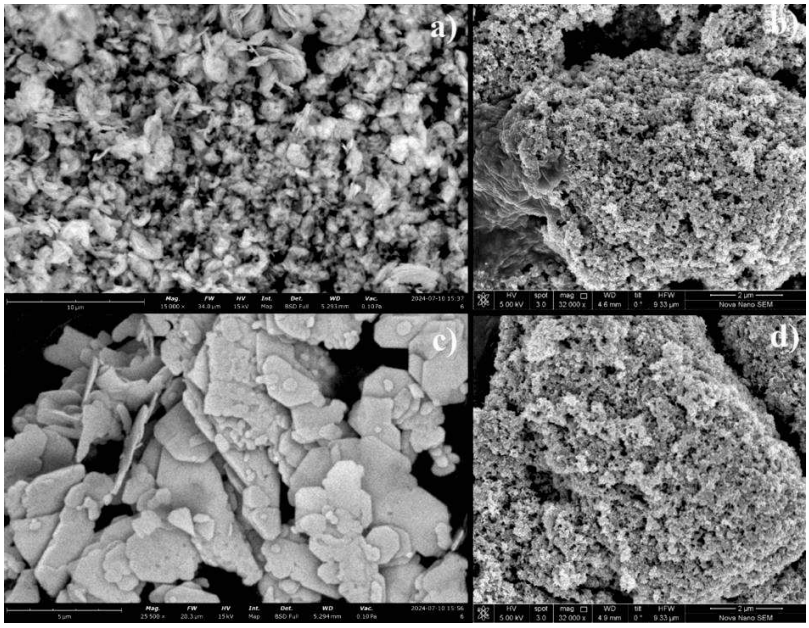

Figure 4.4. SEM images of (a) Bare BiOCl; (b) 5% BiOCl-P25; (c) Bare BiOBr; (d) 5% BiOBr-P25.

4.2.6 Elemental Diffraction Xray (EDX)

In Figures **4.5 e-f,** the elemental mapping illustrates the distribution of Bi, O, Cl, Br, and Ti, showing that all elements are uniformly dispersed and confirming an intimate contact among P25 and BiOCl or BiOBr. It is worth noting that the Bi signal in the EDX analysis was relatively weak, likely due to the heterogeneous distribution of BiOCl/BiOBr within the composite. Since EDX primarily provides information from the surface top layers, it may not fully capture the overall Bi content of the material.

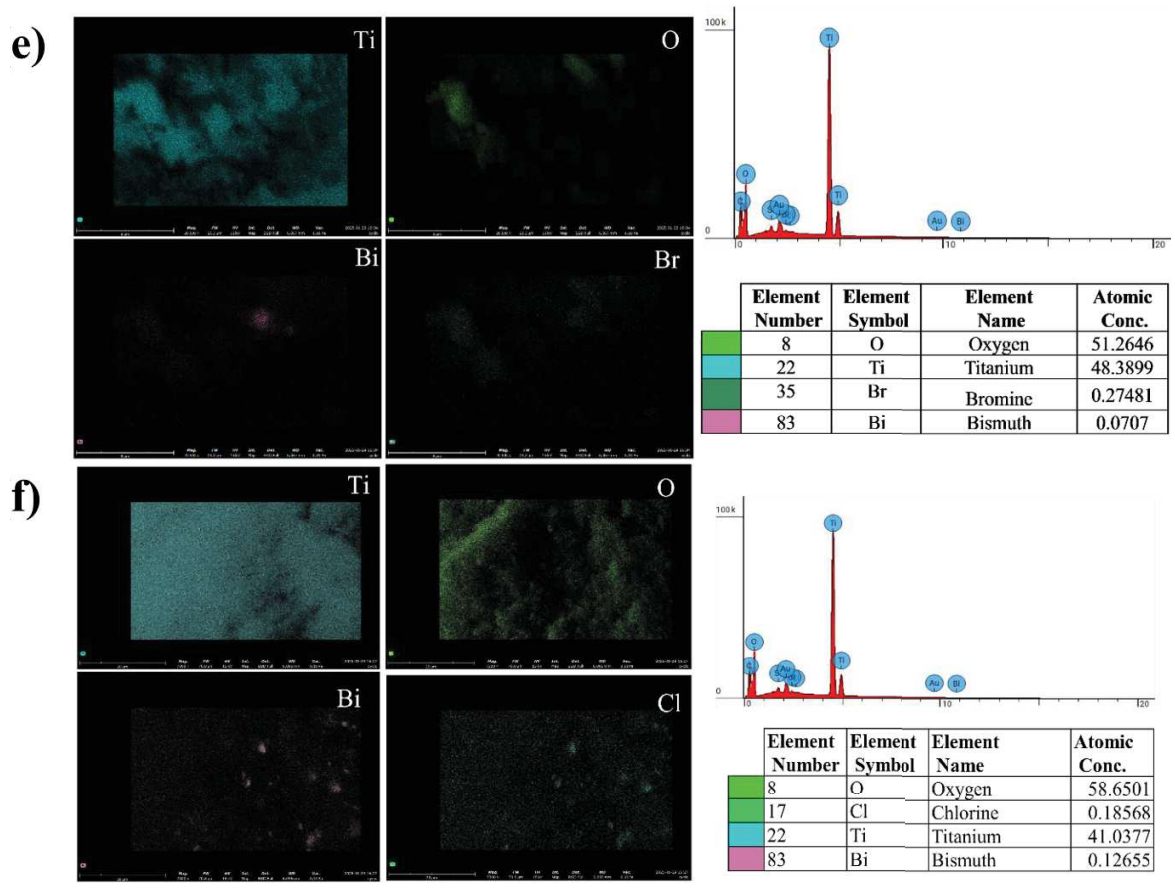

Element Number	Element Symbol	Element Name	Atomic Conc.
8	O	Oxygen	51.2646
22	Ti	Titanium	48.3899
35	Br	Bromine	0.27481
83	Bi	Bismuth	0.0707

Element Number	Element Symbol	Element Name	Atomic Conc.
8	O	Oxygen	58.6501
17	Cl	Chlorine	0.18568
22	Ti	Titanium	41.0377
83	Bi	Bismuth	0.12655

Figure 4.5. EDX analysis of (e) 5%BiOCl-P25; (f) EDX analysis of 5%BiOBr-P25.

4.2.7 Inductively Coupled Plasma Optical Emission Spectroscopy (ICP-OES)

To achieve a more accurate and representative measurement of the Bi concentration throughout the entire sample, ICP-OES analysis was performed, offering a more reliable and bulk-sensitive quantification of the elemental composition.

The Inductively Coupled Plasma Optical Emission Spectroscopy (ICP-OES) technique was used to analyse the elemental composition of 5% BiOX (X=Cl, Br) composites, providing insight into the successful incorporation and retention of BiOCl and BiOBr within the TiO_2 matrix. The measured bismuth (Bi) content in the BiOCl-TiO_2 composite was 2.86 wt%, which is lower than the theoretical value expected for a 5 wt% BiOCl loading. Using the molar mass ratio of Bi to BiOCl (80.26%), the actual BiOCl content was determined to be 3.56 wt%, indicating some degree of underestimation. Similarly, for the BiOBr-TiO_2 composite, the measured Bi content was 3.21 wt%, which is also lower than the theoretical expectation for a 5 wt% BiOBr loading. Considering

the molar mass ratio of Bi to BiOBr (73.91%), the actual BiOBr content was calculated to be 4.34 wt%, demonstrating a comparable deviation from the intended composition.

Several factors may contribute to these discrepancies, including inherent inaccuracies in ICP-OES measurements. Despite these variations, the successful detection of Bi in both samples confirms the incorporation of BiOCl and BiOBr into the TiO_2 matrix, which is crucial for their photocatalytic performance.

4.2.8 High-Resolution Transmission Electron Microscopy (HRTEM)

The structural and morphological properties of the BiOCl-P25 and BiOBr-P25 composites were examined using high-resolution transmission electron microscopy (HRTEM) and selected area electron diffraction (SAED). Figure 4.6 shows Low-magnification TEM images (Figures 4.6a and 4.6d) which provide an overview of the composites' morphology, revealing a heterogeneous distribution of quasi-spherical nanoparticles with distinct contrast variations, indicative of the coexistence of BiOCl, BiOBr, and TiO_2 phases [231]. The observed differences in contrast suggest the layered structure of BiOCl and BiOBr and the agglomerated nature of TiO_2 nanoparticles. High-resolution TEM images (Figures 4.6b and 4.6e) confirm the presence of well-defined lattice fringes, characteristic of BiOCl, BiOBr, and TiO_2. The measured interplanar spacings were compared with standard crystallographic values, where the lattice fringe spacing of 0.35 nm in Figure 4.6b corresponds to the (101) plane of anatase TiO_2, confirming the presence of TiO_2 nanocrystals in the composite [241]. Additionally, a lattice spacing of 0.22 nm is attributed to the (110) plane of BiOCl, supporting the structural integrity of BiOCl within the composite [242]. Figure 4.6e further substantiates these findings, with a d-spacing of 0.75 nm, corresponding to the (001) plane of BiOCl, while the 0.35 nm spacing is again assigned to TiO_2 (101). Moreover, the BiOBr-P25 composite in Figure 5e exhibits a distinct d-spacing of 0.35 nm, attributed to the (101) plane of BiOBr, confirming the successful incorporation of BiOBr within the composite structure [232]. The SAED pattern (Figure 4.c) exhibits distinct diffraction spots forming polycrystalline rings, indicative of the crystalline nature of the BiOCl-TiO_2 composite. The clarity of the diffraction spots further suggests high crystallinity within the composite [243].

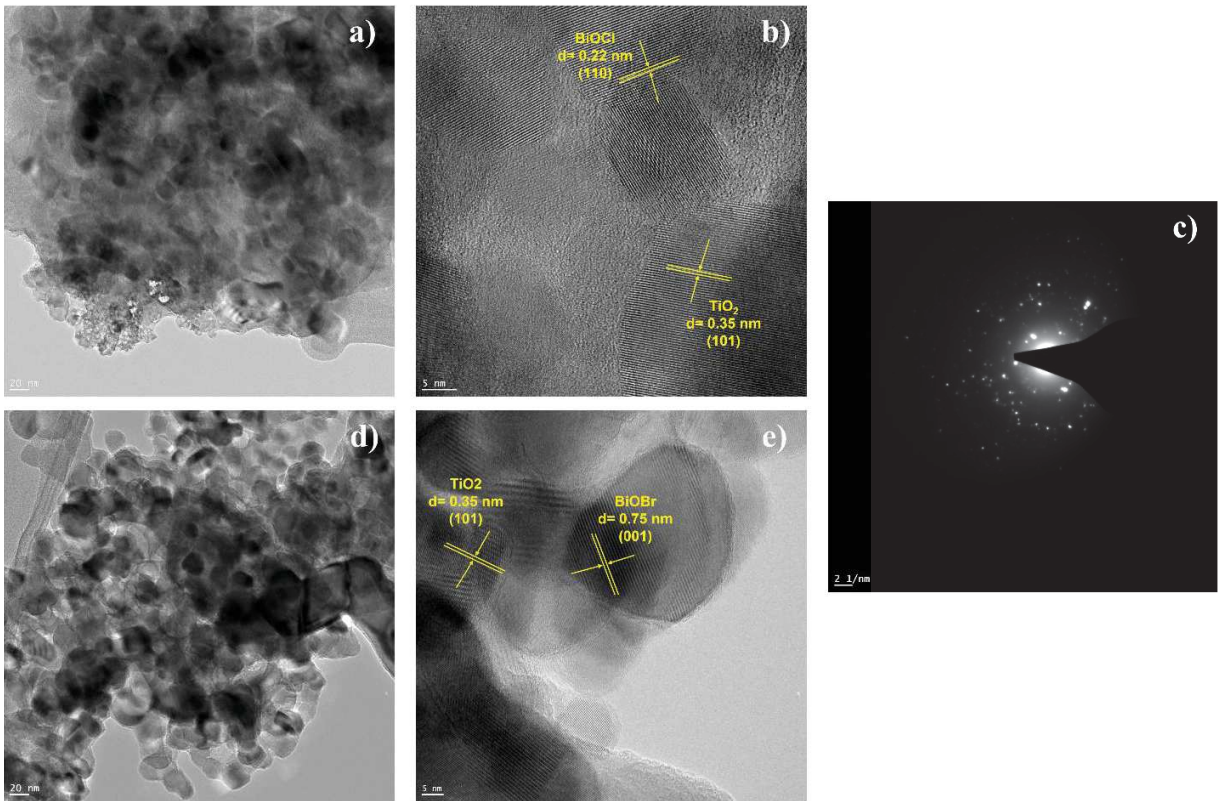

Figure 4.6. TEM images of (a) 5%BiOCl-P25; (d) 5%BiOBr-P25, HRTEM of (b) 5%BiOCl-P25; (e) 5%BiOBr-P25; and SAED of (c) 5%BiOCl-P25.

4.2.9 Photocurrent spectroscopy

Photocurrent spectra were recorded to check the impact of the addition of BiOX on the intrinsic electronic properties of TiO_2 P25. The spectra were obtained in 0.1 M ABE at the applied potential of 0.1 or 0.2 V versus Ag/AgCl and are reported in Figure 4.7.a. In particular, no significant differences can be observed between the spectrum of bare P25 and those of its composites with BiOX: Peaks at around 320 nm are present for all powders. Assuming indirect optical transitions, the band gap values (E_g) can be calculated using Equation 3:

$$\left(Q_{ph} \cdot h\nu\right)^{0.5} \propto \left(h\nu - E_g\right) \qquad Eq.3$$

Q_{ph} is the photocurrent yield and hν is the photon energy. The definition of Q_{ph} requires that the photocurrent is corrected for the efficiency of the monochromator-lamp system and is proportional to the light absorption coefficient for hν values close to the band gap. The optical band gaps of the

photocatalysts are determined by extrapolating to zero the plots $(Q_{ph}\ h\nu)^{0.5}$ vs $h\nu$ (Figure 4.7 b). For example, for P25 and P25 coupled with BiOBr or BiOCl the values of ~3.2 eV is in agreement with those found by applying the Kubelka-Munk function.

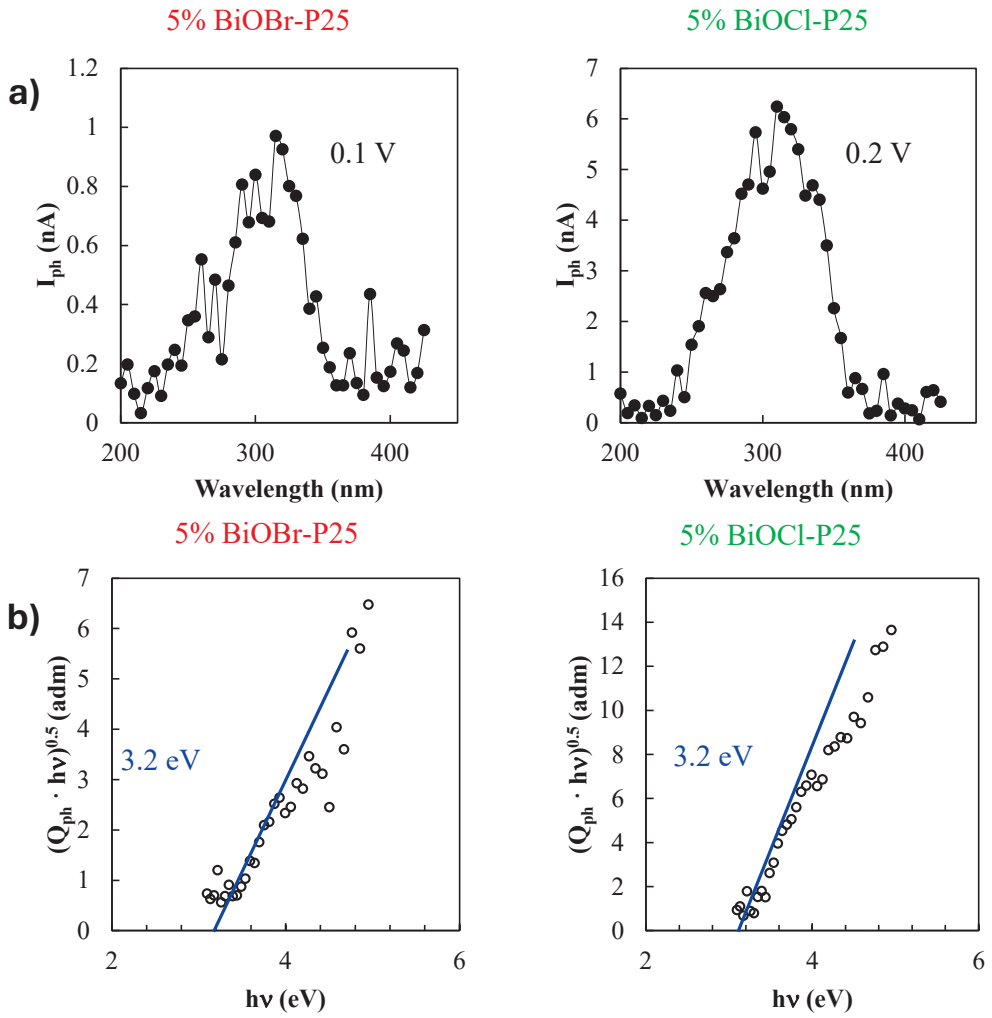

Figure 4.7. Photocurrent spectra for a) 5%BiOBr P25 and 5% BiOCl P25; in figures b) are reported the respective $(Q_{ph} \cdot h\nu)^{0.5}$ vs $h\nu$ plots.

Figure 4.8a shows the photocurrent recorded when the irradiation on the sample is manually stopped by varying the applied potential (0.3-0.2 V vs. Ag/AgCl). The measured photocurrent is of anodic type, as expected for n-type semiconductors where TiO_2 is the main component, and approaches zero for a potential value of -0.2 V. This value can be considered as an estimate of the flat band potential (V_{fb}) [25]. Furthermore, the value of the Open Circuit Potential (OCP) shifts

negatively under the effect of light irradiation (Figure 4.7.2b), confirming the n-type semiconductor behaviour.

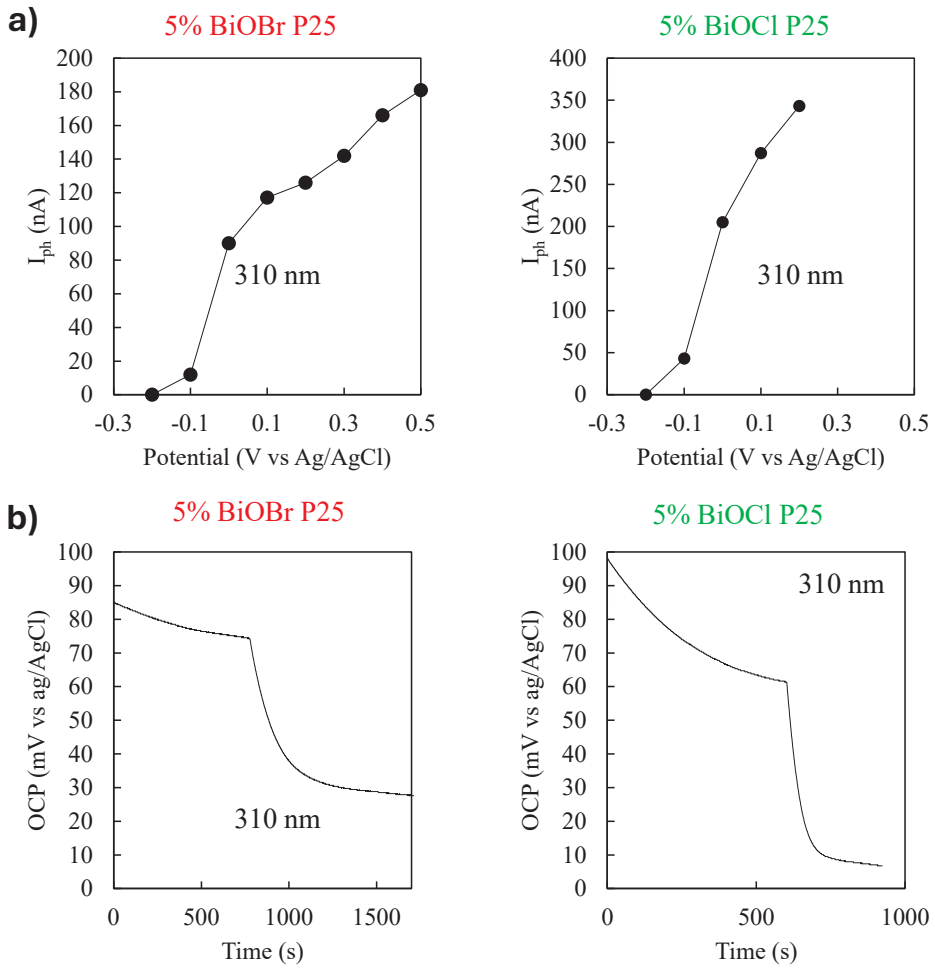

Figure 4.8 a) Current transient under monochromatic light recorded at 310 nm and applied potential ranging from -0.3 to 0.2 V vs Ag/AgCl; b) Photo potential recorded under dark and at 310 nm.

4.2.10 Electron paramagnetic resonance (EPR) Spectroscopy

In Figure 4.9 the EPR spectra recorded under darkness and irradiation for selected photocatalysts are reported. In the presence of DMPO and H_2O_2 in the dark, no radicals were detected, and this indicates that photocatalysts cannot generate radical species in the absence of irradiation. After exposure to light, the formation of hydroxyl radicals (•OH) was detected by the characteristic

1:2:2:1 quartet signal [244] resulting from the paramagnetic resonance absorption of DMPO-$OH^{\cdot}$ adduct.

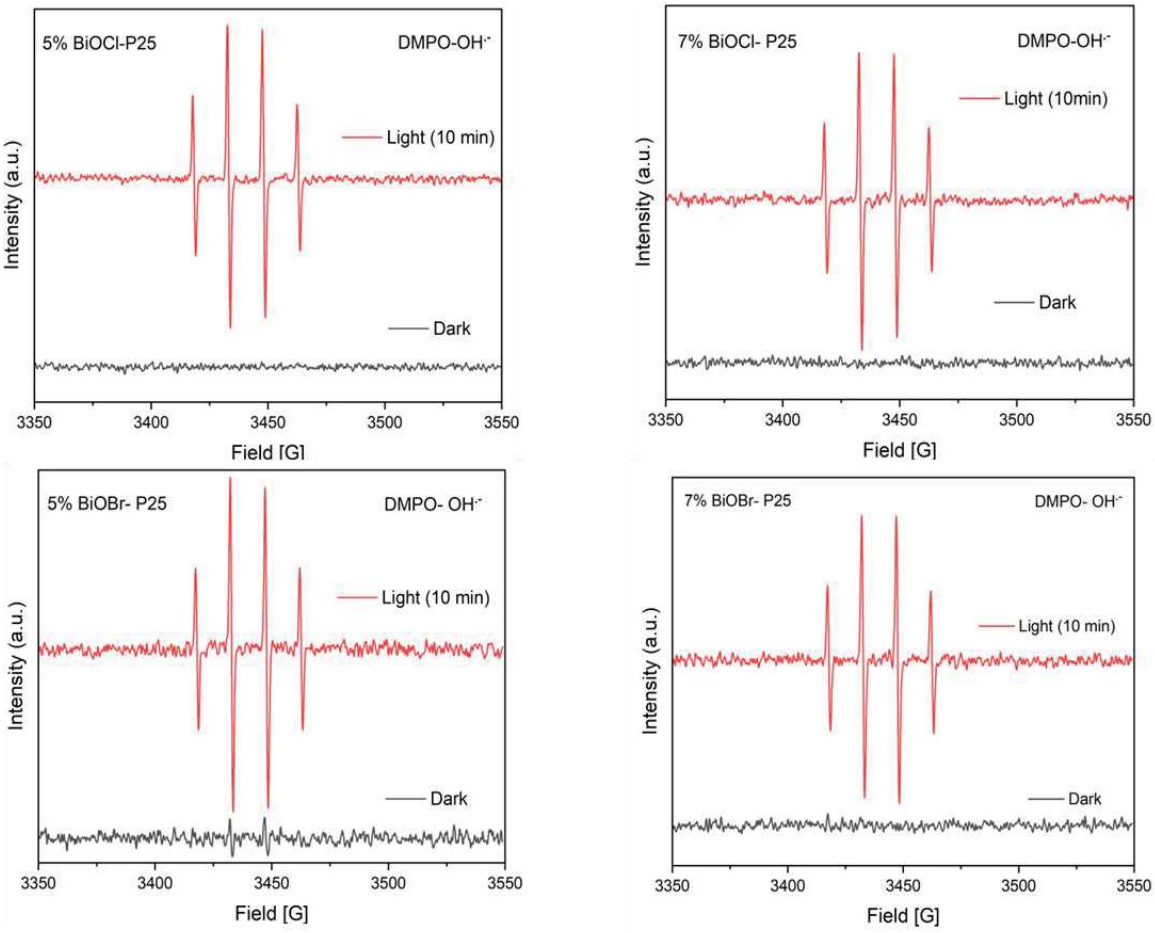

Figure 4.9 EPR spectra of the samples 5% BiOCl-P25, 7% BiOCl-P25, 5%BiOBr-P25 and 7%BiOBr-P25 dispersed in H_2O/DMPO/H_2O_2 solution under dark and light irradiation.

CHAPTER 5

Section-I Photoreforming of Biomass-derived Substrates

CHAPTER 5-I

5-I. Solar driven photocatalytic glycerol and glucose reforming via noble metals free BiOX (X=Cl, Br, I)-TiO_2 (P25) composites

5-I.1 Abstract

Recent research on the valorization of biomass has received great interest as it allows the obtaining of products with high added value. In this regard, this study explores aerobic and anaerobic heterogeneous photocatalytic partial oxidation under both UV and simulated solar irradiation of glycerol and glucose in aqueous medium using bismuth oxyhalide-based photocatalysts BiOX (X = Cl, Br, I). The noble metal-free BiOX-TiO_2 (P25) composites were prepared through a simple ball milling procedure. Both the formation of partial oxidation compounds, namely 1,3-dihydroxyacetone, glyceraldehyde and glycolic acid from glycerol and arabinose and formic acid from glucose in solution, and the production of CO_2 and H_2 in the gas phase, were monitored. Pure BiOBr and BiOCl proved to be more effective than bare TiO_2 P25 (one of the most used and studied photocatalysts) affording a higher selectivity towards high added value products whilst the composites samples displayed high glycerol conversion values that reached 62%. Particularly noteworthy was the effectiveness of BiOCl-P25 and BiOBr-P25 samples containing 5 and 7 wt% of BiOCl or BiOBr with respect to P25, in promoting also H_2 formation under simulated sunlight irradiation and without the presence of noble metal species such as Pt.

5-I.2 Photocatalytic conversion of glycerol

To explore the photoactivity, bare oxyhalides and coupled BiOX-TiO_2 samples were compared with TiO_2 P25 for selective oxidation of glycerol under UV light and atmospheric O_2 as oxidant agent in water solutions. Figure 5-I.1 shows the evolution of glycerol concentration and formation of partial oxidation products as a function of irradiation time for selected photocatalysts under simulated solar light irradiation and anaerobic conditions. In Table 5-I.1 the glycerol conversion and the selectivity towards the identified partial oxidation compounds (1,3-dihydroxyacetone (DHA), glyceraldehyde (GA) and glycolic acid (GLA)) after 5h of irradiation are reported; no formic acid was found probably due to its rapid mineralization to CO_2. P25 afforded ca. 37% of conversion and selectivity values of 5.2%, 10% and 27.9% towards GA, DHA and GLA, respectively. In the presence of bare BiOCl glycerol conversion was a little lower but a higher selectivity, that reached ca. 46% for GLA, was obtained towards the intermediates. In the presence

of BiOBr the conversion was ca. 26%, GA was not detected and good selectivity values only towards DHA and GLA were found whilst a worse performance was shown by BiOI with ca. 20% conversion and only trace amounts of DHA. The composite BiOX-P25 samples generally exhibited higher conversion and lower selectivity than the single components and the 5% showed to be the best combination to enhance the oxidation power of the photocatalysts. In fact, the highest conversion values (up to 62%) were reached by using 5%BiOCl-P25 and 5%BiOBr-P25 samples. Low activity has been measured with the 5%BiOI-P25 composite and for this reason BiOI sample was not fully characterized.

The optimal combination between BiOCl/BiOBr and TiO_2 gave rise to an efficient charges separation that allowed a high oxidation both of glycerol and its intermediates to CO_2 [52,245]. By analysing the adsorption results reported in Table 5-I.2 it can be affirmed that the low selectivity values towards the formed valuable compounds can be ascribable to the high adsorption percentage of these latter on the photocatalysts surface that facilitates their direct mineralization in the adsorbed phase, for GA on P25. Furthermore, the results reported in Table 5-I.1 reveal that the oxidation capability of BiOX follows the order BiOCl > BiOBr > BiOI as observed for other substrates [246]. This finding indicates that with the various photocatalysts a different distribution of the glycerol partial oxidation compounds can be obtained, confirming the determinant role of the structural, electronic and physicochemical properties of the used materials on photoactivity [247,248]. Mechanistic studies during glycerol photoreforming in the presence of different photocatalytic materials revealed that glycerol can be transformed to GA by the partial oxidation of hydroxyl group on C1 or C3, to DHA by the partial oxidation of C2-OH or by the direct cleavage of one C-C bond to generate compounds containing 2 carbon atoms as GLA [249,250]. Sanwald et al, [249] found that GLA derives from the cleavage of DHA with the simultaneous H_2 formation, and successively GLA undergoes decarboxylation forming formic acid and H_2. Our data are in accordance with these results as GA is formed in low amounts, DHA and GLA are the main intermediates, and generally the greater the amount of DHA, the greater that of GLA.

Table 5-I.1 Glycerol conversion (X) and Selectivity (S) towards partial oxidation compounds after 5h irradiation by a UV-125W lamp under atmospheric air.

Samples	X (%)	S_{GA} (%)	S_{DHA} (%)	S_{GLA} (%)
P25	37.3	5.2	10.0	27.9
BiOCl	34.4	9.6	12.8	45.6
3%BiOCl-P25	57.6	-	2.9	7.4
5%BiOCl-P25	62.4	3.7	4.5	8.2
7%BiOCl-P25	35.0	-	8.6	13.8
9%BiOCl-P25	44.4	6.6	7.7	20.8
BiOBr	26.2	-	28.4	44.0
3%BiOBr-P25	31.7	4.3	9.1	24.1
5%BiOBr-P25	48.2	-	8.9	18.6
7%BiOBr-P25	42.7	4.1	11.6	26.3
9%BiOBr-P25	28.3	-	12.4	19.6
BiOI	20.4	-	3.6	-
5%BiOI-P25	37.7	-	9.2	18.2

Bare P25 and BiOCl afforded almost the same glycerol conversion and selectivity towards GA and DHA and a different GLA selectivity. To find a possible explanation, dark adsorption tests of the different compounds were carried out (Table 5-I.2). By considering the percentage of adsorption of the partial oxidation products, it can be deduced that the higher amount of DHA obtained with BiOCl is due to a higher productivity of this catalyst and not to a lower adsorption of DHA on its surface. BiOBr showed a lower activity and a lower surface affinity with the different species.

Table 5-I.2 Molar adsorption (%) in the dark of glycerol and its derivatives on selected catalysts.

Catalysts	Glycerol	GA	DHA	GLA
P25	0.9	44.0	25.0	23.6
BiOCl	2.1	29.0	30.0	26.6
BiOBr	0.7	10.4	10.0	16.7

With the aim of exploiting sunlight for potential use in pilot plant reactor [251], runs were carried out using a halogen lamp which has an emission spectrum like that of the sun (Table 5-I.3). The results are comparable with those obtained under UV light indicating that the irradiation type does not influence the reaction mechanism and confirm the high activity of the bare BiOCl and BiOBr towards glycerol valorization with high conversion and selectivity values towards both DHA and

GLA. The composite samples generally display higher oxidant power but a decrease in selectivity. To evaluate the stability and reusability of the catalysts, a run was carried out by used recovered BiOCl photocatalysts. The results revealed a high activity of the sample being both glycerol conversion and selectivity very similar to those obtained with the fresh BiOCl.

Table 5-I.3 Glycerol conversion (X) and Selectivity (S) towards partial oxidation compounds after 5h irradiation by halogen 150W lamp under atmospheric air.

Samples	**X (%)**	**S_{GA} (%)**	**S_{DHA} (%)**	**S_{GLA} (%)**
P25	39.1	6.0	10.6	19.2
BiOCl	41.3	negligible	14.7	53.2
BiOCl recovered	39.1	-	19.9	45.8
BiOBr	37.1	-	21.2	44.1
BiOI	6.4	-	13.4	44.7
5%BiOI-P25	41.6	-	13.3	23.2
3%BiOCl-P25	30.8	5.5	12.1	22.1
5%BiOCl-P25	49.0	-	9.3	8.3
3%BiOBr-P25	37.8	-	7.0	18.6
5%BiOBr-P25	42.5	-	16.3	22.6
7%BiOBr-P25	30.0	-	17.1	27.9

In Table 5-I.4 the results of photocatalytic runs carried out in anaerobic conditions under simulated solar light irradiation are reported. Also in this case, BiOCl and BiOBr afforded a glycerol conversion virtually like that of the high active P25 but higher selectivity values. Surprisingly, a certain H_2 amount was produced by some of the composites in the absence of Pt, that is essential for H_2 production by using bare TiO_2 samples [247]. In accordance with the previous results, the formation of a heterojunction with proper energy levels of the conduction edges of the components allowed H^+ reduction to H_2 [25, 252-254]. The comparable activity observed under UV and simulated solar irradiation confirms that the reaction mechanism is not strongly dependent on excitation wavelength, highlighting the suitability of BiOX-based photocatalysts for real solar-driven applications and potential scale-up in outdoor photoreactors.

Table 5-I.4 Glycerol conversion (X) and Selectivity (S) towards partial oxidation compounds after 5h irradiation by halogen 150W lamp under anaerobic conditions.

Samples	X (%)	S_{GA} (%)	S_{DHA} (%)	S_{GLA} (%)	H_2 (mM)	CO_2 (mM)
P25	23.4	13.7	19.8	21.5	-	0.04
BiOCl	26.6	12.0	16.4	40.2	-	0.06
BiOBr	23.4	-	30.9	50.1	-	negligible
3%BiOCl-P25	9.8	-	24.7	-	-	negligible
5%BiOCl-P25	23.6	-	25.5	0.0	0.15	0.03
7%BiOCl-P25	24.3	-	4.0	23.2	0.06	0.06
9% BiOCl-P25	37.4	-	12.7	9.8	0.06	0.04
5%BiOBr-P25	26.4	9.5	20.2	27.6	-	0.09
7%BiOBr-P25	26.9	-	8.2	-	0.03	0.02
9%BiOBr-P25	16.8	-	12.1	-	0.02	0.03
3%BiOI-P25	6.4	-	61.3	50.8	0.07	0.01

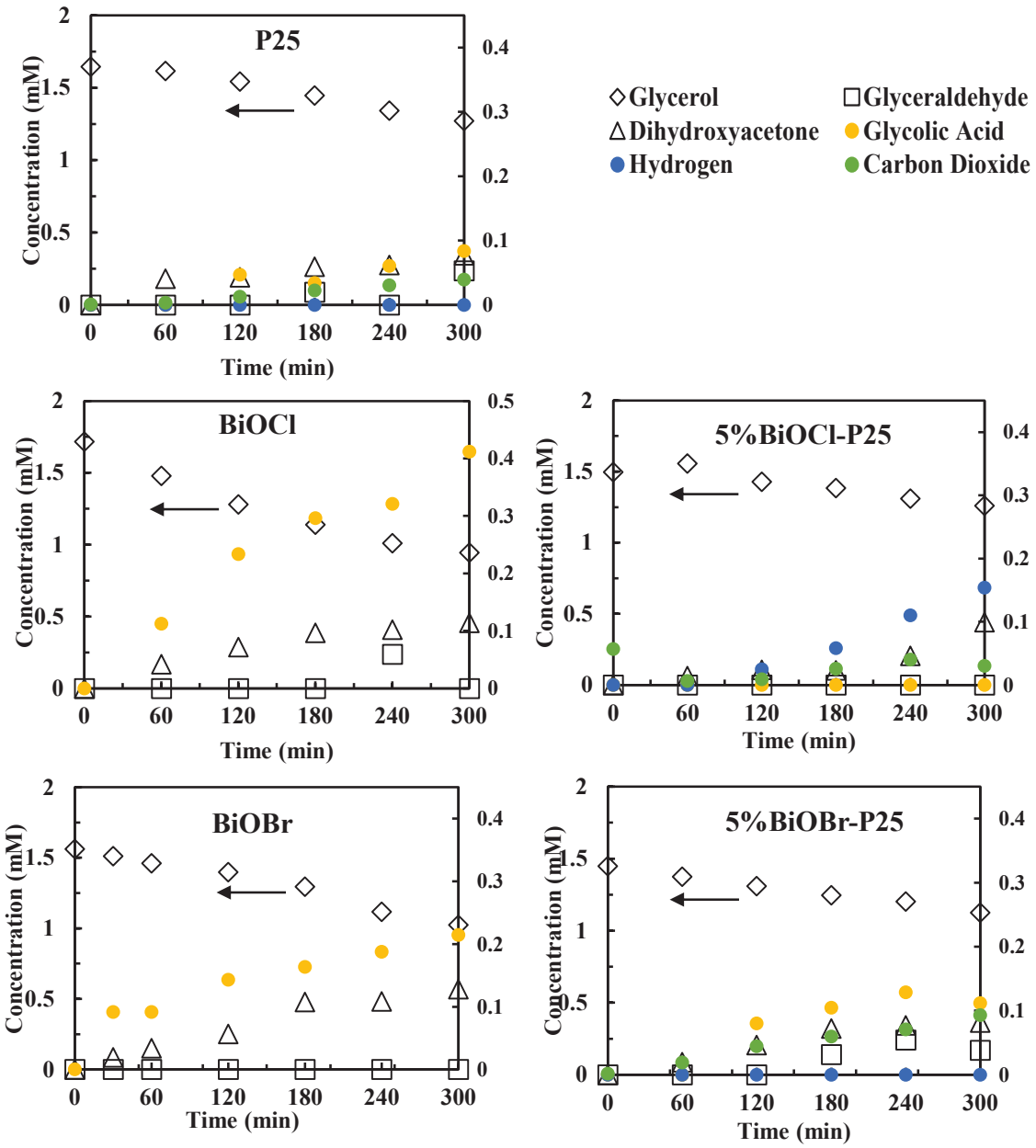

Figure 5-I.1. Evolution of glycerol concentration and formation of partial oxidation products as a function of irradiation time for selected photocatalysts under simulated solar light irradiation and anaerobic conditions.

5-I.3 Photocatalytic degradation mechanism

By coupling BiOX with TiO_2, a p-n heterojunction is generally formed [255, 256]. After the light irradiation, both photocatalysts are excited and electrons move from the conduction band of BiOX to that of TiO_2 and holes from the valence band of TiO_2 to that of BiOX, improving the

photogenerated charges separation (Figure 5-I.2) In particular, BiOBr exhibits a narrower band gap around 2.9eV as compared to BiOCl that shows around 3.5 eV, that enables enhanced visible-light absorption. More importantly, its conduction band (CB) position is less negative than that of TiO_2, while its valence band (VB) is more positive. This band alignment suggests that a conventional type-II heterojunction would promote electron transfer from BiOBr to TiO_2 and hole transfer in the opposite direction. However, such a pathway would reduce the redox ability of charge carriers, limiting hydrogen evolution.

The photogenerated electrons in the CB of TiO_2 recombine with holes in the VB of BiOBr, preserving the highly reducing electrons in the CB of BiOBr and the strongly oxidizing holes in the VB of TiO_2. This mechanism allows simultaneous enhancement of charge separation and retention of strong redox potentials, which is consistent with experimental photocatalytic performance. Considering that H_2 is produced in the presence of the composite photocatalysts, the formation of a BiOX-TiO_2 Z-scheme cannot be excluded as already noted in the literature [257,258].

Although BiOI exhibits extended visible-light absorption, its conduction band position is not sufficiently negative to drive proton reduction efficiently. Consequently, BiOI-based materials display limited hydrogen evolution activity, confirming that light absorption alone is not sufficient without appropriate band-edge alignment.

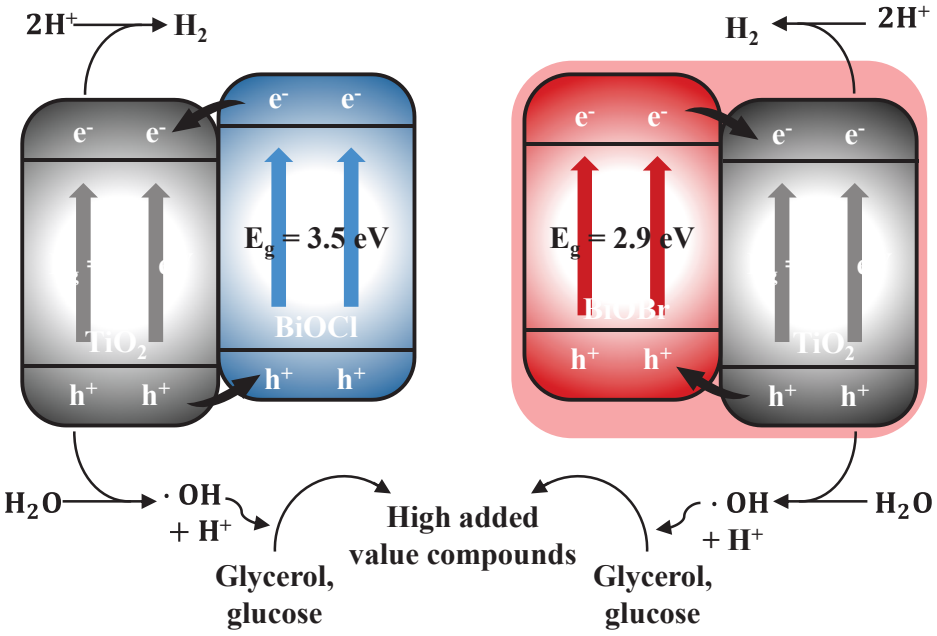

Figure 5-I.2. Hypothesized charges transfer mechanisms in the coupled systems.

The formation of BiOX-TiO_2 heterostructures introduces an internal electric field at the interface, which enhances charge separation and suppresses recombination. Under irradiation, both components are photoexcited, allowing directional migration of charge carriers. The observation of hydrogen evolution in the absence of noble metals strongly suggests that an efficient charge-transfer pathway is established, potentially following a direct Z-scheme mechanism rather than a conventional type-II heterojunction.

Figure 5-I.3 reports the variation of the glycerol concentration under irradiation in the presence of P25, BiOCl, BiOBr, and the different scavengers. A general decrease in the glycerol conversion can be noted in the presence of all the trapping agents with respect to the runs carried out without scavengers. In particular, a consistent activity reduction was observed in the presence of P25 after adding benzoquinone highlighting the crucial role of $^{\bullet}O_2^-$ anion radicals in glycerol conversion. Holes and $^{\bullet}OH$ radicals exert a lesser influence, while in the presence of $AgNO_3$ there is an increase in conversion. Probably, Ag^+ ions, by attracting electrons, make a greater quantity of holes available, favouring the oxidation of glycerol. With BiOCl, superoxide radicals are the main active species (the glycerol conversion apparently suppressed after adding benzoquinone), electrons play a minor role and hydroxyl radicals virtually do not participate in the glycerol conversion process being the glycerol concentration in the presence of tert-butanol very similar to that measured in the absence of scavengers. Finally, when BiOBr is used, $^{\bullet}O_2^-$ radicals are the only active species and electrons display a minor role. These results revealed a different glycerol oxidation mechanism in the presence of the various photocatalysts, probably due to a different energetic band level. The behaviour of 5%BiOCl-P25 composite is like that of P25, this latter component being present in higher amounts with respect to BiOCl.

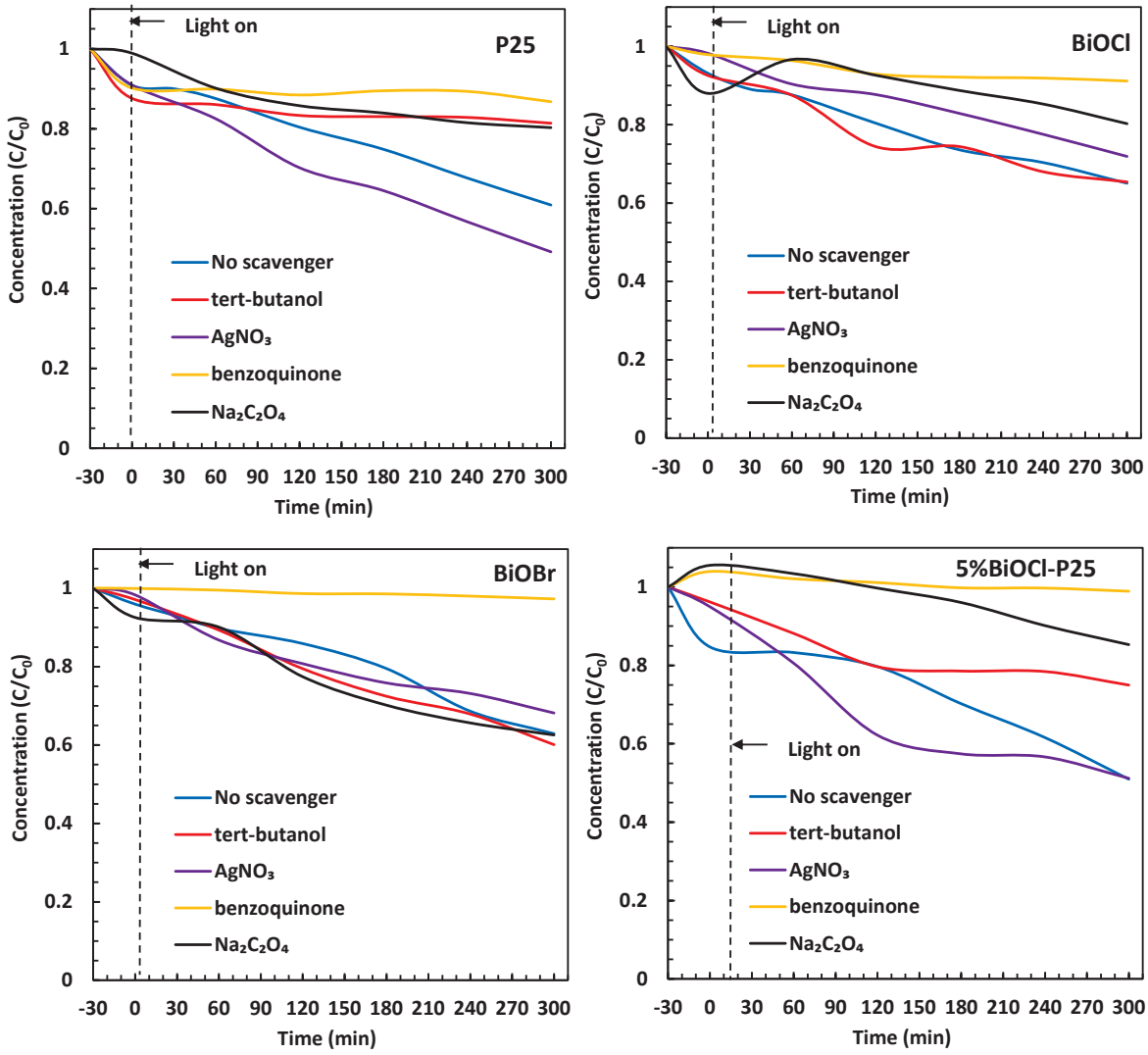

Figure 5-I.3. Photocatalytic conversion of glycerol by using P25, BiOCl, BiOBr and 5%BiOCl-P25 photocatalysts in the presence of different scavengers under halogen lamp irradiation and atmospheric air.

The different response observed upon addition of scavenging agents highlights that glycerol oxidation follows catalyst-dependent reaction pathways. While superoxide radicals dominate in the presence of BiOCl and BiOBr, TiO_2-rich systems show a stronger contribution from photogenerated electrons. This performance reflects the different band-edge alignment and interfacial charge-transfer dynamics within the composite photocatalysts.

Although scavenger experiments provide indirect information on the role of the different reactive species involved in glycerol oxidation, direct spectroscopic evidence is required to unequivocally confirm their formation under irradiation. For this purpose, electron paramagnetic resonance (EPR) measurements were performed in the presence of the spin-trapping agent DMPO to detect the generation of reactive oxygen species (Figure 5-I.4).

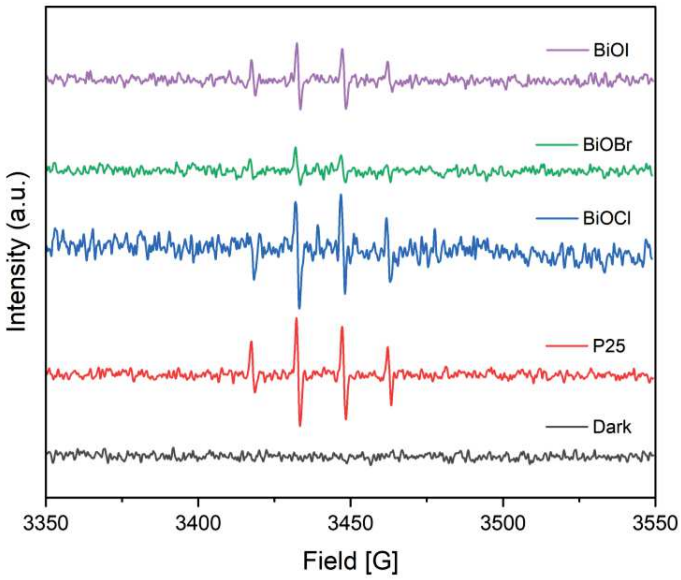

Figure 5-I.4. Electron paramagnetic resonance (EPR) spectra of bare P25, BiOCl, BiOBr and BiOI photocatalysts dispersed in H_2O/DMPO/H_2O_2 solution under dark and light irradiation, showing the formation of reactive oxygen species upon light exposure.

The appearance of characteristic (5,5-Dimethyl-1-pyrroline-N-oxide) DMPO-radical signals under light irradiation and their absence under dark conditions confirm the formation of reactive oxygen species during photocatalysis. These findings are fully consistent with the scavenger experiments discussed above and provide direct spectroscopic evidence that glycerol oxidation proceeds through radical-mediated pathways, with superoxide species playing a dominant role depending on the photocatalyst composition

As can be deduced from the observation of Figure 5-I.5, the addition of scavenging species in the reaction environment influences also the type and the distribution of reaction intermediates as

some are not detected in the presence of the different species. They could therefore be specifically added to the reaction mixture to selectively obtain/not obtain a selected product.

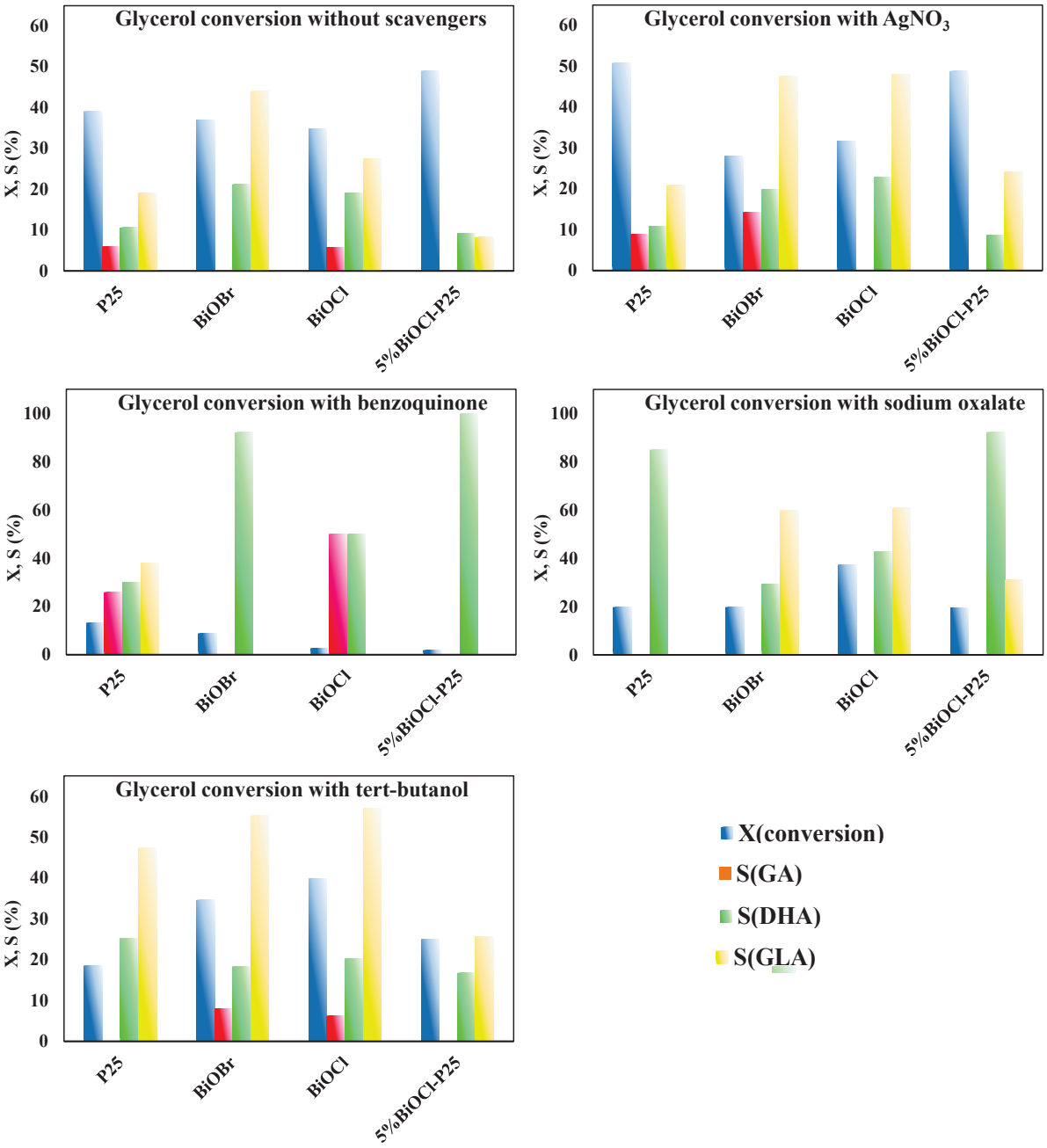

Figure 5-I.5. Conversion (X) and selectivity (S) with and without scavengers in the presence of selected photocatalysts.

The best photocatalysts were also employed for the valorization of glucose under halogen lamp irradiation, both in the presence and absence of O_2 (Table 5-I.5). Also in this case, the home-made bare BiOCl and BiOBr and their composite with P25 displayed a better performance than P25 considering both glucose conversion and the formed compounds. Arabinose and formic acid are the products deriving from glucose partial oxidation and only a small H_2 amount was revealed by using 5%BiOCl-P25 under anaerobic conditions.

Table 5-I.5 Glucose conversion (X) and selectivity (S) towards partial oxidation compounds after 5h irradiation by halogen 150W lamp under both aerobic and anaerobic conditions.

Open reactor							
Samples	**X (%)**	**$S_{(Gluc.acid)}$ (%)**	**$S_{(Arabinose)}$ (%)**	**$S_{(Formic\ acid)}$ (%)**	**$S_{(Erythrose)}$**	**H_2 [mM]**	**CO_2 [mM]**
P25	45.4	-	45.0	52.0	-		
BiOCl	49.8	1.5	52.8	88.9	-		
5%BiOCl-P25	49.1	1.6	40.4	51.6	-		
BiOBr	51.5	0.6	53.3	100.0	3.4		
5%BiOBr-P25	76.9	-	30.7	57.22	-		
Closed Reactor							
P25	20.4	-	-	76.6	-	-	0.01
BiOCl	22.8	3.2	56.6	57.8			
5%BiOCl-P25	27.0	6.1	57.0	60.0		0.08	0.03
BiOBr	50.9			76.3			0.01
5%BiOBr-P25	13.7		negligible	negligible			0.01

5-I.4 Comparison with state-of-the-art Photocatalysts

Pt-TiO_2 is widely recognized as one of the most efficient benchmark photocatalysts for photocatalytic glycerol reforming and hydrogen production due to the excellent electron trapping ability and low overpotential for H_2 evolution provided by Pt nanoparticles [258a]. Au-TiO_2 photocatalysts have also shown enhanced solar-driven hydrogen production from glycerol reforming owing to plasmonic light harvesting and improved charge separation. [258b]. Pd-based cocatalysts have also been reported to improve charge carrier separation and hydrogen evolution rates, although generally at a lower performance-to-cost ratio than Pt [258c]. Silver-containing TiO_2 systems have been investigated as lower-cost alternatives to Pt, although their hydrogen evolution activities are generally lower [258d].

Noble-metal-loaded TiO_2 photocatalysts, particularly Pt-TiO_2, remain the benchmark materials for photocatalytic hydrogen production due to their superior electron extraction and hydrogen evolution kinetics. However, the high cost and limited availability of noble metals motivate the development of alternative systems. In this context, the BiOX-TiO_2 heterostructures developed in a cheap way in this thesis offer a noble-metal-free strategy capable of enhancing charge separation and photocatalytic performance while reducing material costs.

Table 5-I.6. Benchmark comparison of hydrogen production rates achieved by the BiOX-TiO_2 photocatalysts developed in this work and representative state-of-the-art TiO_2-based photocatalysts for photocatalytic glycerol reforming.

Catalyst Type	**H_2 Production Rate**	**Light Source**	**Sacrificial Agent**	**Ref**
Au-TiO_2 (1 wt% Au/anatase)	2.55 mmol g^{-1} h^{-1}	300 W Osram Vitalux solar lamp (10.7 mW cm^{-2})	Glycerol/water mixture	[258b]
Pd-CD-TiO_2	1.167 mmol g^{-1} h^{-1}	Direct sunlight (~65 mW cm^{-2})	5 vol% glycerol (≈0.6 M)	[258c]
Ni-CD- TiO_2	0.494 mmol g^{-1} h^{-1}	Direct sunlight (~65 mW cm^{-2})	5 vol% glycerol (≈0.6 M)	[258e]
Bare TiO_2	0.166 mmol g^{-1} h^{-1}	Direct sunlight (~65 mW cm^{-2})	5 vol% glycerol (≈0.6 M)	[258e]
CuO@ TiO_2 core-shell	0.154 mmol g^{-1} h^{-1} (153.8 μmol g^{-1} h^{-1})	Simulated solar irradiation	Glycerol aqueous solution	[258f]
NiO@ TiO_2 core-shell	0.048 mmol g^{-1} h^{-1}	Simulated solar irradiation	Glycerol aqueous solution	[258f]
Pt-TiO_2 (Ptuv/Ti)	27.5 mmol g^{-1} h^{-1}	UV light (365 nm)	10% (v/v) glycerol solution	[258a]
Ni- TiO_2 @g-C_3N_4	32 mmol g^{-1} h^{-1} (32000 μmol g^{-1} h^{-1})	Solar/Visible photocatalysis	Glycerol	[258g]
5% BiOCl-P25	0.100 mmol g^{-1} h^{-1}	Solar irradiation	Glycerol	This work
5% BiOBr-P25	0.060 mmol g^{-1} h^{-1}	Solar irradiation	Glycerol	This work

Although some literature photocatalysts showed higher hydrogen production rates, most of them contained expensive noble metals such as Pt, Au, or Pd. The aim of this work was to develop low-cost noble-metal-free BiOX-TiO_2 heterostructures with improved charge separation and multifunctional photocatalytic activity. Therefore, the significance of the developed catalysts lies not only in hydrogen production but also in their versatility, low cost, and environmental sustainability. So, the BiOCl-P25 heterostructure offers a noble-metal-free and economically attractive alternative that can also be used in pilot-plant photoreactors.

5-I.5 Conclusion

Bismuth oxyhalides BiOX (X=Cl, Br, I) were successfully synthesized by a simple co-precipitation method. Pristine BiOX and BiOX-TiO_2(P25) coupled photocatalysts revealed high activity towards both glycerol and glucose photoreforming under simulated solar light irradiation. The bare samples were very efficient to partially oxidize glycerol to valuable chemicals such as dihydroxyacetone (DHA), glyceraldehyde (GA) and glycolic acid (GLA) under both aerobic and anaerobic conditions. BiOX-P25 composites, prepared by simply ball milling mixing, showed higher oxidant power than the single oxides and some of them were able to produce H_2 under anaerobic conditions without the presence of Pt. UV-Vis spectra, SEM, EDX and TEM analyses suggest/indicate the formation of a heterostructure in the BiOX-P25 samples, with the latter technique confirming the coexistence of the two phases within the composite. PL intensity of the bands compared to bare P25 indicates a lower recombination rate of the photoproduced e^-/h^+ pairs in the BiOX samples, with an optimum effect between the charge transfer recombination and the formation of defects for a proper BiOX amount. In fact, the best results were obtained with the 5%BiOCl-P25 and 5%BiOBr-P25 samples. The activity under simulated sunlight irradiation encourages the use of these photocatalysts to produce H_2 and high value-added products in large-scale solar power plants.

SECTION-II

PHOTOCATALYTIC ENVIRONMENT REMEDIATION: DEGRADATION OF PHARMACEUTICAL AND PHENOLIC POLLUTANTS

CHAPTER 5-II

5-II. Photocatalytic environment remediation by BiOX-TiO_2 composites: pharmaceuticals and pollutants degradation

5-II.1 Abstract

This study investigates the removal of pharmaceutical and industrial pollutants in the presence of the bare bismuth oxyhalides (BiOX, where X = Br, Cl) photocatalysts and the BiOX-TiO_2 composites described in Chapter 4. Namely, the photooxidation of tetracycline, oxytetracycline, and 4-nitrophenol, which are micropollutants commonly present in wastewater, was performed under both UV and simulated solar light irradiation, even in the absence of a photocatalyst. The homogeneous system proved to be poorly efficient, while for the heterogeneous systems, the composites showed both an almost complete conversion of the initial substrates and a higher degree of mineralization (up to 76%) compared to the bare TiO_2 P25, tested for comparison purposes. Selected runs carried out degrading 4-nitrophenol under simulated sunlight irradiation revealed the efficiency of BiOX-TiO_2 composites also under real conditions, encouraging their future use in pilot plant reactors. The higher activity of the coupled photocatalysts has been ascribed to the improved transfer of the photogenerated charges.

5-II.2 Photocatalytic activity results

The photocatalytic results in terms of TC and OTC conversion and degree of mineralization are shown in Table 5-II.1. In the presence of TiO_2 P25, 95.9% and 66.9% and 97.9% and 60.4% of OTC conversion and TOC reduction were obtained, respectively. Bare BiOCl and BiOBr showed an almost complete conversion of the two antibiotics after 5 hours of irradiation, while the mineralization was lower than that found with P25. With the coupling of the two photocatalysts, a high degree of conversion was observed but also a higher mineralization compared to that in the presence of TiO_2. The percentages of BiOX that gave, generally, the best results were 5 and 7%. The drug conversion, however, was always very high, but the TOC removal increased with the amount of P25 present in the composite, and this can be explained by its higher oxidizing power.

Table 5-II.1 Photocatalytic results in terms of tetracycline (TC, 100 ppm) and oxytetracycline (OTC, 100 ppm) conversion and TOC removal percentage after 5h of UV irradiation.

Catalyst	TC conversion (%)	TOC removal (%)	OTC conversion (%)	TOC removal (%)
P25	95.9	66.9	97.9	60.4
BiOCl	99.8	27.2	99.6	16.1
3%BiOCl-P25	99.5	57.1	98.3	39.8
5%BiOCl-P25	98.9	66.5	99.6	87.3
7%BiOCl-P25	98.5	72.5	95.8	75.9
7%BiOCl-P25[a] re-prepared	99.3	73.8	-	-
7%BiOCl-P25[b] recovered	98.9	70.6	-	-
BiOBr	98.4	20.9	99.81	25.4
3%BiOBr-P25	99.6	70.2	98.3	47.5
5%BiOBr-P25	98.9	72.5	99.7	60.2
7%BiOBr-P25	98.4	75.1	92.1	75.9

[a]Results obtained with fresh re-prepared photocatalyst.
[b]Results obtained with the recovered photocatalyst.

In Figure 5-II.1 the variation of the concentration of tetracycline (TC) and oxytetracycline (OTC) versus irradiation time in the presence of bare and 5%BiOX (X= Cl, Br)-P25 samples is reported. The home prepared samples allow to degrade the two drugs in shorter time with respect to P25.

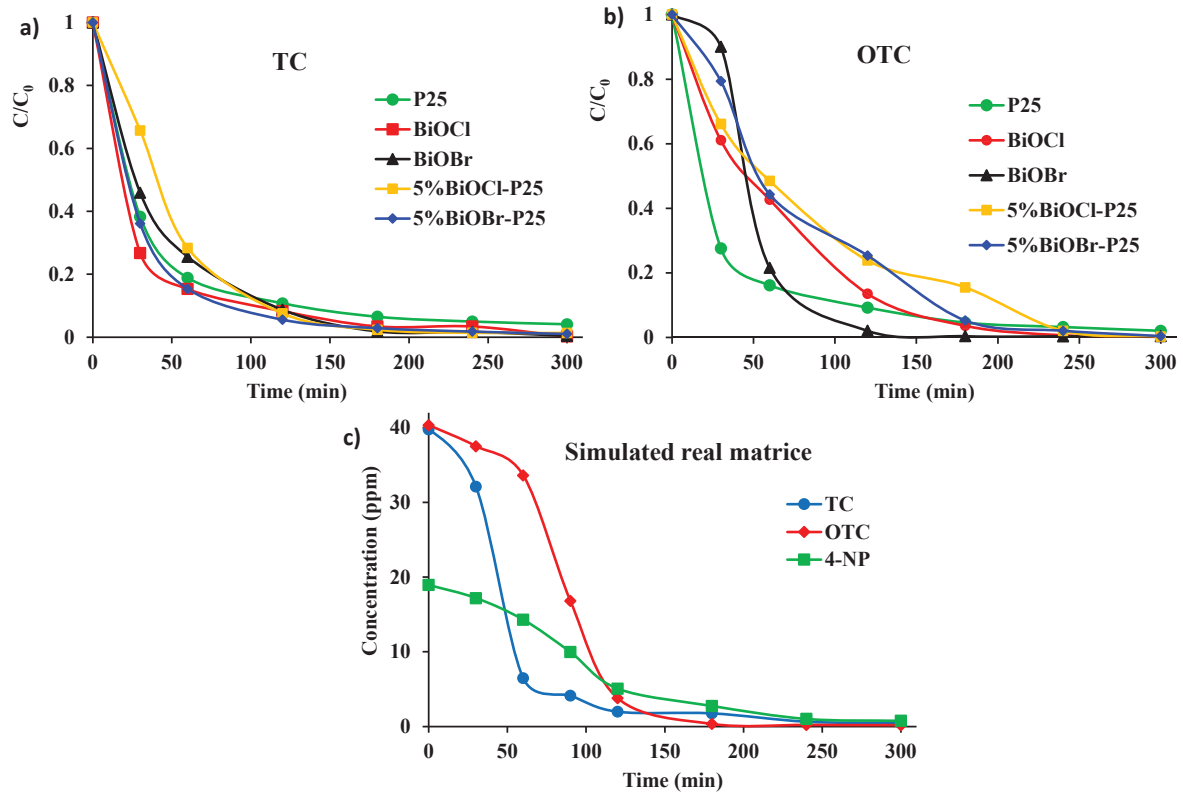

Figure 5-II.1. Variation of the concentration of TC (a) and OTC (b) versus UV light irradiation time in the presence of some representative photocatalysts. The percentage difference between repeated tests is approximately 1.5%; (c) simultaneous degradation of TC, OTC and 4-NP in the presence of 5%BiOCl-P25 sample.

For large-scale industrial applications, the reusability of photocatalysts is crucial. The data reported in Figure 5-II.2a show that the TC conversion remains almost unchanged over four recycling cycles.

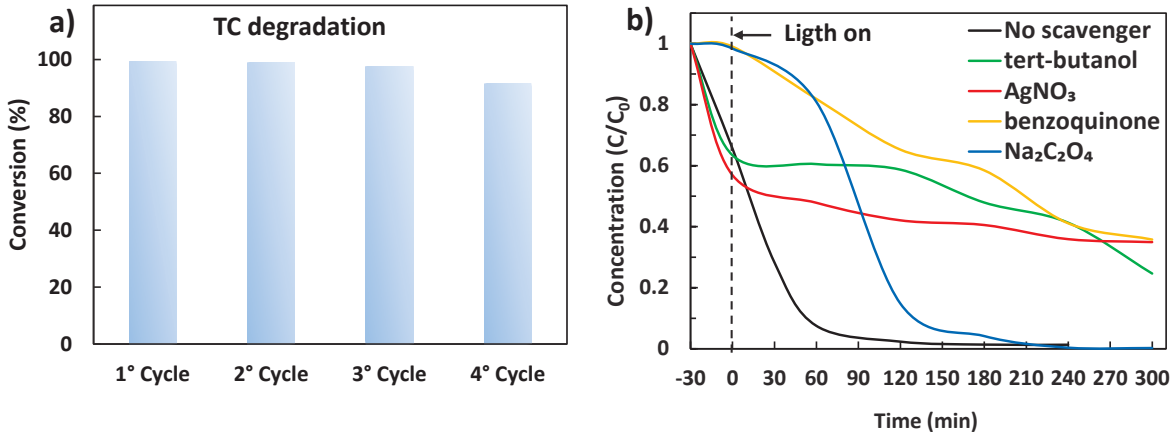

Figure 5-II.2. a) TC degradation by using 7%BiOCl-P25 photocatalyst for four successive cycles; b) TC degradation by using 5%BiOCl-P25 in the presence of different scavenging species.

Figure 5-II.2b presents the variation of the concentration of TC under irradiation by using 5%BiOCl-P25 as photocatalyst in the presence of different scavengers. The decrease in TC degradation after the addition of all the scavenging species reveals an active role for all the species formed after irradiation of the semiconductor, yet with holes playing a minor role.

The photoactivity of the prepared samples was also studied for the degradation of 4-NP, a pollutant often presents in aqueous effluents that is a simpler molecule with respect to the TC and OTC and where a single aromatic ring is present [248, 259]. In this case (see Figure 5-II.3), differently from what observed when the substrates were TC and OTC, the two bare BiOX resulted practically inactive or slightly active, while in the presence of P25 about 74% of this molecule degraded in 2 h, and the composites of BiOX with TiO_2 showed a higher photoactivity reaching a conversion of about 86% and 88% for 5%BiOBr-P25 and 5%BiOCl-P25, respectively. These samples appear to have good performance due to the close contact between the two components which effectively improves the separation of the photogenerated charges.

The performance of the two bare BiOCl and P25 and composite 5%BiOCl-P25 samples was evaluated also under simulated solar light irradiation. Surprisingly, BiOCl displayed a very high photoactivity affording about 72% 4-NP conversion (like P25) while with the 5%BiOCl-P25 heterostructure the conversion was about 85%, similar to that measured under UV irradiation.

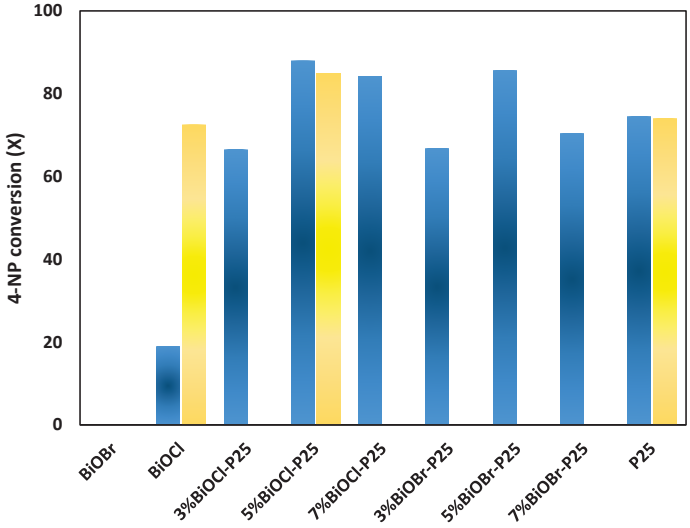

Figure 5-II.3. 4-NP percentage conversion (X) after 2h irradiation in the presence of the different samples under UV irradiation (blue bars) and simulated solar light irradiation (orange bars).

5-II-3 Photocatalytic degradation mechanism

Figure 5-II.4 shows the possible photocatalytic degradation mechanism of the organics used as model wastewater compounds in the presence of BiOX (X= Cl, Br)-TiO_2 composites. According to literature [256-258,260], an efficient type II heterojunction is formed after coupling TiO_2 with both BiOCl and BiOBr, in which electrons move from BiOX to TiO_2 and holes in the opposite directions. Electrons and holes, reacting with O_2 and H_2O, respectively, give rise to the very active radical species $^{\bullet}O_2^-$ and $^{\bullet}OH$, that completely degrade the organics into the eco-friendly molecules CO_2 and H_2O.

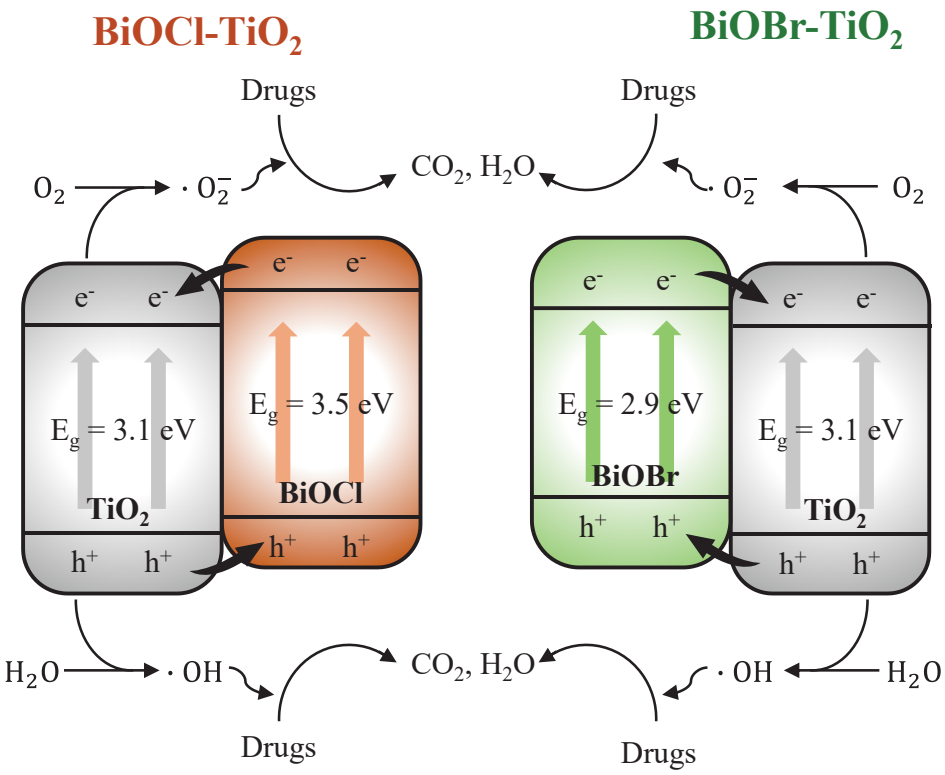

Figure 5-II.4. The possible photocatalytic degradation mechanism of pollutants by using the BiOX-TiO_2 composites.

The data in Table 5-II.2, sourced from the literature, indicate that the photocatalytic systems used are distinct from one another. Although the same pollutants were degraded as in the present study, a direct comparison is not feasible due to the differences in the systems. In general, it can be said that the concentrations of the various substrates in the literature papers are lower than those we investigated, and the catalysts used are often more complex. BiOX-TiO_2 composites have been found to be, in many cases, more active than those reported in the literature, even under irradiation with simulated sunlight. It should also be pointed out that our systems, which are cheap and easy to prepare, could easily be used in actual systems.

Although real water matrices are much more complex than those studied in laboratory, we can still consider remarkable the results obtained since typical environmental concentrations of tetracycline and oxytetracycline in water sources are lower than those used here, ranging from ng/L to µg/L [261]. However, to simulate a real matrix, we mixed the three studied pollutants. A solution

containing 40 ppm TC, 40 ppm OTC and 20 ppm 4-NP (for a total of 100 ppm pollutants) was prepared. After 5 h of irradiation in the presence of 5% BiOCl-P25, the conversion was 99%, 100% and 95% for TC, OTC and 4-NP, respectively. The results demonstrated the high efficiency of the prepared photocatalysts in complex systems in which the pollutants concentration is much higher than that present in real wastewater.

Table 5-II.2 Comparison between literature studies reporting the degradation of TC, OTC and 4-NP.

Photocatalyst	Catalyst amount (g/L)	Light Source	Irradiation time (min)	Conversion (%)	Initial concentration (ppm)	Ref.
BiOBr	1	Visible light	90	94	20 TC	[262]
TiO_2	0.1	UV	90	78	30 TC	[263]
Hydroxyapatite/ BiOCl	0.2	Solar light	60	90	30 OTC	[264]
$Bi_2O_2CO_3$/BiOBr	0.16	Visible light	120	95	10 TC	[265]
ZnO/S-BiOCl	0.4	Visible light	15	51	20 TC	[266]
C–N–S tri-doped TiO_2	0.5	Visible light	180	99 TC removal, 26 OTC removal	5 TC	[267]
$Bi_{25}FeO_{40}$/BiOCl	0.2	300 W Xe lamp	120	86.7	10 OTC	[268]
MIL100(Cr)/BiOCl	0.8	White light LED assembly	120	84 OTC removal; 48.9 TOC removal	40 OTC	[269]
Ti-MOF/BiOCl	0.5	Xenon lamp (300 W)	60	96	15 TC	[270]
MOF902(Ti)/BiOCl	0.2	White light LED (100 W)	40	78 TC removal; 50 TOC removal	20 TC	[271]
3D-BiOCl	0.3	Xenon lamp (300 W)	90	77	20 OTC	[272]
Graphene sand composite/BiOCl	0.5	Solar light (35×10^3 lx)	120	85	10 OTC	[273]
7%BiOCl- TiO_2(P25)	0.3	UV light (125 W)	300	99 TC removal; 74 TOC removal	100 ppm TC	This work
7%BiOCl- TiO_2(P25)	0.3	UV light (125 W)	300	96 OTC removal; 76 TOC removal	100 ppm TC	This work
Ag/AgBr/BiOBr	0.5	Visible light	210	96	10 4-NP	[274]

Pt-BiOBr	1	300 W Xe lamp	60	85	10 4-NP	[275]
Co(II)-BiOCl@biochar	0.5	Vacuum ultraviolet irradiation	90	99	20 4-NP	[276]
5%BiOCl- TiO_2(P25)	0.3	UV light (125 W)	120	88	20 4-NP	This work
7%BiOCl- TiO_2(P25)	0.3	150 W halogen lamp	120	85	20 4-NP	This work

5-II.4 Conclusions

BiOX samples (BiOBr and BiOCl) were prepared by a simple co-precipitation method. They showed good photocatalytic properties under aerobic conditions towards tetracycline and oxytetracycline antibiotics, while they were not efficient towards 4-NP, a common pollutant in wastewater. BiOX-P25 composites, prepared by mixing BiOX and P25 with a planetary ball milling apparatus, on the other hand, were photoactive for all three substrates and mostly achieved higher efficiency than the single components, also under simulated solar light irradiation. The highest conversion and degree of mineralization were obtained by using the 5%BiOCl-P25 (99.6 % conversion and 87.3% mineralization for OTC) and 7%BiOBr-P25 (98.4 % conversion and 75.1% mineralization for TC), thus outperforming TiO_2 P25. These findings can be explained by considering the intimate contact between the two photocatalysts and the enhanced charge transfer process, as highlighted by PL measurements. The presence of a heterostructure in the coupled photocatalysts has been confirmed by the various characterization methods described above. The photocatalysts showed to be (photo)stable after four consecutive runs, thus suggesting their use in real wastewater decontamination systems. Photoactivity under sunlight paves the way for future large-scale application in pilot plants under direct solar irradiation, considering the high effectiveness of the photocatalysts in complex matrices containing all three studied pollutants. Recent techno-economic analyses have identified catalyst lifetime and replacement frequency as major economic factors affecting large-scale photocatalytic processes [276a]. Therefore, future studies should evaluate catalyst durability over extended operational periods, pilot-scale operation, and realistic wastewater conditions.

PERSULFATE-ASSISTED PHOTOCATALYTIC DEGRADATION OF THIABENDAZOLE AND CARBAMAZEPINE USING BISMUTH OXYHALIDES AND P25 COMPOSITES

CHAPTER 5-III

5-III. Persulfate-Assisted Photocatalytic Degradation of Thiabendazole and Carbamazepine using BiOCl-P25 composites

5-III.1 Abstract

The photocatalytic degradation of the benzimidazole, fungicide thiabendazole (TBZ) and carbamazepine (CBZ) was studied using BiOCl and BiOCl-TiO_2 (P25) composite photocatalysts, with particular emphasis on persulfate (PS) activation under irradiation. The performance of BiOCl-P25 catalysts and PS-assisted systems was comparatively evaluated in terms of degradation efficiency, reaction time, and apparent kinetic rate constants.

In the absence of persulfate, BiOCl exhibited high TBZ removal efficiency (≈99%), although requiring prolonged irradiation times, which specifies the limited intrinsic reaction kinetics. The incorporation of BiOCl into TiO_2 (P25) significantly improved degradation rates, achieving complete TBZ removal within shorter times compared to bare BiOCl, indicating enhanced interfacial charge transfer within the composite system.

The introduction of persulfate markedly accelerated TBZ degradation for all catalysts. Notably, BiOCl coupled with 1 mM PS demonstrated superior performance compared to homogeneous PS activation alone and to PS-assisted P25, achieving complete degradation within significantly reduced reaction times and higher apparent rate constants. Increasing the PS concentration further enhanced degradation kinetics, with BiOCl-PS systems reaching complete TBZ removal within minutes under optimized conditions. The highest reaction rates were observed for 5%BiOCl-P25–PS systems at higher catalyst loadings, indicating a positive interaction between heterojunction-mediated charge separation and persulfate activation pathways.

In addition to TBZ, carbamazepine degradation was investigated as a second model pharmaceutical pollutant to evaluate the adaptability of the photocatalytic system. CBZ exhibited faster degradation kinetics compared to TBZ, particularly over the 5%BiOCl–P25 heterojunction, achieving complete degradation within a shorter reaction time. The enhanced degradation of CBZ can be attributed to its molecular structure, which is more vulnerable to oxidative attack by reactive oxygen species.

Overall, the results demonstrate that BiOCl-based heterojunction photocatalysts combined with persulfate activation represent an efficient strategy for the removal of persistent pharmaceutical

contaminants from water, providing improved degradation kinetics and enhanced oxidative pathways under simulated solar irradiation.

5-III.2 Photocatalytic activity

The photocatalytic activity of the prepared TiO_2, BiOCl, and BiOCl–TiO_2 (P25) composite materials was evaluated through the degradation of 10 mg L^{-1} thiabendazole (TBZ) in Milli-Q® water at its natural pH. Commercial TiO_2 P25 (Evonik) was used as a reference photocatalyst. Photocatalytic reactions were carried out in a cylindrical borosilicate glass reactor (300 mL total volume) containing the TBZ aqueous solution and catalyst suspension. The catalyst dosage was fixed at 1 $g \cdot L^{-1}$. The suspension was magnetically stirred continuously and aerated with air throughout the reaction to ensure homogeneous dispersion and oxygen supply. The reactor was placed inside a solar simulator (Solarbox 1500 standard, CO. FO.ME.GRA, Italy) provided with a 1500 W Xenon Lamp and a cutoff filter for $\lambda < 300$ nm. The total irradiance between 300 and 800 nm was estimated to be 328.7 W m^{-2}. During the experiments, aliquots were collected at predetermined time intervals, filtered through a 0.45 μm nylon membrane filter, and analyzed using high-performance liquid chromatography (HPLC).

To investigate the role of sulfate radicals in the photocatalytic process, potassium persulfate ($K_2S_2O_8$) was added to the reaction solution at concentrations of 1 mM and 2 mM The effect of persulfate concentration on degradation efficiency and reaction kinetics was systematically evaluated. For reusability tests, the catalyst was recovered after each reaction cycle. The recovered material was thoroughly washed with ultrapure water and dried at 60°C for 24 hours before being reused. The catalyst was subsequently tested for additional reaction cycles to assess its stability and performance retention.

5-III.3 HPLC-DAD

The concentration of thiabendazole (TBZ) during photocatalytic experiments was determined using a high-performance liquid chromatography system equipped with a diode-array detector (HPLC–DAD, Agilent 1260 Infinity II). Chromatographic separation was achieved using a Poroshell 120 EC-C18 column (4.6 × 100 mm, 2.7 μm particle size).

The mobile phase consisted of:

- **Solvent A:** 5 mM sodium dihydrogen phosphate (NaH_2PO_4) and 12.5 mM sodium hydrogen phosphate (Na_2HPO_4) buffer solution (pH 7.0)
- **Solvent B:** Acetonitrile

The analysis was performed in **gradient mode** at a flow rate of 1.0 mL min^{-1}. The injection volume was 20 µL. TBZ was monitored at a detection wavelength of 300nm.

5-III.4 Photocatalytic Degradation of Thiabendazole

The photocatalytic activity of thiabendazole was investigated by using Bismuth oxyhalide photo-catalyst in both the heterojunction and persulfate assisted system using solar stimulator provided with a 1500 W Xenon Lamp and a cutoff filter for $\lambda < 300$ nm). The results obtained demonstrated that catalytic efficiency strongly depends on charge separation and radical generation pathways. Bare commercial titanium dioxide (P25) exhibited high degradation efficiency (98% in 60 min, k = 0.1357 min^{-1}), which can be attributed to its mixed anatase–rutile composition that enables interfacial charge transfer and reduces electron–hole recombination. In comparison, bare BiOCl showed comparatively lower activity (94% in 120 min, k = 0.0611 min^{-1}). The slower kinetics of BiOCl is mainly correlated with rapid recombination of photogenerated charge carriers and limited redox driving force, which restricts efficient reactive oxygen species (ROS) formation. The 5%BiOCl–P25 composite displayed improved performance compared to pristine BiOCl (k = 0.1196 min^{-1}), indicating enhanced interfacial charge transfer within the composite structure.

5-III.5 Activation of Persulfate

The degradation kinetics of TBZ followed pseudo-first-order behavior, as confirmed by the linear relationship obtained from $\ln(C_0/C)$ versus irradiation time plots. The addition of persulfate (PS) significantly enhanced TBZ degradation. For instance, BiOCl–1 mM PS and BiOCl–2 mM PS systems achieved complete degradation within 45 minutes, with rate constants increasing to 0.1464 and 0.1469 min^{-1}, respectively (see Table 5.III.1). This enhancement can be explained by the electron-scavenging role of persulfate. Upon irradiation, photogenerated electrons reduce $S_2O_8^{2-}$ to produce sulfate radicals ($SO_4^{\bullet-}$), which are strong oxidizing species. Simultaneously, electron consumption suppresses recombination, increasing hole availability and promoting hydroxyl radical formation. The small difference between 1 mM and 2 mM PS indicates that an optimal concentration exists, beyond which radical self-scavenging reactions may limit further improvement.

The heterojunction system (5%BiOCl–P25) exhibited improved photocatalytic performance compared to bare BiOCl due to improved interfacial charge separation. When combined with 2 mM PS, this system achieved the highest rate constant (k = 0.1653 min^{-1}), confirming a synergistic interaction between heterojunction-mediated charge separation and persulfate-driven radical generation. The improved performance suggests efficient spatial separation of photogenerated electrons and holes, leading to simultaneous production of $^{\bullet}OH$ and $SO_4^{\bullet-}$ radicals that actively participate in TBZ oxidation.

5-III.6 Quantitative evaluation of synergic (synergy) effect (rate-constant method)

To quantitatively assess whether the combined system shows a super-additive (synergistic) effect, a **synergy index (SI)** was calculated using pseudo-first-order rate constants:

Given data (from experiments)

- $k_A = 0.1196$ min^{-1}

  (5%BiOCl–P25)

- $k_B = 0.1375$ min^{-1}

  (2 mM PS)

- $k_{A+B} = 0.1653$ min^{-1}

  (5%BiOCl–P25 + 2 mM PS)

1) Synergy Index (SI)

$$SI = \frac{k_{A+B}}{k_A + k_B}$$

$$k_A + k_B = 0.1196 + 0.1375 = 0.2571 \text{ min}^{-1}$$

$$SI = \frac{0.1653}{0.2571} = 0.6429$$

Result:

$$SI \approx 0.643 \ (< 1)$$

Interpretation: SI<1 indicates the combined effect is not strictly super-additive (not mathematically synergistic) under this definition.

However, the combined system shows a clear practical enhancement compared to the individual components, with an increase of approximately 38% relative to the heterojunction alone and about 20% relative to persulfate alone. This improvement can be attributed to complementary mechanisms: enhanced spatial separation of photogenerated charge carriers in the heterojunction and efficient electron scavenging by persulfate, which promotes the formation of additional sulfate radicals ($SO_4^{\bullet-}$). The coexistence of •OH and $SO_4^{\bullet-}$ radicals increase the overall availability of reactive oxidative species responsible for TBZ degradation.

Catalyst stability was evaluated through a recovery experiment. The slight decrease in rate constant (from 0.1653 to 0.1416 min^{-1}) after reuse indicates minor surface deactivation, likely due to intermediate adsorption or partial active site blockage, while confirming the overall structural stability of the catalyst.

When experiments were carried out in real water matrices (tap water and mineral water), a substantial decrease in degradation rate was observed (k = 0.0256 and 0.0424 min^{-1}, respectively). This reduction is attributed to the presence of inorganic ions (e.g., Cl^-, HCO_3^-, SO_4^{2-}) and natural organic matter, which compete with TBZ for reactive radicals and act as radical scavengers. These matrix effects reduce the effective concentration of oxidative species, highlighting the challenges associated with practical water treatment applications.

Table 5-III.1 Degradation of Thiabendazole (TBZ) under simulated solar light irradiation.

Catalyst	%X Degradation	Time [min]	k [min^{-1}]	R^2
P25	98	60	0.1357	0.9868
BiOCl	94	120	0.0611	0.9733
5%BiOCl-P25	100	60	0.1196	1
1mM PS	98	60	0.1055	0.9566
2mM PS	96	45	0.1375	0.9796
P25-1mM PS	96	60	0.1023	0.9868
BiOCl-1mM PS	100	45	0.1464	0.9930
BiOCl-2mM PS	100	45	0.1469	0.9877
5%BiOCl-P25-1mM PS	96	45	0.1464	0.993
5%BiOCl-P25-2mM PS	100	45	0.1654	0.993
5%BiOCl-P25-2mM PS (Recover)	95	45	0.1416	0.9872
BiOCl-2mM PS 15ppm TW	91	90	0.0256	0.9923
BiOCl-2mM PS 15ppm MQW	90	90	0.0424	0.9914

The physicochemical properties and photocatalytic performance of the synthesized and commercial samples are summarized in Table 5.III.2. The results clearly demonstrate that both the synthesis method and composition significantly influence surface area, band gap energy, and reaction kinetics.

The bare BiOCl exhibited a very low specific surface area (3.3 $m^2 g^{-1}$) and a relatively wide band gap (3.48 eV), which limits its light absorption in the visible region. Consequently, it showed the lowest photocatalytic activity with a rate constant of 0.0611 min^{-1}. The regression coefficient (R^2 = 0.9733) indicates that the degradation follows pseudo-first-order kinetics with reasonable linearity.

In contrast, the composite prepared via ball-milling 5% BiOCl-P25, showed a significant enhancement in surface area (32.5 $m^2 g^{-1}$) and a reduced band gap (3.08 eV), which contributed to improve light absorption and more efficient charge separation at the heterojunction interface. As

a result, the rate constant nearly doubled (0.1196 min^{-1}) compared to bare BiOCl. The regression coefficient (R^2 = 1) confirms excellent agreement with pseudo-first-order kinetic behavior.

Interestingly, further increasing the BiOCl loading to 7% leads to a slight increase in surface area (37.8 m^2 g^{-1}); however, the photocatalytic activity decreased (k = 0.0824 min^{-1}). This reduction may be attributed to excessive BiOCl coverage on the P25 surface, which can partially block active sites and hinder efficient interfacial charge transfer. These results indicate the presence of an optimal BiOCl loading (5%) for maximizing photocatalytic performance.

Commercial P25 exhibited the highest surface area (50 m^2 g^{-1}) and the highest rate constant (0.1357 min^{-1}), which can be attributed to its well-known anatase–rutile mixed phase structure that promotes effective charge separation. The high regression coefficient (R^2 = 0.9868) further confirms reliable pseudo-first-order kinetics.

Overall, the results demonstrate that photocatalytic performance is governed by a combination of surface area interfacial charge separation, band gap tuning, and heterojunction formation, with 5% BiOCl–P25 representing the optimum balance between structural and electronic properties.

These trends are further illustrated in Figures 5.III.1. A and B, where the apparent pseudo-first-order kinetic rate constants (k) are compared for the different catalyst systems. The results clearly show that the incorporation of BiOCl into P25 improves the photocatalytic activity, while persulfate addition further accelerates TBZ degradation kinetics.

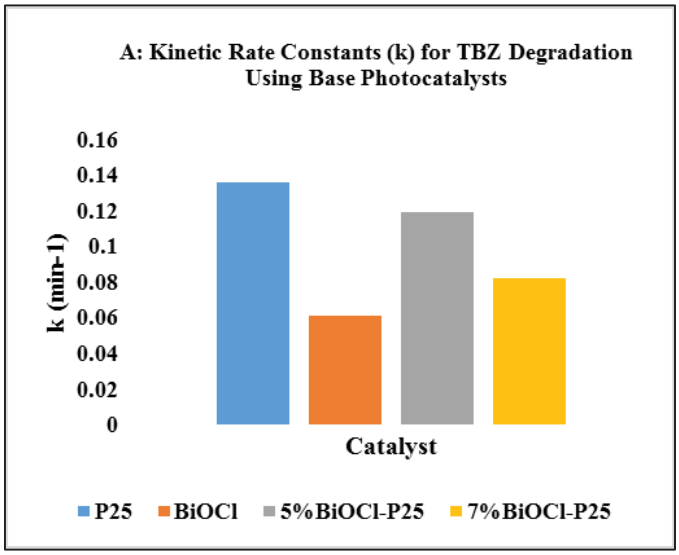

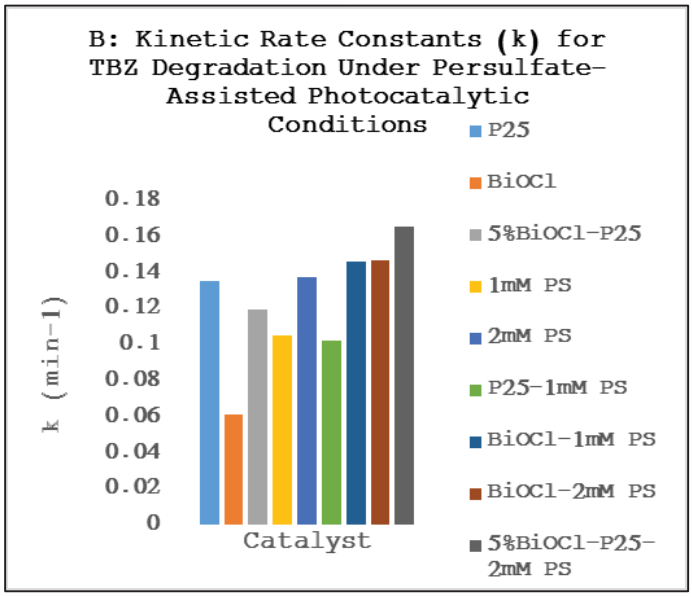

Figure 5-III.1. Apparent pseudo-first-order kinetic rate constants (k) for TBZ degradation under simulated solar irradiation using **A:** different catalyst **B**: under persulfate-assisted photocatalytic conditions using different catalyst–persulfate systems.

Table 5-III.2 Synthesis conditions of catalysts, BET area of samples and their pseudo-first order kinetic rate constants (k) and regression coefficient (R^2) values for TBZ degradation reactions.

Procedure	**Sample**	**S.S.A. (m^2 g^{-1})**	**Band gap (eV)**	**Rate k (min^{-1})**	**Regression coefficient (R^2)**
Co-precipitation	BiOCl	3.30	3.48	0.0611	0.973
Ball-Milling	5%BiOCl-P25	32.5	3.08	0.1196	1.000
Ball-Milling	7%BiOCl-P25	37.8	3.10	0.0824	0.999
Commercial	P25	50.0	3.10	0.1357	0.987

5-III.7 Evolution of the concentration

Figure 5.III.2. shows the evolution of the concentration of thiabendazole vs irradiation time in the presence of some representative photocatalysts.

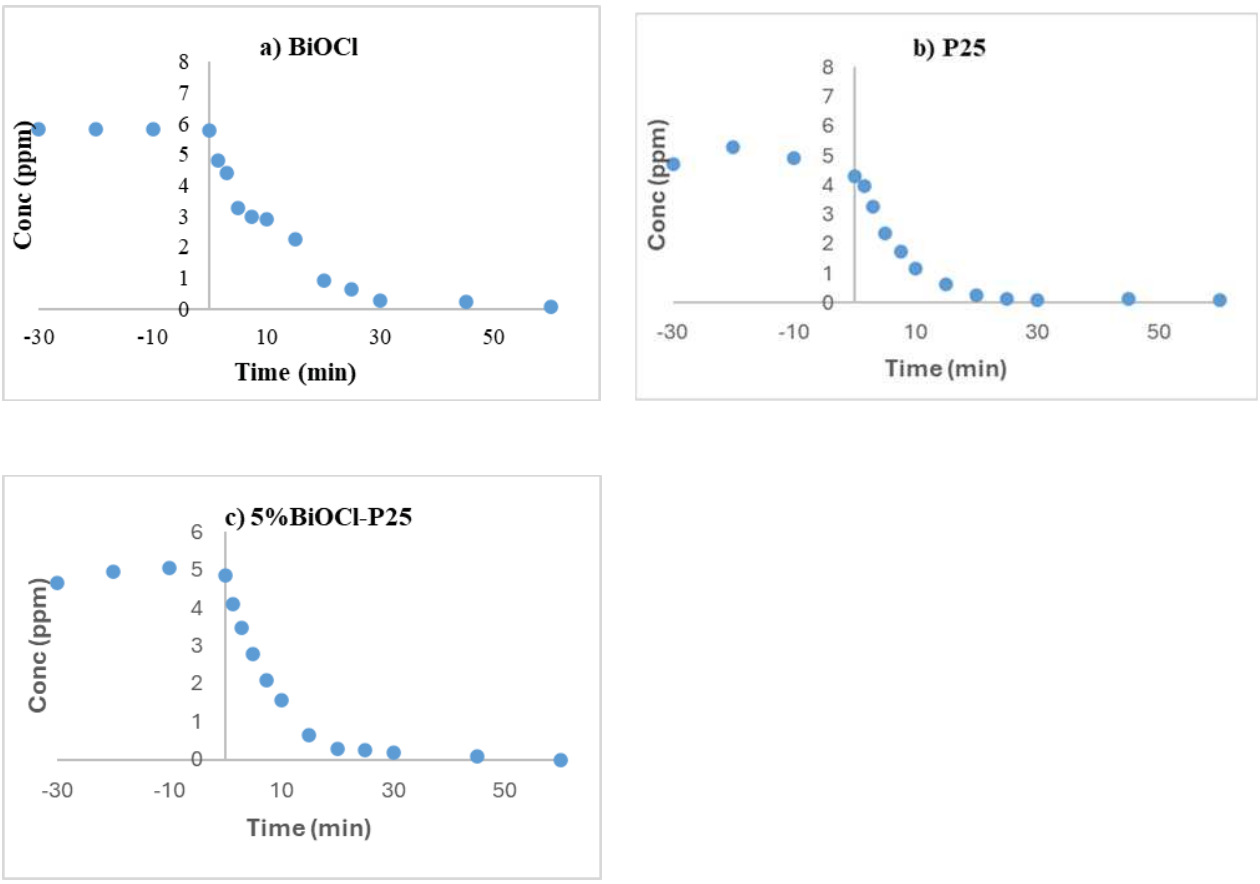

Figure 5-III.2. Evolution of thiabendazole concentration as a function of irradiation time; a) BiOCl, b) P25, c) 5%BiOCl-P25 under simulated solar light irradiation and aerobic conditions.

In Figure 5.III.3, the concentration versus time for thiabendazole degradation is reported with 1mM persulfate assisted system with different catalysts.

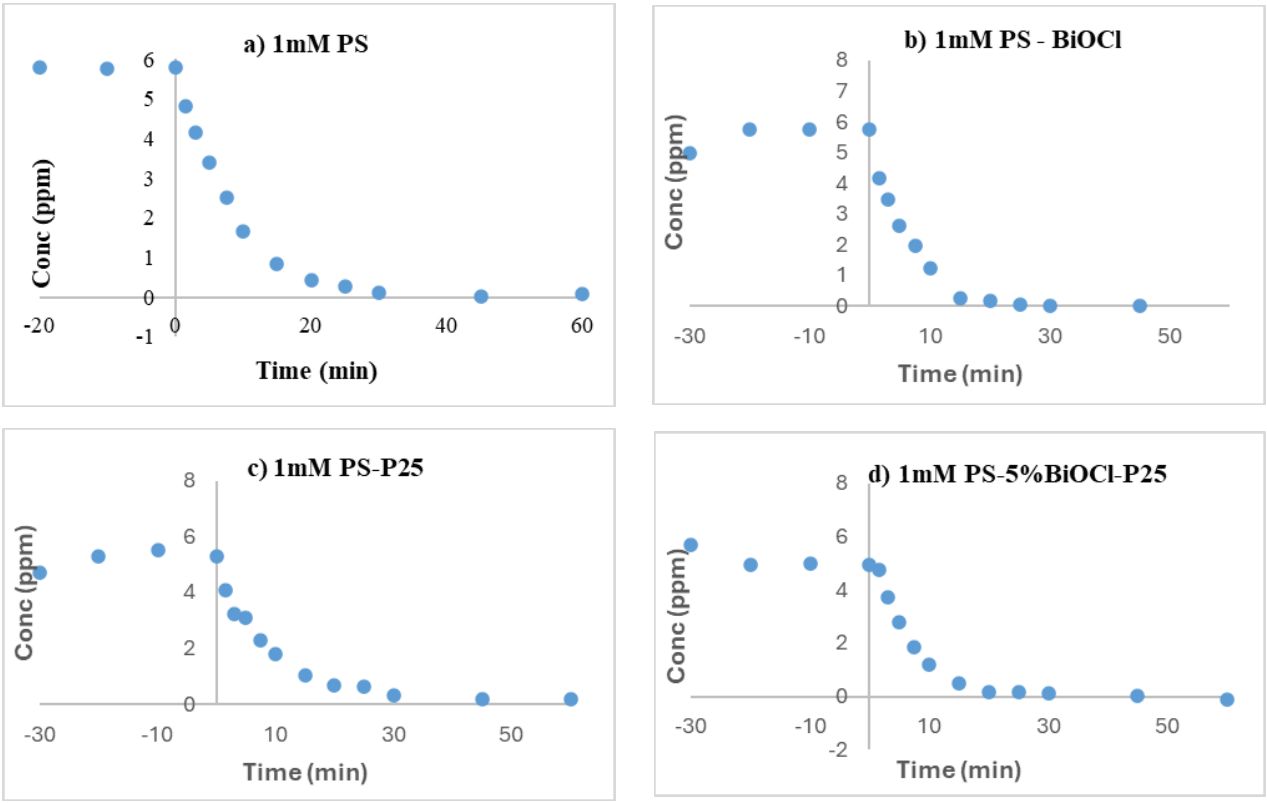

Figure 5-III.3. Evolution of thiabendazole concentration as a function of irradiation time for a) 1mM PS , b) 1mM PS-BiOCl , c) 1mM PS-P25, d) 1mM PS-5%BiOCl-P25 under simulated solar light irradiation and aerobic conditions.

In Figure 5.III.4, the concentration versus time for thiabendazole degradation is reported with 2mM persulfate assisted system with different catalysts.

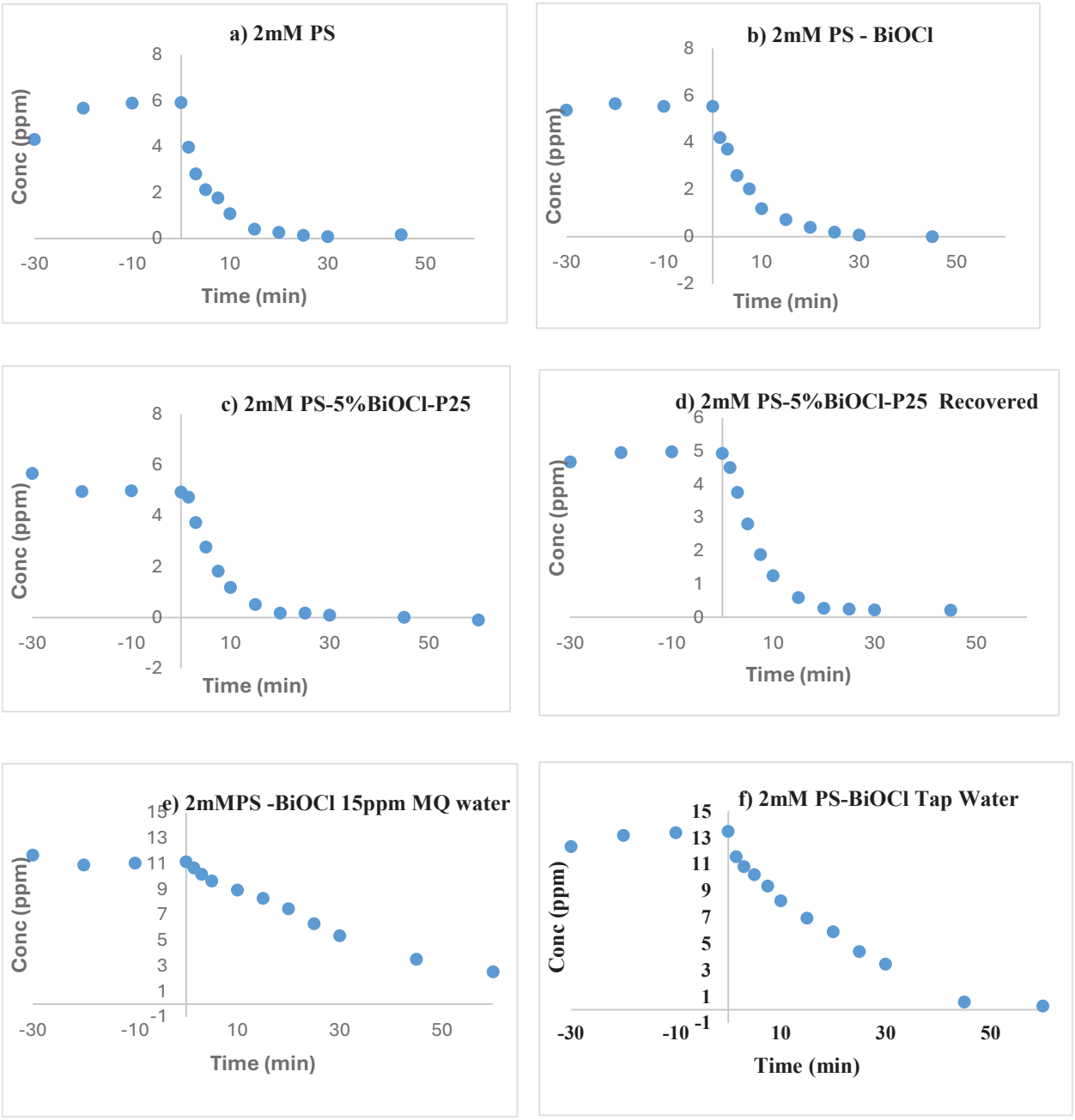

Figure 5-III.4. Evolution of TBZ concentration under simulated solar irradiation for: (a) PS alone, (b) PS/BiOCl, (c) PS/5%BiOCl-P25, (d) recovered PS/5%BiOCl-P25, (e) PS/BiOCl in Milli-Q water, and (f) PS/BiOCl in tap water.

5-III.8 Carbamazepine

The photocatalytic degradation of carbamazepine (CBZ) revealed a strong dependence on catalyst composition. P25 exhibited high activity ($k = 0.2351\ min^{-1}$), achieving 99% degradation within 30 min, which can be attributed to its efficient hydroxyl radical generation under simulated solar irradiation. In contrast, bare BiOCl showed significantly lower activity ($k = 0.0444\ min^{-1}$), likely due to rapid electron–hole recombination and limited ROS production. The 5%BiOCl–P25 heterojunction demonstrated the highest rate constant ($k = 0.2624\ min^{-1}$), achieving complete degradation within 20 min. The improved performance of the heterostructure can be attributed to enhanced interfacial charge separation, which prolongs charge carrier lifetime and increases the availability of reactive oxidative species. These results confirm that coupling BiOCl with TiO_2 effectively enhances photocatalytic efficiency toward CBZ degradation.

Table 5-III.3 Carbamazepine (CBZ) degradation under simulated solar light irradiation.

Catalyst	% Degradation	Time (min)	k (min^{-1})	R^2
P25	99.00	30	0.2351	0.9419
BiOCl	94.74	45	0.0444	0.9520
5%BiOCl–P25	100.0	20	0.2624	0.7375

5-III.8.1 Half-Life Comparison

Formula:

$$t_{1/2} = \frac{0.693}{k}$$

CBZ – 5%BiOCl–P25

$$t_{1/2} = 0.693/0.2624 \approx 2.64\ \text{min}$$

TBZ – 5%BiOCl–P25–PS

$$t_{1/2} \approx 4.2 \text{ min}$$

Carbamazepine clearly degrades faster with 5%BiOCl-P25 composites as shown in Figure 5.III.5. The faster degradation of CBZ with 5%BiOCl-P25 as compared to BiOCl and P25 photocatalyst alone, may also be related to the higher electron density in its aromatic system, which makes it more susceptible to oxidative attack by reactive oxygen species.

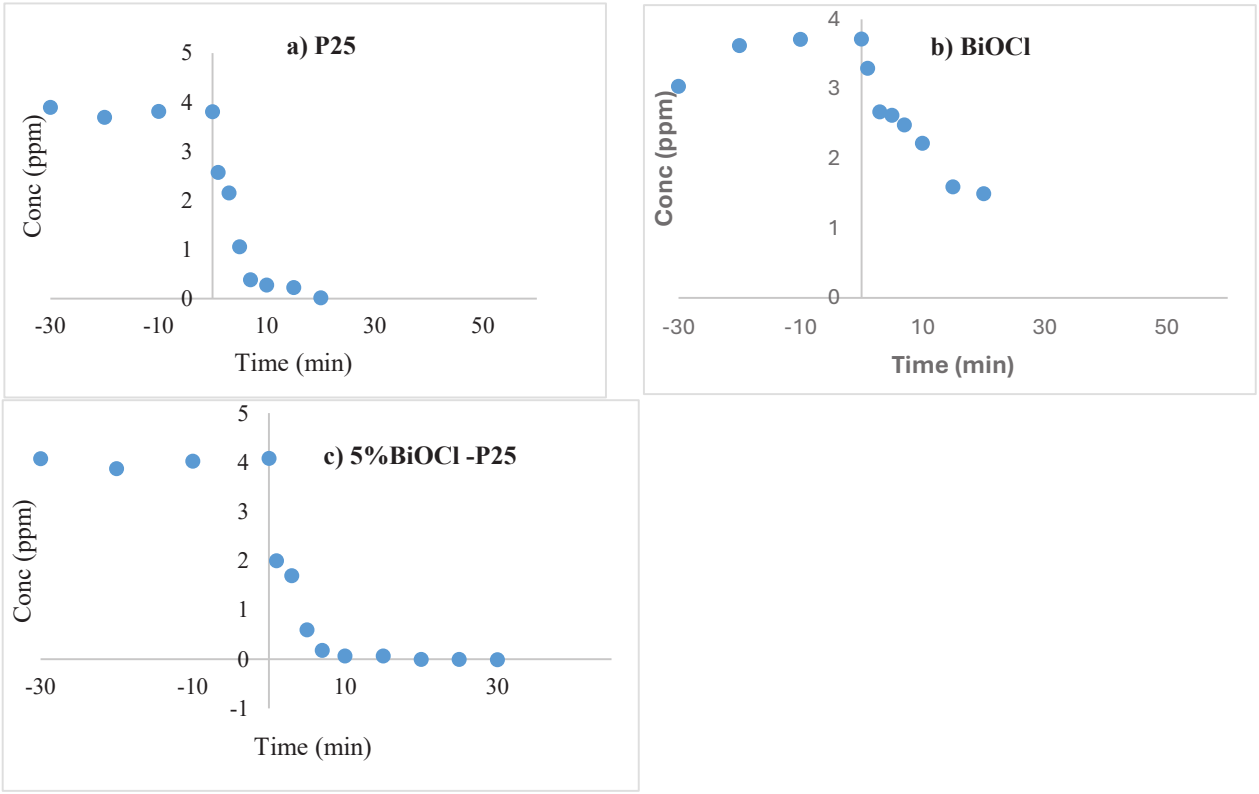

Figure 5-III.5. Concentration versus irradiation time for carbamazepine degradation for a) P25, b) BiOCl, c) 5%BiOCl-P25 under simulated solar light irradiation.

5-III.9 Photocatalytic degradation mechanism

Figure 5-III.6 shows the possible photocatalytic degradation mechanism of the organics used as model wastewater compounds in the presence of BiOCl-TiO_2 composites. According to literature [256-258,260], an efficient type II heterojunction is formed after coupling TiO_2 with BiOCl in which electrons move from BiOCl to TiO_2 and holes in the opposite directions. Electrons and

holes, reacting with O_2 and H_2O, respectively, give rise to the very active radical species $^{\bullet}O_2^-$ and $^{\bullet}OH$ that completely degrade the pollutants into the eco-friendly molecules CO_2 and H_2O.

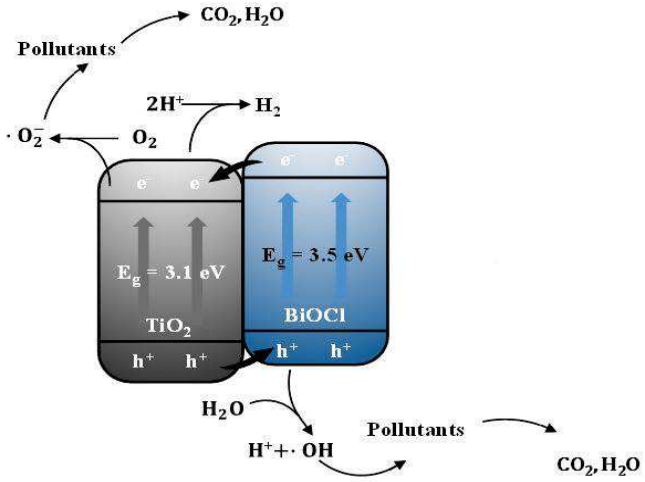

Figure 5-III.6. The possible photocatalytic degradation mechanism of pollutants by using the BiOX-TiO_2 composites

5-III.9 Conclusion

The results indicate that TBZ degradation is primarily limited by charge carrier recombination in bare systems. The introduction of persulfate significantly enhances radical-mediated oxidation, while the BiOCl-P25 heterojunction further improves charge separation efficiency through complementary pathways. Although the synergy index calculated using simple additive kinetics is less than unity (SI ≈ 0.64), the combined system still shows clear kinetic enhancement compared to individual components. This suggests a positive interaction between the heterojunction and persulfate activation, rather than strict mathematical super-additivity. These results demonstrate that combining heterojunction photocatalysts with persulfate activation represents a promising strategy for enhancing the degradation of persistent pharmaceutical contaminants in water

In addition to thiabendazole, carbamazepine (CBZ) was also evaluated to investigate the versatility of the photocatalytic system toward structurally different pharmaceutical pollutants. The results indicate that CBZ exhibits faster degradation kinetics compared to TBZ over P25 and the 5%BiOCl–P25 heterojunction. For instance, the rate constant of CBZ over 5%BiOCl–P25 reached 0.2624 min^{-1}, which is significantly higher than that observed for TBZ under similar conditions.

This difference can be attributed to the molecular structure of CBZ, which contains conjugated aromatic rings that are more susceptible to oxidative attack by reactive oxygen species. In contrast, TBZ, containing heteroatoms such as sulphur and nitrogen, shows relatively higher structural stability, resulting in comparatively slower degradation. These findings confirm that while the heterojunction system enhances charge separation efficiency for both pollutants, the degradation rate strongly depends on the intrinsic chemical structure of the target molecule.

Persulfate was not investigated for CBZ degradation because the heterojunction system already provided rapid degradation kinetics and the objective of the persulfate-assisted system was to improve degradation in relatively slower systems such as TBZ. Since CBZ already exhibited rapid degradation under heterojunction conditions, the addition of persulfate was not prioritized in this study. While the photocatalytic system demonstrated high degradation efficiency toward both TBZ and CBZ, further studies focusing on the identification of degradation intermediates and their ecotoxicological assessment would be valuable to fully evaluate the environmental safety of the treatment process.

SECTION III

TiO_2 BASED PHOTOCATALYSTS FOR DRUGS AND DYES DEGRADATION

CHAPTER 5-IV

5.IV. Efficient photocatalytic removal of drugs in aqueous dispersions by using different TiO_2-based semiconductors under UV and simulated solar light irradiation

5-IV.1 Abstract

Antibiotics are an important class of environmental pollutants. Due to their widespread use, low metabolism by organisms and persistence in the aquatic environment, they pose a serious risk to human health and environmental quality. The effective removal of pharmaceuticals and their metabolites from aqueous wastewater represents an audacious challenge for the scientific community. Heterogeneous photocatalysis has been applied as an effective technology for the removal of organic pollutants because it can induce their complete mineralization into CO_2, H_2O and inorganic species when heteroatoms are present in the degraded molecules without giving rise to the so-called secondary pollution. This study is addressed to enhance the efficiency of differently modified commercial and home-prepared TiO_2-based photocatalysts (heterojunctions with Cu_2O and WO_3, and samples doped with N were also prepared) towards some representative drugs (tetracycline, oxytetracycline and lincomycin). N-doped TiO_2 revealed high photocatalytic activity under both UV and simulated solar light irradiation, allowing not only the drugs removal but also a higher mineralization degree. $O_2^{\bullet-}$ radicals was found to be the main active species in the drugs degradation. Mechanistic investigations revealed first-order kinetics.

5-IV.2 Experimental

5-IV.2.1 Chemicals

Titanium tetrachloride ($TiCl_4$, 98%), titanium(IV) isopropoxide ($Ti(OCH(CH_3)_2)_4 \geq 97\%$) named as TTIP, tungsten trioxide (WO_3), hydrochloric acid (HCl, 37%), pluronic F127, ethanol (C_2H_5OH), tetracycline ($C_{22}H_{24}N_2O_8$), oxytetracycline ($C_{22}H_{24}N_2O_9$), and lincomycin ($C_{18}H_{54}N_2O_6S$) were purchased from Sigma-Aldrich, copper(I) oxide (Cu_2O) from Riedel-de Haën, and platinum chloride ($PtCl_4$) from BDH chemicals. All of them were used without further purification.

5-IV.2.2 Photocatalysts synthesis

Commercial TiO_2 samples P25 (about 80% anatase + 20% rutile) and BDH (anatase) were used as reference photocatalysts.

5-IV.2.3 Brookite/Rutile

210 mL of distilled water, 80 mL of HCl, and 5 mL of $TiCl_4$ were added to a 500 mL beaker and stirred until a clear solution was formed. Then, the mixture was transferred to a Pyrex bottle and heated for 48h at 100 °C. The resulting suspension was a mixture of brookite and rutile. Pure brookite nanoparticles were recovered from the supernatant by performing peptization with water several times while the rutile phase precipitated. The respective samples were simply named brookite and rutile. For comparison, the as prepared brookite was calcined at 450 °C for 2h and named calcined brookite.

5-IV.2.4 X%Cu_2O/WO_3–P25

A Retsch Ball Mills, type PM100 ball milling was used to prepare the mixture of two different oxides (Cu_2O or WO_3) with P25 (TiO_2). WO_3-P25 samples were prepared with three different ratios i.e., 2, 3 and 5% at 150 rpm for 2h. While for Cu_2O-P25, the previously determined best conditions (3% w/w, 150 rpm and 2h) were chosen [25].

5-IV.2.5 TiO_2 HP

Tetraisopropoxide (TTIP), surfactant Pluronic F127, HCl, H_2O and ethanol were used in molar ratios of 1:0.005:0.5:15:40, but TTIP was added to the mixture of the other four precursors after the formation of a solution. The mixture was placed under stirring for ca. 24h at 40 °C. After that it was dried at 110 °C in air. The resulted dried powder was calcined at 500 °C for 6h to remove the organic template and to enhance the crystallinity. The temperature ramp rate was 0.3 °C/min whereas the cooling rate was 10 °C/min. This sample was identified with the code HP1.

5-IV.2.6 TiO_2 HP x%N

$TiCl_4$ and distilled water were added in a molar ratio of 1:75 in a 1000 mL beaker and stirred until a solution was formed. After that, different percentages of NH_4Cl were added to prepare N-doped photocatalysts [277], and the resulting mixture was placed in an oven at 100 °C for 48h. The solids obtained were separated from the suspension and were identified as HP2 (the bare TiO_2 sample) and HP2 1%N, HP2 2%N, and HP2 3%N (the N-doped TiO_2 samples).

5-IV.3 Characterizations

The UV-Vis diffuse reflectance spectra (DRS) were obtained by using a Shimadzu UV-2401 PC spectrophotometer with barium sulphate ($BaSO_4$) as the reference in the wavelength range of 200- 800 nm at room temperature. The band gap values were determined by plotting the modified Kubelka-Munk function, $[F(R'_\infty)\ hv]^{½}$, versus the energy of the exciting light.
The specific surface areas (SSA) were determined by using the single-point BET method in a Flow Sorb 2300 apparatus (Micromeritics). Raman spectra were acquired by a BWTek-i-micro–Raman Plus System, equipped with a 532 nm diode laser. The morphology of the powders was examined using a Nova NanoSEM scanning electron microscope (SEM) operated at 20 kV with the samples covered with a thin layer of gold vapor.

5-IV.4 Photoreactivity

The reactivity experiments were carried out in a Pyrex batch photoreactor of cylindrical shape, containing 0.5 L of aqueous suspension. The optimum amount of photocatalyst ranged from 0.2 to 0.8 $g \cdot L^{-1}$ and it was determined in order to have the same absorbed photon flux in the reacting system. This amount was measured by slowly adding the powder to the suspension and by measuring the transmitted photon flux by the suspension; when the transmitted radiation was less than 10% with respect to the incident one, the catalyst addition was stopped. The photoreactor was provided with ports in its upper section for the inlet and outlet of gases and for sampling. A magnetic stirrer guaranteed a satisfactory suspension of the photocatalyst and the uniformity of the reacting mixture. A 125 W medium pressure Hg lamp (Helios Italquartz) was axially immersed within the photoreactor, and it was cooled by water circulating through a Pyrex thimble. The distance between the cooling jacket and the outer wall was approximately 30 mm while the temperature of the suspension was about 300 K. The average value of photon irradiance impinging on the suspension was 10 $mW \cdot cm^{-2}$, and it was measured by using a radiometer UVX Digital, at $\lambda = 360$ nm. The experimental runs were carried out by bubbling oxygen continuously during the reaction. Selected runs were carried out under simulated solar light irradiation by using a 150 W halogen lamp. Mechanistic aspect related to the degradation of lincomycin and tetracycline in the presence of the most active photocatalyst were investigated by adding selected scavenging species. Namely, tert-butanol, $AgNO_3$, $Na_2C_2O_4$ and benzoquinone were used as hydroxyl radicals, electrons, holes and superoxide anions scavengers, respectively.

5-IV.5 Results and discussion

5-IV.5.1 Raman Spectroscopy

The Raman spectra of the used samples are reported in Figure 5-IV.1. For the single-phase powders, the main bands related to rutile TiO_2 (235.5, 445.8 and 609.5 cm^{-1}), anatase (144, 196, 397, 513 and 639 cm^{-1}) and brookite (153, 323, 366, 413, 459, 500, 545, 584 and 633 cm^{-1}) can be distinguished [278-280].

In the home-made HP1, the characteristic bands of both anatase and rutile are observable, while in the commercial TiO_2 P25 only the anatase peaks are visible. In the heterostructures, no peaks corresponding to Cu_2O or WO_3 are observed, due to their low amount and uniform dispersion on the P25 surface. The Raman spectra of the bare and N-doped HP2 powders reveal the simultaneous presence of anatase and brookite TiO_2 polymorphs, and the presence of nitrogen does not modify the position of the TiO_2 peaks [281].

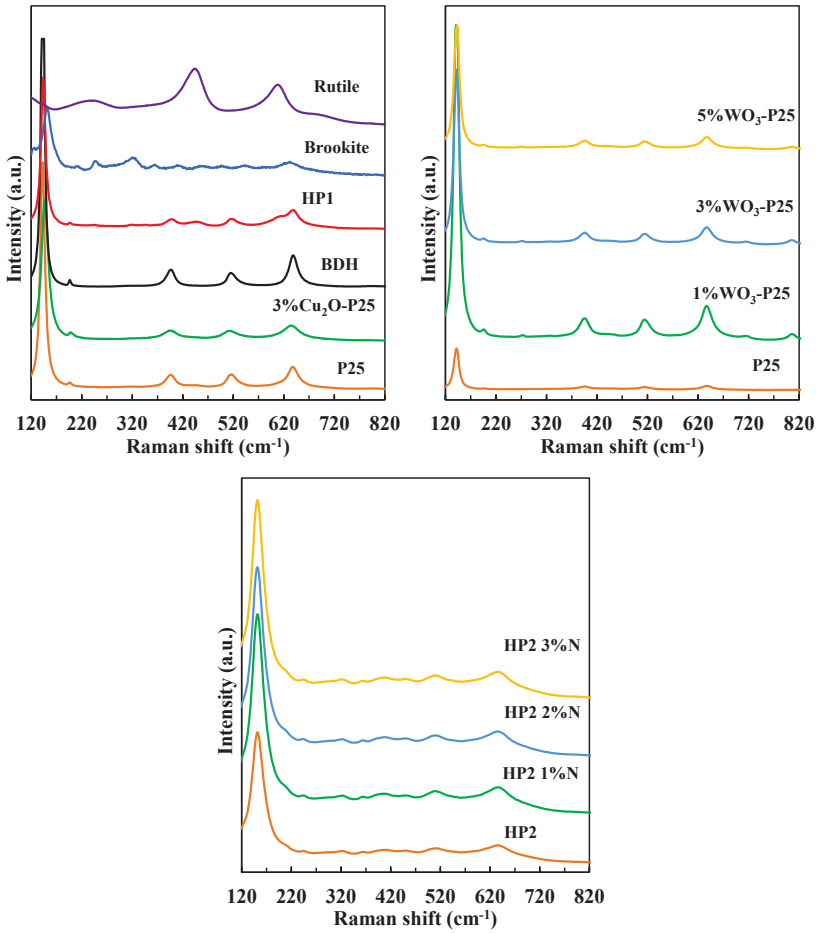

Figure 5-IV.1. Raman spectra of the different samples.

5-IV.5.2 UV-Vis DRS Spectroscopy

Figure 5-IV.2 shows the UV-Vis DRS spectra of the different solids used. BDH and Brookite show an absorption edge at around 360 nm corresponding to the typical band gap of anatase and brookite TiO_2 polymorphs, while a small shift towards higher wavelengths is exhibited by rutile and HP1, which is an anatase-rutile mixture. P25 shows a similar reflectance as anatase which is the main component; after coupling with Cu_2O a slight shift towards higher wavelengths can be noticed together with an enhancement in the light absorption between 400 and 800 nm. Furthermore, the appearance of a second absorption edge attributable to the hosted oxide is present, suggesting the formation of a heterostructure between the two components [25, 253]. After the addition of WO_3, however, only an increase in light absorption at wavelengths above 400 nm is observed for the higher percentages of WO_3. HP2 exhibits the typical TiO_2 reflectance shape with a transition edge in the range of 360-390 nm. A slight decrease in reflectance was observed in the presence of nitrogen. The band gap values of all photocatalysts were calculated by plotting the modified Kubelka-Munk function, $[F(R'\infty)\ h\nu]^{1/2}$, versus the exciting light energy (Figure 5-IV.2). The photocatalysts showed band gap values in the range of 2.96-3.26 eV.

Table 5-IV.1 shows the results of the SSA, and band-gaps values determined for the solids used. The values range from 10 to 115 $m^2\ g^{-1}$, with the lowest values being shown by commercial samples.

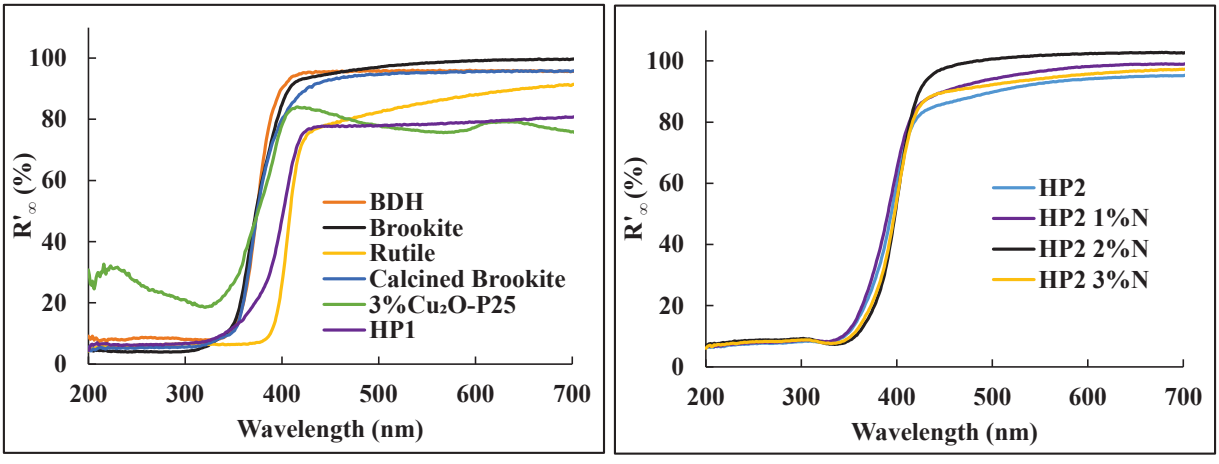

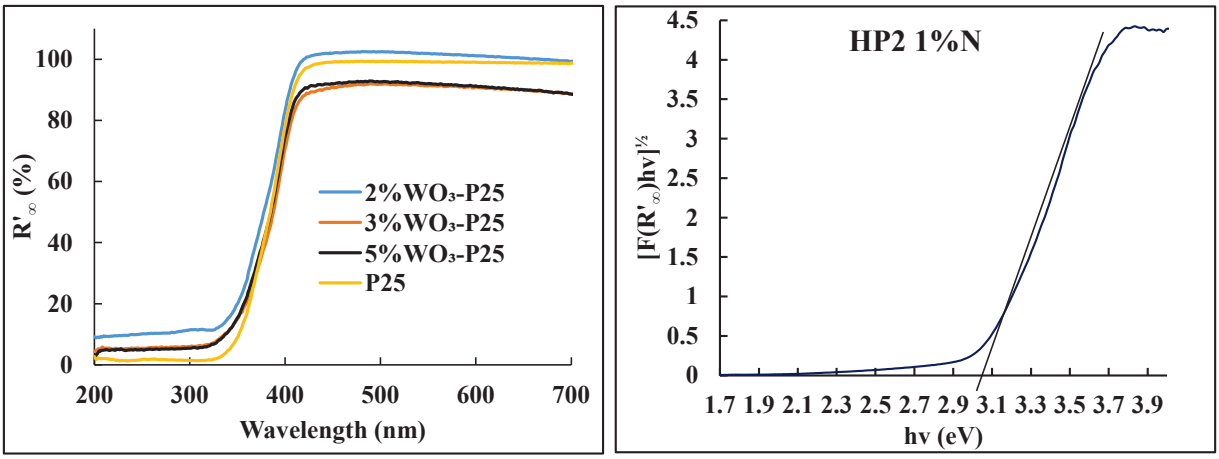

Figure 5-IV.2. UV-Vis DRS spectra of different solids used and $[F(R'\infty)\ hv]^{½}$ versus the energy of the exciting light for a selected catalyst.

Table 5-IV.1 Specific surface areas (SSA) and band gap values of the different photocatalysts. A= Anatase; R= Rutile; B=Brookite.

Samples	TiO_2 Crystalline phase	SSA (m^2/g)	Band gap (eV)
BDH	A	10	3.17
Rutile	R	85	3.02
Brookite	B	88	3.26
Calcined Brookite	B	46	3.26
HP1	A, R	75	2.99
P25	A, R	48	3.18
3%Cu_2O-P25	A, R	48	3.08
2%WO_3-P25	A, R	33	3.09
3%WO_3-P25	A, R	36	3.09
5%WO_3-P25	A, R	34	3.11
HP2	A, R	115	3.03
HP2 1%N	A, R	113	3.04
HP2 2%N	A, R	81	3.02
HP2 3%N	A, R	87	3.03

5-IV.5.3 Scanning Electron microscopy

Figure 5-IV.3 shows SEM images of some selected samples. All samples are formed by aggregates consisting of small particles of irregular shape with sizes of the order of a few hundred

nanometers. The presence of species other than TiO_2 is not observed, and these do not modify the morphology of the oxide that hosts them.

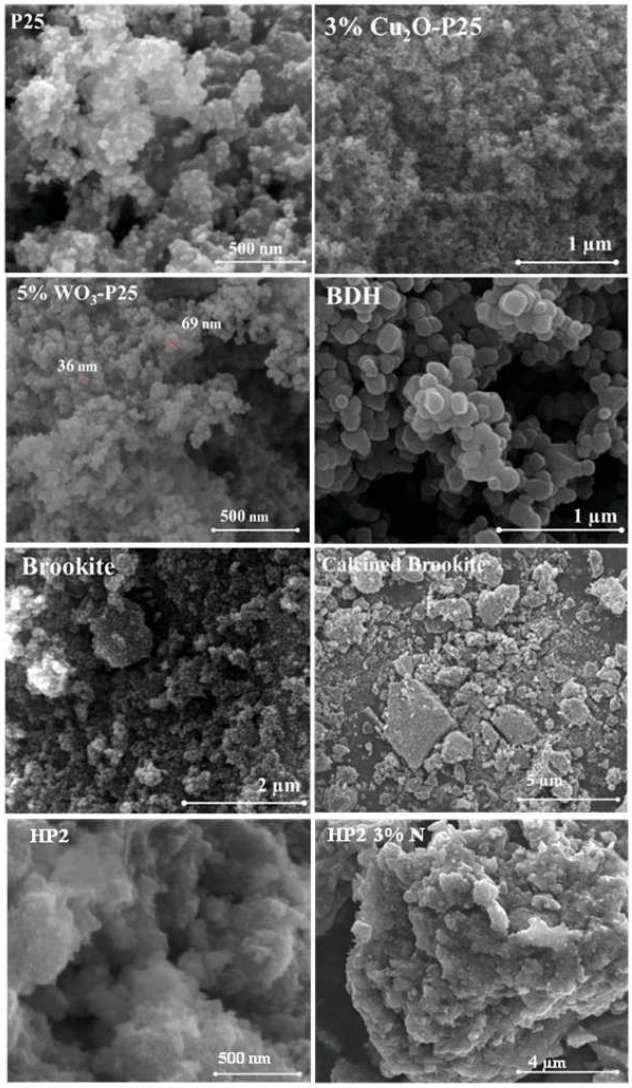

Figure 5-IV.3. SEM images of the selected samples.

5-IV.6.1 Photocatalytic activity

Table 5-IV.2 shows the results of the photocatalytic runs performed using the different photocatalysts in terms of pseudo first order constant and degree of mineralization after 4h of irradiation. P25 was found to be active in the degradation of all drugs with degree of mineralization ranging from 33 to 77%. Commercial anatase (BDH) and home-made Brookite, Rutile and HP1 showed lower activity. For this reason, modified P25-based photocatalysts and a new nitrogen-modified TiO_2 photocatalyst (HP2), produced in the laboratory, were used. The coupling with 3%

Cu_2O, unlike previous investigations related to glycerol photoreforming [25], was not advantageous in this case; only in the presence of LCM a slight improvement of the activity compared to pure P25 was obtained.

The addition of WO_3 to bare P25 caused an increase in the degree of mineralization of TC while it was deleterious in the degradation of drugs and in the mineralization of OTC and LCM. Using HP2, instead, a higher kinetic constant for TC and OTC was obtained together with a higher degree of mineralization of TC. The doping of HP2 with 1%N caused an increase in the kinetic constant for TC and OTC while the mineralization was maximum after the addition of 3% N reaching 81% after 4h of irradiation. The performance of these samples was worse than that of bare P25 for LCM highlighting that it is not possible to establish in absolute terms which is the most performing photocatalyst, but it should be attempted to correlate it to each single substrate considering the specific interactions between the latter and the surface of the photocatalyst [248, 282]. A very detailed analytical study would probably be necessary in order to identify at least the main reaction intermediates for each of the substrates and verify which of these presents a higher surface affinity with each of the photocatalysts used. However, this enormous analytical study is beyond the scope of this work.

Notably, the results reached in this study are valuable in comparison to previous investigations [38], considering that, in the best experimental conditions, TC was completely degraded after 1h of irradiation and a total organic carbon (TOC) removal of 81% was obtained over 4h, with photocatalysts (N doped TiO_2) prepared in an easy and economical way.

Table 5-IV.2 Pseudo first order rate constants (k_{obs}) and mineralization percentages determined by using the different photocatalysts with the used substrates.

Sample	Tetracycline		Oxytetracycline		Lincomycin	
	Rate·10^4 [s^{-1}]	Mineraliz. [%]	Rate·10^4 [s^{-1}]	Mineraliz. [%]	Rate·10^4 [s^{-1}]	Mineraliz. [%]
No catalyst	0.6	5	negligible	negligible	0.04	negligible
P25	15.9	57	7.8	77	9.6	33
BDH	3.5	13	3.4	12	2.8	1
Brookite	7.5	45	4.6	51	2.5	10
Rutile	1.2	5	0.5	3	5.6	1
Calcined Brookite	4.5	34	3.8	19	8.7	4
3%Cu_2O-P25	6.8	55	8.4	44	10.9	32
HP1	5.5	41	6.7	55	2.1	11
2%WO_3-P25	4.1	60	3.9	40	3.2	13
3%WO_3-P25	6.0	75	5.4	36	3.8	30
5%WO_3-P25	3.1	61	3.3	25	3.5	10
HP2	17.7	77	10.6	59	2.3	11
HP2 1%N	22.5	75	9.4	61	3.7	16
HP2 2%N	1.2	76	7.7	69	1.8	13
HP2 3%N	6.7	81	9.0	78	2.5	10

In this work we will try to compare, by using different characterization techniques, the various prepared photocatalysts with other commercial ones and understand which intrinsic

electronic or chemical-physical surface characteristics can give indications on the observed behaviour. However, it must be clear to the reader that this is independent from the influence that the presence of different degradation intermediates deriving from the three drugs can have on the observed photoreactivity. In fact, just as an example, very different photoabsorptions and photodesorptions phenomena and acidity of the intermediate species present during the reaction might significantly influence the interaction with the surface of the photocatalyst and therefore the reaction rate of the system both under UV and simulated solar irradiation.

To evaluate the efficiency of the prepared photocatalysts under real conditions, tests were carried out using a lamp simulating sunlight only in the presence of the most active samples. Figure 5-IV.4 shows the TC concentration versus irradiation time in runs performed using P25 and HP2 1%N. The two powders were effective in converting TC in about 2h and nitrogen-doped TiO_2 was more active than P25 for both conversion and drug mineralization which reached 70% after 4h of irradiation with the home-made photocatalyst and 54% with P25. Probably, the presence of N in the TiO_2 lattice, although does not reduce its band gap, creates some intermediate states close the valence band edge that enable the photocatalyst activation by visible light and reduce the electrons/holes recombination rate [277].

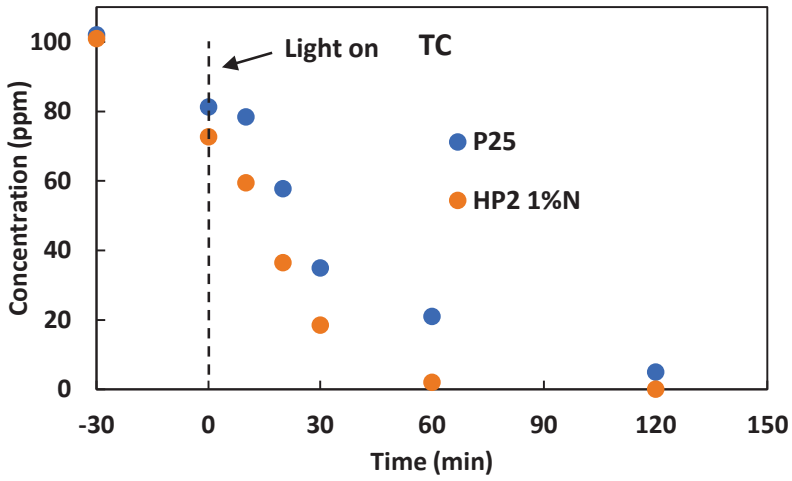

Figure 5-IV.4. Photocatalytic degradation under simulated solar light irradiation of TC by using selected photocatalysts.

5-IV.6.2 Mechanistic aspects

All data fit pseudo first order kinetics very well. Table 5-IV.2 shows the values of the observed pseudo-first order rate constants and the mineralization percentages determined using the different photocatalysts with the antibiotics used under UV irradiation. Figure 5-IV.5 shows typical concentration versus time values for the runs carried out using the three drugs in the presence of HP2 3%N (the sample that gave the highest mineralization percentage for tetracycline (81%) and oxytetracycline (78%)). The exponential curves fit the data very well, thus confirming pseudo first order kinetics. The procedure for determining the kinetic parameters is described below.

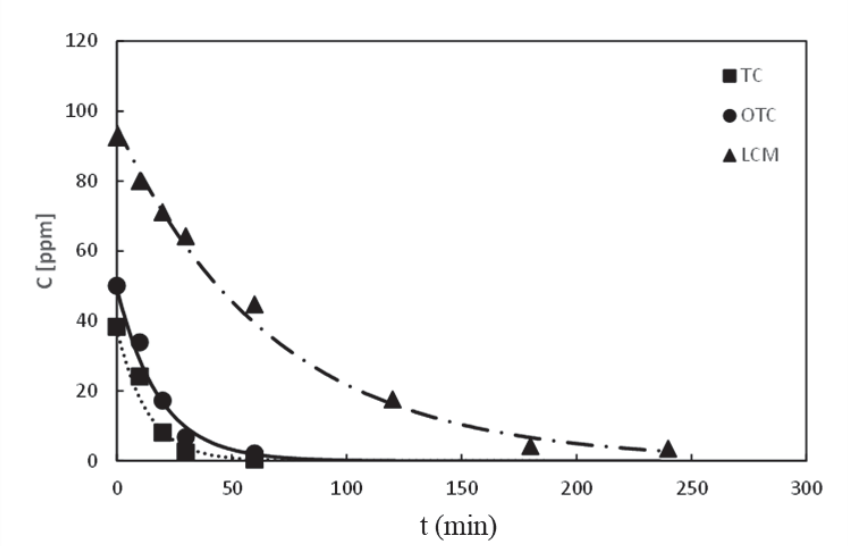

Figure 5-IV.5. Concentration versus irradiation time for runs carried out with TiO_2 HP2 3%N for the three drugs.

Without solid catalyst, an appreciable photolytic degradation of tetracycline and oxytetracycline was observed, and about 70% of the first molecule disappeared in 4 hours. On the contrary, only 20% of lincomycin was destroyed at the same irradiation time.

This behaviour can be explained by comparing the absorption spectrum of the three molecules with the emission spectrum of the lamp (Figure 5-IV.6). Both oxytetracycline and tetracycline reveal, in fact, absorption bands that partially overlap with the emission peaks of the lamp. Therefore, for these molecules it is necessary to take into account the simultaneous occurrence of two photolytic processes, one in the homogeneous phase and one in the adsorbed phase

(heterogeneous photocatalysis). For TC k_{obs} in homogeneous phase was $0.6 \cdot 10^{-4}$ s^{-1} and only 5% of mineralization was observed. The photodegradation of LMC, which was found to be less significant than that observed for the other two molecules, can only be attributed to the photocatalytic reaction in the adsorbed phase as a very low degradation ($k_{obs} = 4 \cdot 10^{-6}$ s^{-1}) and a negligible mineralization degree was measured in homogeneous conditions, in accordance with its absorption spectrum (Figure 5-IV.6).

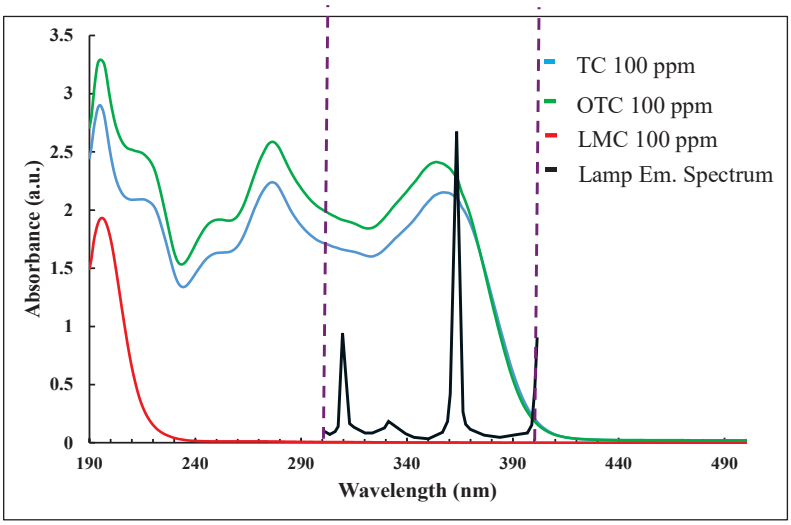

Figure 5-IV.6. Absorption spectra of the drugs and emission spectrum of the medium pressure Hg lamp.

The homogeneous photodegradation of an organic compound generally starts from an electronic excited state:

$$R \xrightarrow{h\nu} R^* \qquad (5\text{-IV.1})$$

The excited R* species can undergo homolytic bond scission to form radicals that eventually react to give final products with or without the participation of molecular oxygen:

$$R^* \rightarrow R_1^g + R_1^g \rightarrow \text{products} \qquad (5\text{-IV.2})$$

As far as the process of electronic transfer with oxygen molecules is concerned:

$$R^g + O_2 \rightarrow R^{g+} + O_2^{g-} \qquad (5\text{-IV.3})$$

Equation 5-IV.3 is a typical quenching reaction. The radical cation, $R^{\bullet+}$, can undergo hydrolysis or mesolytic bond scission to low-weight products, whereas the superoxide radical, $O_2^{\bullet-}$, is a very strong oxidant species able to degrade many aromatic species. Side-chain degradations by deamination, desulfuration and dealkylation are typical of many photolytic processes [283-286]. [286], [287], [288], [289].

The homogeneous degradation of tetracycline can be attributed to a deamination of the molecule [159, 287,288], which occurs when it is irradiated with near-UV light by producing dimethylamine (see Figure 5-IV.7).

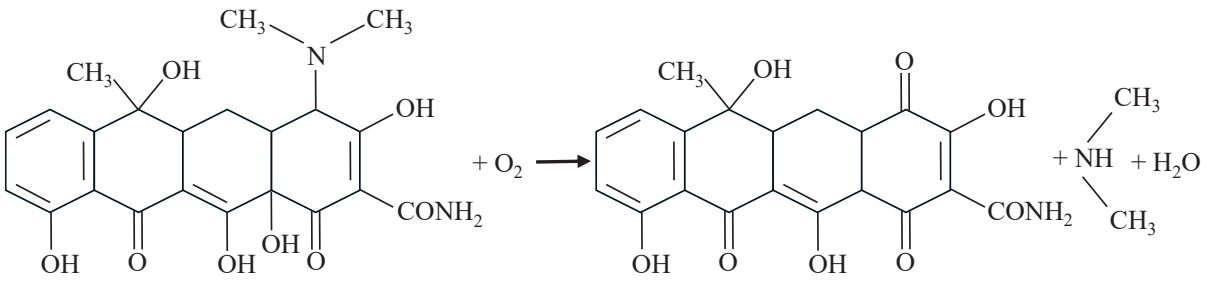

Figure 5-IV.7. Scheme of homogeneous degradation of tetracycline in the presence of oxygen.

The photochemical oxidation of lincomycin probably leads to the conversion of the thiomethyl group into sulfoxide and sulfone derivatives (see Figure 5-IV.8).

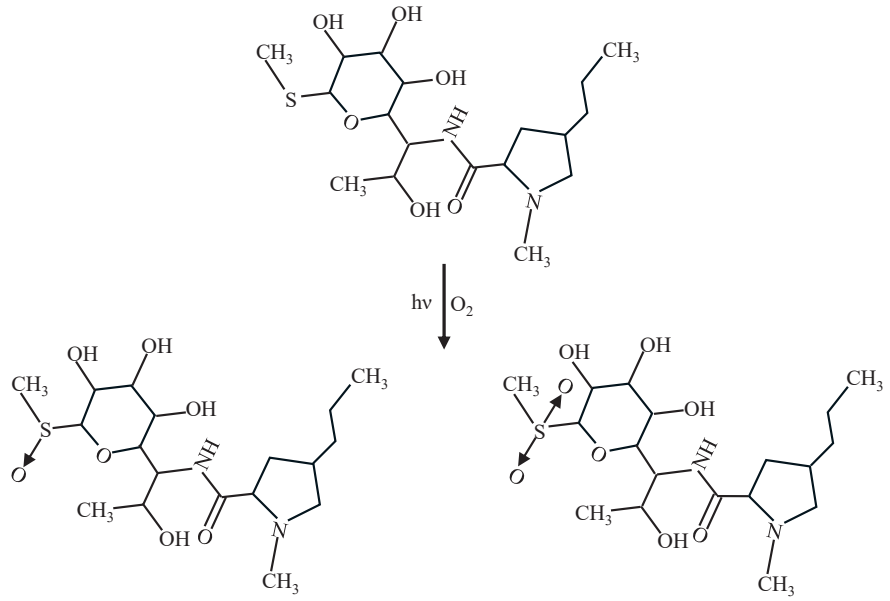

Figure 5-IV.8. Scheme of photochemical degradation of lincomycin.

As far as the mechanism of the heterogeneous photocatalytic reaction is concerned, the primary step is the generation of electrons and holes within the TiO_2 particle when it is irradiated by light of suitable energy.

$$TiO_2 \xrightarrow{h\nu} TiO_2 + e^-_{CB} + h^+_{VB} \qquad (5\text{-IV.4})$$

Electrons and holes, if properly separated, can migrate to the surface of the particles where they can either recombine or participate in interfacial oxidation and reduction reactions.
In aqueous solutions, the positive holes can react, with adsorbed water or with hydroxyl groups to form hydroxyl radicals $OH^{\bullet}$ which give rise to the oxidation reaction of a pollutant [289]:

$$H_2O + h^+_{VB} \rightarrow OH^g + H^+ \qquad (5\text{-IV.5})$$

$$OH^- + h^+_{VB} \rightarrow OH^g \qquad (5\text{-IV.6})$$

Hydroxyl radicals can also be formed by the photoproduced electrons via the following reactions

$$O_2 + e^-_{CB} \rightarrow O_2^{g-} \quad \text{(5-IV.7)}$$

$$O_2^{g-} + H_2O \rightarrow HO_2^g + OH^- \quad \text{(5-IV.8)}$$

$$HO_2^g + H_2O \rightarrow H_2O_2 + OH^g \quad \text{(5-IV.9)}$$

To disclose the structural changes of TC during irradiation in the presence of HP2, the UV–Vis spectra recorded before and after the catalyst addition under irradiation are reported in Figure 5-IV.9. TC displays three main peaks at 200, 280 and 365 nm. The peak at 275 nm is related to the aromatic ring 1 , the one at 365 nm derives from aromatic rings 2-4, including the chromophore groups. The progressive reduction of the last peak under irradiation indicates the fragmentation of phenolic groups linked to aromatic ring 2 while the reduction of absorbance at 280 nm is attributed to the formation of acylamino and hydroxyl groups.

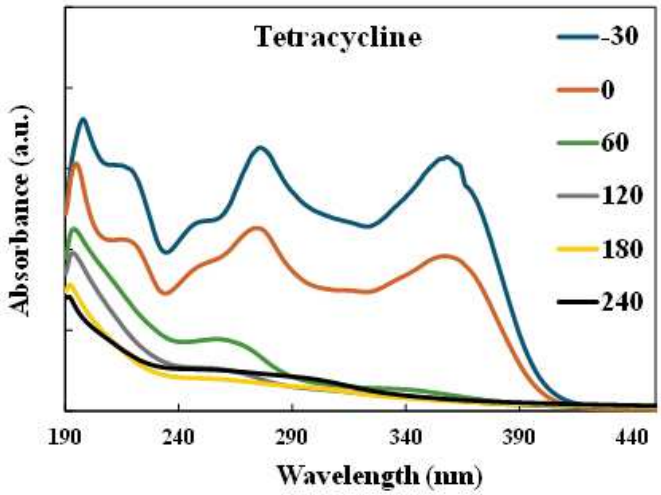

Figure 5-IV.9. Absorption spectra of tetracycline under irradiation.

In Figure 5-IV.10 is reported the variation of concentration of TC and LCM under irradiation by using HP2 as photocatalyst in the absence and presence of various selected scavengers. The curves shown in the two graphs have the same trend, demonstrating that the photocatalyst behaves in the same way with the two drugs. Only after adding benzoquinone a decrease in the activity is

observed indicating that $O_2^{\bullet -}$ radicals are active species in the drugs degradation. On the contrary the removal of $OH^{\bullet}$ radicals, e^- and h^+ had a positive effect being the degradation enhanced in the presence of tert-butanol, $AgNO_3$ and $Na_2C_2O_4$, respectively. It can be assumed that the decrease in the amount of these species from the system, reduces the recombination rate of the photogenerated charges thus improving the photoactivity.

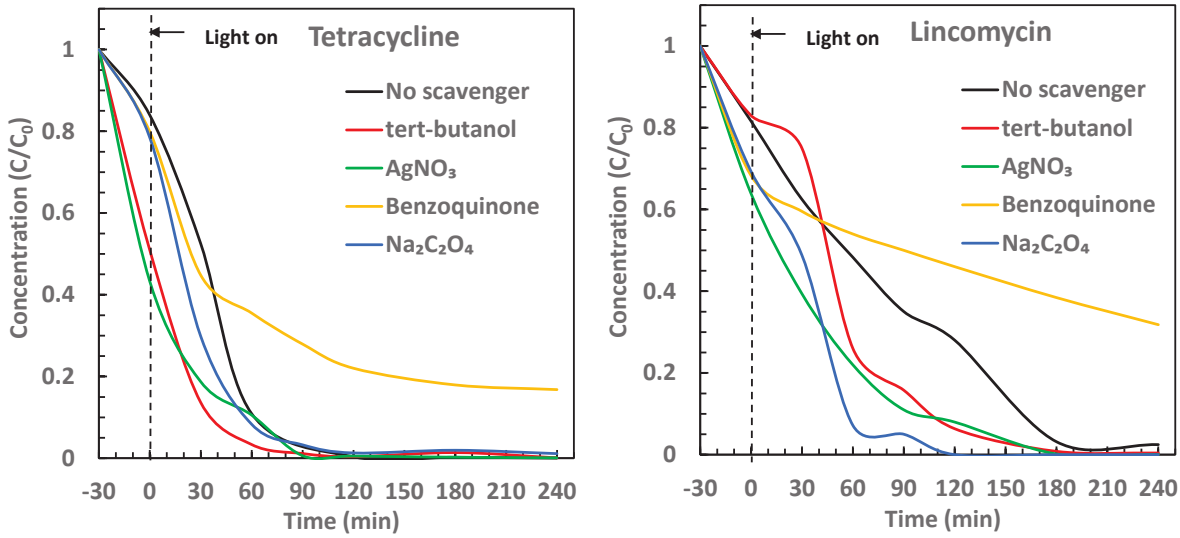

Figure 5-IV.10. Concentration of TC and LCM versus irradiation time by using HP2 photocatalyst in the absence and presence of different scavenging species.

5-IV.6.3 Kinetic aspects

In the presence of an excess of molecular oxygen, the quenching of the excited state (Equation 5-IV.3) is not a limiting step. By hypothesizing that the absorption of light is uniform in the reaction volume and the lifetimes of radicals and other reactive species are sufficiently long so that uniform concentrations throughout the reaction volume result from diffusion, it can be assumed that the rate of tetracycline degradation by homogeneous photochemical reaction, r_{hom}, can be written as:

$$-r_{hom} = -\frac{1}{V}\frac{dN_D}{dt} = -\frac{dC_D}{dt} = k_{hom} I_a^n C_D^{\alpha} C_{Ox}^{\beta} \qquad (5\text{-IV.10})$$

In which V is the reaction volume, N_D the moles of drug (tetracycline or lincomycin), t the irradiation time, C_D and C_{Ox} the molar concentration of drug and oxygen, respectively, k_{hom} the

rate constant, I_a the absorbed photon flow, an exponent ranging between 0.5 and 1, and α and β represent the reaction orders of tetracycline and oxygen, respectively.

The experimental data suggest that the optical properties of the reacting solution do not change much during the photochemical degradation so that it may be assumed that the substrate and its oxidation intermediates have similar extinction coefficients. For this reason, the absorbed photon flow, I_a, may be assumed constant during the photoreaction.

All the experimental data obtained from the photochemical runs show exponential decreases of substrate concentration versus irradiation time, thus indicating first order kinetics with respect to the drug concentration. By assuming that the oxygen concentration in the solution is constant during the experiment (continuous bubbling), the reaction rate, Equation 5-IV.10 can be written as:

$$-r_{hom} = -\frac{dC_D}{dt} = k'_{hom} C_D \qquad (5\text{-IV.11})$$

where k'_{hom} is the pseudo-first order rate constant and is equal to $k_{hom} I_a^n \cdot C_{Ox}$. It should be noticed that k'_{hom} inversely depends on the initial drug concentration. Equation 5-IV.11 can be integrated with the limiting condition that at t = 0, the substrate concentration is the initial one, $C_D = C_{D,0}$. The following relationship between C_D and t is determined:

$$C_D = C_{D,0} e^{\left(-k'_{hom} \cdot t\right)} \qquad (5\text{-IV.12})$$

The values of the observed rate constants were determined by applying a least squares best fitting procedure to the reactivity data. Table 5-IV.3 reports the k'_{hom} values obtained from runs carried out at different initial concentrations. The figures reported in Table 5-IV.3 indicate that, as expected, the values of k'_{hom} decrease with increasing initial drug concentration and are higher for TC.

Table 5-IV.3 Values of observed rate constants for reactions carried out in homogeneous regimen.

Drug	Observed rate constants (s^{-1})	50 ppm	75 ppm	100 ppm
Tetracycline	$k'_{homTC} \cdot 10^4$	0.827	0.623	0.582
Lincomycin	$k'_{homLCM} \cdot 10^4$	0.182	0.168	0.021

Also, for the heterogeneous photocatalytic degradation the reactivity data fit well exponential curves, indicating that the degradation rate follows first order kinetics, as reported in the literature [291-296].

It must be remembered that the heterogeneous reaction occurs together with the homogeneous one, but the presence of the photocatalyst strongly reduces the intensity of the radiant field inside the reacting medium.

It can therefore be reasonably hypothesized that during the heterogeneous reaction the contribution of the homogeneous one to the overall drug degradation can be neglected, hypothesis supported by the results of the homogeneous runs above reported. The rate of the heterogeneous photocatalytic reaction, $-r_{hete}$, can be expressed in terms of the Langmuir–Hinshelwood model as:

$$-r_{hete} = -\frac{1}{S}\frac{dN_D}{dt} = -\frac{V}{S}\frac{dC_D}{dt} = k''\theta \qquad (5\text{-IV.13})$$

where S is the photocatalyst active surface area, k'' the second order surface rate constant, and θ the drug fractional site coverage which is given by:

$$\theta = \frac{K_D C_D}{1 + K_D C_D + \sum K_I C_I} \qquad (5\text{-IV.14})$$

where K_D and K_I are the equilibrium adsorption constants of the drug and of the intermediate products, and C_D and C_I the concentrations in the fluid phase, respectively.

The first intermediates products generally are similar to the initial substrate and then it can be hypothesised that the interactions of the drug and the intermediate products with the catalyst surface are similar. For this reason, it can be assumed that the values of the equilibrium adsorption constants are approximately equal [294, 296] and the following relationship can be written:

$$-\frac{dC_D}{dt} = \frac{S}{V}\left(\frac{k''K_D}{1 + K_D C_{D,0}}\right)C_D = \frac{S}{V}k_{hete}C_D \qquad (5\text{-IV.15})$$

where $C_{D,0}$ is the initial drug concentration and k_{hete} is the observed first order rate constant. Equation 15 can be integrated with the limiting condition that at the beginning of the reaction, t = 0, the substrate concentration is the initial one, $C_D = C_{D,0}$. The integral relationship between C_D and t is:

$$C_D = C_{D,0} e^{\left(\frac{S}{V} k_{hete} t\right)} \qquad (5\text{-IV.16})$$

By applying a least squares best fitting procedure to the experimental data, the values of the observed rate constants were determined, and they are reported in Table 5-IV.4.

Table 5-IV.4 Values of observed rate constants for reactions carried out in heterogeneous systems.

Drug	**Observed rate constants ($m \cdot s^{-1}$)**	**50 ppm**	**75 ppm**	**100 ppm**
Tetracycline	$k_{hete} \cdot 10^9$	21.0	13.0	9.0
Lincomycin	$k_{hete} \cdot 10^9$]	3.9	3.2	2.4

The dependence of k_{hete} on the initial drug concentration may be linearized by considering its definition as:

$$\frac{1}{k_{hete}} = \frac{1}{k''} C_{D,0} + \frac{1}{k'' K_D} \qquad (5\text{-IV.17})$$

Equation 5-IV.17 represents a straight line by plotting $1/k_{hete}$ versus the initial tetracycline concentrations, $C_{T,0}$ (see Figure 5-IV.11A). The value of the second order rate constant, k'' and of the equilibrium adsorption constant, K_T have been obtained by means of a least squares best fitting procedure by using HP2 3%N as the photocatalyst.

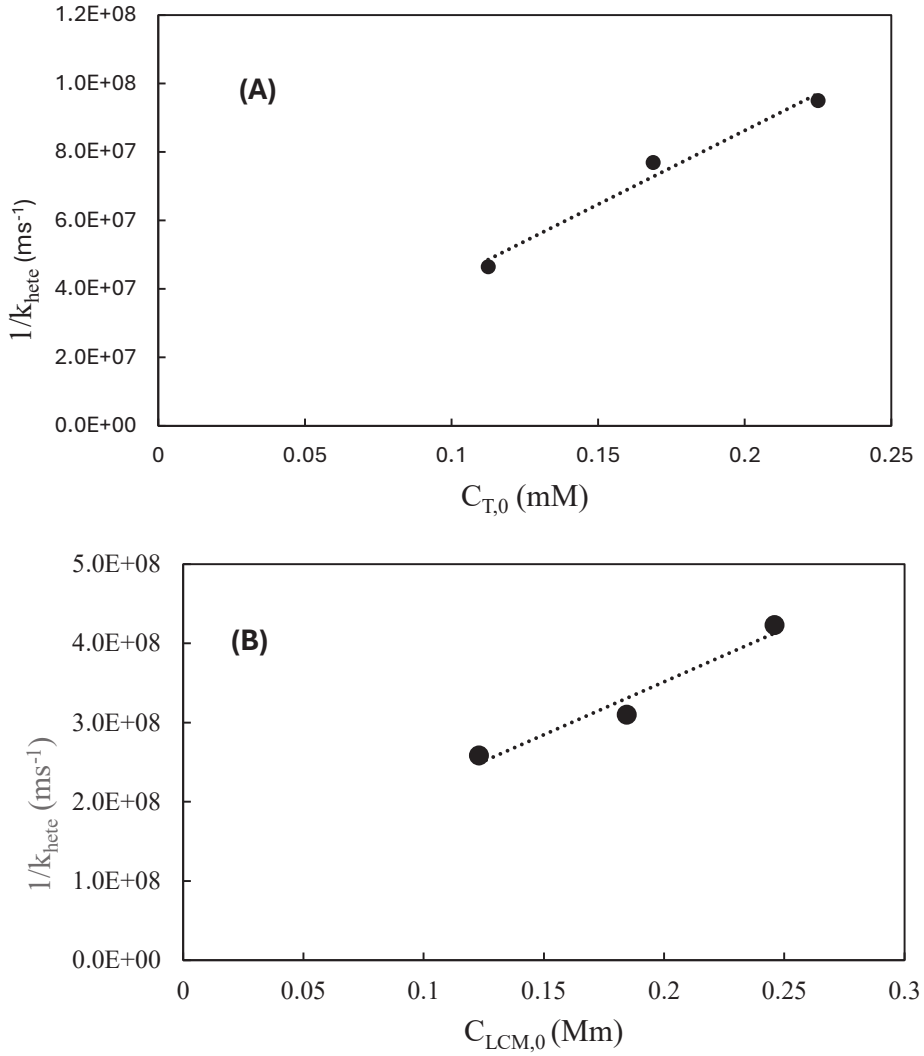

Figure 5-IV.11. Values of $1/k_{hete}$ versus the initial concentrations for TC (A) and LCM (B) in the presence of HP2 3%N as the photocatalyst.

The value of k'' obtained is $2.32 \cdot 10^{-9}$ mM·m·s^{-1} whereas the value of K_T is 10952.5 mM^{-1}.

Figure 5-IV.11B shows the plot of $1/k_{hete}$ versus the initial concentration of Lincomycin. Also in this case a straight line well fit the data. By applying a least square best fitting procedure the following values were determined: k'' is $7.48 \cdot 10^{-10}$ mM·m·s^{-1} and K_L is 15.9 mM^{-1}.

It can be noticed that, under the operative conditions used, the second order reaction rate for TC is higher than that of LCM as well the adsorption constant. This last one indicates that under the same concentration the fractional sites coverage for TC is higher than that of LMC.

5-IV.7 Conclusions

Heterogeneous photocatalysis in the presence of differently modified TiO_2 based semiconductors was successfully applied to degrade drugs such as tetracycline, oxytetracycline and lincomycin present in wastewater. Homogeneous irradiation leads to partial degradation of both tetracycline and oxytetracycline and no degradation of lincomycin and causes almost negligible mineralization for all the drugs. Photocatalysis increases both the reaction rate of the main compounds and the mineralization of the organic intermediates. TiO_2 based home prepared photocatalysts performed well and in some cases better than the commercial ones. The nitrogen doped TiO_2 samples were the best photocatalysts both for the degradation and the mineralization of the drugs, obtaining results comparable or superior to those obtained with the commercial TiO_2 powders also under simulated solar light irradiation. The experimental runs in the presence of selected scavengers highlighted that $O_2^{\bullet-}$ radicals are the active species in the drugs degradation. First order kinetics described adequately the experimental results and allowed the determination of the kinetic parameters of the homogeneous and the heterogeneous systems for the degradation reactions in the presence of the best photocatalyst. However, from the results obtained, it clearly emerges that the photocatalytic method cannot be used efficiently as a primary process for the treatment of waters where the concentration of polluting species is quite high, but rather as a final treatment at the outlet of traditional plants to eliminate traces of recalcitrant species such as those reported in this paper.

The search for photocatalysts, prepared under simple and economical synthetic conditions, effective upon direct solar irradiation opens the door to the use of pilot-scale reactors for convenient large-scale wastewater treatment that have not yet been sufficiently reported.

TiO_2-Based Photocatalysts for Drugs and Dyes Degradation

CHAPTER 5-V

5-V. From Synthesis to Simulation: Data-Driven Optimization of Ce-TiO_2 Photocatalysts for Water Purification

5-V.1 Abstract

In this study, a series of cerium (Ce atomic amount 1, 2, and 4%)-doped TiO_2 photocatalysts was synthesized via a sol-gel route to enhance their photocatalytic activity towards pollutants degradation under both UV and visible light irradiation. Comprehensive characterization, namely, XRD, FTIR, SEM, BET, Photocurrent spectroscopy, Raman, UV-Vis DRS, and PL spectroscopy, was carried out to elucidate structural, optical, and morphological properties. The 2%Ce-TiO_2 sample exhibited the most favorable features, including reduced band gap (2.78 eV), high surface area (89.88 $m^2 g^{-1}$), and improved charge separation efficiency. Photocatalytic degradation tests using methylene blue (MB), Rose Bengal (RB), and tetracycline (TC), confirmed a marked enhancement in pollutant removal, reaching 91.57%, 99.01%, and 99.47% degradation, respectively. Total Organic Carbon (TOC) analyses revealed a good mineralization degree of the organics. Reactive species trapping studies identified photogenerated holes and superoxide radicals as the dominant oxidative agents. Furthermore, Gaussian Process Regression (GPR) combined with an Improved Grey Wolf Optimizer (IGWO) was employed to model and optimize the degradation of MB. The model demonstrated excellent predictive performance ($R^2 > 0.999$), with minimal deviation between experimental and predicted values. External validation on RB and TC confirmed the robustness of the optimized conditions. This study highlights the potential of Ce-doped TiO_2 photocatalysts as efficient, reusable, and solar-responsive materials for the treatment of dye-laden wastewater and demonstrates the power of hybrid AI models in guiding photocatalytic process optimization.

5-V.2 Experimental Section

The synthesis of TiO_2 powders was carried out using a controlled sol-gel approach. Cerium was introduced at various atomic concentrations of 1, 2, and 4 atomic % to evaluate the effect of dopant level on the physicochemical and photocatalytic properties of TiO_2. Tetrabutyl orthotitanate (TBOT; $(C_4H_9O)_4Ti$, Fluka-Chemika) was employed as the titanium precursor due to its high reactivity and compatibility with sol-gel chemistry.

5-V.2.1 Undoped and Ce-doped TiO_2 preparations

5-V.2.1.1 TiO_2 sol preparation

The preparation of the TiO_2 sol started by mixing 1 mole of bidistilled water with 1 mole of butanol (C_4H_9OH, purity 99.5%, Reidel-de Haën) and 4 moles of glacial acetic acid (CH_3COOH, purity 99-100%, Biochem Chemopharma). The acidic medium is needed not only to stabilize the hydrolysis reaction but also to improve the homogeneity of the sol. The mixture was magnetically stirred at room temperature for 30 minutes to ensure complete homogenization. Subsequently, 1 mole of TBOT was added dropwise into the solution over a period of 2 hours (120 minutes) under continuous stirring to promote controlled hydrolysis and condensation reactions. This slow addition helps to prevent premature gelation and ensures the formation of a uniform sol (**Figure 5-V.1a**).

5-V.2.1.2 Cerium (Ce)-doping TiO_2 solutions

Calculated amounts of cerium acetate hydrate, corresponding to Ce concentrations of 1, 2, and 4 at. % relative to Ti, were used to obtain Ce-doped TiO_2 sols. Each required amount of Ce acetate hydrate was initially dissolved in 3 mL of ethanol (C_2H_5OH, 95%, Reidel-de Haën), with the addition of a few drops of acetic acid to enhance solubility and prevent precipitation. The resulting clear cerium solutions were then slowly added to 30 mL aliquots of the previously prepared TiO_2 sol. The mixtures were stirred magnetically at room temperature for 8 hours to ensure thorough incorporation of the cerium ions into the sol matrix and to allow for equilibrium dispersion. A simplified diagram of the dopant addition protocol is illustrated in **Figure 5-V.1b**.

5-V.2.1.3 Undoped and Ce-doped TiO_2 powders

The final powders both undoped and cerium-doped TiO_2 were obtained through a carefully controlled multi-step process aimed to ensure optimal structural, morphological, and photocatalytic properties. After sol preparation and doping stages, the mixtures were first allowed to undergo spontaneous gelation at ambient temperature. This step involved the gradual transformation of the liquid sol into a three-dimensional gel network, as the hydrolyzed and partially condensed titanium species linked together through continued condensation reactions. The resulting gel structure encapsulated the dopant species and solvent molecules, thereby initiating the structural organization necessary for the subsequent formation of a solid matrix. Once gelation was completed, the wet gels commonly referred to as xerogels were subjected to a thermal

drying process. This drying stage was carried out in a convection oven at 130 °C for 12 hours. The relatively mild temperature was selected to ensure the effective removal of residual solvents, water, and loosely bound organic species, while preserving the integrity of the gel network. A slow and uniform drying process is crucial at this stage, as it prevents the formation of cracks or heterogeneities within the material that could later compromise the photocatalytic performance of the final powders. After drying, the xerogels were thermally treated by calcination in air at 550 °C for 20 minutes. This high-temperature step played a dual role: it facilitated the complete decomposition of any remaining organic matter and induced crystallization of the amorphous TiO_2 matrix. The calcination temperature was carefully chosen to promote the formation of the anatase phase, known for its superior photocatalytic activity compared to the rutile one. Moreover, in the case of Ce-doped samples, the thermal treatment encouraged the incorporation of cerium ions into the TiO_2 lattice or their stabilization on the particle surface, which can influence light absorption and charge carrier dynamics. After calcination, the solid materials were allowed to cool at room temperature, then they were carefully ground by using an agate mortar and pestle. This manual grinding process ensured the reduction of agglomerates into fine powders with a relatively homogeneous grain size distribution, thereby maximizing the surface area available for photocatalytic reactions. The resulting powders were then stored in sealed containers until further characterization and application in photocatalytic experiments. (**Figure 5-V.1c**)

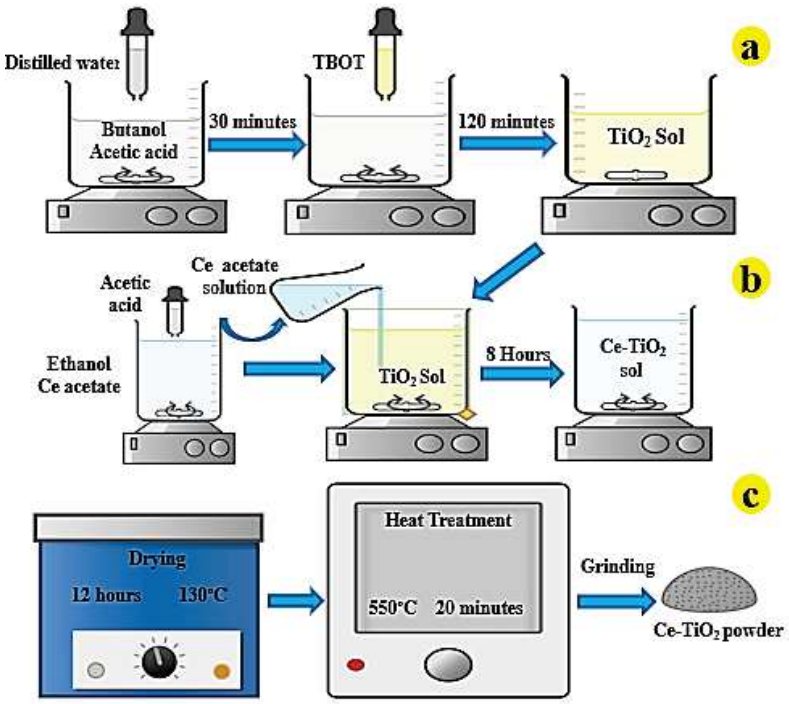

Figure 5-V.1 Preparation steps: **(a)** TiO_2 Sol Preparation, **(b)** 1, 2, and 4% Ce doped TiO_2 Sol, **(c)** TiO_2, Ce-TiO_2 powders preparation

5-V.3 Characterization of the Powders

To investigate the structural, morphological, textural, and optical properties of the synthesized materials, a comprehensive set of characterization techniques was employed. Fourier Transform Infrared Spectroscopy (FTIR) was performed using a spectrometer equipped with an ATR module to identify the vibrational modes of chemical bonds and to confirm the presence of functional groups, such as hydroxyl and metal–oxygen bonds. The spectra were collected in the range of 4000–400 cm^{-1} with a resolution of 4 cm^{-1}. X-ray diffraction (XRD) analysis was carried out to determine the crystalline structure, phase composition, and average crystallite size. The measurements were carried out using a diffractometer equipped with Cu Kα radiation (λ = 1.5406 Å) over a 2θ range typically between 10° and 80°, using a scanning speed of 0.02°/s. The surface morphology and microstructure of the powders were examined by Scanning Electron Microscopy (SEM), using a FEI Quanta 200 ESEM operating at 30 kV. Specific surface area and porosity of the powders were analyzed using nitrogen adsorption–desorption measurements at 77 K. The Brunauer–Emmett–Teller (BET) method was used to calculate the surface area, before

measurement, samples were degassed under vacuum at 150 °C for 12 hours. Raman spectroscopy was used to investigate the vibrational modes of the crystal lattice and to confirm the structural integrity of the TiO_2 framework after doping. The measurements were carried out using a confocal Raman microscope equipped with a 532 nm laser source and a spectral resolution suitable for identifying anatase-related modes. Diffuse reflectance UV-Visible spectroscopy (UV-Vis DRS) was employed to analyze the optical absorption behavior of the powders in the range of 200–800 nm. The bandgap energy (E_g) was subsequently estimated using the Kubelka–Munk transformation followed by Tauc plots, allowing the assessment of the influence of Ce doping on the optical properties. Photoluminescence (PL) spectroscopy was performed at room temperature by means of a JASCO FP-8550 Spectrofluorometer with an excitation wavelength of 320 nm. This technique was used to gain insight into the recombination dynamics of photogenerated electron–hole pairs, which are critical in determining photocatalytic activity. Mineralization was measured by calculating the reduction in Total Organic Carbon (TOC) content compared to the starting solution, using a Shimadzu TOC-5000A instrument.

Photoelectrochemical measurements were carried out by using photoelectrodes prepared by dispersing each powdered photocatalysts in ethanol and subsequently drop-casting the suspensions onto carbon paper substrates (Toray, 40% wet-proofed, E-Tek). The resulting photoelectrodes were employed as working electrodes in a three-electrode electrochemical cell operated under air atmosphere, with a platinum wire as the counter electrode and an Ag/AgCl (saturated KCl) electrode as the reference. The electrolyte consisted of 0.1 M ammonium biborate tetrahydrate (ABE, $(NH_4)_2B_4O_7 \cdot 4H_2O$; Sigma-Aldrich). Illumination was provided by a 1000 W UV–vis xenon lamp, with the incident light directed towards a monochromator and onto the electrode surface through a cell quartz window. The electrode potential was controlled using a VersaSTAT potentiostat. Photocurrent spectra (photocurrent as a function of wavelength) were acquired at open-circuit potential (OCP) by processing the measured current with a two-phase lock-in amplifier to discriminate the photocurrent from the total cell current. A mechanical chopper operating at 13 Hz was used to periodically interrupt the incident light. The photocurrent spectra were reported as photocurrent yield (Q_{ph}), calculated by normalizing the photocurrent to the relative photon flux at each wavelength, thereby accounting for the wavelength-dependent efficiency of the lamp–monochromator system.

All instruments were operated under standard conditions and calibrated before use to ensure accuracy and reproducibility of the measurements. The combination of these techniques provided a detailed profile of the undoped and Ce-doped TiO_2 materials, serving as a basis for understanding their behavior in photocatalytic applications.

5-V.4 Photocatalytic activity experiments

The photocatalytic efficiency of the synthesized powders was evaluated through the degradation of three different organic pollutants under both UV for MB and visible light irradiation for RB, and TC. These molecules were selected as model pollutants representing cationic dyes, anionic dyes, and pharmaceutical compounds, respectively.

Photocatalytic degradation tests for MB (10 mg/L) were carried out by dispersing 250 mg of each photocatalyst into 250 mL of MB aqueous solution. Before irradiation, all suspensions were stirred in the dark for 30 minutes to establish adsorption–desorption equilibrium between the dye and the catalyst surface. A 3 mL aliquot was withdrawn after this dark phase to evaluate the initial absorption; thereafter, UV irradiation was applied for 300 minutes. Samples were taken at 30 minutes and then every 60 minutes, centrifuged to remove solid residues, and the supernatant was analyzed by UV-Visible spectrophotometry to quantify the concentration of MB.

The visible-light photocatalytic activity was assessed by degrading RB and TC. In each experiment, 150 mg of catalyst was suspended in 150 mL of aqueous RB or TC solution at a concentration of 10^{-5} mol L^{-1}, and the mixture was stirred in the dark for 30 minutes to ensure equilibrium adsorption. Subsequently, the system was irradiated with a 150 W halogen lamp simulating sunlight. At specified time intervals (0, 30, 60, 90, and 120 minutes), 3 mL aliquots were collected, centrifuged, and the RB and TC concentration was measured via UV-Vis spectroscopy.

The photocatalytic degradation efficiency was calculated using Equation (S1)

$$X\ (\%) = ((C_0 - C)/C_0) \times 100 \qquad \text{(Eq. S1)}$$

where "C_0" represents the initial pollutant concentration (mol/L) and "C" indicates the concentration at various irradiation times (mol/L).

Organics' mineralization was evaluated by measuring the reduction in Total Organic Carbon (TOC) content compared to the starting solution, using a Shimadzu TOC-5000A instrument.

It's well-established that holes (h^+), electrons (e^-), hydroxyl radicals ($^{\bullet}OH$), and superoxide radicals ($^{\bullet}O_2^-$) are the primary reactive species involved in photocatalytic oxidation. To understand the role that each of them plays in the degradation of the studied pollutants and to explain the reaction mechanism, we used specific quenching agents: $Na_2C_2O_4$ (NO) for h^+, tert-butanol (*t*-BOH) for $^{\bullet}OH$, $AgNO_3$ for e^- and benzoquinone (BQ) for $^{\bullet}O_2^-$.

5-V.6 Results and Discussion

5-V.6.1 Fourier Transform Infrared Spectroscopy (FTIR) Analysis

Figure 5-V.2a displays the FTIR spectra of both TiO_2 and Ce-doped TiO_2 samples. The comparative analysis reveals the presence of several well-defined vibrational bands, whose intensities and positions provide valuable information on the chemical environment, surface functionalities, and structural integrity of the materials. Among the most prominent bands, the one observed at 3717 cm^{-1} is attributed to the stretching vibrations of H–O–H bonds, corresponding to surface-adsorbed water molecules. This feature indicates either incomplete desorption of physiosorbed water or residual hydration following thermal treatment, a common observation in porous metal oxides with high surface areas .The weak band at 2954 cm^{-1} is associated with C–H stretching vibrations, most likely originating from residual organic species such as unreacted precursors, solvents, or acetate ligands that may persist after gelation and calcination. A particularly intense and well-defined band appears at 2324 cm^{-1}, which is assigned to the asymmetric stretching vibrations of surface-bound carboxylate groups (Ti–COO). These functionalities likely result from the interaction of titanium ions with acetic acid or decomposition products of cerium precursors, forming intermediate complexes during the sol-gel process or thermal decomposition stages. Additional absorption features located at 1522 cm^{-1} and 1058 cm^{-1} correspond to the bending and stretching vibrations of Ti–OH groups, respectively. These surface hydroxyl groups are known to play a central role in photocatalytic processes, acting as active sites for the generation of highly reactive hydroxyl radicals ($^{\bullet}OH$) upon photoactivation. Their presence enhances the material's ability to interact with water molecules and pollutants during catalytic reactions, thereby improving photocatalytic efficiency. Finally, a strong absorption band around 440 cm^{-1} is characteristic of Ti–O–Ti lattice vibrations within the tetragonal anatase phase of TiO_2. This low-frequency feature reflects the stretching modes of metal–oxygen bonds in the TiO_6 octahedral framework and confirms the retention of anatase crystalline structure following doping. The identification of this peak is consistent with X-ray diffraction patterns (**Figure 5V.2b**), further

supporting the structural stability of the anatase phase upon cerium incorporation. Notably, the Ce-doped TiO_2 samples exhibit enhanced band intensities across the entire spectral range when compared to the undoped material. This enhancement may be attributed to increased surface polarization and defect formation resulting from the partial substitution of Ti^{4+} by Ce^{3+}/Ce^{4+} ions, which differ in ionic radius and electronic configuration. The substitution of cerium into the TiO_2 lattice may also induce local lattice distortions or oxygen vacancies, which influence the vibrational dynamics of the material. Moreover, the higher atomic mass and polarizability of cerium may lead to an increased infrared absorption cross-section, contributing to the observed spectral amplification [297]. FTIR spectroscopy confirms the preservation of the fundamental TiO_2 framework after cerium doping, while also revealing modifications in surface chemistry indicative of structural and electronic interactions between the dopant and the host matrix. The identification of surface hydroxyls, carboxylates, and lattice vibrations provides a comprehensive view of the functional groups likely to participate in photocatalytic reactions, thereby establishing a crucial link between structural features and photocatalytic performance.

5-V.6.2 X-ray diffraction analysis

Figure 5-V.2b presents the XRD patterns of TiO_2 and cerium-doped TiO_2 samples at different doping levels (1, 2, and 4%). All diffraction peaks observed for the synthesized powders correspond to the pure anatase phase of TiO_2, as confirmed by comparison with the standard JCPDS card no. 01-071-1167. The most prominent peaks appear at 2θ values of 25.3°, 37.0°, 37.8°, 38.5°, 48.0°, 54.0°, 55.1°, 62.7°, 68.7°, 70.3°, and 75.1°, corresponding to the (101), (103), (004), (112), (200), (105), (211), (204), (116), (220), and (215) crystal planes, respectively. These characteristic reflections clearly indicate the formation of the tetragonal anatase structure, which is widely recognized for its superior photocatalytic performance.

Importantly, no additional diffraction peaks corresponding to cerium oxide phases such as CeO_2 or Ce_2O_3 were detected, even at higher doping concentrations. This suggests that cerium species are either well-dispersed at the atomic level within the TiO_2 lattice or segregated in an amorphous form that remains undetectable by conventional XRD techniques [298]. It is plausible that the cerium ions are located at interstitial positions or preferentially occupy grain boundaries, modifying the microstructural properties without inducing long-range crystalline ordering of separate Ce-based phases. A notable feature in the XRD diffractograms is the gradual decrease in peak intensity, particularly for the main anatase (101) reflection at 25.3°, with increasing cerium

content. This attenuation in intensity is often associated with a decrease in crystallinity or the introduction of lattice distortions caused by the incorporation of dopant ions. Given that cerium ions (Ce^{3+}: ~1.14 Å; Ce^{4+}: ~0.92–0.97 Å) possess significantly larger ionic radii than titanium ions (Ti^{4+}: ~0.61–0.68 Å), their substitution within the TiO_2 lattice could introduce local strain, which inhibits crystal growth or induces the formation of oxygen vacancies. These distortions disrupt the periodicity of the anatase framework, resulting in the observed broadening and weakening of the diffraction peaks.

To further investigate the crystallite size evolution, the average grain size (D) of the anatase phase was estimated using the Debye Scherrer equation (Equation 5-V.1) [299].

$$D = \frac{K \cdot \lambda}{\beta \cdot \cos\theta} \qquad \text{(Eq. 5-V.1)}$$

where D is the average crystallite size (in nm), K is the shape factor (taken as 0.94), λ is the X-ray wavelength for Cu Kα radiation (1.54056 Å), β is the full width at half maximum (FWHM) of the (101) peak in radians, and θ is the Bragg angle. The calculated values of FWHM and crystallite size are summarized in **Table 5-V.1.**

Table 5-V.1 Full Width at Half Maximum (FWHM), grain Size (D), BET Specific Surface Area (S.S.A), and band-gap (E_g) of undoped TiO_2 and Ce-doped TiO_2.

Samples	**FWHM (°)**	**Crystallite Size (D) (nm)**	**S.S.A ($m^2 g^{-1}$)**	**E_g (eV)**
TiO_2	0.2289	35.58	55.33	3.18
1Ce-TiO_2	0.2454	33.19	110.36	3.08
2Ce-TiO_2	0.6381	12.76	89.88	2.88
4Ce-TiO_2	0.2290	35.57	88.01	2.78

As illustrated in Table 5-V.1, a clear reduction in crystallite size is observed with cerium doping, especially at the 2% level, where the crystallite size drops significantly to 12.76 nm. This pronounced size reduction is typically attributed to the role of cerium as a grain growth inhibitor during thermal treatment. At this optimal concentration, Ce species may segregate at the crystallite interfaces, effectively pinning grain boundaries and suppressing their coalescence during calcination. Interestingly, at a higher doping level of 4%, the grain size increases again to a value nearly identical to that of undoped TiO_2. This could suggest a dopant saturation effect, where

excessive cerium may start forming amorphous surface clusters or may no longer be effectively incorporated into the lattice, thus reducing its ability to inhibit crystal growth. The observed trend in crystallite size with doping is of particular importance, as smaller crystallite dimensions generally enhance photocatalytic activity by increasing the specific surface area and shortening the diffusion paths of photogenerated charge carriers. Moreover, the incorporation of Ce ions may influence the defect chemistry and electron trapping dynamics, which are critical in determining the reactivity and efficiency of the photocatalyst [300].

5-V.6.3 Brunauer-Emmett-Teller (BET)

Table 5-V.1 summarizes the BET specific surface area values measured for the synthesized photocatalysts. The bare TiO_2 exhibited a specific surface area of 55.33 $m^2 g^{-1}$, which falls within the expected range for nanostructured anatase-phase materials synthesized via sol–gel method and reflects the moderately porous nature and relatively fine particle size of the material. Following Ce-doping, a notable enhancement in specific surface area was observed for all the samples. The 1Ce-TiO_2 sample demonstrated a significant increase, reaching 110.36 $m^2 g^{-1}$, 2Ce-TiO_2 sample 89.88 $m^2 g^{-1}$ while the 4Ce-TiO_2 exhibited an even higher value of 88.88 $m^2 g^{-1}$. These increases are indicative of structural modifications induced by the incorporation of cerium ions into the TiO_2 framework resulting in smaller crystallites size and a more open texture, both of which contribute to an increased surface area [301]. This remarkable value suggests an optimal balance between crystallite size suppression, particles dispersion, and pores formation. The extremely small crystallite size observed for this composition (12.76 nm) likely facilitates the formation of a loosely agglomerated nanoparticle network with abundant interstitial voids and mesoporosity. These textural features enhance the accessible surface area available for adsorption and interaction with reactants, a key factor in photocatalytic applications. Additionally, the homogeneous distribution of cerium dopants may also play a role in stabilizing the surface structure and preventing pore collapse during thermal treatment. Overall, the increase in BET surface area observed upon cerium doping highlights the dopant's beneficial effect on the textural properties of TiO_2. A high surface area is crucial for effective photocatalysis, as it promotes greater adsorption of pollutant molecules, enhances light absorption due to multiple scattering effects, and facilitates efficient separation and migration of photogenerated charge carriers.

5-V.6.4 Raman Spectroscopy analysis

The Raman spectra (**Figure 5-V.2c-d)** display well-defined vibrational bands characteristic of the anatase phase of TiO_2, thereby confirming the retention of the anatase crystal structure following cerium incorporation. The major Raman active modes observed include the prominent E_g modes at approximately 146 and 198 cm^{-1}, the B_{1g} mode at 397 cm^{-1}, the superimposed A_{1g} + B_{1g} mode at 517 cm^{-1}, and another E_g mode at 639 cm^{-1} [301]. Among these, the low-frequency band at 146 cm^{-1} is particularly intense and is often used as a fingerprint for anatase TiO_2. This mode, along with that at 397 cm^{-1}, is associated with O–Ti–O bending vibrations, which are sensitive to local distortions and crystalline order [302]. Notably, no additional vibrational bands corresponding to cerium oxide phases (e.g., CeO_2 or Ce_2O_3) were detected in the Raman spectra of the doped samples. This observation is consistent with the XRD analysis and suggests that cerium species are either well-dispersed at atomic level. The absence of these secondary phases further confirms that the structural integrity of the TiO_2 anatase framework is maintained despite the introduction of cerium dopants. A closer examination of the Raman spectra reveals a systematic decrease in the intensity of Raman bands, particularly the one at 146 cm^{-1}, as the cerium content increases. This attenuation is indicative of several microstructural effects induced by doping. First, the incorporation of Ce ions, given their larger ionic radii compared to Ti^{4+}, introduces strain and lattice distortion within the TiO_2 crystal structure. Such distortions disrupt the long-range periodicity required for strong Raman scattering, leading to weakened vibrational signals [303]. [306]. Moreover, the decrease in Raman intensity can also be linked to the reduction in crystallite size observed in the XRD analysis. Smaller grains lead to increased surface-to-volume ratios, and surface defects and phonon confinement effects become more pronounced, both of which tend to reduce Raman signal intensities and broaden spectral features [304]. This phenomenon is further amplified by the presence of cerium at grain boundaries, which may enhance local disorder and diminish the coherence length of phonon vibrations. Another plausible explanation involves the introduction of oxygen vacancies or other types of structural defects due to cerium doping. These defects can alter the local polarizability and symmetry of the lattice, resulting in changes in Raman scattering behavior. Additionally, the redistribution of electronic density around the Ti and O atoms due to Ce^{3+}/Ce^{4+} interactions may weaken the vibrational modes associated with the anatase lattice [305]. In summary, the Raman spectroscopy results reinforce the conclusions drawn from XRD analysis, confirming that the anatase structure is preserved across all compositions, with

cerium dopants effectively incorporated without forming separate crystalline phases. The observed changes in Raman peak intensity and line shape are consistent with a reduction in crystallite size, increased structural disorder, and possible defect formation all of which may contribute to the altered photocatalytic behavior of the Ce-doped TiO_2 materials.

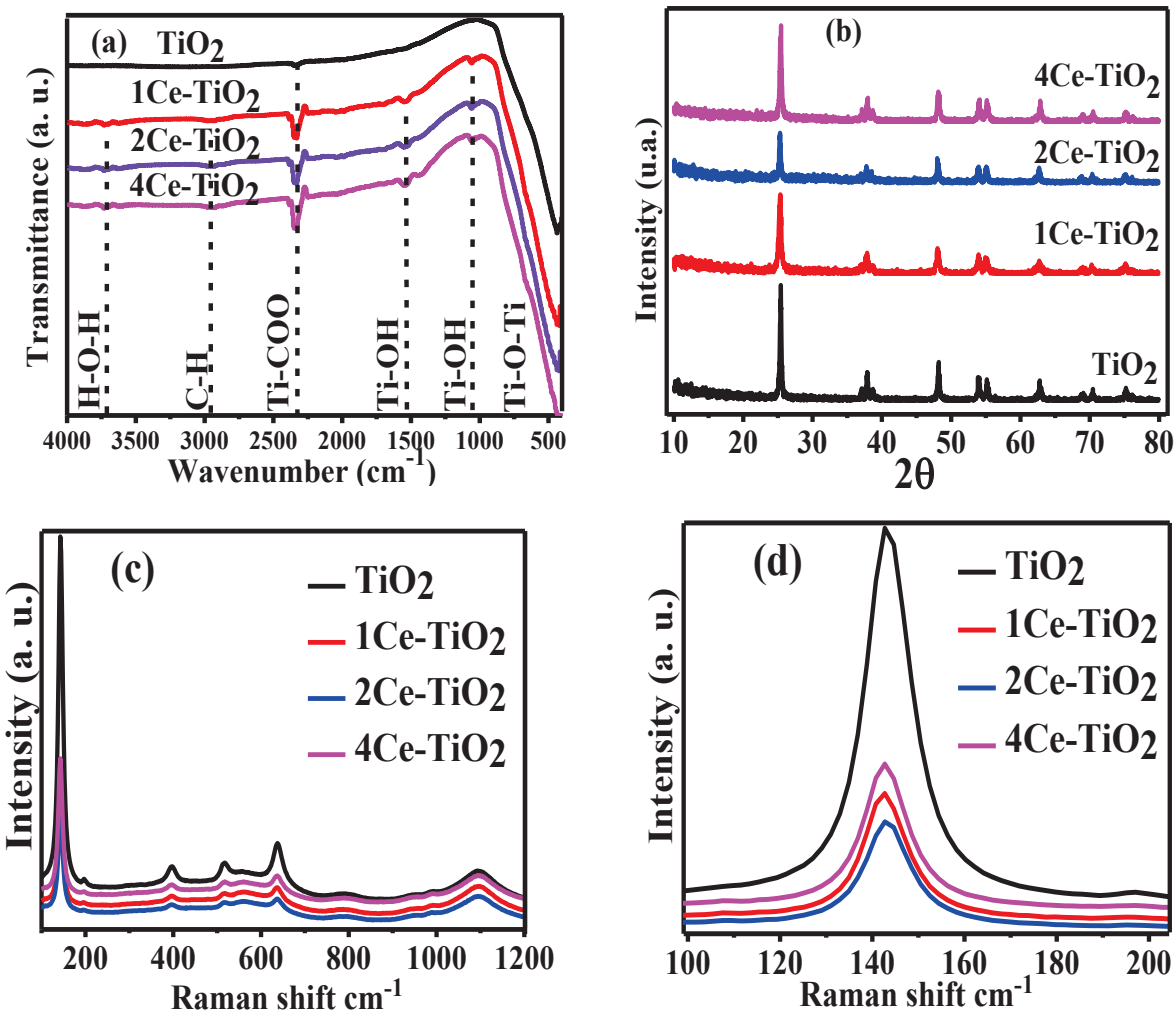

Figure 5-V.2 (a) FTIR spectra, **(b)** XRD spectra and **(c-d)** Raman spectra of TiO_2, 1, 2, and 4% Ce-TiO_2

5-V.6.5 UV-Vis Spectroscopy and Photoluminescence

The optical properties of the used photocatalysts were investigated by UV-Vis DRS (see **Figure 5V.3 a**), and the corresponding Tauc plots are presented in **Figure 5-V.3 b**. These plots were built to estimate the band-gap energy (E_g) values by applying Tauc's equation (Equation 5-V.2), which

relates the absorption coefficient (α) to the incident photon energy (hν). Since TiO_2 is an indirect bandgap semiconductor, the parameter n was set to 2 in this case [305].

$$(\alpha h\nu)^{\frac{1}{n}} = A\,(h\nu - E_g) \qquad \text{(Eq. 5-V.2)}$$

Where α is absorption coefficient, $(h\nu)$ is photon energy, "A" is a constant, E_g is the optical band gap energy of the material and $n = 2$ for allowed indirect transitions.

All synthesized samples displayed a prominent absorption edge in the ultraviolet region, which is indicative of intrinsic electronic transitions from the valence band to the conduction band of anatase-phase TiO_2 [305].

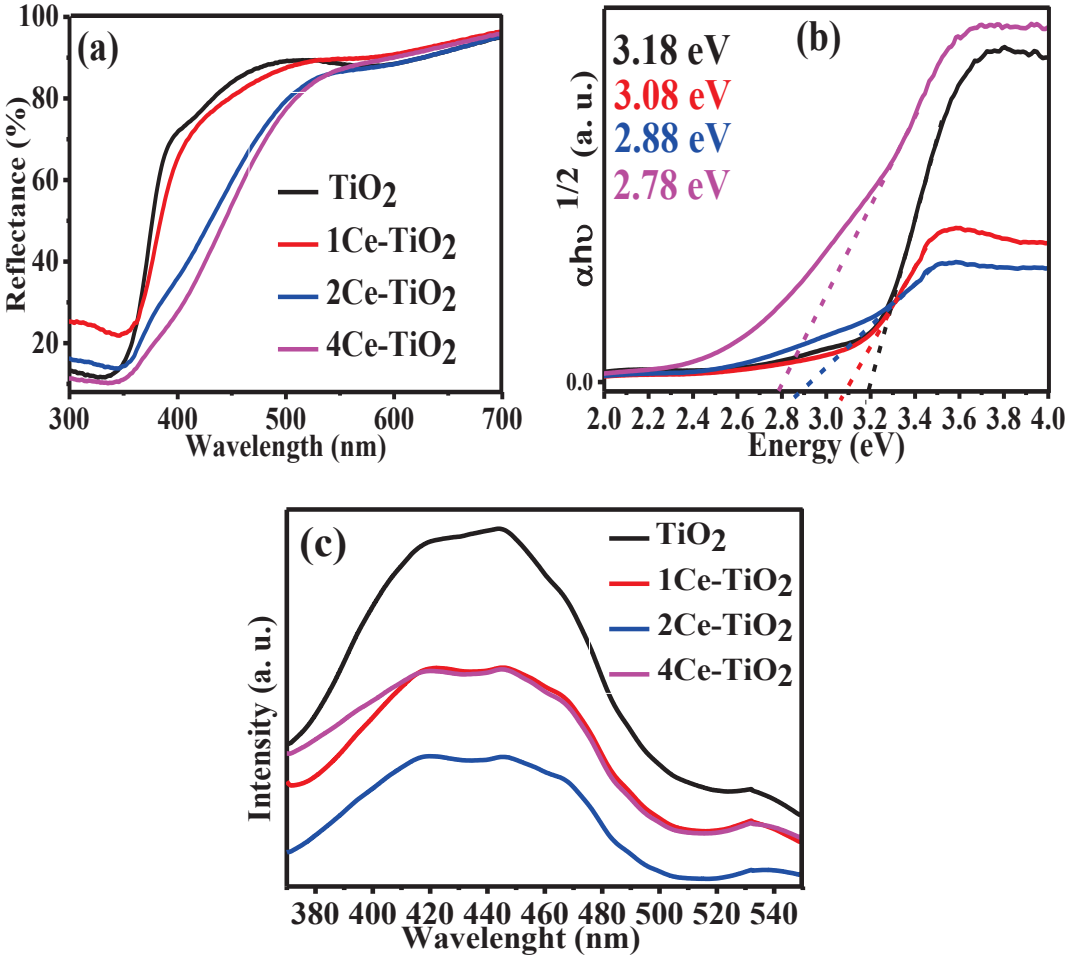

Figure 5-V.3 UV–Vis reflectance spectra **(a);** Tauc's Plot **(b)** and PL spectra of the different photocatalysts **(c)**.

A comparative analysis of **Figures 5-V.3 a-b** revealed a systematic redshift in the absorption edge with increasing cerium content. The band-gap energy of undoped TiO_2 was found to be approximately 3.18 eV, in close agreement with reported values for anatase-phase TiO_2. Upon cerium doping, the band-gap energies decreased to 3.08 eV (1Ce), 2.78 eV (2Ce), and 2.88 eV (4Ce), respectively. This notable narrowing is an important outcome, as it directly impacts the photocatalytic response of the material under solar and visible light illumination in real decontamination processes. The presence of Ce 4f states near the valence band contributes to band structure modification. The 4f orbitals can hybridize with the O 2p states of the valence band, leading to an upward shift of the valence band edge and, consequently, to a narrower bandgap [306]. Promoting a more efficient utilization of visible light photons, thereby enhancing the material's photocatalytic efficiency [307]. The defect states induced by lattice imperfections and Ce^{4+} substitution act as intermediary energy levels facilitating electronic transitions at lower photon energies than the intrinsic band-gap threshold of undoped TiO_2. Therefore, cerium doping effectively overcomes one of the principal limitations of pristine TiO_2, which is its exclusive UV-light responsiveness due to its wide bandgap.

PL spectroscopy is a powerful and non-destructive technique widely used to probe the electronic structure and charge carrier dynamics of semiconductor materials. In photocatalytic systems such as TiO_2, the PL signal primarily arises from the radiative recombination of photogenerated electron-hole (e^-/h^+) pairs. Therefore, the intensity and profile of PL emissions can provide valuable insight in the efficiency of charge separation, the presence of recombination centers, and the overall photocatalytic potential of the material. **Figure 5-V.2c** presents the PL spectra of bare and cerium-doped TiO_2 nanoparticles after irradiation.

The spectra of all the powders exhibit similar emission profiles, with two dominant emission peaks centered around 410 nm and 470 nm. The first peak is typically associated with band-edge free exciton recombination, reflecting the intrinsic radiative transitions within the TiO_2 lattice; the second one is commonly attributed to radiative recombination processes involving defect states, probably oxygen vacancies or surface defects, which act as shallow trapping sites for charge carriers [308]. Despite the preservation of these characteristic features across all samples, a clear variation in PL intensity is observed with increasing cerium content. Specifically, the PL intensity diminishes progressively from the undoped up to the 2Ce- TiO_2 sample. This attenuation is widely interpreted as evidence of a reduction in the recombination rate of photogenerated electron-hole

pairs. The incorporation of $Ce^{3+/}Ce^{4+}$ ions within the TiO_2 lattice introduces electron trapping states, which act as temporary reservoirs for photogenerated electrons. By capturing and holding electrons, these trap states prolong the lifetime of charge carriers, thereby enhancing their probability of participating in surface redox reactions rather than recombining radiatively. This improved charge separation is highly beneficial for photocatalysis, as it increases the generation of reactive oxygen species (ROS) such as hydroxyl radicals ($^{\bullet}OH$) and superoxide anions ($^{\bullet}O_2^-$), which are primarily responsible for the oxidative degradation of organic pollutants. However, beyond the optimal doping level of 2Ce, the PL intensity begins to rise again. This increase may be attributed to the formation of new recombination centers at higher doping concentrations. Excessive Ce doping can lead to the accumulation of cerium species at the surface or the formation of Ce-rich clusters, which may introduce deep-level defect states or act as non-radiative centers. These defects can promote rapid carrier recombination or even hinder light absorption due to surface coverage effects, thereby counteracting the beneficial effects observed at moderate doping levels [308]. PL spectroscopy confirms that moderate cerium doping (particularly at 2%) enhances the charge separation efficiency in TiO_2 by suppressing electron-hole recombination, a critical factor for improving photocatalytic performance. Conversely, over-doping may introduce adverse effects, highlighting the need for careful optimization of dopant concentration in semiconductor photocatalysts.

5-V.6.6 Scanning electron microscopy (SEM)

Figures 5-V.4 a–c and d–f present SEM images of bare TiO_2 and 2Ce-TiO_2, respectively. All samples consist of aggregates of irregularly shaped particles with characteristic sizes of approximately 10 μm. No significant morphological changes are observed upon Ce addition to TiO_2, indicating that its incorporation does not promote particle aggregation. Moreover, Ce particles are not discernible in the micrographs, suggesting a high degree of Ce dispersion within the TiO_2 matrix.

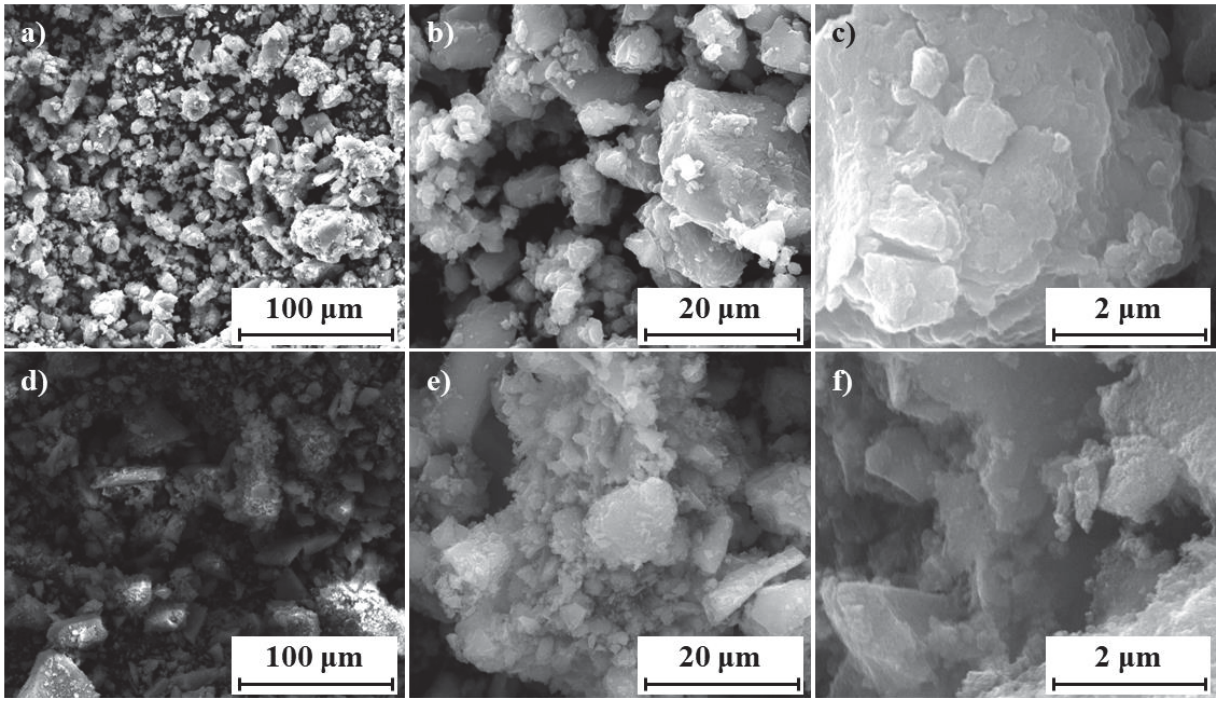

Figure 5-V.4 SEM images at various magnification of a) – c) TiO_2 and d) – f) 2Ce-TiO_2

Figure 5-V.5 shows the results of the photoelectrochemical characterization carried out in 0.1 M ABE to investigate the electronic properties of TiO_2 and 2Ce-TiO_2 samples. The effect of light irradiation on the open-circuit potential (OCP) was evaluated for both materials. Upon illumination, the OCP shifts toward more negative values, as expected for n-type semiconductors (**Figure 5-V.5 a,b**) [309].

The photocurrent spectra shown in **Figure 5-V.5 c,d** were recorded at open-circuit potentials of 35 mV for TiO_2 and -170 mV vs Ag/AgCl for 2%Ce-TiO_2. In both cases, the spectra display a maximum in the photocurrent associated with band-to-band electronic transitions. In particular, the highest photocurrent intensity is observed at approximately 330 nm for both samples. The n-type nature of these photocatalysts is further confirmed by the transient current recorded when irradiation was manually stopped by varying the applied potential (see **Figure 5-V.5 e,f**), indicating the presence of an anodic photocurrent. The photocurrent was measured as zero at ~ -0.1 V for both samples. This value can therefore be considered as an estimation of the flat band potential (V_{fb}) and assumed, for n-type semiconductors, equal to the conduction band potential.

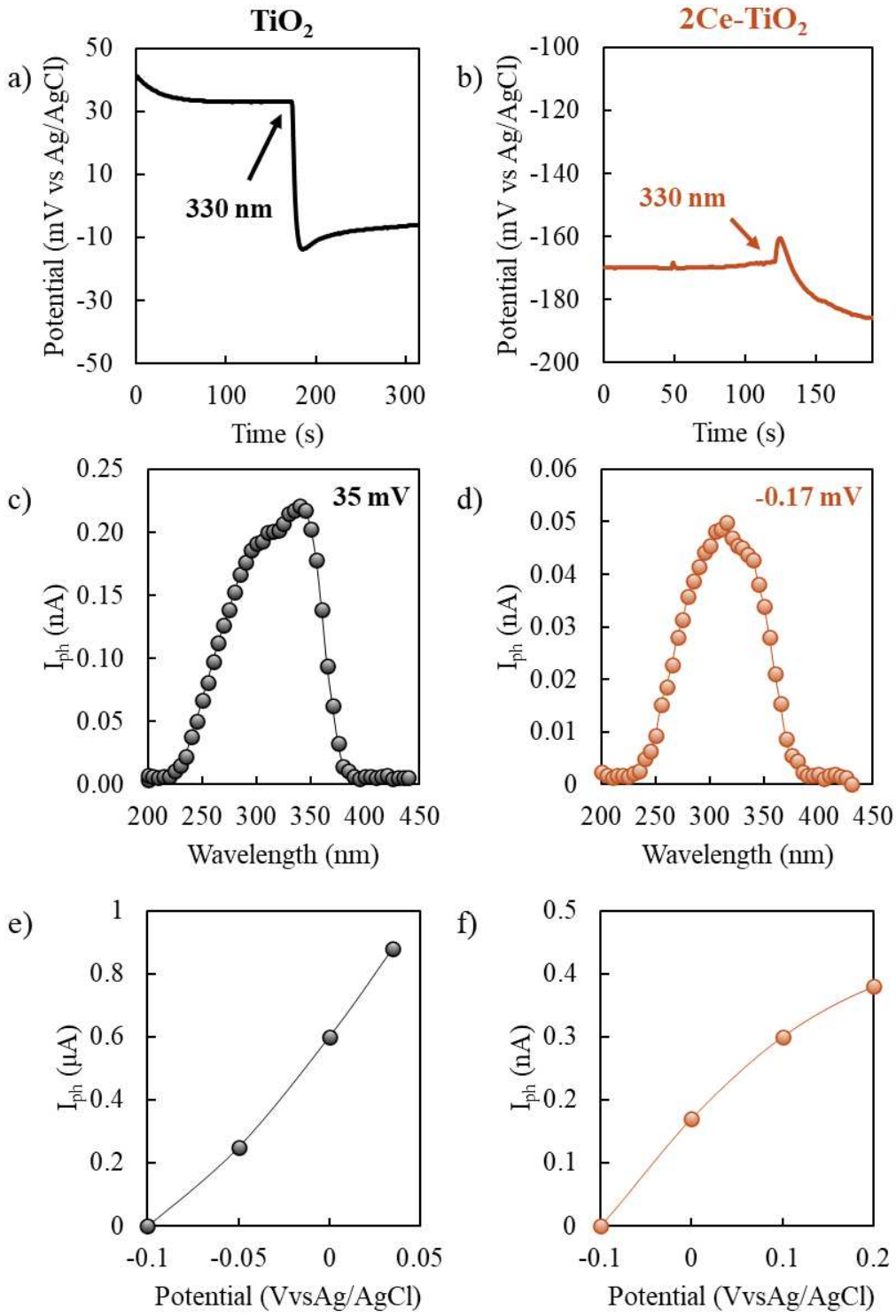

Figure 5-V.5 Photopotential recorded in dark and under 330nm irradiation for a) TiO_2 and b) 2Ce-TiO_2. Photocurrent spectra for TiO_2 and 2Ce-TiO_2 are reported in c) and d), respectively.

The photocurrent–potential transients recorded at 330 nm are reported in e), and f) for TiO_2 and 2Ce-TiO_2 respectively.

5-V.7 Photocatalysis tests

5-V.7.1 Methylene blue degradation under UV light

The photocatalytic performance of the synthesized materials was initially evaluated by monitoring the degradation of MB under ultraviolet irradiation for a total duration of 420 minutes. Before assessing the influence of cerium doping, a systematic optimization of experimental parameters as photocatalyst mass, initial dye concentration, and solution pH was conducted by using pristine TiO_2.

a) Effect of Solution pH

As shown in **Figure 5-V.5 a**, the pH of the solution played a pivotal role in controlling the photocatalytic degradation of MB. Among the tested conditions (pH 4, 7, and 9), the neutral medium (pH 7) yielded the highest degradation efficiency (50%), whereas acidic (pH 9) and basic (pH 4) conditions led to reduced efficiencies of 45% and 40%, respectively. These results are consistent with the known influence of pH on surface charge distribution, dye ionization, and catalyst–pollutant interaction. At neutral pH, the surface of TiO_2 maintains a balanced charge that enhances electrostatic interaction with the dye molecules, thereby improving photocatalytic performance.

b) Effect of Initial Dye Concentration

Figure 5-V.5 b highlights the effect of initial MB concentration on degradation efficiency. A noticeable decline in performance was observed as the dye concentration increased. The maximum degradation (55%) occurred at 5 mg L^{-1}, while a concentration of 10 mg L^{-1} still produced a substantial efficiency of 52%. However, further increases in concentration to 20 and 40 mg L^{-1} resulted in significant decreases in degradation, with efficiencies of 44% and 24%, respectively. This trend is attributed to the fixed number of reactive species (such as hydroxyl radicals) generated per unit of surface area of the catalyst . As dye concentration increases, the number of pollutant molecules exceeds the availability of oxidizing species, leading to competitive adsorption and shielding effects that reduce light penetration and reactive interactions [310].

c) Effect of Photocatalyst Mass

As presented in **Figure 5-V.6 c**, the mass of TiO_2 also exerted a notable influence on degradation efficiency. An optimal catalyst loading of 100 mg in 100 mL of MB solution resulted in a maximum degradation efficiency of 60%. Lower (50 mg) and higher (150 mg, 200 mg) amounts led to reduced efficiencies of 40%, 58%, and 40%, respectively. The improved performance at 100 mg is associated with the increased surface area and greater availability of active sites for radical formation. In contrast, excessive catalyst loading increased turbidity (shielding effect), limiting light penetration and causing light scattering, which ultimately hindered photocatalytic efficiency. Based on these findings, the optimal experimental conditions for subsequent studies were established as follows: neutral pH (7), catalyst mass of 100 mg, and an initial MB concentration of 10 mg L^{-1} [311].

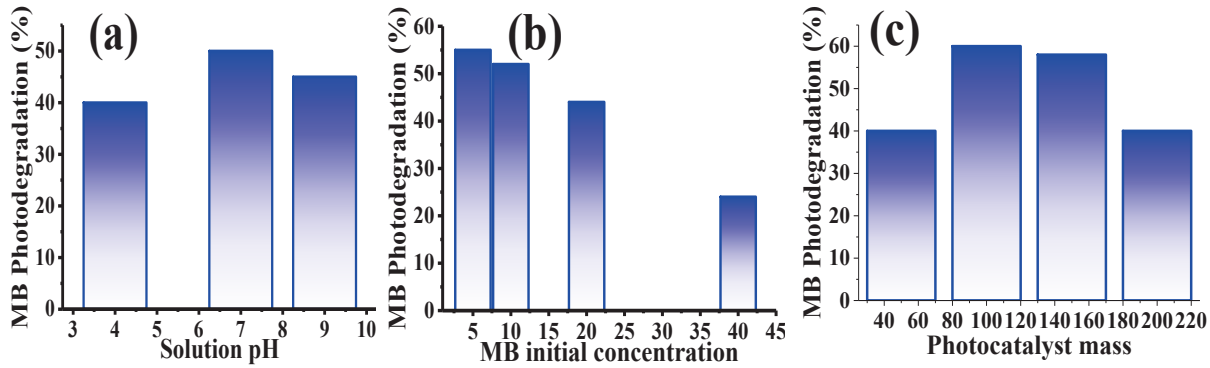

Figure 5-V.6 (a) Effect of solution pH, **(b)** initial MB concentration and **(c)** TiO_2 mass on MB photodegradation.

d) Influence of Cerium concentration

Following the optimization of base parameters, the effect of cerium incorporation on TiO_2 photocatalytic efficiency was investigated. **Table 5-V.6** summarizes the degradation efficiencies of MB using undoped TiO_2 and Ce-doped samples containing 1, 2, and 4% Ce. The results clearly demonstrate a substantial enhancement in photocatalytic activity after cerium doping. The undoped TiO_2 sample exhibited a degradation efficiency of 61.45%, while doping with 1, 2, and 4% Ce increased the efficiency to 83.06%, 91.57%, and 77.67%, respectively. The data reveal a bell-shaped trend, with an optimal photocatalytic response at 2% Ce doping. This behavior is well documented in the literature and is generally attributed to an optimal balance between enhanced

charge separation, improved visible-light absorption, and minimization of recombination centers [25]. At higher doping levels (e.g., 4%), the presence of an excessive amount of cerium may induce the formation of surface clusters or secondary phases, leading to recombination sites, surface blockage, or decreased photon absorption, factors that ultimately reduce the photocatalytic efficiency.

Table 5-V.2 MB conversion (X), kinetic constant and R^2 in the presence of the different samples.

Samples	**TiO_2**	**1Ce-TiO_2**	**2Ce-TiO_2**	**4Ce-TiO_2**
X (%)	61.45	83.06	91.57	77.67
k (min^{-1})	0.0022	0.00414	0.00508	0.00367
R^2	0.97147	0.99439	0.87139	0.98234

e) Kinetic Study of MB Degradation

To further elucidate the degradation mechanism, the kinetics of MB photodegradation were analyzed using a pseudo-first-order kinetic model, commonly applied in heterogeneous photocatalysis. The model is governed by the following expression (**Equation 5-V.4**)

$$\ln\left(\frac{C_0}{C}\right) = -kt \qquad \text{(Eq. 5-V.4)}$$

where C_0 and C represent the initial and residual concentrations of MB, t is the irradiation time, and k is the apparent rate constant.

Figure 5-V.7a illustrates the temporal evolution of MB degradation (C_0/C), and **Figure 5-V.7b** presents the corresponding linear plots used to extract the kinetic constants. The calculated values of k and the associated coefficients of determination (R^2) are compiled in **Table 5-V.2**. The 2Ce-TiO_2 sample exhibited the highest apparent rate constant (k= 0.00508 min^{-1}), confirming its superior photocatalytic performance. These findings reinforce the conclusion that moderate Ce doping optimally promotes electron-hole separation and suppresses recombination, thereby accelerating the degradation process.

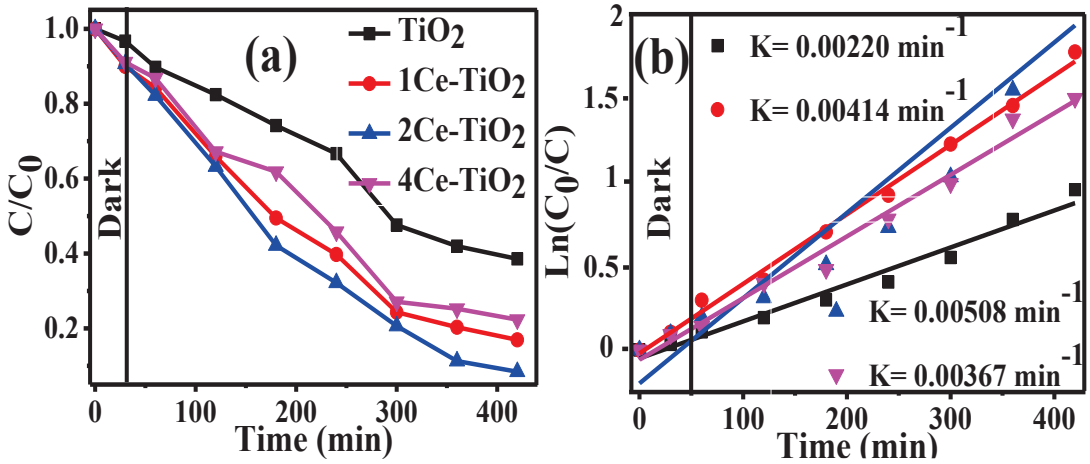

Figure 5-V.7 Photodegradation of MB under UV irradiation **(a)**, ln(C_0/C) plots vs irradiation time for first-order kinetic fitting **(b)**.

f) Scavenger's effect

Figure 5-V.8, shows that when NO and BQ were added, the photodegradation efficiency towards MB dropped significantly, from 91.57% to 20.58% and 23.97%, respectively. This clearly indicates that h^+ and $^{\bullet}O_2^-$ radicals are the main reactive species responsible for the MB photodegradation process, whilst e^- and $^{\bullet}OH$ radicals play a minor role.

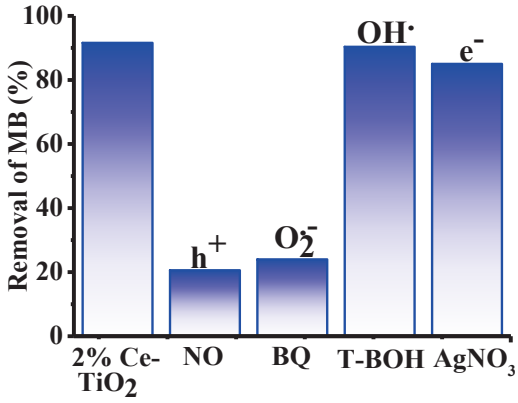

Figure 5-V.8 Effect of a series of scavengers on the degradation efficiency of MB for 2Ce-TiO_2. Blank, NO, BQ, *t*-BOH, and $AgNO_3$

g) Photocatalytic Reusability of MB

The long-term stability and reusability of the 2Ce-TiO_2 sample were evaluated over five successive photocatalytic cycles. The degradation performance remained consistently high, with efficiencies

of 90%, 90%, 89%, 87%, and 85% over the five cycles, as shown in **Figure 5-V.9**. The minimal decline in activity (approximately 5%) is primarily attributed to slight material loss during filtration and centrifugation steps, rather than structural degradation of the catalyst. This high degree of recyclability highlights the material's robustness and suitability for repeated use in practical wastewater treatment applications.

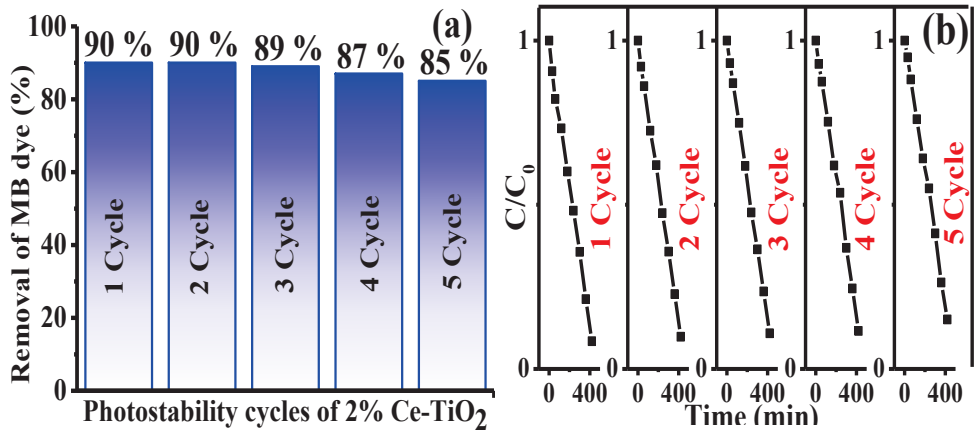

Figure 5-V.9 Photostability of 2Ce-TiO_2 Photocatalyst. **(a)** Photostability across multiple cycles, represented as a bar **(b)** Degradation of Methylene Blue (MB) over five cycles under UV irradiation.

5-V.9 Photocatalytic Degradation of Rose Bengal

Tests carried out with RB showed excellent photocatalytic activity under the optimal conditions determined for MB. **Figure 5-V.10a** shows a rapid drop in the normalized concentration (C_0/C) of RB under simulated solar irradiation, particularly with the 2Ce-TiO_2 photocatalyst that achieved 99.01% RB degradation in just 30 minutes, significantly outperforming undoped TiO_2 (92.37%) and other Ce concentrations (1%: 97.49% and 4%: 98.75%), as shown in **Figure 5-V.10b**. This high efficiency can be attributed to cerium's ability to act as an electron trap, promoting the separation of photo-induced charges and increasing the generation of reactive oxygen species (ROS).

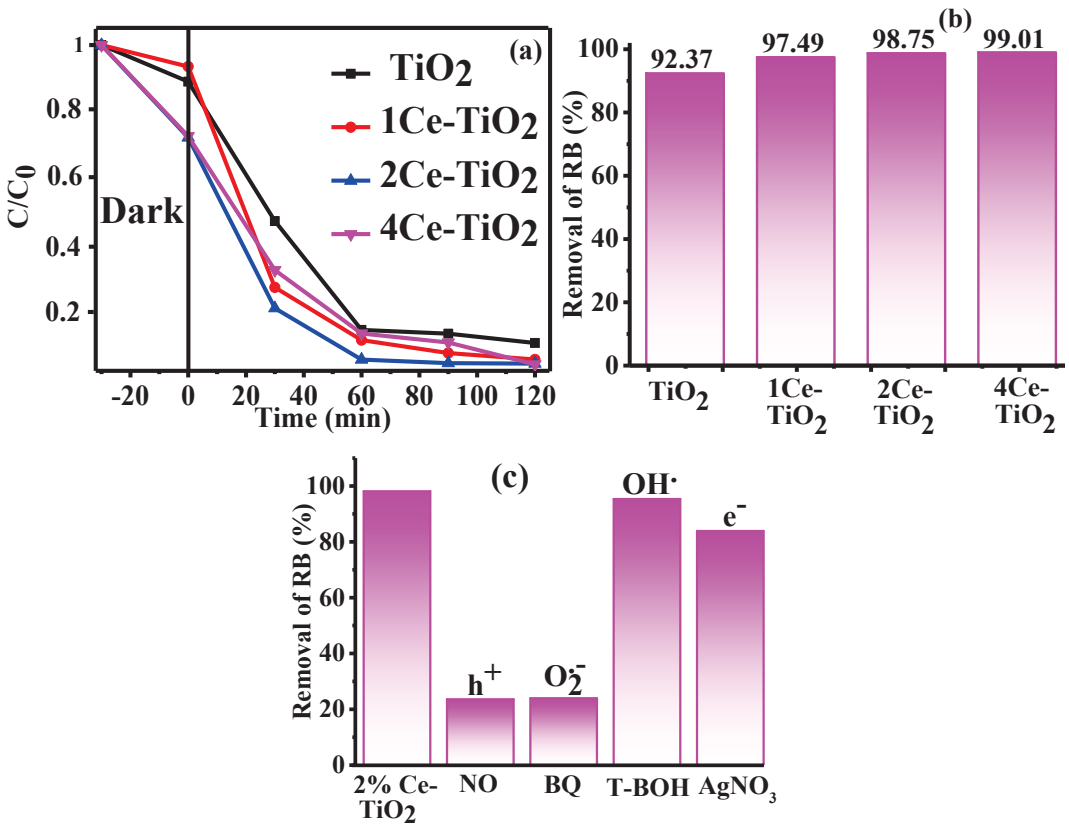

Figure 5-V.10 Degradation of RB over time for different catalysts **(a)**; RB conversion efficiencies after 2h of irradiation **(b);** effect of a series of scavengers on the degradation efficiency of RB for 2Ce-TiO_2 **(c)**.

As depicted in **Figure 5-V.10c**, the addition of NO and BQ dramatically reduced the photodegradation efficiency towards RB from 99.01% to 20.16% and 17.90% respectively. This compelling evidence highlights that also for this molecule h^+ and $^{\bullet}O_2^-$ are the primary reactive species driving the photodegradation process.

5-V.10 TC removal under simulated solar light irradiation

The experiments on TC, a broad-spectrum antibiotic frequently found in hospital and agricultural effluents, also confirmed the effectiveness of our optimized conditions. **Figure 5-V.11a** shows that the 2Ce-TiO_2 catalyst achieved 99.47% TC degradation in only 30 minutes. This substantially outperformed undoped TiO_2 (85.02%) and showed better performance than both 1% (94.82%) and 4% (98.63%) doping levels (**Figure 5-V.11b**). These results confirm the optimal impact of moderate Ce doping (2%) on photocatalytic efficiency. Since TC is a more complex and oxidation-

resistant molecule than RB or MB, these finding reinforces the relevance of 2Ce-TiO_2 as a very versatile photocatalyst.

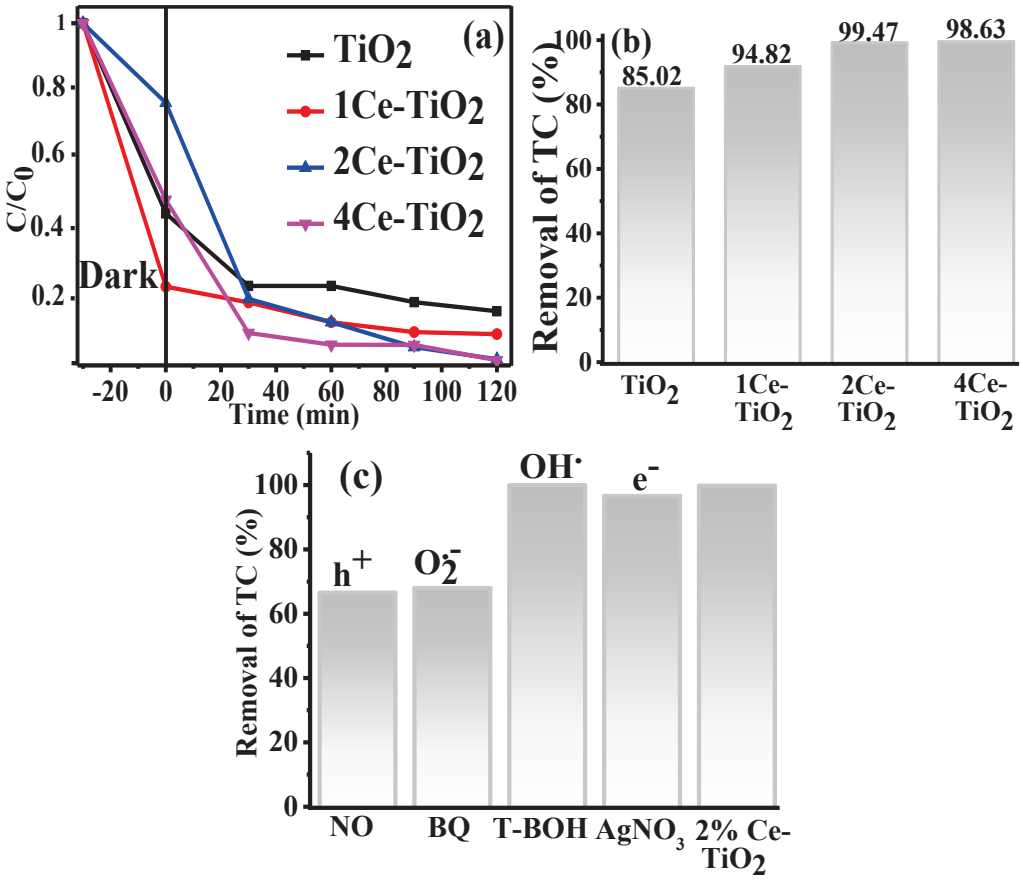

Figure 5-V.11 Catalyst performance in TC degradation. **(a)** TC degradation profiles as a function of time for different catalysts. **(b)** Percentage of TC converted after 2 hours of irradiation. **(c)** Effect of a series of scavengers on the degradation efficiency of TC for 2Ce-TiO_2.

5-V.11 Mineralization assessment: TOC analysis

Detailed Total Organic Carbon (TOC) removal percentages for the degradation of TC and RB achieved after 120 minutes of visible light irradiation with both bare and Ce-doped TiO_2 are discussed below.

Table 5-V.3 shows the TOC removal percentages for TC and RB degradation after 120 minutes of visible light irradiation using both bare and Ce-doped TiO_2 photocatalysts. For RB, the 2Ce-TiO_2 photocatalyst achieved a maximum TOC removal of 35%, which is a significant improvement over

the 13% seen with pure TiO_2. Similarly, for TC, TOC removal percentages were 8% for bare TiO_2, 29% for 1Ce-TiO_2, 34% for 2Ce-TiO_2, and 30% for 4Ce-TiO_2.

Table 5-V.3 TOC removal percentages during the degradation of TC and RB under solar light irradiation in the presence of different catalysts after 2 h of irradiation.

Samples	RB TOC (%)	TC TOC (%)
TiO_2	13	8
1Ce-TiO_2	28	29
2Ce-TiO_2	35	34
4Ce-TiO_2	30	32

These results confirm the good efficiency of these catalysts in achieving a fair degree of mineralization, ensuring that pollutants are not just transformed into potentially more dangerous by-products. However, complete mineralization is generally a slower process than decolorization. TOC removal data for these pollutants after 6 hours of visible light exposure using the optimized 2Ce-TiO_2 photocatalyst, are also presented in **Table 5-V.4.**

Table 5-V.4 shows the Total Organic Carbon (TOC) removal percentages for RB and TC dyes using 2Ce-TiO_2 under solar irradiation. For RB, the TOC removal reaches a plateau quickly, showing 35.01% at 2 h and only a marginal increase to 35.52% after 6 h, indicating that both degradation and the extent of mineralization possible for this molecule under these conditions are completed within the first two hours. In contrast, TC shows a continuous increase in mineralization from 28.3% at 1 h to 78.5% at 6 h. Although the parent TC molecule achieves near-complete degradation (approx. 99%) by 2 h, the TOC continues to rise significantly thereafter. This discrepancy occurs because the parent molecule breaks down into smaller, colourless organic intermediates. The photocatalyst requires the additional time (from 2 to 6 h) to further oxidize these persistent intermediates into CO_2 and H_2O, a process more accurately captured by TOC analysis than by simple decolorization measurements

Table 5-V.4 TOC removal percentages for TC and RB degradation after 6 hours of visible light irradiation using 2Ce-TiO_2.

Time	RB TOC (%)	TC TOC (%)
1 h	25.81	28.3
2 h	35.01	34.2
3 h	35.21	62.69
4 h	35.25	76.07
5 h	35.41	77.7
6 h	35.52	78.5

Therefore, future efforts could focus on improving process effectiveness, perhaps by extending reaction times under direct, inexpensive, and non-polluting solar radiation.

5-V.12 Comparative Study of Pollutant Degradation Mechanisms by Reactive Species

The photocatalytic degradation mechanism for MB, RB and TC was determined to primarily involve holes and superoxide radicals. This was confirmed by the significant reduction in degradation efficiency when specific scavengers, namely $Na_2C_2O_4$ (a scavenger for h^+) and benzoquinone (a scavenger for $^{\bullet}O_2^-$), were introduced. This established mechanism is summarized in **Figure 5-V.12**.

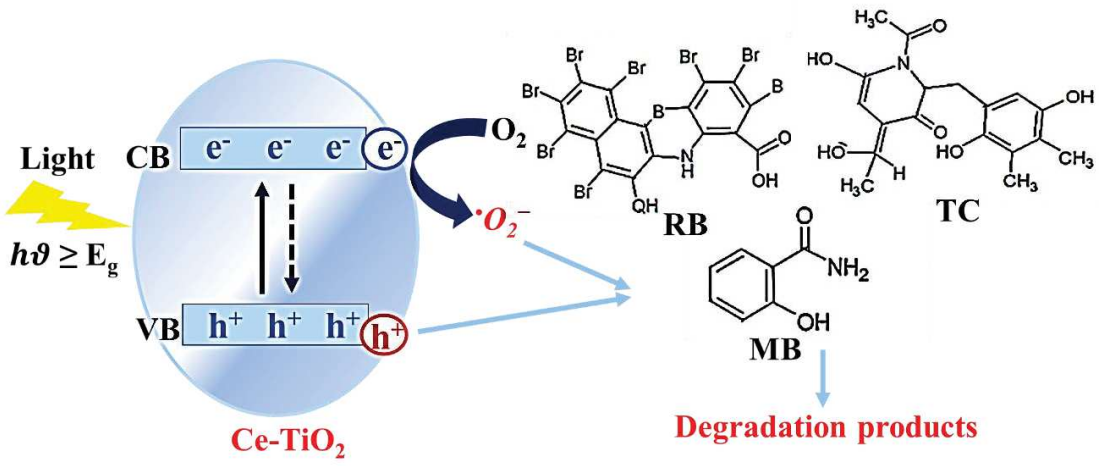

Figure 5-V.12 Proposed mechanisms of MB, RB, and TC using Ce-TiO_2

5-V.13 Conclusion

This work provides compelling evidence that strategic cerium doping of TiO_2 significantly enhances its photocatalytic efficiency for the degradation of persistent organic pollutants under both UV and visible light. Among the synthesized materials, the 2Ce-TiO_2 photocatalyst emerged as the optimal formulation, combining a reduced bandgap (2.78 eV), increased surface area (634.87 $m^2 g^{-1}$), and enhanced electron–hole separation, as supported by PL spectroscopy and BET analysis. These properties allowed excellent photocatalytic performance, achieving 91.57% degradation of methylene blue, 99.01% of Rose Bengal and 99.47% of tetracycline under UV or simulated solar irradiation. Mechanistic studies revealed that holes and superoxide radicals were the dominant reactive species involved, highlighting a universal oxidative pathway applicable to structurally diverse pollutants. The photocatalyst also showed high structural integrity and stability across five degradation cycles, confirming its suitability for real-world applications. A major novelty of this work lies in the integration of advanced machine learning through Gaussian Process Regression (GPR) coupled with the Improved Grey Wolf Optimizer (IGWO). This hybrid approach not only enabled precise modelling of MB degradation with excellent predictive accuracy ($R^2 > 0.999$), but also significantly reduced experimental efforts by identifying optimal degradation conditions with a prediction error below 0.3%. External validation further confirmed the model's transferability to other pollutants, demonstrating its robustness and generalization capability. Beyond the development of a high-performance photocatalyst, this study underscores the synergy between materials engineering and artificial intelligence for designing efficient, data-driven environmental remediation strategies. The findings pave the way for the implementation of solar-assisted, AI-optimized photocatalytic systems in decentralized wastewater treatment units, especially in regions lacking access to advanced technologies. Future work should extend this framework to pilot-scale systems and explore co-doping or heterojunction strategies to further boost visible-light activation and degradation selectivity.

SECTION-IV

Selective Photocatalytic Oxidation of Alcohols to Value-Added Aldehydes

CHAPTER 6

6. Investigating the surface processes addressing the selective photocatalytic oxidation of aromatic alcohols by BiOCl/HP-TiO_2 composites

6.1 Abstract

In this study, the photocatalytic partial oxidation of piperonyl alcohol, furfuryl alcohol, 2-hydroxybenzyl alcohol (salicyl alcohol), and 4-methoxybenzyl alcohol as probe molecules were investigated under eco-friendly conditions. The process was carried out by using BiOCl, Home-prepared TiO_2, and BiOCl/TiO_2 composites as photocatalysts in aqueous dispersion, to disclose the surface catalysts's features addressing conversion and selectivity. The composite photocatalysts were prepared by ball-milling and characterized using XRD, DRS, BET, PL, and FTIR techniques. The formation of a heterojunction between BiOCl and TiO_2 improved light absorption and promoted more efficient separation of photogenerated charge carriers. Among them, the 5%BiOCl-TiO_2 heterostructure showed the highest selectivity towards aldehyde formation, particularly for 4-methoxybenzyl alcohol. This superior selectivity can be attributed to its enhanced stability against oxidative degradation and reduced adsorption of 4-methoxybenzaldehyde on the catalyst's surface. Interestingly, despite achieving high alcohol conversion values, the selectivity towards 4-methoxybenzaldehyde remained notably high. This finding contrasts with conventional reports in the literature, which often describe a significant decline in selectivity with increasing substrate conversion.

6.2 Photocatalyst Preparation

6.2.1 BiOCl Synthesis

In the present study bismuth oxychloride (BiOCl) photocatalyst was synthesized as reported in chapter 4.

6.2.2 HP TiO_2 Synthesis

Titanium chloride ($TiCl_4$, Fluka 98%) was used without further purification as the precursor. Fixing the molar ratio Ti/H_2O equal to 1:60 (volume ratio 1:10), $TiCl_4$ was slowly added dropwise to distilled water under vigorous stirring to control the exothermic hydrolysis reaction. After 12 h of

stirring at room temperature, the clear solution was boiled for 30 min while stirring. A milky white suspension was obtained, which was dried at 80 °C to obtain the powdered TiO_2 [292,311].

6.2.3 BiOCl/TiO_2 Composites

Powdered BiOCl and TiO_2 were mixed in different weight percentages and named X(X=3, 5, 7) %-BiOCl-TiO_2. The powders were placed in a chrome steel jar lined with zirconium oxide and containing six zirconium oxide balls. They were then ground in ambient conditions at room temperature for 2 h using a planetary ball mill (PM 100, Retsch-Allee 1–5, 42,781 Haan, Germany), with a rotation speed set at 150 rpm [312]. After that, the mixtures were hand-ground.

6.3 Photocatalytic runs

The photocatalytic experiments were carried out in an annular Pyrex reactor containing 150 mL of an aqueous solution of the selected aromatic alcohols, used as model compounds. The initial concentration of each alcohol was set at 0.5 mM, with photocatalyst loadings of 1 g/L for bare BiOCl, 1.5 g/L for HP TiO_2 and the composites. Transmitted photon flux measurements using a Quantum Photo radiometer were used to optimize the concentration of the photocatalysts in the reaction mixture. A 150 W halogen lamp, positioned axially inside the reactor, was used as the irradiation source. To ensure adsorption–desorption equilibrium between the substrate and the catalyst, the reacting mixture was mixed under dark condition for 30 minutes after adding the photocatalyst to the alcohol solution. The reaction proceeded for a total duration of 4 h. At fixed time intervals, 2 mL samples were extracted from the reaction mixture and immediately filtered through 0.2 μm membranes (HA, Millipore) to remove photocatalyst particles before analysis via HPLC. The identification and quantification of the initial alcohols and their oxidation products were performed using a Beckman Coulter HPLC system (System Gold 126 Solvent Module and 168 Diode Array Detector) equipped with a Phenomenex Kinetex 5μ C18 column (150 mm × 4.6 mm). The mobile phase consisted of acetonitrile and an aqueous solution of 2 mL trifluoroacetic acid in an 80:20 volumetric ratio, with a flow rate set at 0.8 mL/min.

6.4 Results and discussion

6.4.1 X-Ray Diffraction Spectroscopy

The XRD pattern of home prepared TiO_2 revealed the presence of anatase and rutile phases of TiO_2, which is confirmed from the characteristic diffraction peaks observed at approximately 25.3° (A (101) and 27.4° (R (110)) (see Figure 6.1). The presence of both phases confirms that the home-

prepared TiO_2 (HP05) is a biphasic material, in which anatase provides high photocatalytic activity due to its larger surface area, while rutile phase contributes to enhance the charge transport. This anatase-rutile intergrowth naturally improves internal electron transfer between the two phases, that minimizes recombination losses and improves charge separation efficiency. In the composites, the presence of peaks related to BiOCl are visible for the higher loadings.

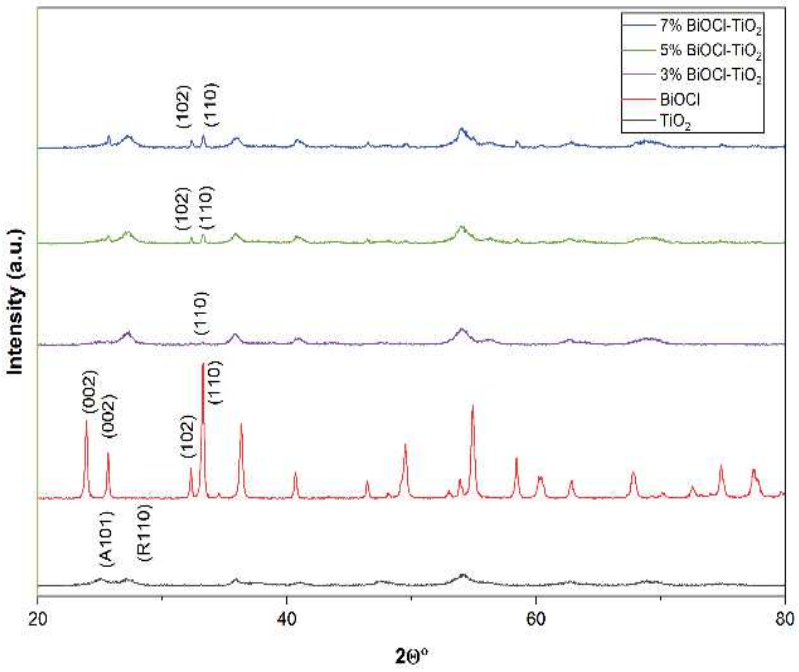

Figure 6.1. XRD spectra for TiO_2, BiOCl, 3%BiOCl-TiO_2, 5%BiOCl-TiO_2, 7%BiOCl-TiO_2.

When BiOCl particles interact with the TiO_2 (in 3%, 5%, and 7% BiOCl–HP05 composites) surface during the ball-milling process, the formation of a heterojunction interface occurs. Indeed, the layered BiOCl (p-type) couples with mixed-phase TiO_2 (n-type), resulting in an effective p-n heterojunction which facilitates charge separation and controls electron-holes extending visible-light absorption. Consequently, the overall photocatalytic performance of the composite is enhanced.

6.4.2 Diffuse Reflectance Spectroscopy

The diffuse reflectance spectra were used to study the optical absorption properties of the synthesized photocatalysts. As shown in Figure 6.2, the home-prepared TiO_2 exhibited a strong

absorption edge in the ultraviolet region at 400 nm with band gap 3.0 eV (Table 6.1), which is typical for TiO_2 due to its wide band gap. After the incorporation of BiOCl in the composites, the absorption edge slightly shifted toward longer wavelengths which indicates improved light harvesting ability of the composite materials. This shift can be recognized to the electronic interaction between TiO_2 and BiOCl in the heterostructure. Among the synthesized photocatalyst, the 5%BiOCl-TiO_2 composite showed a broader absorption region compared to the individual components, suggesting enhanced utilization of incident light. The improved optical response of the composite photocatalyst is beneficial for photocatalytic reactions because it allows the material to absorb a greater portion of the irradiation energy and generate more charge carriers.

6.4.3 BET

Specific surface area values (Table 6.1) are 76.1 and 3.3 $m^2 g^{-1}$ for TiO_2 and BiOCl, respectively, for the two bare powders; in the composites, a progressive increase in surface area with increasing BiOCl loading can be noticed up to 117.5 $m^2 g^{-1}$.

Table 6.1 Specific surface area and band gap of the different photocatalysts.

Catalyst	**Band gap (eV)**	**S.S.A. ($m^2 g^{-1}$)**
TiO_2	3.04	76.1
BiOCl	3.45	3.3
3%BiOCl- TiO_2	3.06	81.4
5%BiOCl- TiO_2	3.06	84.6
7%BiOCl- TiO_2	3.06	117.5

6.4.4 Photoluminescence (PL) spectroscopy

Photoluminescence spectroscopy was used to study the recombination behaviour of photogenerated charge carriers in the synthesized photocatalysts as shown in Figure 6.2. Generally, PL emission originates from the radiative recombination of electrons and holes generated during light excitation. Therefore, a higher PL intensity corresponds to a higher recombination rate of charge carriers, whereas a lower PL intensity indicates more efficient charge separation. As shown

in Figure 6.2, the 5%BiOCl-TiO_2 composite demonstrates significantly lower PL intensity compared to pure BiOCl and home-prepared TiO_2, suggesting an improved separation of photogenerated charge carriers. This behaviour can be due to the formation of a heterojunction between BiOCl and TiO_2, which facilitates interfacial charge transfer between the two semiconductor phases. The improved separation of photogenerated charge carriers increases the lifetime of electrons and holes, making them more available for photocatalytic reactions.

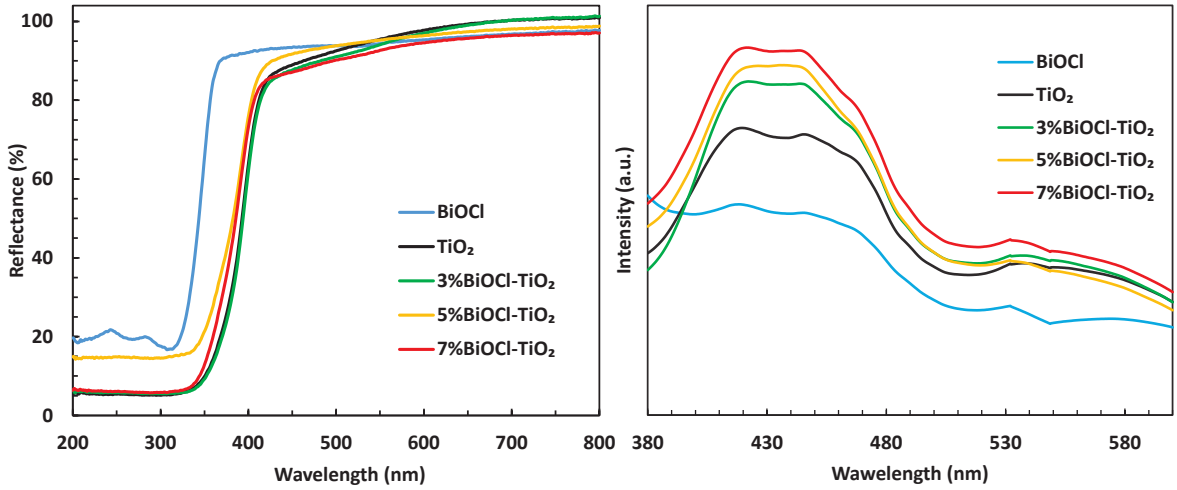

Figure 6.2. Reflectance and photoluminescence spectra of synthesized photocatalysts.

6.4.5 Fourier Transform Infrared spectroscopy

FTIR spectroscopy was used to investigate the surface functional groups and bonding characteristics of home-prepared BiOCl, TiO_2, and BiOCl-TiO_2 composites with different percentages (3, 5, 7%) in the wavenumber range of 400-4000 cm^{-1} (see Figure 6.3).

Transmittance, observed around high wavenumber region 3200-3500 cm^{-1} in all spectra, corresponds to the O-H stretching vibration, that are originating from water molecules and hydroxyl groups absorbed on surface. This band indicates hydroxylation which is beneficial for photocatalytic reactions as it facilitates charge transfer and reactive radical formation.

The weak band appearing in mid infrared red region near 1600 cm^{-1} corresponds to the H-O-H bending vibration of physically adsorbed water. This confirms the hydrophilic nature of the catalyst surfaces. A visible decrease in transmittance in the region of 1000-1100 cm^{-1} is associated with metal-oxygen related vibrations and surface lattice distortions. In the composite samples, slight shifts in band position and variations in transmittance intensity compared to bare BiOCl and TiO_2

indicate strong interfacial interactions between the two phases, confirming the formation of a BiOCl-TiO_2 heterojunction. The transmittance observed below 800 cm^{-1} in low wavenumber region are characteristic of metal-oxygen (M-O) stretching vibrations. The bands appearing around 500–600 cm^{-1} are attributed to Ti-O and Ti-O-Ti stretching vibrations of TiO_2. The additional bands observed in the BiOCl and BiOCl-TiO_2 composite samples within this region correspond to Bi-O and Bi-Cl lattice vibrations. The improvement and slight shift of this transmittance bands in the composite samples compared to that of the bare samples indicate successful coupling between BiOCl and TiO_2 and modification of the local bonding environment. These observations demonstrate improved interfacial interaction in the composite catalysts, which is essential to facilitate enhanced charge separation and improved photocatalytic performance.

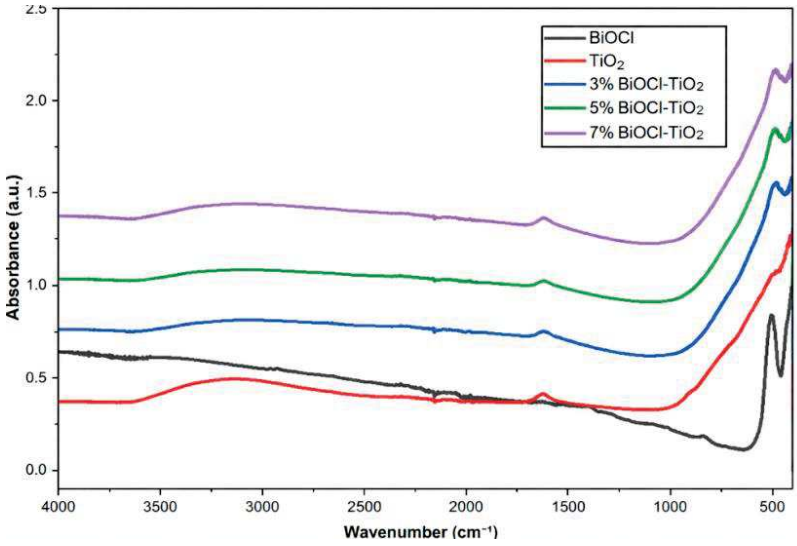

Figure 6.3. FTIR Spectra of synthesized photocatalysts.

6.5 Photocatalytic Activity

The results of the photocatalytic activity with different substrates i.e., 4-methoxybenzyl alcohol (4MBA), 2-hydroxybenzyl alcohol (2HBA), furfuryl alcohol (FA), and piperonyl alcohol (PA) are reported in Figure 6.4 below, in which the evolution of the concentrations of the different alcohols and corresponding aldehydes and acids are plotted versus irradiation time.

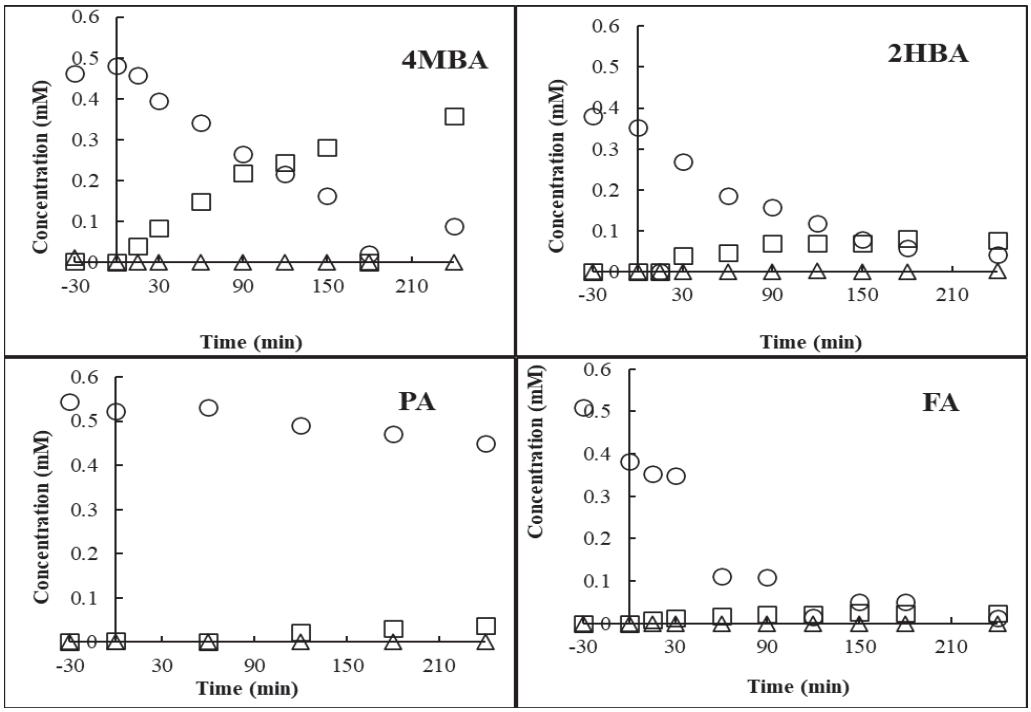

Figure 6.4. Evolution of the concentration vs. time for different alcohols with 5%BiOCl-HP05 (Alcohol ○, aldehyde & and acid ~) under simulated solar light irradiation.

In Table 6.2 are reported the values of alcohols conversion (X) (Equation 6.1), selectivity (S) (Equation 6.2) towards the main intermediates, after 4h of irradiation. The following equations were used for the determination of X and

$$X = \frac{[Alcohol]i - [Alcohol]t}{[Alcohol]i} * 100 \quad (6.1)$$

$$S = \frac{[P]t}{[Alcohol]i - [Alcohol]t} * 100 \quad (6.2)$$

where: $[Alcohol]_i$ and $[Alcohol]_t$ are the initial molar concentration and molar concentration at time t of the different alcohols, respectively. $[P]_t$ is the molar concentration of the obtained product (aldehyde or acid) at time t.

The performance of the photocatalysts investigated towards the aromatic alcohols was variable, affording different conversion and selectivity values (Table 6.2).

BiOCl photocatalysts and the composites with Home-prepared TiO_2 and commercial TiO_2-P25 were very active for the conversion of all the used substrates under simulated solar light irradiation

apart from PA for which the maximum conversion is 37%. Only trace amounts of acids were formed. After 4 h of irradiation, high selectivity values were obtained with almost all substrates except for furfuryl alcohol.

By using commercial P25 low selectivity values were obtained for all the substrates, in accordance with literature data [311,313]. In the presence of BiOCl, higher selectivity values were obtained at elevated conversion degrees of the aromatic alcohols. These results seem to be quite outstanding, given that the reactions were carried out in pure water and under simulated solar light irradiation. The best result was obtained with 5% BiOCl coupled with home prepared TiO_2.

By using as initial substrates 4-MBA and FA (2HBA), high conversion values were generally obtained, followed by high and low selectivity towards the corresponding aldehydes, respectively. With FA, instead, both low conversion and selectivity value were obtained. For 2HBA an intermediates behaviour can be noticed.

Among the investigated catalysts, the 5%BiOCl-TiO_2 composite provided the best compromise between conversion and selectivity as shown in Table 6.2. The variation in selectivity among the investigated alcohols is strongly influenced by their molecular structure and adsorption behaviour on the catalyst surface.

Table 6.2 Alcohols Conversion (X) and selectivity to corresponding aldehyde (S) in the presence of different catalysts.

Samples	**4-MBA**		**FA**		**2HBA**		**PA**	
	X	**S**	**X**	**S**	**X**	**S**	**X**	**S**
BiOCl	40	76	85	1	49	3	23	11
TiO_2	86	68	95	2	49	12	37	15
3%BiOCl-TiO_2	69	95	72	6	49	29	10	44
5%BiOCl-TiO_2	81	96	98	5	49	23	18	39
7%BiOCl-TiO_2	75	83	86	5	49	28	17	25
P25	64	13	83	2	45	11	34	11
5%BiOCl-P25	46	88	75	4	40	11	37	9

Mechanistic insights from scavenger tests

Figure 6.5 shown below reports the conversion (X) of the investigated aromatic alcohols and the selectivity (S) towards the corresponding aldehydes obtained in the presence of the 5%BiOCl-HP05 photocatalyst under simulated solar irradiation. A clear substrate-dependent behaviour can be observed, indicating that the photocatalytic performance strongly depends on the molecular structure of the alcohol and on the interaction between the substrate and the catalyst surface.

Among the investigated substrates, 4-methoxybenzyl alcohol (4MBA) showed the most favourable results, with high conversion (~80%) and very high selectivity (~96%) towards the corresponding aldehyde. This behaviour can be attributed to the presence of the electron-donating methoxy group in the para position, which facilitates the oxidation of the benzyl alcohol group while limiting further oxidation of the aromatic ring.

In contrast, furfuryl alcohol (FA) exhibited very high conversion but extremely low selectivity towards the aldehyde. This indicates that the formed intermediate is rapidly converted into further oxidation products, most likely due to strong adsorption of furfural on the photocatalyst surface and its susceptibility to subsequent oxidation reactions.

For 2-hydroxybenzyl alcohol (2HBA) an intermediate behaviour was observed, showing high conversion but only moderate selectivity. This can be attributed to the presence of the hydroxyl group in the ortho position, which can promote stronger adsorption of the corresponding aldehyde on the catalyst surface, thus favouring further oxidation.

Piperonyl alcohol (PA) showed relatively low conversion and moderate selectivity towards the corresponding aldehyde. These results explain that the substrate is less reactive under the investigated conditions, even though once oxidation occurs the formation of the aldehyde is still partially favoured. Overall, these results demonstrate that the 5% BiOCl-TiO_2 heterostructure is particularly effective in achieving selective oxidation of aromatic alcohols, although the catalytic performance strongly depends on the chemical structure of the substrate and the adsorption behaviour of the reaction intermediates.

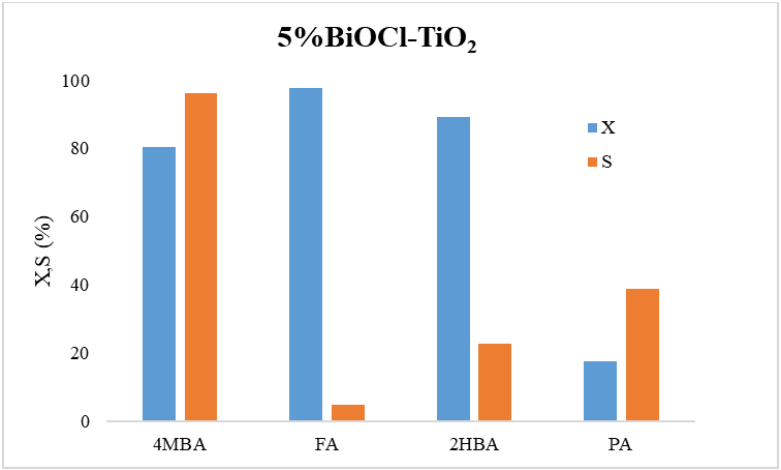

Figure 6.5. Conversion and selectivity (%) in the presence of different alcohols with 5%BiOCl-TiO_2.

In a previous work it has been noticed an increase in salicylaldehyde selectivity in basic solutions [187]. Table 6.3 indicates that the selectivity of salicylaldehyde increased by increasing the pH under basic conditions. In case of the bare home prepared TiO_2, with increase of pH, selectivity increased with slight decrease in conversion of 2HBA, but with BiOCl-TiO_2 composite at pH 11 the selectivity and conversion both increases, following same trend reported in the literature [187].

Table 6.3 Photocatalytic activity results of 2HBA (0.5mM) under UV irradiation for pH 11 in presence of Home prepared TiO_2 and their composites with BiOCl. X=conversion, S=selectivity towards salicylaldehyde after 4 h of irradiation.

Photocatalyst	**pH**	**Scavengers**	**X**	**S_{2HBAld}**
TiO_2	-	-	95	12
TiO_2	11	-	91	18
3%BiOCl-TiO_2	-	-	66	29
3%BiOCl-TiO_2	11	-	81	33
3%BiOCl-TiO_2	11	$Na_2C_2O_4$	86	16
3%BiOCl-TiO_2	11	$AgNO_3$	86	18

The photocatalytic conversion of 2-hydroxybenzyl alcohol (2HBA), by using various scavengers with 3%BiOCl-TiO_2 as the photocatalyst, is shown in Figure 6.6. The addition of $AgNO_3$ and $Na_2C_2O_4$ was used to study the role of photogenerated electrons and holes in the reaction mechanism. $AgNO_3$ acts as an electron scavenger, whereas $Na_2C_2O_4$ acts as a hole scavenger. It can be noted that, the presence of these species slightly changes the reaction behavior as compared to that without scavengers, which indicates that photogenerated e^-/h^+ pairs do not play an important role in the oxidation process.

These results indicate that the oxidation of 2HBA mainly occurred by electron-mediated pathways, most likely involving the formation of reactive oxygen species such as superoxide radicals ($^{\bullet}O_2^-$) generated from the reaction between dissolved oxygen and photogenerated electrons. Such species can participate in the oxidation of the aromatic alcohol into the corresponding aldehyde. Therefore, these experiments suggest that electron-derived reactive species play a key role in the photocatalytic conversion process over the BiOCl-TiO_2 heterostructure.

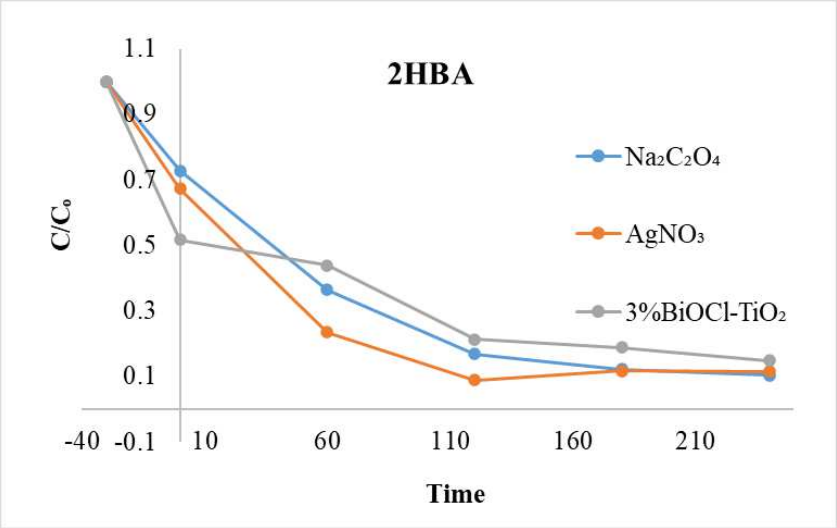

Figure 6.6. Photocatalytic conversion of 2HBA in the presence of different scavengers and 3%BiOCl-TiO_2 as photocatalyst.

6.6 Conclusion

The photocatalytic partial oxidation of different aromatic alcohols with home prepared BiOCl TiO_2 (home prepared HP05) composites was investigated under visible light irradiation. The photocatalysts displayed different activity towards the various alcohols confirming the important role of the peculiar catalysts' surface-substrate interaction [314-316]. In our case, the selective photocatalytic oxidation of some alcohols into corresponding aldehydes proceeded with both high conversion (>86%) and high selectivity (>96%). These results were attributed to the synergistic interaction between BiOCl and TiO_2, which improves charge separation and modifies the adsorption behaviour of the reaction intermediates. The results obtained are consistent with previous studies reported for $ZnIn_2S_4$ photocatalyst [317], which has shown high efficiency for the selective oxidation of aromatic alcohols under simulated solar irradiation in aqueous medium. In that work, high aldehyde selectivity was observed particularly for substrates containing electron-donating substituents, such as 4-methoxybenzyl alcohol, while lower selectivity was obtained for alcohols whose corresponding aldehydes exhibited stronger adsorption on the catalyst surface. A similar behaviour was observed in the present study, where the photocatalytic performance strongly depended on the structure of the alcohol and on the interaction between the reaction intermediates and the catalyst surface. These results confirm that selective oxidation is governed

not only by the oxidative power of the photocatalyst but also by adsorption–desorption processes and charge separation efficiency.

SECTION-V

PHOTOELECTROCATALYSIS

CHAPTER 7

7. PHOTOELECTROCATALYSIS

7.1 Abstract

In this chapter Photoelectrocatalytic (PEC) oxidation of biomass-derived substrates using TiO_2 nanotube (NT) arrays and modified electrodes under UV irradiation was investigated. TiO_2 NTs were synthesized via anodization and consequently modified with nickel, copper and tungsten species at different concentrations to enhance charge separation and catalytic activity. The PEC experiments were performed in an undivided glass reactor using Na_2SO_4 solution as the electrolyte under an applied bias, with glycerol, 5-hydroxymethylfurfural (HMF), and 4-methoxybenzyl alcohol (4-MBA) as the substrates. The results demonstrated that bare TiO_2 NTs show significant photoelectrocatalytic activity, primarily due to efficient hole-mediated oxidation processes. Although Ni, Cu and W-modified electrodes were assumed to improve charge transfer and hydrogen evolution, only limited enhancement in performance was observed along with selective formation of value-added oxidation products, while Faradaic efficiency calculations confirmed the dominant contribution of oxidation pathways over competing reactions. Moreover, the study highlights that TiO_2 nanotube-based photoanodes are effective for PEC biomass valorization; however, simple metal modification strategies are not sufficient to significantly improve performance. The findings emphasize the importance of optimizing interfacial charge transfer and catalyst design to achieve higher efficiency in photoelectrocatalytic systems.

7.2 Electrodes Preparation

TiO_2 nanotube (NT) photoanodes were prepared through an electrochemical anodization approach, a method widely reported for producing highly ordered nanotubular oxide layers. Titanium fiber felt (0.2–0.3 mm thickness) was used as starting substrates. Prior to anodization, the metallic titanium was cut into suitable pieces and subjected to a brief chemical pretreatment in a mixed solution of hydrofluoric acid, nitric acid, and deionized water (1:1:3 v/v) (HF, Sigma Aldrich, purity 39.5%), nitric acid (Sigma Aldrich, purity 69.0%). The etching duration was adjusted according to the substrate morphology, with shorter exposure applied to the fiber felt. After the chemical cleaning, the samples were ultrasonically treated in acetone and ethanol to eliminate surface contaminants, rinsed thoroughly with deionized water, and allowed to dry under

ambient conditions. The nanotubular TiO_2 layer was generated in an ethylene glycol electrolyte containing ammonium fluoride 0.25% and a controlled amount of water 0.75%. Anodization was carried out in a two-electrode configuration, employing aluminum foil as the counter electrode. A constant potential of 45 V was maintained during the process, while the anodization time (10 min) was adjusted to tune the nanotube growth (see figure 7.1 (a,b,c)). To convert the formed amorphous oxide into its crystalline phase, the samples underwent a thermal treatment in air. Annealing was performed at elevated temperatures (450 °C) for a duration of 3 hours, followed by a slow cooling inside the furnace. The annealing conditions were carefully selected to promote crystallization while limiting the formation of a thick compact oxide layer at the Ti/ TiO_2 interface, which could otherwise hinder charge transport.

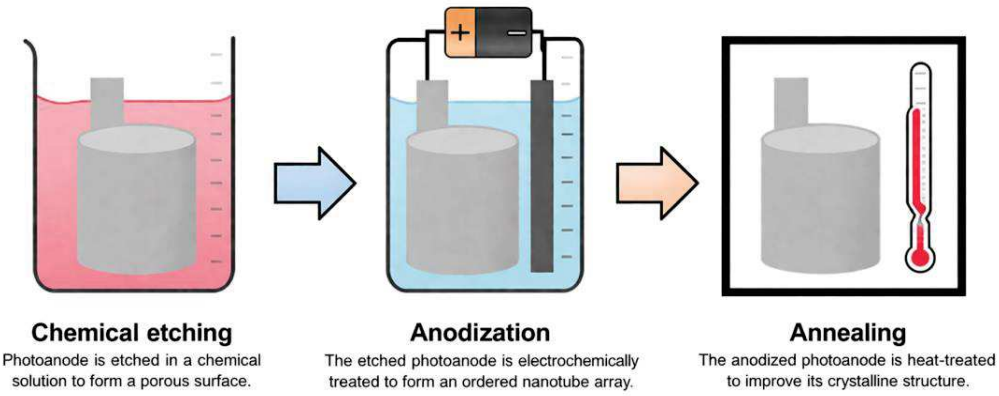

Figure 7.1. Schematic illustration of the photoanode preparation process: a) chemical etching, b) anodization, c) annealing.

Table 7.1 Synthesis conditions for Nanotubes synthesis.

Step	Bare TiO_2	1 mM Ni	5 mM Ni	10mM Ni	1mM W
Etching	5 s in 1:1:3 v $HF:HNO_3:H_2O$ 5 min US in acetone, 5 min US in EtOH	5 s in 1:1:3 v $HF:HNO_3:H_2O$ 5 min US in acetone 5, min US in EtOH	5 s in 1:1:3 v $HF:HNO_3:H_2O$ 5 min US in acetone, 5 min US in EtOH	5 s in 1:1:3 v $HF:HNO_3:H_2O$	5 s in 1:1:3 v $HF:HNO_3:H_2O$
Anodization	10 min @ 45 V in EG, 0.25 wt% NH_4F , 0.75 wt% H_2O	10 min @ 45 V in EG, 0.25 wt% NH_4F , 0.75 wt% H_2O	10 min @ 45 V in EG, 0.25 wt% NH_4F , 0.75 wt% H_2O	5 min US in Acetone	5 min US in Acetone
I annealing	3 h @ 450°C, air	3 h @ 450°C, air	3 h @ 450°C, air	5 min US in EtOH	5 min US in EtOH
Loading	—	1 h immersion in 1 mM Ni_2SO_4	1 h immersion in 5 mM Ni_2SO_4	10 min @ 45 V in EG, 0.25%wt NH_4F, 0.75%wt H_2O	10 min @ 45 V in EG, 0.25%wt NH_4F, 0.75%wt H_2O
II annealing	—	3 h @ 450°C	3 h @ 450°C	3h@450°C, air,/ 2h immersion in 10mM Ni_2SO_4, 3h@450°C	3h @ 450°C

7.3 Photoelectrocatalytic experiments

The Photoelectrocatalytic activity was performed by using TiO_2 nanotube arrays (NTs) as the photoanode, nickel foam as the cathode, and Na_2SO_4 as the electrolyte. The constant potential of 1 V was applied between the two electrodes. The initial glycerol concentration was 0.1 M and as far as 4-MBA and 5-HMF is concerned was 5mM. All experiments were performed in a glass reactor (Figure 7.2) by using a two-electrode configuration and a UV medium-pressure mercury lamp (125 W). TiO_2 NTs synthesized as described above and modified with dopping of Nickel and Tungstic acid with 1mM, 5mM and 10mM concentration. Electrochemical measurements and

kinetic data were collected using a Parstat 2263 potentiostat (PAR), equipped with electrochemical impedance spectroscopy (EIS) capabilities. Prior to each experiment, the reaction mixture was purged with helium under stirring in the dark for 30 minutes to eliminate dissolved oxygen and to ensure proper adsorption of substrates onto the electrode surface. After purging, the reactor was sealed, and irradiation was started. The reactions were carried out for 3 hours at room temperature, with continuous water circulation through a cooling jacket to maintain thermal stability. The samples were withdrawn in both liquid and gaseous phases to measure high value-added products and formation of hydrogen. After each run, the photoanode was cleaned by sonication in acetone and distilled water for 5 minutes each to remove any adsorbed residues. The nickel foam cathode was regenerated by sonication in ethanol for 5 minutes.

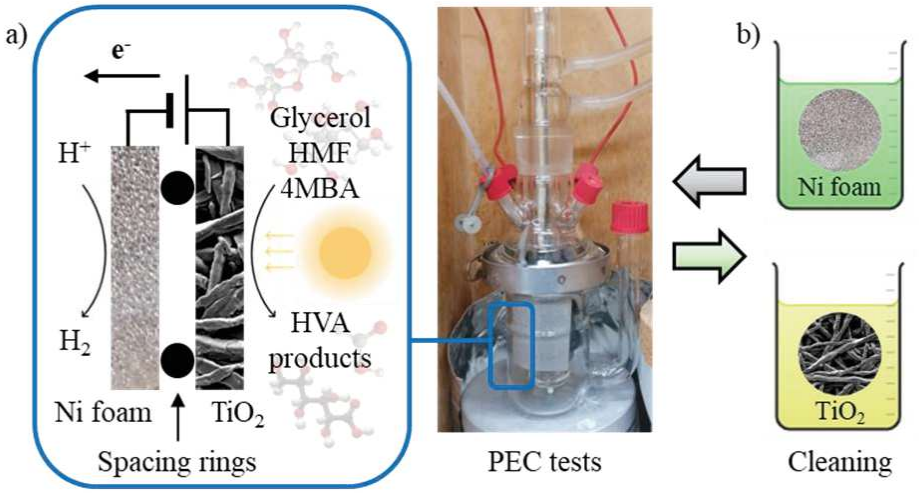

Figure 7.2 a) Image of the PEC cell used, and the corresponding schematic illustration b) Schematic representation of the electrode cleaning process.

7.4 Photoelectrochemical measurements

Photoelectrochemical measurements were carried out to study the electronic properties of the photocatalysts. The photocurrent spectrum (i.e. photocurrent vs wavelength curve) recorded in 0.5M Na_2SO_4 at pH 2 and 0.5 V vs Ag/AgCl is reported in Fig. 7.3a and 7.4a. It can be noted a maximum photocurrent value at ca. 320 nm. By assuming a non-direct optical transitions, it is possible to estimate an optical band gap value, Eg, by extrapolating to zero $(Q_{ph} \cdot h\nu)^{0.5}$ vs hν plot (see Fig. 7.3b. and 7.4b). Current transients were recorded under monochromatic irradiation (l ¼

320 nm) at several constant potentials. The photocurrent was measured by manually stopping the irradiation at applied potential varying from 1 to 0.75 V vs Ag/AgCl (Fig. 7.3c and 7.4c). An anodic photocurrent was measured confirming the n-type semiconductor behavior of the oxide, and the photocurrent was zero at ~ 0.75VvsAg/AgCl, that can be therefore assumed as an estimate of the flat band potential, Vfb.

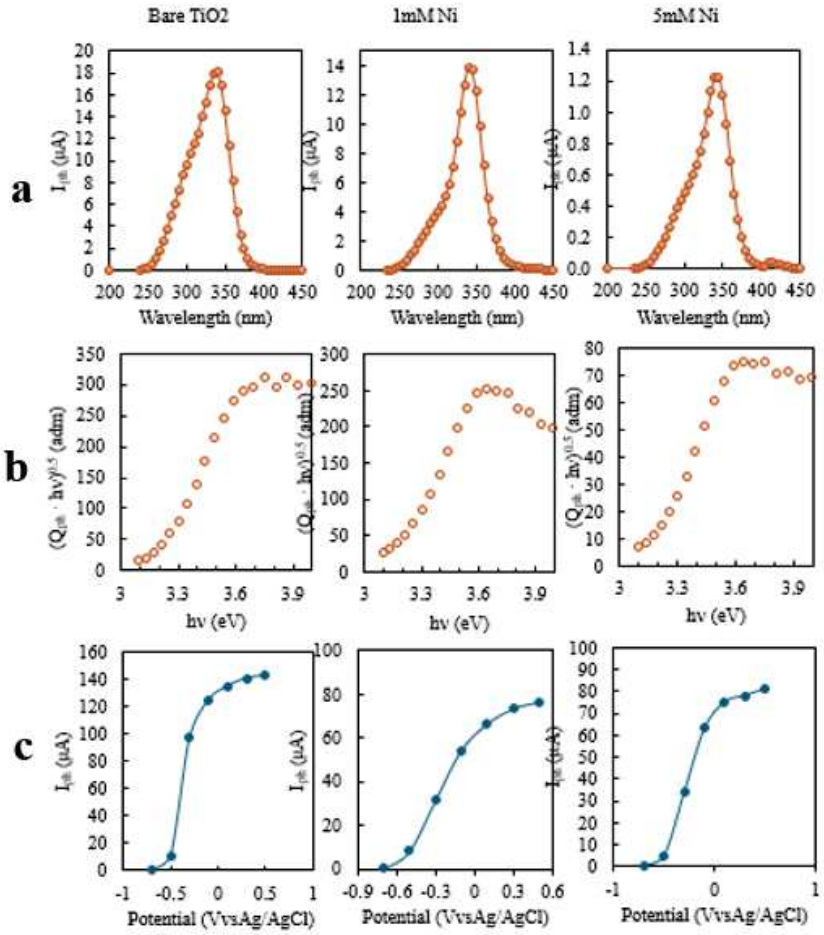

Figure 7.3 a) Photocurrent spectra recorded in a 0.1 M ABE aqueous solution at 0.5 V vs Ag/AgCl, **b)** respective $(Q_{ph}\cdot h\nu)^{0.5}$ vs hν estimation**, c)** photocurrent transients under monochromatic light recorded at 340 nm and applied potential from 0.5 to 0.5 V vs Ag/AgCl of bare TiO_2, 1mM Ni-TiO_2 and 5mM Ni-TiO_2.

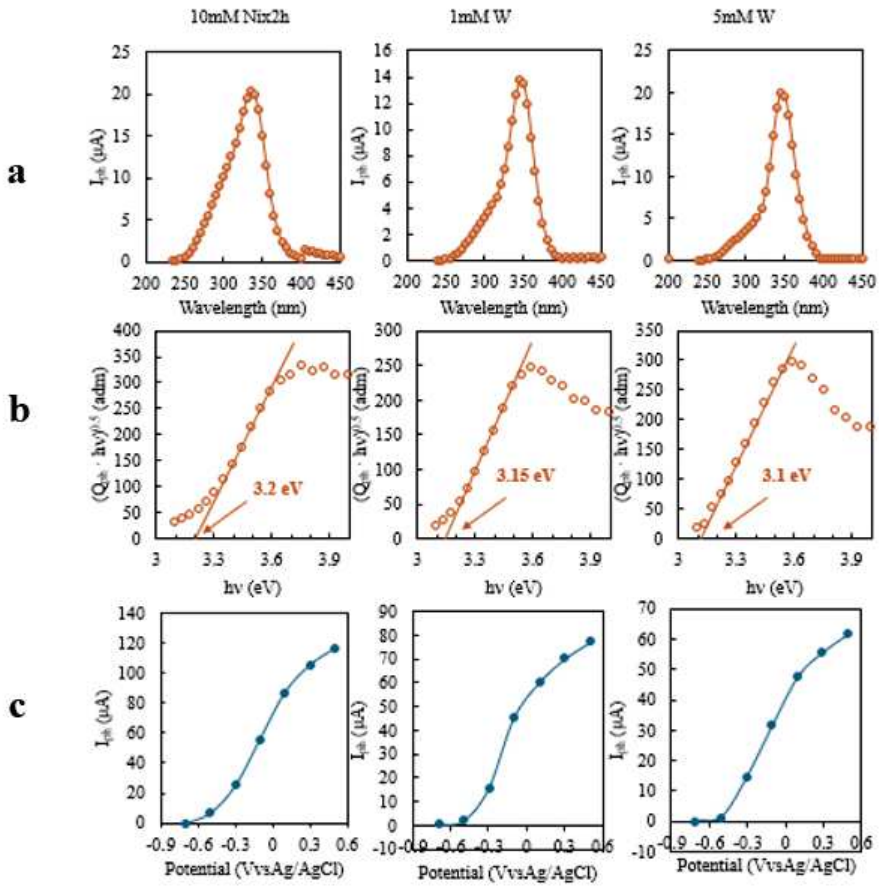

Figure 7.4. a) Photocurrent spectra recorded in a 0.1 M ABE aqueous solution at 0.5 V vs Ag/AgCl, **b)** respective $(Q_{ph}\cdot h\nu)^{0.5}$ vs hν estimation**, c)** photocurrent transients under monochromatic light recorded at 340 nm and applied potential from 0.5 to 0.5 V vs Ag/AgCl of 10mM Ni-TiO_2 and 5mM W-TiO_2 and 10mM W-TiO_2.

The incorporation of Ni and W species slightly modifies the electronic properties of TiO_2 nanotubes. Tungsten contributes to improve the charge transport and reduce the recombination through the modification of the band structure. Nickel, although generally considered a co-catalyst for hydrogen evolution, did not lead to a significant enhancement in hydrogen production under the present experimental conditions. This suggests that further optimization of catalyst loading and interfacial properties is required. The photoelectrochemical characterization demonstrates that

TiO_2 nanotube photoanodes exhibit strong UV-driven activity, stable photocurrent response, and efficient charge separation under applied bias.

7.5 Oxidation of organic substrates and formation of value-added products

Organic substrates like glycerol, 4-methoxybenzyl alcohol (4-MBA), and 5-hydroxymethylfurfural (HMF) play a double role in the photoelectrocatalytic (PEC) system. By using the photogenerated holes these substrates act as sacrificial agents, and simultaneously they act as reactants for oxidation processes to form high value added products. These species undergo oxidation at photoanode by interacting with the photogenerated holes h^+ and the reactive oxygen species. This process is supposed to enhance the charge separation and suppress electron-hole recombination to improve photoelectrocatalytic efficiency. The substitution of the oxygen evolution reaction (OER) with the oxidation of organic substrates is particularly beneficial due to its lower kinetic barrier. As a result, the system operates more efficiently, promoting both hydrogen production at the cathode and the selective formation of high-value oxidation products from glycerol, 4-MBA, and HMF.

7.6 Mechanism of the Photoelectrocatalytic Process

The Photoelectrocatalytic (PEC) mechanism is hypothesized to occurs by the synergistic interaction between light irradiation and an externally applied electrical bias, which together enhance charge separation and redox reaction efficiency. When irradiated by a suitable light radiation of energy equal or higher than that of its band bap, TiO_2 absorbs photons rise to electrons excitation from valence to conduction bands generating electron-hole pairs.

$$TiO_2 + h\nu \rightarrow e^- + h^+ \qquad \text{Eq (7.1)}$$

The external applied potential allows electrons to move towards cathode and holes towards photoanode. This process reduces the electron-hole recombination and increases the PEC efficiency. At the cathode, reduction reactions occur, leading to hydrogen evolution as shown in Eq. (7.2).

$$2H^+ + 2e^- \rightarrow H_2 \qquad \text{Eq. (7.2)}$$

At the photoanode, oxidation reactions take place, and organic substrates such as glycerol, 4-methoxybenzyl alcohol (4-MBA), and 5-hydroxymethylfurfural (HMF) are oxidized by photogenerated holes shown in equation 7.3.

Organic substrate + h^+ → oxidation products Eq. (7.3)

Ni incorporation is expected to enhance hydrogen evolution reaction (HER) kinetics, acting as a co-catalyst. The improved performance of W-modified TiO_2 may be attributed to enhanced charge transport and reduced recombination. The presence of oxygen vacancies may facilitate charge mobility, thereby improving the overall photoelectrochemical response. Moreover, the PEC system enables the simultaneous occurrence of reduction and oxidation reactions, allowing for hydrogen production at the cathode and selective oxidation of organic substrates into value-added products at the photoanode.

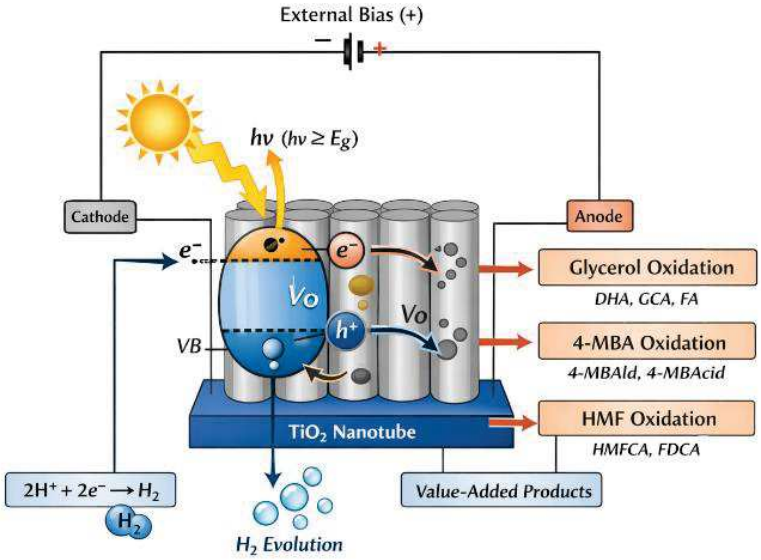

Figure 7.5. Schematic illustration of photoelectrocatalysis

7.7 Faradaic Efficiency

The Faradaic efficiency (FE) for hydrogen (H_2), CO_2, and the oxidation products derived from glycerol, 4-MBA, and HMF were calculated using Equation shown below:

$$FE(\%) = \frac{n_i \cdot z \cdot F}{Q} \times 100 \qquad Eq.\ 7.4$$

where:

- n_i= number of moles of product *i* formed
- Q= total charge passed (Coulomb)
- z= number of electrons transferred in the corresponding reaction
- F= Faraday constant (96,485 C mol^{-1})

The number of electrons transferred (z) was determined by the stoichiometry of the oxidation and reduction half-reactions corresponding to glycerol, 4-MBA, and HMF transformations.

Table 7.2 Faradaic efficiency (FE%) of oxidation products obtained during Photoelectrocatalytic oxidation of glycerol, HMF, and 4-MBA over different TiO_2-based photoanodes.

Photoanode	Glycerol Products (FE %)		HMF Products (FE %)				4-MBA Products (FE %)	
	DHA	GA	FDC	FCA	FDCA	HMFCA	4-MBALD	4-MBAcid
Bare TiO_2	54.70	0	0.024	0.127	0	0.141	13.05	0.67
10 mM Ni– TiO_2	—	0	—	—	—	—	—	—
5 mM W–TiO_2	35.38	0	—	—	—	—	11.67	1.63
Cu_2O–TiO_2 nanorods	—	—	0	0.337	0	0.282	—	—
WO_3–TiO_2 nanorods	—	—	0.020	0.206	0.034	0.179	14.64	2.05

The Faradaic efficiency results show that bare TiO_2 nanotubes primarily utilize photogenerated circulated charge for selective glycerol oxidation toward DHA, showing the highest FE (54.70%). In comparison to this, photoanodes impregnated with nickel, tungstic acid and copper such as WO_3-TiO_2 and Cu_2O-TiO_2 redistribute the charge toward HMF and 4-MBA oxidation products, including FCA, FDCA, and acids, reflecting enhanced multistep oxidation

pathways. Notably, WO_3-TiO_2 shows higher FE% toward oxidation products, confirming the more efficient charge utilization and the improved photoelectrocatalytic activity. Overall, electrode modification does not enhance the faradaic efficiency but shifts the charge consumption from selective to more extensive oxidation reactions.

7.8 Conclusion

Preliminary PEC tests to produce H_2 were carried out by using glycerol, 4-MBA and 5-HMF as sacrificial agents. The results indicate that the modification of TiO_2 nanotube electrodes by doping them with Ni, Cu and W species did not lead to a significant enhancement in hydrogen evolution compared to the unmodified TiO_2 NTs. This behaviour suggests that, although Ni and Cu are generally considered effective co-catalysts for hydrogen evolution reaction (HER), its incorporation in the present system did not substantially improve catalytic activity. This could be attributed to several factors, including non-optimal loading, limited active site availability, or inefficient charge transfer at the electrode–electrolyte interface. Additionally, the presence of tungsten, while beneficial for modifying the electronic structure and reducing recombination, may not directly contribute to HER activity. Instead, its role is more associated with charge transport rather than catalytic hydrogen production. The lack of significant improvement in hydrogen production emphasizes that the catalyst modification alone is not sufficient, and further optimization of loading, morphology, and interfacial properties is required. It is also possible that the applied bias and intrinsic properties of TiO_2 NTs already provide sufficient charge separation, limiting the observable impact of co-catalyst modification.

8. SUMMARY, CONCLUSION AND PERSPECTIVES

8. Main Conclusion

In this Ph.D. thesis, heterogeneous photocatalysis and photoelectrocatalysis were investigated as sustainable approaches for hydrogen production, biomass valorization, and environmental remediation under mild experimental conditions, including ambient temperature and pressure using water as a green solvent. The study focused on TiO_2-based systems and their modification by coupling with bismuth oxyhalides (BiOX, X = Cl, Br, I) or WO_3, doping (with N or Ce) to improve charge separation, light utilization, surface interactions and catalytic performance.

Photocatalytic experiments demonstrated that biomass-derived substrates such as glycerol and glucose can effectively act as sacrificial agents, promoting hydrogen evolution while simultaneously generating high value-added products. In particular, BiOX- TiO_2 heterostructures exhibited enhanced activity compared to bare TiO_2 due to improved interfacial charge transfer and reduced recombination, confirming the importance of heterojunction engineering.

In addition to energy production, the synthesized photocatalysts showed excellent performance in environmental applications, achieving efficient degradation of pharmaceuticals, pollutants, dyes such as tetracycline, oxytetracycline, carbamazepine, thiabendazole, para nitrophenol, Rose Bengal, Methylene Blue. Mechanistic investigations highlighted the role of reactive oxygen species and surface interactions in governing degradation pathways.

Selective oxidation processes were also achieved with different efficiency, including the conversion of biomass-derived molecules and aromatic alcohols into valuable intermediates under mild conditions. The key role of surface interaction between the photocatalysts and the substrate have been highlighted. Studies aimed at discovering the interactions of the various substrates with the catalyst surface are underway.

The obtained results demonstrate the potential of photocatalysis as a green synthetic route for producing fine chemicals alongside energy generation.

Furthermore, the modification of TiO_2 nanotube arrays in photoelectrocatalytic systems enabled improved charge separation under applied bias. While bare TiO_2 nanotubes exhibited stable and efficient performance, the incorporation of Ni, Cu, and W species resulted in only marginal improvements. This indicates that catalytic performance is predominantly governed by interfacial

charge transfer rather than simple metal modification. Faradaic efficiency analysis confirmed that PEC systems efficiently utilize photogenerated charge, although electrode modification primarily affects product distribution rather than overall efficiency.

Overall, this work demonstrates that TiO_2-based photocatalytic and photoelectrocatalytic systems represent a versatile and scalable platform for solar-driven applications, enabling the simultaneous production of hydrogen, selective oxidation of biomass-derived compounds, and degradation of environmental pollutants. Thus, we can conclude that:

- Bismuth oxyhalides BiOX (X= Br, Cl, I) photocatalysts were successfully synthesized by a simple co-precipitation method.
- BiOX (X= Br, Cl, I) were coupled with both commercial and home-prepared TiO_2 samples simply by ball milling treatment.
- The BiOCl-TiO_2 resulted the most active composites displaying high activity towards both biomass derivatives valorization and pollutants degradation.
- The composites exhibited higher activity than bare TiO_2, owing to an optimal balance between charge transfer and recombination processes, together with the controlled formation of defects achieved at an appropriate BiOCl content.
- The activity under simulated sunlight irradiation encourages the use of these photocatalysts under real conditions in large-scale solar power plants.

So, future research should focus on advanced interface engineering, controlled cocatalyst deposition, and band structure optimization to further enhance charge separation and catalytic efficiency. The development of visible-light-responsive systems and the scaling-up of photocatalytic reactors are essential steps toward practical implementation as mentioned for large scale solar power plants. Additionally, coupling photocatalytic systems with separation technologies may enable efficient recovery of value-added products, improving the overall economic feasibility of these developments.

8.1. Main Scientific Contributions

1. Successful noble-metal-free BiOX-TiO_2 heterostructures synthesis.
2. Demonstration of enhanced hydrogen evolution and high-value-added products formation from glycerol and glucose.

3. Efficient degradation of pharmaceuticals and other emerging contaminants.
4. Selective oxidation of aromatic alcohols to valuable aldehydes.
5. Development of TiO_2 nanotube photoelectrodes for photoelectrocatalysis.

8.2 Economic Viability

From an economic perspective, photocatalysts developed in this work present several advantages. The BiOX-TiO_2 heterostructures were prepared by using relatively inexpensive and commercially available precursors, avoiding the use of costly noble metals such as platinum, gold, or palladium. Consequently, these materials may represent a cost-effective alternative for large-scale photocatalytic applications. Nevertheless, a detailed techno-economic assessment considering synthesis costs, operational expenses, catalyst lifetime, and process efficiency would be necessary to fully evaluate their commercial feasibility.

8.3. Scale-Up and Practical Implementation

For perspectives of a practical implementation, the economic feasibility of photocatalytic technologies not only relies on photocatalytic activity but also on the lifetime of catalyst, its replacement frequency, reactor design, and requirements for operational energy. Recent techno-economic analyses have identified catalyst replacement intervals and electricity consumption as the major factors influencing the overall treatment cost of industrial-scale photocatalytic systems. Furthermore, advances in low-cost solar photoreactor designs have shown that efficient photon utilization and simplified reactor configurations can significantly reduce operational costs and improve the prospects for large-scale implementation. Therefore, future studies should include detailed techno-economic assessments considering precursor costs, catalyst regeneration requirements, long-term stability, and operational expenditures under realistic conditions. [276a]. Although the photocatalytic systems investigated in this work demonstrated promising performance at laboratory scale, further research is required to evaluate their applicability under pilot-scale and industrial conditions. The synthesis methods employed, including coprecipitation and ball-milling, are relatively simple and potentially scalable. Future studies should focus on the development of continuous-flow photocatalytic reactors, optimization of catalyst loading, light distribution, and mass transfer conditions, as well as the treatment of real wastewater matrices. Such investigations will provide valuable information regarding the practical implementation of these photocatalytic systems for environmental remediation and solar fuel production [317a].

In addition, although high degradation efficiency values were obtained for investigated pollutants, mineralization was assessed only for selected pharmaceutical contaminants, including tetracycline, oxytetracycline, and lincomycin, through TOC measurements. These evaluations provided valuable information regarding the extent of organic carbon removal during the photocatalytic process. However, for the other contaminants studied in this work, such as thiabendazole and carbamazepine, a more comprehensive evaluation of degradation intermediates and their potential toxicity would be beneficial. Although advanced oxidation processes can convert contaminants into carbon dioxide, water, and inorganic ions, intermediate transformation products may be generated during degradation pathways. Therefore, future investigations should focus on the identification of intermediate species and ecotoxicity assessments to confirm that photocatalytic treatment does not produce products with greater environmental risk than the parental compounds and achieves environmentally safe mineralization. Such studies would further reinforce the environmental consequence and practical applicability of the developed photocatalytic systems.

8.4. Catalyst Stability and Reusability

Catalyst stability and long-term reusability are crucial factors for the practical application of photocatalytic technologies. Although the photocatalysts investigated in this dissertation exhibited high activity under the studied experimental conditions, additional long-term cycling experiments would be beneficial to assess their durability under prolonged operation. Future investigations should evaluate possible structural modifications, surface deactivation phenomena, and catalyst recovery strategies after several repetitions. Such studies would contribute to a more comprehensive evaluation of the practical potential of the developed photocatalysts. The catalyst maintained high activity during recycling tests, indicating good structural stability. However, long-term stability over tens of cycles and pilot-scale operation remains to be investigated.

8.5. Future Industrial Perspectives

Future research should be focused

- Pilot-scale testing of the most active photocatalysts.
- Application in real wastewater treatment systems.
- Long-term stability and reusability assessment.
- Solar photoreactor design and optimization.
- Techno-economic evaluation for industrial implementation.

- Apparent Quantum Yield (APY) and energy-efficiency determination.

The energetic efficiency of the heterogeneous photocatalytic system can be determined by evaluating two quantities: (i) the rate of photon absorption (rpa) and (ii) the specific reaction rate (srr):

$$\text{rpa} = \frac{\text{number of absorbed photons}}{\text{time} \cdot \text{surface area}} \left[\frac{\text{Einstein}}{\text{s} \cdot \text{m}^2}\right]$$

$$\text{srr} = \frac{\text{number of reacted molecules}}{\text{time} \cdot \text{surface area}} \left[\frac{\text{moles}}{\text{s} \cdot \text{m}^2}\right]$$

Both these rates should be evaluated on the bases of the active sites but this last quantity is very difficult to determine experimentally, and then the BET surface area can be used as an approximated reference parameter. From the experimental determination of rpa and srr, the quantum efficiency (η) can be found and used to compare different conditions:

$$\eta = \frac{\text{number of reacted molecules}}{\text{number of absorbed photons}}$$

The number of absorbed photons was determined by neglecting the diffusion and/or reflection phenomena and considering only the photon emitted by the lamp (ϕ_i) and the photons transmited by the dispersion (ϕ_t). Then the absorbed photons (ϕ_a) can be calculated by the following equation:

$$\phi_a = \phi_i - \phi_t$$

In order to have the maximum exploit of the photons emitted by the lamp, the optimum amount of photocatalyst was determined by adding quantities of the powder in the reacting solution and measuring the transmitted flow at the external wall of the reactor. When the transmitted flow reached the 10% of the emitted one the value of the weight of the solid was chosen. A value not null of the transmitted flow assured us that all the catalyst was irradiated thus avoiding shielding effects.

ϕ_i was measured by filling the reactor with water and measuring, by means of a radiometer, its value at the external wall.

In this study, the amount of the different photocatalysts is such that the absorbed photons are the same. Then, it is not necessary to know the quantum efficiency to compare the performances of the different solids, the comparison between the reacted molecules (i.e. conversion) is sufficient.

Nevertheless, recent studies have highlighted that quantitative performance indicators such as AQY, photon utilization efficiency, quantum yield, radiation transport efficiency, and energy efficiency are essential for assessing the practical viability of photocatalytic systems. [317b].

REFERENCES

[1] K. E. Trenberth, A. Dai, G.V.D. Schrier, P. D. Jones, J. Barichivich, K. R. Briffa, J. Sheffield, Global warming and changes in drought, Nature Climate Change 4 (2004) 17-22. doi: 10.1038/nclimate2067.

[2] A. Kudo, Y. Misek, Heterogeneous photocatalyst materials for water splitting, Chemical Society Reviews 38.1 (2009) 253-278. doi: 10.1039/b800489g.

[3] K. Maeda, K. Domen, Photocatalytic water splitting: Recent progress and future challenges, Journal of Physical Chemistry Letters, 1 18 (2010) 2655-2661. doi: 10.1021/jz1007966.

[4] S. Chu, A. Majumdar, Opportunities and challenges for a sustainable energy future, Nature 488 (2012) 294-303. doi: 10.1038/nature11475.

[5] P. Friedlingstein, M.O. Sullivan, M.WJones, Global Carbon Budget, Earth System Science Data 14 (2022) 4811-4900, doi.org/10.5194/essd-14-4811-2022.

[6] A. Fujishima, K. Honda, Electrochemical Photolysis of Water at a Semiconductor Electrode, *Nature*, 238 (1972), 37-38.

[7] J. A. Turner, Sustainable hydrogen production, *Science* 305 (2004) 972–974. doi: 10.1126/science.1103197.

[8] M.A. Green, E.D. Dunlop, M.Yoshita, N.Kopidakis, K.Bothe, G.Siefer, X.Hao, Solar cell efficiency tables, Progress in Photovoltaics: Research and Applications, 31 (2023) 651-663. doi: 10.1002/pip.3726.

[9] N. S. Lewis, D. G. Nocera, *Powering the planet: Chemical challenges in solar energy utilization,* Proc. Natl. Acad. Sci. U.S.A. 103 (43) (2006) 15729-15735. doi: 10.1073/pnas.0603395103.

[10] X. Chen, S. Shen, L. Guo, S. S. Mao, Semiconductor-based photocatalytic hydrogen generation, Chemical Reviews 110 (2010) 6503-6570. doi: 10.1021/cr1001645.

[11] W. J. Ong, L. L. Tan, Y. H. Ng, S. T. Yong, S. P. Chai, Graphitic Carbon Nitride ($g\text{-}C_3N_4$)-Based Photocatalysts for Artificial Photosynthesis and Environmental Remediation: Are We a Step Closer to Achieving Sustainability, Chemical Reviews 116 (2016) 7159-7329. doi: 10.1021/acs.chemrev.6b00075.

[12] X. Liao , T.T Li, H.T Ren , X. Zhang, B. Shen, J. H. Lin , C. W. L. X. Liao, Construction of $BiOI/TiO_2$ flexible and hierarchical S-scheme heterojunction nanofibers membranes for visible-light-driven photocatalytic pollutants degradation, *Science of the Total Environment* 806 (2022). doi: 10.1016/j.scitotenv.2021.150698.

[13] R. Ahorsu, F. Medina, M. Constantí, Significance and challenges of biomass as a suitable feedstock for bioenergy and biochemical production: A review, *Energies (Basel)* 11 (2018). doi: 10.3390/EN11123366.

[14] M. Ventura, A. Marinas, M. E. Domine, Catalytic Processes for Biomass-Derived Platform Molecules Valorisation, *Top Catalysis* 63 846-865 (2020) 846-865. doi: 10.1007/s11244-020-01309-9.

[15] J. C. Serrano-Ruiz, R. Luque, A. Sepúlveda-Escribano, Transformations of biomass-derived platform molecules: From high added-value chemicals to fuels via aqueous-phase processing, Chemical Society Reviews 40 (2011) 5266-5281. doi: 10.1039/C1CS15131B.

[16] I. Dincer, Renewable energy and sustainable development: a crucial review, *Renewable and Sustainable Energy Reviews* 4 (2000) 157-175. doi: 10.1016/S1364-0321(99)00011-8.

[17] A. Speltini, M. Sturini, D. Dondi, E. Annovazzi, F. Maraschi, V. Caratto, A. Profumo, A. Buttafava, Sunlight-promoted photocatalytic hydrogen gas evolution from water-suspended cellulose: A systematic study, *Photochemical and Photobiological Sciences* 13 (2014) 1410-1419. doi: 10.1039/c4pp00128a.

[18] C. Li, H. Wang, S. B. Naghadeh, J. Z. Zhang, P. Fang, Visible light driven hydrogen evolution by photocatalytic reforming of lignin and lactic acid using one-dimensional NiS/CdS nanostructures, *Applied Cataysis B* 227 (2018) 229-239. doi: 10.1016/j.apcatb.2018.01.038.

[19] C. H. Zhou, X. Xia, C. X. Lin, D. S. Tong, J. Beltramini, Catalytic conversion of lignocellulosic biomass to fine chemicals and fuels, *ChemicalSociety Reviews* 40 (2011) 5588-5617. doi: 10.1039/c1cs15124j.

[20] M. Bellardita, V. Loddo, L. Palmisano, Formation of High Added Value Chemicals by Photocatalytic Treatment of Biomass, Mini-Reviews in Organic Chemistry 17 (2020) 884-901. doi: 10.2174/1570193x17666200131112856.

[21] F. W. Lichtenthaler and S. Peters, Carbohydrates as green raw materials for the chemical industry, *Comptes Rendus Chimie* 7 (2004) 65-90. doi: 10.1016/j.crci.2004.02.002.

[22] G. W. Huber, S. Iborra, A. Corma, Synthesis of transportation fuels from biomass: Chemistry, catalysts, and engineering, *Chemical Reviews* 106 (2006) 4044-4098. doi: 10.1021/cr068360d.

[23] A. V. Puga, Photocatalytic production of hydrogen from biomass-derived feedstocks, *Coordination Chemistry Reviews 315* (2016) 1-66. doi.org/10.1016/j.ccr.2015.12.009.

[24] V. Maslova, A. Fasolini, M. Offidani, S. Albonetti, F. Basile, Solar-driven valorization of glycerol towards production of chemicals and hydrogen, *Catalysis Today* 380 (2021) 147-155. doi: 10.1016/j.cattod.2021.03.008.

[25] C. M. Pecoraro, M. Bellardita, V. Loddo, F. Di Franco, L. Palmisano, M. Santamaria, A facile way to synthesize noble metal free TiO_2 based catalysts for glycerol photoreforming, *Journal of Industrial and Engineering Chemistry* 118 (2023) 247-258. doi: 10.1016/j.jiec.2022.11.010.

[26] C. M. Pecoraro, L. Mino, E. Kozyr, L. Palmisano, F. Di Franco, V. Loddo, M. Santamaria, M. Bellardita, Pt-TiO_2 catalysts for glycerol photoreforming: comparison of anatase, brookite and rutile polymorphs, *Chemical Communications* (2024). doi: 10.1039/d4cc00353e.

[27] V. Maslova, E. A. Quadrelli, P. Gaval, A. Fasolini, S. Albonetti, F. Basile, Highly dispersed ultrafine Pt nanoparticles on microemulsion-mediated TiO_2 for production of hydrogen and valuable chemicals via oxidative photo-dehydrogenation of glycerol, Journal of Environmental Chemical Engineering 9 (2021). doi: 10.1016/j.jece.2021.105070.

[28] C. Cotellessa, Glycolic acid and its use in dermatology, *Journal of the European Academy of Dermatology and Venereology* 5 (1995) 215-217. doi: 10.1016/0926-9959(95)00084-5.

[29] J. Sharad, Glycolic acid peel therapy - A current review, Clinical, Cosmetic and Investigational Dermatology (2013). doi: 10.2147/CCID.S34029.

[30] M. Umair, G. Palmisano, R. Al Sakkaf, S. Al Jitan, A. Pintar, G. Zerjav, L. Palmisano, V. Loddo, M. Bellardita, Pt-Nb_2O_5-TiO_2 based semiconductors for photoreforming of glucose and fructose aqueous solutions, Applied Surface Science 648 (2024). doi: 10.1016/j.apsusc.2023.159030.

[31] M. N. Catrinck, E. S. Ribeiro, R. S. Monteiro, R. M. Ribas, M. H. P. Barbosa, R. F. Teófilo, Direct conversion of glucose to 5-hydroxymethylfurfural using a mixture of niobic acid and niobium phosphate as a solid acid catalyst, *Fuel* 210 (2017). doi: 10.1016/j.fuel.2017.08.035.

[32] L. Da Vià, C. Recchi, E. O. Gonzalez-Yañez, T. E. Davies, J. A. Lopez-Sanchez, Visible light selective photocatalytic conversion of glucose by TiO_2 Applied *Catalysis B* 202 (2017) 81-288. doi: 10.1016/j.apcatb.2016.08.035.

[33] X. Xu, L. Shi, S. Zhang, Z. Ao, J. Zhang, S. Wang, H. Sun, Photocatalytic reforming of lignocellulose: A review, *Elsevier B.V.* (2023). doi: 10.1016/j.cej.2023.143972.

[34] G. Iervolino, V. Vaiano, J. J. Murcia, A. E. Lara, J. S. Hernández, H. Rojas, J. A. Navío, M. C. Hidalgo, Photocatalytic production of hydrogen and methane from glycerol reforming over Pt/TiO_2–Nb_2O_5, *International Journal of Hydrogen Energy* 46 (2021) 38678-38691. doi: 10.1016/j.ijhydene.2021.09.111.

[35] C. Yue, Y. Lin, J. Sang, Z. Li, P. Zhang, M. Fan, Y. Leng, P. Jiang, A. Haryono, BiOBr/$Bi_{24}O_{31}Br_{10}$ heterojunctions in situ prepared by microwave-assisted hydrothermal

method for aerobic oxidation of glycerol to formic acid, Materials Today Communications 31 (2022) 103270. doi: 10.1016/j.mtcomm.2022.103270.

[36] G. C. de Assis, I. M. A. Silva, T. G. dos Santos, T. V. dos Santos, M. R. Meneghetti, S. M. P. Meneghetti, Photocatalytic processes for biomass conversion, *Royal Society of Chemistry* (2021). doi: 10.1039/d0cy02358b.

[37] M. R. Karimi Estahbanati, M. Feilizadeh, F. Attar, and M. C. Iliuta, "Current Developments and Future Trends in Photocatalytic Glycerol Valorization: Photocatalyst Development," Industrial & Engineering Chemistry Research 59 (2020) 22330-22352. doi: 10.1021/acs.iecr.0c04765.

[38] L. Zhang, C. (Charles) Xu, and P. Champagne, Overview of recent advances in thermo-chemical conversion of biomass, *Energy Convers. Manag* (2010) 51 969-982. doi: 10.1016/J.ENCONMAN.2009.11.038.

[39] K. Nakata and A. Fujishima, TiO_2 photocatalysis: Design and applications, *Journal of Photochemistry and Photobiology C: Photochemistry Reviews* 13 (2012) 169-189. doi: 10.1016/j.jphotochemrev.2012.06.001.

[40] M. Pelaez, N. T. Nolan, S. C. Pillai, M. K. Seery, P. Falaras, A. G. Kontos, P. S. M. Dunlop, J. W. J. Hamilton, J. A. Byrne, K. O'Shea, M. H. Entezari, D. D. Dionysiou, A review on the visible light active titanium dioxide photocatalysts for environmental applications, *Applied Catalysis B: Environmental* 125 (2012) 331-349. doi: 10.1016/j.apcatb.2012.05.036.

[41] U. I. Gaya, A. H. Abdullah, Heterogeneous photocatalytic degradation of organic contaminants over titanium dioxide: A review of fundamentals, progress and problems, *Journal of Photochemistry and Photobiology C: Photochemistry Reviews* 9 (2008) 1-12. doi: 10.1016/j.jphotochemrev.2007.12.003.

[42] W. W. Lee, C. Lu, C. Chuang, Y. Chen, J. Fu, C. Siao, C. Chen, *Synthesis of bismuth oxyiodides and their composites: Characterization, photocatalytic activity, and degradation mechanisms*, RSC Advances 5 (2015) 23450-23463. https://doi.org/10.1039/c4ra15072d

[43] C.-H. Ho, C.-H. Chan, Y.-S. Huang, L.C. Tien, L.C. Chao, The study of optical band edge property of bismuth oxide nanowires α-Bi_2O_3, *Opt. Express* 21 (2013) 11965. doi: 10.1364/oe.21.011965.

[44] X. Wei, M. U. Akbar, A. Raza, G. Li, A review on bismuth oxyhalide based materials for photocatalysis, *Royal Society of Chemistry (2021)*. doi: 10.1039/d1na00223f.

[45] Z. Chen, J. Xu, Z. Ren, Y. He, G. Xiao, Low temperature synthesis of $ZnIn_2S_4$ microspheres as a visible light photocatalyst for selective oxidation, *Catal. Commun*41 (2013) 83-86. doi: 10.1016/j.catcom.2013.07.016.

[46] A. M. Djaballah, M. Bellardita, V. Loddo, L. Palmisano, F. Parrino, Facile preparation of $CuBi2O_4/TiO_2$ hetero-systems employed for simulated solar-light selective oxidation of 4-methoxybenzyl alcohol model compound, *Mol. Catal.* 546 (2023) 113251. doi: 10.1016/j.mcat.2023.113251.

[47] J. Low, J. Yu, M. Jaroniec, S. Wageh, A. A. Al-Ghamdi, Heterojunction Photocatalysts, *Wiley-VCH Verlag (2017)* . doi: 10.1002/adma.201601694.

[48] J. Duan, H. Zhao, Z. Zhang, W. Wang, The Z-scheme heterojunction between TiO_2 nanotubes and Cu_2O nanoparticles mediated by Ag nanoparticles for enhanced photocatalytic stability and activity under visible light, *Ceram. Int* 44 (2018) 22748-22759. doi: 10.1016/j.ceramint.2018.09.062.

[49] A. Henríquez, H. D. Mansilla, A. Martínez–de la Cruz, L. Cornejo-Ponce, E. Schott, D. Contreras, "Selective oxofunctionalization of cyclohexene over titanium dioxide-based and bismuth oxyhalide photocatalysts by visible light irradiation, *Catalysts* 10 (2020) 1-14. doi: 10.3390/catal10121448.

[50] A. Shoja, A. Habibi-Yangjeh, M. Mousavi, and S. Ghosh, BiOBr and BiOCl decorated on TiO_2 QDs: Impressively increased photocatalytic performance for the degradation of pollutants under visible light, *Advanced Powder Technology* (2020) 31 3582-3596. doi: 10.1016/j.apt.2020.07.002.

[51] S. Juntrapirom, N. Chanlek, P. Kidkhunthod, S. Namuangruk, M. Chareonpanich, T. Limtrakul, Natural sunlight driven photocatalytic coupling of primary amines over TiO_2/BiOBr heterojunction, *Appl. Surf. Sci.* 545 (2021) 149015. doi: 10.1016/j.apsusc.2021.149015.

[52] R. Fiorenza, M. Bellardita, T. Barakat, S. Scirè, L. Palmisano, Visible light photocatalytic activity of macro-mesoporous TiO_2-CeO_2 inverse opals, *J. Photochem. Photobiol. A Chem.* 352 (2018) 25-34, Feb. doi: 10.1016/j.jphotochem.2017.10.052.

[53] S. Meng, W. Sun, S. Zhang, X. Zheng, X. Fu, S. Chen, Insight into the Transfer Mechanism of Photogenerated Carriers for WO_3/TiO_2 Heterojunction Photocatalysts: Is It the Transfer of Band-Band or Z-Scheme? Why, *Journal of Physical Chemistry C* 122, 46 (2018) 26326-26336. doi: 10.1021/acs.jpcc.8b07524.

[54] S. Lv, Y. Wang, Y. Zhou, Q. Liu, C. Song, D. Wang, *Oxygen vacancy stimulated direct Z-scheme of mesoporous Cu_2O/TiO_2 for enhanced photocatalytic hydrogen production from water and seawater*, J. Alloys Compd. 868 (2021) 159144. doi: 10.1016/j.jallcom.2021.159144.

[55] J. Li, Y. Yu, L. Zhang, *Bismuth oxyhalide nanomaterials: Layered structures meet photocatalysis*, Nanoscale 6 (15) (2014) 8473–8488. doi: 10.1039/c4nr02553aJ.

[56] J. Liu, J. Shi, H. Deng, *Current status of research on BiOX-based heterojunction photocatalytic systems: Synthesis methods, photocatalytic applications and prospects*, J. Environ. Chem. Eng. (2023) 110311.

[57] C. Y. Wang, X. Zhang, H. Q. Yu, *Bismuth oxyhalide photocatalysts for water purification: Progress and challenges*, Coord. Chem. Rev. (2023) 215339. doi: 10.1016/j.ccr.2023.215339.

[58] X. Zhang, Z. Ai, F. Jia, L. Zhang, *Generalized one-pot synthesis, characterization, and photocatalytic activity of hierarchical BiOX (X = Cl, Br, I) nanoplate microspheres*, J. Phys. Chem.C112(3) (2008)747-753. doi: 10.1021/jp077471t.

[59] S. Song, Z. Xing, H. Zhao, Z. Li, W. Zhou, *Recent advances in bismuth-based photocatalysts: Environment and energy applications*, Green Energy Environ. (2023). doi: 10.1016/j.gee.2022.04.004.

[60] H. Li, X. Cheng, Y. Dong, Z. Xu, J. Wang, and others, Recent advances in the application of bismuth-based catalysts for degrading environmental emerging organic contaminants through photocatalysis, *Journal of Environmental Chemical Engineering* 11 (2023) 110371. https://doi.org/10.1016/j.jece.2023.110371

[61] K. L. Zhang, C. M. Liu, F. Q. Huang, C. Zheng, W. D. Wang, *Study of the electronic structure and photocatalytic activity of the BiOCl photocatalyst*, Appl. Catal. B 68 (3–4) (2006) 125-129. doi: 10.1016/j.apcatb.2006.08.002.

[62] Q. Li, J. Zhang, W. Xu, H. Wang, J. Zhou, Q. Chen, J. Chen, D. Chen, Oxygen vacancies mediated flower-like BiOX microspheres for photocatalytic purification of methyl mercaptan odor: Significant distinction induced by halogen elements, *Chem. Eng. J.* 471 (2023) 144658. https://doi.org/10.1016/j.cej.2023.144658

[63] T. Jiang, J. Li, Z. Sun, X. Liu, T. Lu, L. Pan, *Reduced graphene oxide as co-catalyst for enhanced visible light photocatalytic activity of BiOBr*, Ceram. Int. 42 (15) (2016) 16463-16468. doi: 10.1016/j.ceramint.2016.06.079.

[64] Q. Li, X. Zhao, J. Yang, C. J. Jia, Z. Jin, W. Fan, *Exploring the effects of nanocrystal facet orientations in g-C_3N_4/BiOCl heterostructures on photocatalytic performance*, Nanoscale 7 (45) (2015) 18971-18983. doi: 10.1039/c5nr05154a.

[65] W. Li, X. Zhang, Y. Wang, Z. Li, Novel BiOCl/ TiO_2 hierarchical composites: Synthesis, characterization and application on photocatalysis, Appl. Catal. A Gen. 516 (2016) 81-89. doi: 10.1016/j.apcata.2016.02.006.

[66] G. Zhao, A. S. Pedersen, Life Cycle Assessment of Hydrogen Production and Consumption in an Isolated Territory, Procedia CIRP 69 (2018) 529-533. doi: 10.1016/j.procir.2017.11.100.

[67] R. Bhandari, C. A. Trudewind, P. Zapp, Life cycle assessment of hydrogen production via electrolysis-A review, J. Clean. Prod. 85 (2014) 151-163. doi: 10.1016/j.jclepro.2013.07.048.

[68] M. Voldsund, K. Jordal, R. Anantharaman, Hydrogen production with CO_2 capture, Int. J. Hydrogen Energy 41 (2016) 4969-4992. doi: 10.1016/j.ijhydene.2016.01.009.

[69] G. Glenk, S. Reichelstein, Economics of converting renewable power to hydrogen, Nat. Energy 4 (2019) 216-222. doi: 10.1038/s41560-019-0326-1.

[70] P. Friedlingstein et al., Update on CO_2 emissions, Nat. Geosci. 3 (2010) 811-812. doi: 10.1038/ngeo1022.

[71] M. Raugei, Net energy analysis must not compare apples and oranges, Nat. Energy 4 (2019) 86-88. doi: 10.1038/s41560-019-0327-0.

[72] S. Nishioka, F. E. Osterloh, X. Wang, T. E. Mallouk, K. Maeda, Photocatalytic water splitting, Nat. Rev. Methods Primers 3 (2023) 1-15. doi: 10.1038/s43586-023-00226-x.

[73] R. D. Tentu, S. Basu, Photocatalytic water splitting for hydrogen production, Curr. Opin. Electrochem. 5 (2017) 56-62. doi: 10.1016/j.coelec.2017.10.019.

[74] C. Bie, L. Wang, J. Yu, Challenges for photocatalytic overall water splitting, Chem 8 (2022) 1567-1574. doi: 10.1016/j.chempr.2022.04.013.

[75] P. McKendry, Energy production from biomass (Part 1): Overview of biomass, Bioresour. Technol. 83 (2002) 37-46.

[76] X. He, T. Kai, P. Ding, Heterojunction photocatalysts for degradation of the tetracycline antibiotic: A review, Environ. Sci. Pollut. Res. 28 (2021) 1-19. doi: 10.1007/s10311-021-01295-8.

[77] X. Meng et al., Microporous nano-MgO/diatomite ceramic membrane with high positive surface charge for tetracycline removal, J. Hazard. Mater. 320 (2016) 495-503. doi: 10.1016/j.jhazmat.2016.08.068.

[78] Z. Li, C. Guo, J. Lyu, Z. Hu, M. Ge, Tetracycline degradation by persulfate activated with magnetic Cu/$CuFe_2O_4$ composite: Efficiency, stability, mechanism and degradation pathway, J. Hazard. Mater. 373 (2019) 85-96. doi: 10.1016/j.jhazmat.2019.03.075.

[79] Y. Han et al., Removal of veterinary antibiotics from swine wastewater using anaerobic and aerobic biodegradation, Sci. Total Environ. 709 (2020) 136094. doi: 10.1016/j.scitotenv.2019.136094.

[80] F. E. Osterloh, Inorganic materials as catalysts for photochemical splitting of water, Chemical Society Reviews 42 (2013) 2294–2320. doi.org/10.1039/c2cs35266d.

[81] M. Bellardita, E. I. García-López, G. Marcì, L. Palmisano, Photocatalytic formation of H_2 and value-added chemicals in aqueous glucose (Pt)-TiO_2 suspension, Int. J. Hydrogen Energy 41 (2016) 5934-5947. doi: 10.1016/j.ijhydene.2016.02.103.

[82] M. Bellardita, E. I. García-López, G. Marcì, G. Nasillo, L. Palmisano, Photocatalytic solar light H_2 production by aqueous glucose reforming, Eur. J. Inorg. Chem. (2018) 4522-4532. doi: 10.1002/ejic.201800663.

[83] L. Xiong, J. Tang,Strategies and challenges on selectivity of photocatalytic organic synthesis toward high-value chemicals, Advanced Energy Materials, 2021, Article 2003216.DOI: 10.1002/aenm.202003216.

[84] R. Shen, J. Xie, Q. Xiang, X. Chen, J. Jiang, X. Li, Ni-based photocatalytic H_2-production cocatalysts, Chin. J. Catal. 40 (2019) 240-288. doi: 10.1016/S1872-2067(19)63294-8.

[85] R. Singh, S. Dutta, A review on H_2 production through photocatalytic reactions using TiO_2-based catalysts, Fuel 220 (2018) 607-620. doi: 10.1016/j.fuel.2018.02.068.

[86] K. C. Christoforidis, P. Fornasiero, Photocatalytic hydrogen production: A rift into the future energy supply, ChemCatChem 9 (2017) 1523-1544. doi: 10.1002/cctc.201601659.

[87] C. M. Pecoraro, M. Bellardita, V. Loddo, D. Virtù, F. Di Franco, M. Santamaria, Photocatalytic and photoelectrocatalytic H_2 evolution combined with valuable furfural production, Appl. Catal. A Gen. 650 (2023) 118987. doi: 10.1016/j.apcata.2022.118987.

[88] B. A. Pinaud et al., Technical and economic feasibility of centralized facilities for solar hydrogen production via photocatalysis and photoelectrochemistry, Energy Environ. Sci. 6 (2013) 1983-2002. doi: 10.1039/c3ee40831k.

[89] K. Sivula, R. van de Krol, Semiconducting materials for photoelectrochemical energy conversion, Nature Reviews Materials 1 (2016) 15010. doi.org/10.1038/natrevmats.2015.10

[90] A. Mills, S. Le Hunte, An overview of semiconductor photocatalysis, J. Photochem. Photobiol. A Chem. 108 (1997) 1-35. doi: 10.1016/S1010-6030(97)00118-4.

[91] D. Kong et al., Recent advances in visible light-driven water oxidation and reduction in suspension systems, Mater. Today 21 (2018) 897-924. doi: 10.1016/j.mattod.2018.04.009.

[92] Z. K. Shen, Y. J. Yuan, L. Pei, Z. T. Yu, Z. Zou, Black phosphorus photocatalysts for photocatalytic H_2 generation: A review, Chem. Eng. J. 386 (2020) 123997. doi: 10.1016/j.cej.2019.123997.

[93] X. Chen, S. S. Mao, Titanium dioxide nanomaterials: Synthesis, properties, modifications and applications, Chem. Rev. 107 (2007) 2891-2959. doi: 10.1021/cr0500535.

[94] R. Mu, Z. J. Zhao, Z. Dohnálek, J. Gong, Structural motifs of water on metal oxide surfaces, Chem. Soc. Rev. 46 (2017) 1785-1806. doi: 10.1039/c6cs00864j.

[95] A. L. Linsebigler, G. Lu, and J. T. Yates Jr., "Photocatalysis on TiO_2 surfaces: Principles, mechanisms, and selected results," *Chemical Reviews*, vol. 95, no. 3, pp. 735–758, 1995. **DOI:** 10.1021/cr00035a013

[96] K. Hashimoto, H. Irie, A. Fujishima, TiO_2 photocatalysis: A historical overview and future prospects, Jpn. J. Appl. Phys. 44 (2005) 8269-8285. doi: 10.1143/JJAP.44.8269.

[97] H. Dong et al., An overview on limitations of TiO_2-based particles for photocatalytic degradation of organic pollutants and the corresponding countermeasures, Water Res. 79 (2015) 128-146. doi: 10.1016/j.watres.2015.04.038.

[98] C. Thambiliyagodage, L. Usgodaarachchi, Photocatalytic activity of N, Fe and Cu co-doped c nanoparticles under sunlight, Curr. Res. Green Sustain. Chem. 4 (2021) 100186. doi: 10.1016/j.crgsc.2021.100186.

[99] A. Makdee, P. Unwiset, K. C. Chanapattharapol, P. Kidkhunthod, Effects of Ce addition on the properties and photocatalytic activity of TiO_2 investigated by X-ray absorption spectroscopy, Mater. Chem. Phys. 213 (2018) 431-443. doi: 10.1016/j.matchemphys.2018.04.016.

[100] J. Yan, G. Wu, N. Guan, L. Li, Nb_2O_5/TiO_2 heterojunctions: Synthesis strategy and photocatalytic activity, Appl. Catal. B 152-153 (2014) 280-288. doi: 10.1016/j.apcatb.2014.01.049.

[101] J. Surmacki, P. Wroński, M. Szadkowska-Nicze, H. Abramczyk, Raman spectroscopy of visible-light photocatalyst-Nitrogen-doped titanium dioxide generated by irradiation with electron beam, Chem. Phys. Lett. 566 (2013) 54-59. doi: 10.1016/j.cplett.2013.02.066.

[102] F. Le Formal, S. R. Pendlebury, M. Cornuz, S. D. Tilley, M. Grätzel, J. R. Durrant, Back electron-hole recombination in hematite photoanodes for water splitting, J. Am. Chem. Soc. 136 (6) (2014) 2564-2574. doi: 10.1021/ja412058x.

[103] H. Du, Y. N. Liu, C. C. Shen, A. W. Xu, Nanoheterostructured photocatalysts for improving photocatalytic hydrogen production, Chin. J. Catal. (2017). doi: 10.1016/S1872-2067(17)62866-3.

[104] K. Qi, B. Cheng, J. Yu, W. Ho, A review on TiO_2-based Z-scheme photocatalysts, Chin. J. Catal. (2017). doi: 10.1016/S1872-2067(17)62962-0.

[105] Y. Wang, Z. Ding, N. Arif, W. C. Jiang, Y. J. Zeng, 2D material based heterostructures for solar light driven photocatalytic H_2 production, Mater. Adv. (2022). doi: 10.1039/d2ma00191h.

[106] P. Zhou, J. Yu, M. Jaroniec, All-solid-state Z-scheme photocatalytic systems, Adv. Mater. (2014). doi: 10.1002/adma.201400288.

[107] K. Maeda, Z-scheme water splitting using two different semiconductor photocatalysts, ACS Catal. 3 (7) (2013) 1486-1503. doi: 10.1021/cs4002089.

[108] M. Bellardita, V. Loddo, V. Augugliaro, L. Palmisano, S. Yurdakal, Exploring the photothermo-catalytic performance of brookite TiO_2-CeO_2 composites, Catalysts 10 (7) (2020). doi: 10.3390/catal10070765.

[109] J. Low, C. Jiang, B. Cheng, S. Wageh, A. A. Al-Ghamdi, J. Yu, A review of direct Z-scheme photocatalysts, Small Methods (2017). doi: 10.1002/smtd.201700080.

[110] L. Zhang, J. Zhang, H. Yu, J. Yu, Emerging S-scheme photocatalyst, Adv. Mater. (2022). doi: 10.1002/adma.202107668.

[111] Q. Xu, L. Zhang, B. Cheng, J. Fan, J. Yu, S-scheme heterojunction photocatalyst, Chem (2020). doi: 10.1016/j.chempr.2020.06.010.

[112] X. Wang, Y. Ma, X. Chen, H. Yu, and J. Yu, *A review of step-scheme photocatalysts,* Applied Materials Today 27 (2022) 101609. doi.org/10.1016/j.apmt.2022.101609

[113] V. Loddo, L. Palmisano, M. Bellardita, Environmental Applications of Light-Activated Processes, Elsevier, 2025. doi: 10.1016/B978-0-443-15742-4.00003-X.

[114] M. Bowker, L. Gilbert, J. Counsell, C. Morgan, Dehydrogenation versus decarbonylation of oxygenates on Pd (110): Pure, clean Pd is a poor catalyst, J. Phys. Chem. C 114 (40) (2010) 17142-17147. doi: 10.1021/jp104837t.

[115] S. Cao, C. J. Wang, W. F. Fu, Y. Chen, Metal phosphides as co-catalysts for photocatalytic and photoelectrocatalytic water splitting, ChemSusChem 10 (22) (2017) 4306-4323. doi: 10.1002/cssc.201701450.

[116] R. Shen et al., Carbon nanotube-supported Cu_3P as high-efficiency and low-cost cocatalysts for semiconductor-free photocatalytic H_2 evolution, ACS Sustain. Chem. Eng. 7 (3) (2019) 3243-3250. doi: 10.1021/acssuschemeng.8b05185.

[117] X. Lu, J. Xie, S. Y. Liu, A. Adamski, X. Chen, X. Li, Low-cost Ni_3B/Ni $(OH)_2$ as ecofriendly hybrid cocatalyst for boosting photocatalytic H_2 production over g-C_3N_4 nanosheets, ACS Sustain. Chem. Eng. 6 (10) (2018) 13140-13150. doi: 10.1021/acssuschemeng.8b02653.

[118] R. Shen, J. Xie, P. Guo, L. Chen, X. Chen, X. Li, Bridging g-C_3N_4 nanosheets and CuS cocatalysts for durable photocatalytic H_2 production, ACS Appl. Energy Mater. 1 (5) (2018) 2232-2241. doi: 10.1021/acsaem.8b00311.

[119] S. Cao, L. Piao, X. Chen, Emerging photocatalysts for hydrogen evolution, Trends Chem. 2 (1) (2020) 57-70. doi: 10.1016/j.trechm.2019.06.009.

[120] S. Chaturvedi, P. N. Dave, Photocatalytic hydrogen production, Mater. Sci. Forum 764 (2013) 151-168. doi: 10.4028/www.scientific.net/MSF.764.151.

[121] A. Pajares, Y. Wang, M. J. Kronenberg, P. Ramírez de la Piscina, N. Homs, Photocatalytic H_2 production from ethanol using TiO_2 with tungsten carbide cocatalyst, Int. J. Hydrogen Energy 45 (40) (2020) 20558-20567. doi: 10.1016/j.ijhydene.2020.04.010.

[122] M. Serhan, M. Sprowls, D. Jackemeyer, N. Long, M. Perez, G. M. M. M. N. N. G. H. A. K. R. B. H. L. J. M. H. M. A. H. S. H. S. B., Total iron measurement in human serum with a smartphone, AIChE Annual Meeting Proceedings (2019). doi: 10.1039/x0xx00000x.

[123] C. W. Huang, B. S. Nguyen, D. V. N. Vo, S. Nanda, V. H. Nguyen, Photocatalytic reforming for sustainable hydrogen production over titania-based photocatalysts, Elsevier, 2020. doi: 10.1016/B978-0-12-819553-6.00008-8.

[124] J. P. Jeon, D. H. Kweon, B. J. Jang, M. J. Ju, J. B. Baek, Enhancing the photocatalytic activity of TiO_2 catalysts, Adv. Sustain. Syst. (2020). doi: 10.1002/adsu.202000197.

[125] M. A. Fox, M. T. Dulay, Heterogeneous photocatalysis, Chem. Rev. 93 (1) (1993) 341-357. doi: 10.1021/cr00017a016.

[126] M. J. Muñoz-Batista, R. Luque, Heterogeneous photocatalysis, ChemEngineering 5 (2) (2021) 26. doi: 10.3390/chemengineering5020026.

[127] M. Bellardita, V. Loddo, V. Augugliaro, L. Palmisano, S. Yurdakal, Selective photocatalytic and photoelectrocatalytic synthesis of valuable compounds, Catal. Today 432 (2024) 114587. doi: 10.1016/j.cattod.2024.114587.

[128] A. J. Nozik, Photoelectrochemical cells, Int. Telemetering Conf. Proc. (1978) 6-12.

[129] D. A. Tryk, A. Fujishima, K. Honda, Recent topics in photoelectrochemistry, Electrochim. Acta 45 (15–16) (2000) 2363-2376. doi: 10.1016/S0013-4686(00)00337-6.

[130] G. G. Bessegato, T. T. Guaraldo, J. F. de Brito, M. F. Brugnera, M. V. B. Zanoni, Achievements and trends in photoelectrocatalysis, Electrocatalysis 6 (5) (2015) 415-441. doi: 10.1007/s12678-015-0259-9.

[131] P. Lianos, Review of recent trends in photoelectrocatalytic conversion of solar energy, Appl. Catal. B 210 (2017) 23-254. doi: 10.1016/j.apcatb.2017.03.067.

[132] T. Yao, X. An, H. Han, J. Q. Chen, C. Li, Photoelectrocatalytic materials for solar water splitting, Adv. Energy Mater. 8 (21) (2018). doi: 10.1002/aenm.201800210.

[133] P. Alulema-Pullupaxi et al., Fundamentals and applications of photoelectrocatalysis for pollutant removal, Chemosphere 281 (2021). doi: 10.1016/j.chemosphere.2021.130821.

[134] M. H. Khan, H. Muslim, J. Karim, J. Ali, R. Ahmad, M. Muzaffar, M. Muzaffar, K. Gul, A. Abubakar, Photoelectrocatalytic synthesis of hybrid organic–inorganic nanomaterials for sustainable energy and CO_2 conversion, Haya Saudi J Life Sci 10 (2025) 744–764. doi: 10.36348/sjls. 2025.v10i11.007.

[135] A. Dey, F. A. Houle, M. Sevilla, W. J. Shaw, C. E. Lubner, Renewable energy, Chem. Commun. (2021).

[136] V. Loddo, M. Bellardita, G. Camera Roda, L. Palmisano, F. Parrino, Water depollution by advanced oxidation technologies, in: A.A. Inamuddin (Ed.), *Sustainable Green Chemical Processes and their Allied Applications*, Springer, 2020, pp. 501–537. https://doi.org/10.1007/978-3-030-42284-4_22

[137] R. Changotra, H. Rajput, A. Dhir, Natural soil mediated photo-Fenton processes for pharmaceuticals removal, Chemosphere 188 (2017) 345-353. doi: 10.1016/j.chemosphere.2017.09.016.

[138] B. A. Wols, C. H. M. Hofman-Caris, D. J. H. Harmsen, E. F. Beerendonk, Degradation of pharmaceuticals by UV/H_2O_2, Water Res. 47 (15) (2013) 5876-5888. doi: 10.1016/j.watres.2013.07.008.

[139] J. Wang, L. Chu, L. Wojnárovits, E. Takács, Occurrence and fate of antibiotics in wastewater treatment plants, Sci. Total Environ. 744 (2020) 140997. doi: 10.1016/j.scitotenv.2020.140997.

[140] J. Wang, S. Wang, Removal of pharmaceuticals and personal care products from wastewater, J. Environ. Manage. 182 (2016) 620-640. doi: 10.1016/j.jenvman.2016.07.049.

[141] S. Jodeh, F. Abdelwahab, N. Jaradat, I. Warad, W. Jodeh, Adsorption of diclofenac using activated carbon, J. Assoc. Arab Univ. Basic Appl. Sci. 20 (2016) 32-38. doi: 10.1016/j.jaubas.2014.11.002.

[142] P. H. Roberts, K. V. Thomas, Occurrence of pharmaceuticals in wastewater effluent, Sci. Total Environ. 356 (2006) 143-153. doi: 10.1016/j.scitotenv.2005.04.031.

[143] R. Mirzaei et al., Occurrence of antibiotics in water environments, Sci. Total Environ. 619–620 (2018) 446-459. doi: 10.1016/j.scitotenv.2017.07.272.

[144] R. K. Szabó, C. S. Megyeri, E. Illés, K. Gajda-Schrantz, P. Mazellier, A. Dombi, Phototransformation of ibuprofen and ketoprofen, Chemosphere 84 (11) (2011) 1658-1663. doi: 10.1016/j.chemosphere.2011.05.012.

[145] H. T. T. Tran et al., Photocatalytic performance of brookite vs anatase and rutile, Appl. Catal. B 200 (2017) 647-658. doi: 10.1016/j.apcatb.2016.07.017.

[146] W. Liu, N. B. Sutton, H. H. M. Rijnaarts, A. A. M. Langenhoff, Anaerobic biodegradation of pharmaceuticals, J. Hazard. Mater. 388 (2020) 119361. doi: 10.1016/j.jhazmat.2018.04.078.

[147] N. Taoufik, A. Elmchaouri, F. Anouar, S. A. Korili, A. Gil, TiO_2-coated activated carbon for emerging contaminants removal, J. Water Process Eng. 31 (2019). doi: 10.1016/j.jwpe.2019.100876.

[148] D. I. De Souza, E. M. Dottein, A. Giacobbo, M. A. S. Rodrigues, M. N. De Pinho, A. M. Bernardes, Nanofiltration for norfloxacin removal, J. Environ. Chem. Eng. 6 (5) (2018) 6147-6153. doi: 10.1016/j.jece.2018.09.034.

[149] L. N. Nguyen, F. I. Hai, J. A. McDonald, S. J. Khan, W. E. Price, L. D. Nghiem, Transformation of pharmaceuticals in membrane bioreactors, Water Sci. Technol. 76 (7) (2017) 1816-1826. doi: 10.2166/wst.2017.331.

[150] N. Taoufik, W. Boumya, M. Achak, M. Sillanpää, N. Barka, Advanced oxidation processes for pharmaceutical removal, J. Environ. Manage. 288 (2021). doi: 10.1016/j.jenvman.2021.112404.

[151] S. Wu, X. Li, Y. Tian, Y. Lin, Y. H. Hu, Excellent photocatalytic degradation of tetracycline over black anatase-TiO_2 under visible light, Chemical Engineering Journal 406 (2021) 126747. doi: 10.1016/j.cej.2020.126747.

[152] A. H. Khan, N. A. Khan, S. Ahmed, A. Dhingra, C. P. Singh, S. U. Khan, I. Ali, Application of advanced oxidation processes followed by different treatment technologies for hospital wastewater treatment, Journal of Cleaner Production 269 (2020) 122411. doi: 10.1016/j.jclepro.2020.122411.

[153] N. Abdel-Raouf, A. A. Al-Homaidan, I. B. M. Ibraheem, Microalgae and wastewater treatment, Saudi Journal of Biological Sciences 19 (2012) 257-275. doi: 10.1016/j.sjbs.2012.04.005.

[154] T. Zhang, Y. Liu, Y. Rao, X. Li, D. Yuan, S. Tang, Q. Zhao, Enhanced photocatalytic activity of TiO_2 with acetylene black and persulfate for degradation of tetracycline hydrochloride under visible light, Chemical Engineering Journal 384 (2020) 123350. doi: 10.1016/j.cej.2019.123350.

[155] K. Ayoub, E. D. van Hullebusch, M. Cassir, A. Bermond, Application of advanced oxidation processes for TNT removal: A review, Journal of Hazardous Materials 178 (2010) 10-28. doi: 10.1016/j.jhazmat.2010.02.042.

[156] M. Klavarioti, D. Mantzavinos, D. Kassinos, Removal of residual pharmaceuticals from aqueous systems by advanced oxidation processes, Environment International 35 (2009) 402-417. doi: 10.1016/j.envint.2008.07.009.

[157] M. A. Rauf, S. S. Ashraf, Fundamental principles and application of heterogeneous photocatalytic degradation of dyes in solution, Chemical Engineering Journal 151 (2009) 10-18. doi: 10.1016/j.cej.2009.02.026.

[158] I. M. F. Cardoso, R. M. F. Cardoso, J. C. G. Esteves da Silva, Advanced oxidation processes coupled with nanomaterials for water treatment, Nanomaterials 11 (2021) 2045. doi:10.3390/nano11082045.

[159] P. Calza, S. Baudino, R. Aigotti, C. Baiocchi, E. Pelizzetti, Ion trap tandem mass spectrometric identification of thiabendazole phototransformation products on titanium dioxide, Journal of Chromatography A 984 (2003) 59-66. doi: 10.1016/S0021-9673(02)01837-X.

[160] Z. Marín, D. Rojas, I. F. Pérez, J. A. Santaballa, M. Canle, Phototransformation of the aqueous fungicide thiabendazole by direct photolysis and heterogeneous photocatalysis, Industrial & Engineering Chemistry Research 64 (2025) 11624-11629. doi: 10.1021/acs.iecr.4c04696.

[161] R. Ibarz, A. Garvín, K. Aguilar, A. Ibarz, Kinetic study and modelling of the UV photo-degradation of thiabendazole, Food Research International 81 (2016) 133-140. doi: 10.1016/j.foodres.2015.12.014.

[162] D. B. Soro, D. L. Kouadio, K. N. Aboua, M. Diarra, L. Meite, K. S. Traore, Dégradation photocatalytique du thiabendazole en solution aqueuse, Afrique Science 14 (2018) 55-63.

[163] N. Nair, V. Gandhi, A. Shukla, S. Ghotekar, Mechanisms in the photocatalytic degradation of pesticide molecules over TiO_2-based photocatalysts: A review. Journal of Physics: Condensed Matter 36 (2024) doi: 10.1088/1361-648X/ad5fd6.

[164] X. Gao, X. Zhang, Y. Wang, S. Peng, B. Yue, C. Fan, Photocatalytic degradation of carbamazepine using hierarchical BiOCl microspheres: Some key operating parameters, degradation intermediates and reaction pathway, Chemical Engineering Journal 273 (2015) 156-165. doi: 10.1016/j.cej.2015.03.063.

[165] M. Wang, B. Zhang, J. Wang, C. Cai, Y. Xin, H. Liu, Degradation of lincomycin in aqueous solution with hydrothermal treatment: Kinetics, pathway, and toxicity evaluation, Chemical Engineering Journal 343 (2018) 138-145. doi: 10.1016/j.cej.2018.03.008.

[166] X. Zhu, X. Wang, L. Wang, X. Fan, X. Li, Y. Jiang, Biodegradation of lincomycin in wastewater by two-level bio-treatment using chloroperoxidase and activated sludge: Degradation route and eco-toxicity evaluation, Environmental Technology & Innovation 20 (2020) 101114. doi: 10.1016/j.eti.2020.101114.

[167] L. Li, J. Sun, B. Liu, D. Zhao, J. Ma, H. Deng, Y. Liu, Quantification of lincomycin resistance genes associated with lincomycin residues in waters and soils adjacent to representative swine farms in China, Frontiers in Microbiology 4 (2013) 1-9. doi: 10.3389/fmicb.2013.00364.

[168] X. Huang, J. Zheng, C. Liu, L. Liu, Y. Liu, H. Fan, Removal of antibiotics and resistance genes from swine wastewater using vertical flow constructed wetlands: Effect of hydraulic flow direction and substrate type, Chemical Engineering Journal 308 (2017) 692-699. doi: 10.1016/j.cej.2016.09.110.

[169] Y. Wang, D. Han, Z. Wang, F. Gu, Efficient photocatalytic degradation of tetracycline under visible light by an all-solid-state Z-scheme Ag_3PO_4/MIL-101(Cr) heterostructure with metallic Ag as a charge transmission bridge, ACS Applied Materials & Interfaces 15 (2023) 22085-22100. doi: 10.1021/acsami.3c01255.

[170] X. Chen, L. Yao, J. He, J. Li, S. Xu, N. Li, R. Zhu, Enhanced degradation of tetracycline under natural sunlight through the synergistic effect of Ag_3PO_4/MIL-101(Fe) photocatalysis and Fenton catalysis: Mechanism, pathway, and toxicity assessment, Journal of Hazardous Materials 449 (2023) 131024. doi: 10.1016/j.jhazmat.2023.131024.

[171] S. Zeinali Heris, M. Etemadi, S. B. Mousavi, M. Mohammadpourfard, B. Ramavandi, Preparation and characterizations of TiO_2/ZnO nanohybrid and its application in photocatalytic degradation of tetracycline in wastewater, Journal of Photochemistry and Photobiology A: Chemistry 443 (2023) 114893. doi: 10.1016/j.jphotochem.2023.114893.

[172] A. Majumdar, U. Ghosh, A. Pal, Novel 2D/2D g-C_3N_4/Bi_4NbO_8Cl nanocomposite for enhanced photocatalytic degradation of oxytetracycline under visible LED light irradiation, Journal of Colloid and Interface Science 584 (2021) 320–331. doi: 10.1016/j.jcis.2020.09.101.

[173] K. Changanaqui, E. Brillas, H. Alarcón, I. Sirés, ZnO/TiO_2/Ag_2Se nanostructures as photoelectrocatalysts for the degradation of oxytetracycline in water, Electrochimica Acta 331 (2020) 135194. doi: 10.1016/j.electacta.2019.135194.

[174] R. Hassandoost, A. Kotb, Z. Movafagh, M. Esmat, R. Guégan, S. Endo, E. Doustkhah, Nanoarchitecturing bimetallic manganese cobaltite spinels for sonocatalytic degradation of oxytetracycline, Chemical Engineering Journal 431 (2022) 133851. doi: 10.1016/j.cej.2021.133851.

[175] Y. Li, L. Fu, X. Li, Y. Wang, Y. Wei, J. Tang, H. Liu, Novel strains with superior degrading efficiency for lincomycin manufacturing biowaste, Ecotoxicology and Environmental Safety 209 (2021) 111802. doi: 10.1016/j.ecoenv.2020.111802.

[176] J.Radjenović, M.Petrović, D.Barceló, Fate and distribution of pharmaceuticals in wastewater and sewage sludge of the conventional activated sludge (CAS) and advanced membrane bioreactor (MBR) treatment, Water Research 43 (3) (2009) 831-841. doi: 10.1016/j.watres.2008.11.043.

[177] G. Rhodes, G. Huys, J. Swings, P. McGann, M. Hiney, P. Smith, R. W. Pickup, Distribution of oxytetracycline resistance plasmids between aeromonads in hospital and aquaculture environments: Implication of Tn1721 in dissemination of the tetracycline resistance determinant Tet A, Applied and Environmental Microbiology (2000). https://doi.org/10.1128/AEM.66.9.3883-3890.2000.

[178] C. Zhao, H. Deng, Y. Li, Z. Liu, Photodegradation of oxytetracycline in aqueous by 5A and 13X loaded with TiO_2 under UV irradiation, Journal of Hazardous Materials 176 (2010) 884-892. doi: 10.1016/j.jhazmat.2009.11.119.

[179] I. Michael, L. Rizzo, C. S. McArdell, C. M. Manaia, C. Merlin, T. Schwartz, C. Dagot, D. Fatta-Kassinos, Urban wastewater treatment plants as hotspots for the release of antibiotics in the environment: A review, Water Research 47 (2013) 957–995. doi.org/10.1016/j.watres.2012.11.027

[180] M. Addamo, V. Augugliaro, A. Di Paola, E. García-López, V. Loddo, G. Marcì, L. Palmisano, Removal of drugs in aqueous systems by photoassisted degradation, Journal of Applied Electrochemistry 35 (2005) 765-774. doi: 10.1007/s10800-005-1630-y.

[181] F. Nawaz, Y. Xie, H. Cao, J. Xiao, X. Zhang, M. Li, F. Duan, Catalytic ozonation of 4-nitrophenol over a mesoporous α-MnO_2 with resistance to leaching, Catalysis Today 258 (2015) 595-601. doi: 10.1016/j.cattod.2015.03.044.

[182] M. S. Dieckmann, K. A. Gray, A comparison of the degradation of 4-nitrophenol via direct and sensitized photocatalysis in TiO_2 slurries, Water Research 30 (1996) 1169-1183. doi: 10.1016/0043-1354(95)00240-5.

[183] A. Di Paola, V. Augugliaro, L. Palmisano, G. Pantaleo, E. Savinov, Heterogeneous photocatalytic degradation of nitrophenols, Journal of Photochemistry and Photobiology A: Chemistry 155 (2003) 207-214. doi: 10.1016/S1010-6030(02)00390-8.

[184] T. Seadira, G. Sadanandam, T. A. Ntho, X. Lu, C. M. Masuku, M. Scurrell, Hydrogen production from glycerol reforming: Conventional and green production, Reviews in Chemical Engineering 34 (2018) 695-726. doi: 10.1515/revce-2016-0064.

[185] K. E. Sanwald, T. F. Berto, W. Eisenreich, O. Y. Gutiérrez, J. A. Lercher, Catalytic routes and oxidation mechanisms in photoreforming of polyols, Journal of Catalysis 344 (2016) 806-816. doi: 10.1016/j.jcat.2016.08.009.

[186] L. Palmisano, V. Augugliaro, M. Bellardita, A. Di Paola, E. García López, V. Loddo, S. Yurdakal, Titania photocatalysts for selective oxidations in water, ChemSusChem (2011). doi: 10.1002/cssc.201100196.

[187] S. Yurdakal, M. Bellardita, I. Pibiri, L. Palmisano, V. Loddo, Aqueous selective photocatalytic oxidation of salicyl alcohol by TiO_2 catalysts: Influence of some physico-chemical features, Catalysis Today 380 (2021) 16-24. doi: 10.1016/j.cattod.2021.06.030.

[188] T. D. Bui, A. Kimura, S. Ikeda, M. Matsumura, lowering of photocatalytic activity of TiO_2 particles during oxidative decomposition of benzene in aerated liquid, Applied Catalysis B: Environmental 94 (2010) 186-191. doi: 10.1016/j.apcatb.2009.11.008.

[189] A. Fujishima, T. N. Rao, D. A. Tryk, Titanium dioxide photocatalysis, Journal of Photochemistry and Photobiology C: Photochemistry Reviews 1 (2000) 1-21. doi.org/10.1016/S1389-5567(00)00002-2

[190] O. Tomita, T. Otsubo, M. Higashi, B. Ohtani, R. Abe, Partial oxidation of alcohols on visible-light-responsive WO_3 photocatalysts loaded with palladium oxide cocatalyst, ACS Catalysis 6 (2016) 1134-1144. doi: 10.1021/acscatal.5b01850.

[191] M. Y. Qi, Q. Lin, Z. R. Tang, Y. J. Xu, Photoredox coupling of benzyl alcohol oxidation with CO_2 reduction over CdS/TiO_2 heterostructure under visible light irradiation, Applied Catalysis B: Environmental 307 (2022) 121158. doi: 10.1016/j.apcatb.2022.121158.

[192] G. S. Wolde, D. H. Kuo, M. H. Urgesa, T. N. Gemeda, Photocatalytic oxidation of benzyl alcohol coupled with p-dinitrobenzene reduction over poly(o-phenylenediamine) nanowires-decorated Gd-TiO_2 nanorods, Chemical Engineering Journal 469 (2023) 143916. doi: 10.1016/j.cej.2023.143916.

[193] F. Parrino, M. Bellardita, E. I. García-López, G. Marcì, V. Loddo, L. Palmisano, Heterogeneous photocatalysis for selective formation of high-value-added molecules: Some chemical and engineering aspects, ACS Catalysis 8 (2018) 11191-11225. doi: 10.1021/acscatal.8b03093.

[194] A. M. Carozo, F. J. López-Tenllado, M. C. Herrera-Beurnio, J. Hidalgo-Carrillo, J. Martín-Gómez, R. Estevez, A. Ariza-Pérez, F. J. Urbano, A. Marinas, Pt-TiO_2 systems for enhanced

hydrogen production from glycerol: Direct vs sequential incorporation through photodeposition, Materials 17 (2024) 5109. doi: 10.3390/ma17205109.

[195] P. Limpachanangkul, P. Nimmmanterdwong, L. Liu, M. Hunsom, K. Pruksathorn, P. Piumsomboon, B. Chalermsinsuwan, Glycerol photocatalytic oxidation to higher value-added compounds via bismuth oxyhalide photocatalysts, Scientific Reports 13 (2023). doi: 10.1038/s41598-023-42246-3.

[196] G. Zhang, Z. Sun, X. Hu, A. Song, S. Zheng, Synthesis of BiOCl/TiO_2-zeolite composite with enhanced visible light photoactivity, Journal of the Taiwan Institute of Chemical Engineers 81 (2017) 435-444. doi: 10.1016/j.jtice.2017.09.030.

[197] M. Guerrero, A. Altube, E. Garcia-Lecina, E. Rossinyol, M. D. Baró, E. Pellicer, J. Sort, Facile in situ synthesis of BiOCl nanoplates stacked to highly porous TiO_2: A synergistic combination for environmental remediation, ACS Applied Materials & Interfaces 6 (2014) 13994-14000. doi: 10.1021/am5033549.

[198] X. Liu, X.Duan, T. Bao, D. Hao, Z. Chen, W. Wei, B.J. Ni, High-performance photocatalytic decomposition of PFOA by BiOX-TiO_2 heterojunctions: Self-induced inner electric fields and band alignment, Journal of Hazardous Materials 430 (2022) 128195. doi: 10.1016/j.jhazmat.2021.128195.

[199] M. Du, A. Peng, H. Liu, H. Chen, Q. Li, Z. Fang, R. Yan, TiO_2-coated BiOCl nanosheet p-n heterojunctions for photocatalytic H_2O_2 production under simulated sunlight, ACS Applied Nano Materials 8 (2025) 12222-12229. doi: 10.1021/acsanm.5c01898.

[200] S. Yao, J. Wang, X. Zhou, S. Zhou, X. Pu, W. Li, One-pot low-temperature synthesis of BiOX-TiO_2 hierarchical composites of adsorption coupled with photocatalysis for quick degradation of colored and colorless organic pollutants, Advanced Powder Technology 31 (2020) 1924-1932. doi: 10.1016/j.apt.2020.02.023.

[201] G. Zhang, Y. Tan, Z. Sun, S. Zheng, Synthesis of BiOCl-TiO_2 heterostructure composites and their enhanced photocatalytic activity, Journal of Environmental Chemical Engineering 5 (2017) 1196-1204. doi: 10.1016/j.jece.2017.01.040.

[202] Mohd. Shkir, A. M. Ali, Novel 2D/3D BiOBr/TiO_2 S-scheme heterostructures photocatalyst fabrication for remarkable ciprofloxacin degradation under solar light, FlatChem 52 (2025) 100891. doi: 10.1016/j.flatc.2025.100891.

[203] R. Hou, M. Xu, Z. Fan, R. Zhong, Y. Xie, Y. Ling, Y. Wang, BiOCl modified TiO_2 based catalyst with enhanced hydrogen generation properties under visible light via promoted photogenerated electron-hole separation, Materials Today Physics 44 (2024) 101426. doi: 10.1016/j.mtphys.2024.101426.

[204] N. A. Phakathi, S. M. Tichapondwa, E. M. N. Chirwa, Photocatalytic degradation of tetracycline using visible-light-driven porous g-C_3N_4 nanosheets catalyst, Chemical Engineering Transactions 96 (2022) 391-396. doi: 10.3303/cet2296066.

[205] S. Gaffar, A. Kumar, J. Alam, U. Riaz, Efficient visible light–induced photocatalytic degradation of tetracycline hydrochloride using Cu Fe_2O_4 and PANI/$CuFe_2O_4$ nanohybrids, Environmental Science and Pollution Research 2023. doi: 10.1007/s11356-023-29976-7.

[206] X. Jia, F. Wang, X. Xu, C. Liu, L. Zhang, S. Jiao, G. Zhu, X. Wang, G. Yu, Highly efficient photocatalytic degradation of tetracycline by modifying UiO-66 via different regulation strategies, ACS Omega 8 (2023) 27375-27385. doi: 10.1021/acsomega.3c02762.

[207] S. Li, C. Wang, Y. Liu, M. Cai, Y. Wang, H. Zhang, Y. Guo, W. Zhao, Z. Wang, X. Chen, Photocatalytic degradation of tetracycline antibiotic by a novel $Bi_2Sn_2O_7$/Bi_2MoO_6 S-scheme heterojunction: Performance, mechanism insight and toxicity assessment, Chemical Engineering Journal 429 (2022) 132519. doi: 10.1016/j.cej.2021.132519.

[208] Z. Zhang, C. Du, Y. Zhang, G. Yu, Y. Xiong, L. Zhou, Y. Liu, T. Chi, G. Wang, Y. Su, Y. Lv, H. Zhu, Degradation of oxytetracycline by magnetic MOFs heterojunction photocatalyst with persulfate: High stability and wide range, Environmental Science and Pollution Research 29 (2022) 30019–30029. doi: 10.1007/s11356-021-17971-9.

[209] Y. Ma, R. Wang, C. Gao, R. Han, Carbon nanotube-loaded copper-nickel ferrite activated persulfate system for adsorption and degradation of oxytetracycline hydrochloride, Journal of Colloid and Interface Science 640 (2023) 761-774. doi: 10.1016/j.jcis.2023.03.001.

[210] K. Li, A. Yediler, M. Yang, S. Schulte-Hostede, M. Hung, Ozonation of oxytetracycline and toxicological assessment of its oxidation by-products, Chemosphere 72 (2008) 473-478. doi: 10.1016/j.chemosphere.2008.02.008.

[211] M. El-Kemary, H. El-Shamy, I. El-Mehasseb, Photocatalytic degradation of ciprofloxacin drug in water using ZnO nanoparticles, Journal of Luminescence 130 (2010) 2327-2331. doi: 10.1016/j.jlumin.2010.07.013.

[212] X. J. Wen, C. G. Niu, L. Zhang, C. Liang, H. Guo, G. M. Zeng, Photocatalytic degradation of ciprofloxacin by a novel Z-scheme CeO_2-Ag/AgBr photocatalyst: Influencing factors, possible degradation pathways, and mechanism insight, Journal of Catalysis 358 (2018) 141-154. doi: 10.1016/j.jcat.2017.11.029.

[213] L. Yang, Y. Xiang, F. Jia, L. Xia, C. Gao, X. Wu, L. Peng, J. Liu, S. Song, Photo-thermal synergy for boosting photo-Fenton activity with rGO-$ZnFe_2O_4$: Novel photo-activation process and mechanism toward environmental remediation, Applied Catalysis B: Environmental 292 (2021) 120198. doi: 10.1016/j.apcatb.2021.120198.

[214] X. Ge, G. Meng, B. Liu, Ultrasound-assisted preparation of $LaFeO_3$/polystyrene for efficient photo-Fenton degradation of ciprofloxacin hydrochloride, Journal of Industrial and Engineering Chemistry 115 (2022) 390-401. doi: 10.1016/j.jiec.2022.08.023.

[215] M. Mohammadi, S. Sabbaghi, M. Binazadeh, S. Ghaedi, Type-1 α-Fe_2O_3/TiO_2 photocatalytic degradation of tetracycline from wastewater using CCD-based RSM optimization, Chemosphere 336 (2023) 139311. doi: 10.1016/j.chemosphere.2023.139311.

[216] M. Sharma, M. K. Mandal, S. Pandey, R. Kumar, K. K. Dubey, Visible-light-driven photocatalytic degradation of tetracycline using heterostructured Cu_2O-TiO_2 nanotubes: Kinetics and toxicity evaluation of degraded products on cell lines, ACS Omega 7 (2022) 33572-33586. doi: 10.1021/acsomega.2c04576.

[217] M. Ahmadi, H. R. Motlagh, N. Jaafarzadeh, A. Mostoufi, R. Saeedi, G. Barzegar, S. Jorfi, Enhanced photocatalytic degradation of tetracycline and real pharmaceutical wastewater using MWCNT/TiO_2 nanocomposite, Journal of Environmental Management 186 (2017) 55-63. doi: 10.1016/j.jenvman.2016.09.088.

[218] W. Wang, J. Fang, S. Shao, M. Lai, C. Lu, Compact and uniform TiO_2@g-C_3N_4 core-shell quantum heterojunction for photocatalytic degradation of tetracycline antibiotics, Applied Catalysis B: Environmental 217 (2017) 57-64. doi: 10.1016/j.apcatb.2017.05.037.

[219] W. Liu, C. Wei, R. Peng, R. Chu, H. Sun, X. Zhang, F. Xie, Persulfate-assisted photocatalytic degradation of tetracycline by bismuth titanate under visible light irradiation, New Journal of Chemistry 46 (2022) 10854-10862.

[220] S. Kaushal, A. Kumar, H. Bains, P. P. Singh, Photocatalytic degradation of tetracycline antibiotic and organic dyes using biogenic synthesized CuO/Fe_2O_3 nanocomposite: Pathways and mechanism insights, Environmental Science and Pollution Research 30 (2023) 37092-37104. doi: 10.1007/s11356-022-24848-y.

[221] P. Semeraro, S. Bettini, S. Sawalha, S. Pal, A. Licciulli, F. Marzo, N. Lovergine, L. Valli, G. Giancane, Photocatalytic degradation of tetracycline by ZnO/γ-Fe_2O_3 paramagnetic nanocomposite material, *Nanomaterials* 10 (2020) 1458. https://doi.org/10.3390/nano10081458

[222] L. J. Nguetsa Kuate, Z. Chen, J. Lu, H. Wen, F. Guo, W. Shi, Photothermal-assisted photocatalytic degradation of tetracycline in seawater based on black g-C_3N_4 nanosheets with cyano group defects, Catalysts 13 (2023) 1147. doi: 10.3390/catal13071147.

[223] F. Chen, Q. Yang, J. Sun, F. Yao, S. Wang, Y. Wang, X. Wang, X. Li, C. Niu, D. Wang, G. Zeng, Enhanced photocatalytic degradation of tetracycline by AgI/$BiVO_4$ heterojunction under visible-light irradiation: Mineralization efficiency and mechanism, ACS Applied Materials & Interfaces 8 (2016) 32887-32900. doi: 10.1021/acsami.6b12278.

[224] A. O. Oluwole, O. S. Olatunji, Photocatalytic degradation of tetracycline in aqueous systems under visible light irradiation using needle-like SnO_2 nanoparticles anchored on exfoliated g-C_3N_4, Environmental Science Europe 34 (2022). doi: 10.1186/s12302-021-00588-7.

[225] X. X. Zhang, X. J. Wang, Y. Y. Niu, Photocatalytic degradation of tetracycline by supramolecular materials constructed with organic cations and silver iodide, Catalysts 12 (2022) 1581. doi: 10.3390/catal12121581.

[226] M. Doosti, R. Jahanshahi, S. Laleh, S. Sobhani, J. M. Sansano, Solar light induced photocatalytic degradation of tetracycline in the presence of ZnO/$NiFe_2O_4$/Co_3O_4 as a highly efficient magnetically separable photocatalyst, Frontiers in Chemistry 10 (2022) 1013349. doi: 10.3389/fchem.2022.1013349.

[227] Y. Zhang, J. Zhou, X. Chen, L. Wang, W. Cai, Coupling of heterogeneous advanced oxidation processes and photocatalysis in efficient degradation of tetracycline hydrochloride by Fe-based MOFs: Synergistic effect and degradation pathway, Chemical Engineering Journal 369 (2019) 745-757. doi: 10.1016/j.cej.2019.03.108.

[228] J. Huang, P. Xue, S. Wang, S. Han, L. Lin, X. Chen, Z. Wang, Fabrication of zirconium-based metal-organic frameworks@tungsten trioxide (UiO-66-NH_2@WO_3) heterostructure on carbon cloth for efficient photocatalytic removal of tetracycline antibiotic under visible light, Journal of Colloid and Interface Science 606 (2022) 1509-1523. doi: 10.1016/j.jcis.2021.08.108.

[229] J. Wang, Z. Zhang, Co-precipitation synthesis and photocatalytic properties of BiOCl microflowers, Optik 204 (2020) 164149. doi: 10.1016/j.ijleo.2019.164149.

[230] X. Guo, D. J. Guo, X. P. Qiu, L. Q. Chen, W. T. Zhu, Excellent dispersion and electrocatalytic properties of Pt nanoparticles supported on novel porous anatase TiO_2 nanorods, Journal of Power Sources 194 (2009) 281-285. doi: 10.1016/j.jpowsour.2009.05.035.

[231] X. Qu, M. Liu, J. Yang, C. Wang, H. Meng, S. Li, F. Du, A novel ternary TiO_2/CQDs/BiOX (X = Cl, Br, I) heterostructure as photocatalyst for water purification under solar irradiation, Journal of Solid-State Chemistry 264 (2018) 77-85. doi: 10.1016/j.jssc.2018.05.002.

[232] K. Wang, Y. Zhang, L. Liu, N. Lu, Z. Zhang, BiOBr nanosheets-decorated TiO_2 nanofibers as hierarchical p–n heterojunction photocatalysts for pollutant degradation, Journal of Materials Science 54 (2019) 8426–8435. doi: 10.1007/s10853-019-03466-z.

[233] D. S. Shinde, P. D. Bhange, R. K. Jha, D. S. Bhange, TiO_2 nanoparticles decorated on BiOCl flakes with enhanced visible-light photocatalytic activity, ChemistrySelect 5 (2020) 2618-2626. doi: 10.1002/slct.201904656.

[234] S. Challagulla, K. Tarafder, R. Ganesan, S. Roy, Structure-sensitive photocatalytic reduction of nitroarenes over TiO_2, Scientific Reports 7 (2017). doi: 10.1038/s41598-017-08599-2.

[235] A. Khalid, P. Ahmad, A. I. Alharthi, S. Muhammad, M. U. Khandaker, M. R. Iqbal Faruque, I. Ud Din, M. A. Alotaibi, Unmodified titanium dioxide nanoparticles as a potential contrast agent in photon emission computed tomography, Crystals 11 (2021) 171. doi: 10.3390/cryst11020171.

[236] X. B. Wang, C. Song, K. W. Geng, F. Zeng, F. Pan, Photoluminescence and Raman scattering of Cu-doped ZnO films prepared by magnetron sputtering, Applied Surface Science 253 (2007) 6905-6909. doi: 10.1016/j.apsusc.2007.02.013.

[237] Y. Yu, C. Cao, H. Liu, P. Li, F. Wei, Y. Jiang, W. Song, A Bi/BiOCl heterojunction photocatalyst with enhanced electron-hole separation and excellent visible-light photodegrading activity, Journal of Materials Chemistry A 2 (2014) 1677-1681. doi: 10.1039/c3ta14494a.

[238] D. Wrana, T. Gensch, B. R. Jany, K. Cieślik, C. Rodenbücher, G. Cempura, A. Kruk, F. Krok, Photoluminescence imaging of defects in TiO_2: The influence of grain boundaries and doping on charge carrier dynamics, Applied Surface Science 569 (2021) 150909. doi: 10.1016/j.apsusc.2021.150909.

[239] Q. Xiao, Z. Si, J. Zhang, C. Xiao, Z. Yu, G. Qiu, Effects of samarium dopant on photocatalytic activity of TiO_2 nanocrystallite for methylene blue degradation, Journal of Materials Science 42 (2007) 9194-9199. doi: 10.1007/s10853-007-1919-9.

[240] M. Bellardita, S. Yurdakal, B. S. Tek, Ç. Değirmenci, G. Palmisano, V. Loddo, V. Augugliaro, Tuning the selectivity to aldehyde via pH regulation in the photocatalytic oxidation of 4-methoxybenzyl alcohol and vanillyl alcohol by TiO_2 catalysts, Journal of Environmental Chemical Engineering 9 (2021) 105308. doi: 10.1016/j.jece.2021.105308.

[241] Z. Saddique, M. Imran, A. Javaid, S. Latif, N. Hussain, P. Kowal, G. Boczkaj, Band engineering of BiOBr-based materials for photocatalytic wastewater treatment via advanced oxidation processes (AOPs): A review, Water Research Innovations (2023) 100211. doi: 10.1016/j.wri.2023.100211.

[242] G. Zhang, Y. Tan, Z. Sun, S. Zheng, Synthesis of BiOCl/TiO_2 heterostructure composites and their enhanced photocatalytic activity, Journal of Environmental Chemical Engineering 5 (2017) 1196-1204. doi: 10.1016/j.jece.2017.01.040.

[243] M. M. Obeid, C. Stampfl, A. Bafekry, Z. Guan, H. R. Jappor, C. V. Nguyen, D. Gogova, First-principles investigation of nonmetal doped single-layer BiOBr as a potential photocatalyst with a low recombination rate, Physical Chemistry Chemical Physics 22 (2020) 15354-15364. doi: 10.1039/d0cp02007a.

[244] R. Konaka, E. Kasahara, W. C. Dunlap, Y. Yamamoto, K. C. Chien, M. Inoue, Ultraviolet irradiation of titanium dioxide in aqueous dispersion generates singlet oxygen, Redox Report 6 (2001) 319-325. doi: 10.1179/135100001101536463.

[245] G. Palmisano, S. Yurdakal, V. Augugliaro, V. Loddo, L. Palmisano, Photocatalytic selective oxidation of 4-methoxybenzyl alcohol to aldehyde in aqueous suspension of home-prepared titanium dioxide catalyst, Advanced Synthesis & Catalysis 349 (2007) 964-970. doi: 10.1002/adsc.200600435.

[246] J. Lv, Q. Hu, C. Cao, Y. Zhao, Modulation of valence band maximum edge and photocatalytic activity of BiOX by incorporation of halides, Chemosphere 191 (2018) 427-437. doi: 10.1016/j.chemosphere.2017.09.149.

[247] M. Bellardita, E. I. García-López, G. Marcì, L. Palmisano, Photocatalytic formation of H_2 and value-added chemicals in aqueous glucose (Pt)-TiO_2 suspension, International Journal of Hydrogen Energy 41 (2016) 5934-5947. doi: 10.1016/j.ijhydene.2016.02.103.

[248] M. Bellardita, M. Feilizadeh, R. Fiorenza, S. Scirè, L. Palmisano, V. Loddo, Selective aqueous oxidation of aromatic alcohols under solar light in the presence of TiO_2 modified with different metal species, Photochemical & Photobiological Sciences (2022). doi: 10.1007/s43630-022-00284-2.

[249] K. E. Sanwald, T. F. Berto, W. Eisenreich, O. Y. Gutiérrez, J. A. Lercher, Catalytic routes and oxidation mechanisms in photoreforming of polyols, Journal of Catalysis 344 (2016) 806-816. doi: 10.1016/j.jcat.2016.08.009.

[250] M. C. Herrera-Beurnio, F. J. López-Tenllado, J. Hidalgo-Carrillo, J. Martín-Gómez, R. Estévez, F. J. Urbano, A. Marinas, Glycerol photoreforming for photocatalytic hydrogen production on binary and ternary Pt-g-C_3N_4-TiO_2 systems: A comparative study, Catalysis Today 430 (2024) 114548. doi: 10.1016/j.cattod.2024.114548.

[251] J. G. Villachica-Llamosas, A. Ruiz-Aguirre, G. Colón, J. Peral, S. Malato, CuO-TiO_2 pilot-plant system performance for solar photocatalytic hydrogen production, International Journal of Hydrogen Energy 51 (2024) 1069-1077. doi: 10.1016/j.ijhydene.2023.07.149.

[252] R. Fiorenza, M. Bellardita, S. Scirè, L. Palmisano, Photocatalytic H_2 production over inverse opal TiO_2 catalysts, Catalysis Today (2019) 113-119. doi: 10.1016/j.cattod.2017.12.011.

[253] M. Umair, A. M. Djaballah, M. Bellardita, R. Bagtache, L. Palmisano, M. Trari, Visible-light photoreforming of biomass derivatives through MBi_2O_4-P25 heterostructures: Study of the influence of metals (M = Cu, Ni, Zn, Co), Advanced Sustainable Systems (2024). doi: 10.1002/adsu.202400298.

[254] M. Muscetta, S. Al Jitan, G. Palmisano, R. Andreozzi, R. Marotta, S. Cimino, I. Di Somma, Visible light-driven photocatalytic hydrogen production using Cu_2O/TiO_2 composites prepared by facile mechanochemical synthesis, Journal of Environmental Chemical Engineering 10 (2022) 107735. doi: 10.1016/j.jece.2022.107735.

[255] S. Juntrapirom, D. Tantraviwat, O. Thongsook, S. Anuchai, S. Pornsuwan, D. Channei, B. Inceesungvorn, Natural sunlight driven photocatalytic coupling of primary amines over TiO_2/BiOBr heterojunction, Applied Surface Science 545 (2021) 149015. doi: 10.1016/j.apsusc.2021.149015.

[256] P. Zhou, Y. Shen, S. Zhao, G. Li, B. Cui, D. Wei, Y. Shen, Synthesis of clinoptilolite-supported BiOCl/TiO_2 heterojunction nanocomposites with highly enhanced photocatalytic activity for the complete degradation of xanthates under visible light, Chemical Engineering Journal 407 (2021) 126697. doi: 10.1016/j.cej.2020.126697.

[257] S. Zhang, Y. Liu, G. Liao, J. He, F. Long, Nano particle/microsphere TiO_2/BiOBr Z-scheme heterojunction with high visible-light photocatalytic activity in tetracycline hydrochloride degradation, Journal of Materials Science: Materials in Electronics 33 (2022) 25878-25890. doi: 10.1007/s10854-022-09278-3.

[258] H. Dong, M. Xiao, J. Li, W. Hu, X. Sun, Y. Liu, P. Zhang, G. Che, C. Liu, Construction of H-TiO_2/BiOCl heterojunction with improved photocatalytic activity under visible and near-infrared light, Journal of Photochemistry and Photobiology A: Chemistry 392 (2020) 112369. doi: 10.1016/j.jphotochem.2020.112369.

[258] (a)] M.C. Herrera-Beurnio, F.J. López-Tenllado, J. Hidalgo-Carrillo, J. Martín-Gómez, R. Estévez, F.J. Urbano, A. Marinas, Glycerol photoreforming for photocatalytic hydrogen production on binary and ternary Pt-g-C3N4-TiO2 systems: A comparative study, Catal. Today 430 (2024) 114548. DOI: 10.1016/j.cattod.2024.114548

[258] (b) S.A. Balsamo, S. Sciré, M. Condorelli, R. Fiorenza, Photocatalytic H2 Production on Au/TiO2: Effect of Au Photodeposition on Different TiO2 Crystalline Phases, J. 5 (2022) 92–104. DOI: 10.3390/j5010006

[258] (c) A. Abraham, K.N. Salgaonkar, T.R. Nivedhitha, V.A. Ekal, D. Kondhekar, S. Chakraborty, C.S. Gopinath, A. Saha, Synthesis of Pd-Integrated Carbon Dot@TiO2 Thin Film for Photocatalytic Glycerol Reforming Reaction for Producing Hydrogen, Chem. Asian J. 20 (2025) e202500757. DOI: 10.1002/asia.202500757

[258] (d) Z. Yang, W. Zhong, Y. Chen, C. Wang, S. Mo, J. Zhang, R. Shu, Q. Song, Improving Glycerol Photoreforming Hydrogen Production Over Ag2O-TiO2 Catalysts by Enhanced Colloidal Dispersion Stability, Front. Chem. 8 (2020) 342. DOI: 10.3389/fchem.2020.00342

[258] (e) A. Abraham, K.N. Salgaonkar, T.R. Nivedhitha, V.A. Ekal, D. Kondhekar, S. Chakraborty, C.S. Gopinath, A. Saha, Synthesis of Pd-Integrated Carbon Dot@TiO2 Thin Film for Photocatalytic Glycerol Reforming Reaction for Producing Hydrogen, Chem. Asian J. 20 (2025) e202500757. DOI: 10.1002/asia.202500757

[258] (f) S.P. Ramírez, J.A. Wang, M.A. Valenzuela, L.F. Chen, A. Dalai, CuO@TiO2 and NiO@TiO2 Core-Shell Catalysts for Hydrogen Production from the Photocatalytic Reforming of Glycerol Aqueous Solution, J. Appl. Res. Technol. 18 (2020) 390–409. DOI: 10.1016/j.jart.2017.02.005

[258] (g) M. Eisapour, T. Roostaei, M. Kaur, J. Hu, H. Zhao, Z. Chen, Coproduction of Hydrogen and Value-Added Chemicals Using Ni-TiO2@g-C3N4 Nanocomposites from Glycerol Photoreforming, Ind. Eng. Chem. Res. 64 (2025) 20516–20524. DOI: 10.1021/acs.iecr.5c02187.

[259] M. Umair, C. M. Pecoraro, F. Di Franco, M. Santamaria, L. Palmisano, V. Loddo, M. Bellardita, Efficient photocatalytic partial oxidation of aromatic alcohols by using $ZnIn_2S_4$ under green conditions, ChemSusChem (2024). doi: 10.1002/cssc.202400404.

[260] S. Juntrapirom, D. Tantraviwat, O. Thongsook, S. Anuchai, S. Pornsuwan, D. Channei, B. Inceesungvorn, *Natural sunlight driven photocatalytic coupling of primary amines over TiO_2/BiOBr heterojunction*, Applied Surface Science 545 (2021) 149015. doi: 10.1016/j.apsusc.2021.149015

[261] R. Daghrir, P. Drogui, Tetracycline antibiotics in the environment: a review, Environmental Chemistry Letters 11 (2013) 209-227. doi: 10.1007/S10311-013-0404-8.

[262] J. Lyu, Z. Hu, Z. Li, and M. Ge, Removal of tetracycline by BiOBr microspheres with oxygen vacancies: Combination of adsorption and photocatalysis, Journal of Physics and Chemistry of Solids 129 (2019) 61-70. doi: 10.1016/j.jpcs.2018.12.041.

[263] X. Wang, J. Jia, Y. Wang, Combination of photocatalysis with hydrodynamic cavitation for degradation of tetracycline, Chemical Engineering Journal 315 (2017) 274-282. doi: 10.1016/j.cej.2017.01.011.

[264] P. Raizda, S. Gautam, B. Priya, and P. Singh, Preparation and photocatalytic activity of hydroxyapatite supported BiOCl nanocomposite for oxytetracycline removal, Advanced Materials Letters 7 (2016) 312-318. doi: 10.5185/amlett.2016.5847.

[265] X. Yan, Q. Ji, C. Wang, J. Xu, and L. Wang, In situ construction bismuth oxycarbonate/bismuth oxybromide Z-scheme heterojunction for efficient photocatalytic removal of tetracycline and ciprofloxacin, Journal of Colloid and Interface Science 587 (2021) 820-830. doi: 10.1016/j.jcis.2020.11.043.

[266] X. Yang, S. Sun, L. Ye, D. Yun, C. Liu, Y. Guo, B. Yang, M. Yang, Q. Yang, S. Liang, J. Cui, One-pot integration of S-doped BiOCl and ZnO into type-II photocatalysts: simultaneously boosting bulk and surface charge separation for enhanced antibiotic removal, Separation and Purification Technology 299 (2022) 121725. doi: 10.1016/j.seppur.2022.121725.

[267] P. Wang, P. S. Yap, T. T. Lim, C–N–S tridoped TiO_2 for photocatalytic degradation of tetracycline under visible-light irradiation, Applied Catalysis A: General 399 (2011) 252-261. doi: 10.1016/j.apcata.2011.04.008.

[268] R. Zhang, J. Dong, L. Li, J. Zhao, M. Ji, B. Wang, J. Xia, H. Li, Low concentration of peroxymonosulfate coupled with visible light triggers oxygen reactive species generation over constructed $Bi_{25}FeO_{40}$/BiOCl Z-scheme heterojunction for various tetracycline antibiotics removal, Journal of Colloid and Interface Science 665 (2024) 825-837. doi: 10.1016/j.jcis.2024.03.138.

[269] Y. Wang, T. Chen, H. Xu, J. Yu, T. Zhang, A flower-like heterojunction for highly photocatalytic treating oxytetracycline based on chromium-based metal-organic frameworks decorated BiOCl nanosheet, Colloids and Surfaces A: Physicochemical and Engineering Aspects 685 (2024) 133259. doi: 10.1016/j.colsurfa.2024.133259.

[270] C. Wang, Z. Chen, R. Yu, Construction of BiOCl/Ti-MOFs type-II heterojunction photocatalyst for enhanced photocatalytic performance for multiple antibiotics removal, Environmental Science and Pollution Research 30 (2023) 42140-42151. doi: 10.1007/s11356-022-24987-2.

[271] Y. Wang, D. Wang, H. Xu, J. Yu, T. Chen, A flower-like metal-organic frameworks fabricated BiOCl heterojunction with enhanced visible light photocatalytic activity, Journal of Alloys and Compounds 957 (2023) 170376. doi: 10.1016/j.jallcom.2023.170376.

[272] J. Song, Z. Zhang, S. Zhi, B. Niu, H. Dong, D. Wu, K. Jiang, Oxygen-vacancy-rich BiOCl with 3D network structure for enhanced photocatalytic CO_2 reduction and antibiotic degradation, Journal of the Taiwan Institute of Chemical Engineers 128 (2021) 380-387. doi: 10.1016/j.jtice.2021.08.044.

[273] B. Priya, P. Shandilya, P. Raizada, P. Thakur, N. Singh, P. Singh, Photocatalytic mineralization and degradation kinetics of ampicillin and oxytetracycline antibiotics using graphene sand composite and chitosan supported BiOCl, Journal of Molecular Catalysis A: Chemical 423 (2016) 400-413. doi: 10.1016/j.molcata.2016.07.043.

[274] T. Li, S. Luo, L. Yang, Microwave-assisted solvothermal synthesis of flower-like Ag/AgBr/BiOBr microspheres and their high efficient photocatalytic degradation for p-nitrophenol, Journal of Solid-State Chemistry 206 (2013) 308-316. doi: 10.1016/j.jssc.2013.07.019.

[275] Y. Jia et al., Simulated sunlight photocatalytic degradation of aqueous p-nitrophenol and bisphenol A in Pt/BiOBr film-coated quartz fiber photoreactor, Dalton Transactions (2010) doi: 10.1039/c0xx00000x.

[276] T. T. Cao, H. Cui, Q. W. Zhang, C. W. Cui, Facile synthesis of Co (II)-BiOCl@biochar nanosheets for photocatalytic degradation of p-nitrophenol under vacuum ultraviolet (VUV)

irradiation, Applied Surface Science 559 (2021) 149938. doi: 10.1016/j.apsusc.2021.149938.

[276] (a) Liu, H.; Song, M. Techno-Economic Assessment and Process Design Considerations for Industrial-Scale Photocatalytic Wastewater Treatment. *Water* **2026**, *18*(2), 221. doi: org/10.3390/w18020221.

[277] M. Bellardita, M. Addamo, A. Di Paola, L. Palmisano, A. M. Venezia, Preparation of N-doped TiO_2: characterization and photocatalytic performance under UV and visible light, Physical Chemistry Chemical Physics 11 (2009) 4084-4093. doi: 10.1039/b816708g.

[278] U. Balachandran, N. G. Eror, Raman spectra of titanium dioxide, Journal of Solid State Chemistry 42 (1982) 276-282. doi: 10.1016/0022-4596(82)90006-8.

[279] H. L. Ma, J. Y. Yang, Y. Dai, Y. B. Zhang, B. Lu, G. H. Ma, Raman study of phase transformation of TiO_2 rutile single crystal irradiated by infrared femtosecond laser, Applied Surface Science 253 (2007) 7497-7500. doi: 10.1016/j.apsusc.2007.03.047.

[280] A. Di Paola, G. Cufalo, M. Addamo, M. Bellardita, R. Campostrini, M. Ischia, R. Ceccato, L. Palmisano, Photocatalytic activity of nanocrystalline TiO_2 (brookite, rutile and brookite-based) powders prepared by thermohydrolysis of $TiCl_4$ in aqueous chloride solutions, Colloids and Surfaces A: Physicochemical and Engineering Aspects 317 (2008) 366-376. doi: 10.1016/j.colsurfa.2007.11.005.

[281] J. Surmacki, P. Wroński, M. Szadkowska-Nicze, H. Abramczyk, Raman spectroscopy of visible-light photocatalyst – nitrogen-doped titanium dioxide generated by irradiation with electron beam, Chemical Physics Letters 566 (2013) 54-59. doi: 10.1016/j.cplett.2013.02.066.

[282] M. Bellardita, G. Escolano-Casado, L. Palmisano, L. Mino, Surface processes in selective photocatalytic oxidation of hydroxybenzyl alcohols by TiO_2 P25, Catalysis Today 413 (2023) 113983. doi: 10.1016/j.cattod.2022.12.014.

[283] V. Héquet, C. Gonzalez, P. Le Cloirec, Photochemical processes for atrazine degradation: methodological approach, Water Research 35 (2001) 4253-4260. doi: 10.1016/S0043-1354(01)00166-X.

[284] U. Raschke, G. Werner, H. Wilde, U. Stottmeister, Photodecomposition of 4-amino-1,2,4-triazin-3,5-diones and-thiones in oxygenated aqueous solutions, Journal of Photochemistry and Photobiology A: Chemistry 115 (1998) 191-197. doi: 10.1016/S1010-6030(98)00265-2.

[285] S. Pal, P. N. Moza, and A. Kettrup, *Photochemistry of pendimethalin*, J. Agric. Food Chem. 39 (1991) 797–800.

[286] Y. Sanlaville, S. Guittonneau, M. Mansour, E. A. Feicht, P. Meallier, A. Kettrup, Photosensitized degradation of terbuthylazine in water, Chemosphere 33 (1996) 353-362. doi: 10.1016/0045-6535(96)00176-2.

[287] A. Di Paola, M. Addamo, V. Augugliaro, E. García-López, V. Loddo, G. Marcì, L. Palmisano, Photolytic and TiO_2-assisted photodegradation of aqueous solutions of tetracycline, Fresenius Environmental Bulletin 13 (2004) 1275-1280.

[288] A. K. Davies, J. F. McKellar, G. O. Phillips, A. G. Reid, Photochemical oxidation of tetracycline in aqueous solution, Journal of the Chemical Society, Perkin Transactions 2 (1979) 369-375. doi: 10.1039/P29790000369.

[289] C. S. Turchi, D. F. Ollis, Photocatalytic degradation of organic water contaminants: mechanisms involving hydroxyl radical attack, Journal of Catalysis 122 (1990) 178-192. doi: 10.1016/0021-9517(90)90269-P.

[290] K. I. Okamoto, Y. Yamamoto, H. Tanaka, M. Tanaka, A. Itaya, Heterogeneous photocatalytic decomposition of phenol over TiO_2 powder, Bulletin of the Chemical Society of Japan 58 (1985) 2015-2022. doi: 10.1246/bcsj.58.2015.

[291] C. Minero, C. Aliberti, E. Pelizzetti, R. Terzian, N. Serpone, Kinetic studies in heterogeneous photocatalysis. 6. AM1 simulated sunlight photodegradation over titania in aqueous media: a first case of fluorinated aromatics and identification of intermediates, Langmuir 7 (1991) 928-936. doi: 10.1021/la00053a020.

[292] J. C. D'Oliveira, G. Al-Sayyed, P. Pichat, Photodegradation of 2- and 3-chlorophenol in titanium dioxide aqueous suspensions, Environmental Science & Technology 24 (1990) 990-996. doi: 10.1021/es00017a010.

[293] A. Di Paola, V. Augugliaro, L. Palmisano, G. Pantaleo, E. Savinov, Heterogeneous photocatalytic degradation of nitrophenols, Journal of Photochemistry and Photobiology A: Chemistry 155 (2003) 207-214. doi: 10.1016/S1010-6030(02)00390-8.

[294] V. Augugliaro, L. Palmisano, A. Sclafani, C. Minero, E. Pelizzetti, Photocatalytic degradation of phenol in aqueous titanium dioxide dispersions, Toxicological & Environmental Chemistry 16 (1988) 89-109. doi: 10.1080/02772248809357253.

[295] K. H. Wang, Y. H. Hsieh, M. Y. Chou, C. Y. Chang, Photocatalytic degradation of 2-chloro and 2-nitrophenol by titanium dioxide suspensions in aqueous solution, Applied Catalysis B: Environmental 21 (1999) 1-8. doi.org/10.1016/S0926-3373(98)00116-7.

[296] V. Augugliaro, L. Palmisano, M. Schiavello, A. Sclafani, L. Marchese, G. Martra, F. Miano, *Photocatalytic degradation of nitrophenols in aqueous titanium dioxide dispersion*, Applied Catalysis, 69 (1991) 323-340. doi: 10.1016/S0166-9834(00)83310-2.

[297] Z. N. Kayani, M. Riaz, S. Naseem, Magnetic and antibacterial studies of sol-gel dip coated Ce doped TiO_2 thin films: influence of Ce contents, Ceramics International 46 (2020) 381-390. doi: 10.1016/j.ceramint.2019.08.272.

[298] R. Fiorenza, M. Bellardita, L. Palmisano, S. Scirè, A comparison between photocatalytic and catalytic oxidation of 2-propanol over Au/ TiO_2 -CeO_2 catalysts, J. Mol. Catal. A Chem. 415 (2016) 56-64. doi: 10.1016/j.molcata.2016.01.025.

[299] P. He et al., Photocatalytic degradation of deoxynivalenol using cerium doped titanium dioxide under ultraviolet light irradiation, Toxins (Basel) 13 (7) (2021). doi: 10.3390/toxins13070481.

[300] R. Nematollahi, C. Ghotbi, F. Khorasheh, A. Larimi, Ni-Bi co-doped TiO_2 as highly visible light response nano-photocatalyst for CO_2 photo-reduction in a batch photo-reactor, J. CO_2 Util. 41 (2020) 101289. doi: 10.1016/j.jcou.2020.101289.

[301] J. Zhu et al., Hydrothermal doping method for preparation of Cr^{3+}-TiO_2 photocatalysts with concentration gradient distribution of $Cr^{3+,}$ Appl. Catal. B 62 (3-4) (2006) 329-335. doi: 10.1016/j.apcatb.2005.08.013.

[302] D. C. Ghosh, R. Biswas, Theoretical calculation of absolute radii of atoms and ions. Part 1. The atomic radii, Int. J. Mol. Sci. 3 (2) (2002) 87-113. doi: 10.3390/i3020087.

[303] J. F. Coetzee, T. H. Chang, Purification of solvents for electroanalysis: Tetrahydrofuran and dioxane, Pure Appl. Chem. 57 (4) (1985) 633–638. doi: 10.1351/pac198557040633.

[304] A. L. T. Zheng, S. Sabidi, T. Ohno, T. Maeda, Y. Andou, Cu_2O/ TiO_2 decorated on cellulose nanofiber/reduced graphene hydrogel for enhanced photocatalytic activity and antibacterial applications, Chemosphere 286 (2022) 131731. doi: 10.1016/j.chemosphere.2021.131731.

[305] O. Beldjebli, R. Bensaha, Y. S. Ocak, L. Amirache, R. Boukherroub, Synthesis and photocatalytic efficiency of sol-gel Al^{3+} doped TiO_2 thin films: Correlation between structural, morphological and optical properties, Mater. Res. Express 6 (8) (2019). doi: 10.1088/2053-1591/ab1d36.

[306] T. Ali et al., Photocatalytic performance of Fe-doped TiO_2 nanoparticles under visible-light irradiation, Mater. Res. Express 4 (1) (2017). doi: 10.1088/2053-1591/aa576d.

[307] M. K. Hossain, M. M. Hossain, S. Akhtar, Studies on synthesis, characterization, and photocatalytic activity of TiO_2 and Cr-doped TiO_2 for degradation of p-chlorophenol, ACS Omega 8 (2) (2023) 1979-1988. doi: 10.1021/acsomega.2c05107.

[308] A. Amritha, M. Sundararajan, R. G. Rejith, M. A. Mohammed-Aslam, La–Ce doped TiO_2 nanocrystals: A review on synthesis, characterization and photocatalytic activity, SN Appl. Sci. 1 (11) (2019) 1-11. doi: 10.1007/s42452-019-1455-7.

[309] N. Yan, Z. Zhu, J. Zhang, Z. Zhao, Q. Liu, Preparation and properties of Ce-doped TiO_2 photocatalyst, Mater. Res. Bull. 47 (8) (2012) 1869-1873. doi: 10.1016/j.materresbull.2012.04.077.

[310] C. M. Pecoraro, M. Bellardita, V. Loddo, F. Di Franco, L. Palmisano, M. Santamaria, A facile way to synthesize noble metal free TiO_2 based catalysts for glycerol photoreforming, J. Ind. Eng. Chem. 118 (2023) 247-258. doi: 10.1016/j.jiec.2022.11.010.

[311] G. Palmisano, S. Yurdakal, V. Augugliaro, V. Loddo, L. Palmisano, Photocatalytic selective oxidation of 4-methoxybenzyl alcohol to aldehyde in aqueous suspension of home-prepared titanium dioxide catalyst, Adv. Synth. Catal. 349 (6) (2007) 964-970. doi: 10.1002/adsc.200600435.

[312] A. M. Djaballah et al., Facile preparation of $CuBi_2O_4$/ TiO_2 hetero-systems employed for simulated solar-light selective oxidation of 4-methoxybenzyl alcohol model compound, Mol. Catal. 546 (2023) 113251. doi: 10.1016/j.mcat.2023.113251.

[313] L. Su, X. Ye, S. Meng, X. Fu, S. Chen, Effect of different solvent on photocatalytic activity of $ZnIn_2S_4$ for selective oxidation of aromatic alcohols to aldehydes under visible light, Appl. Surf. Sci. 384 (2016) 161-174. doi: 10.1016/j.apsusc.2016.04.084.

[314] M. Bellardita, M. Feilizadeh, R. Fiorenza, S. Scirè, L. Palmisano, V. Loddo, Selective aqueous oxidation of aromatic alcohols under solar light in presence of TiO_2 modified with different metal species, Photochem. Photobiol. Sci. 21 (12) (2022) 2139-2151. doi: 10.1007/s43630-022-00284-2.

[315] S. Yurdakal, M. Bellardita, I. Pibiri, L. Palmisano, V. Loddo, Aqueous selective photocatalytic oxidation of salicyl alcohol by TiO_2 catalysts: Influence of physico-chemical features, Catal. Today 380 (2021) 16-24. doi: 10.1016/j.cattod.2021.06.030.

[316] M. Bellardita, G. Escolano-Casado, L. Palmisano, L. Mino, Surface processes in selective photocatalytic oxidation of hydroxybenzyl alcohols by TiO_2 P25, Catal. Today 413-415 (2023). doi: 10.1016/j.cattod.2022.12.014.

[317] M. Umair, C. M. Pecoraro, F. Di Franco, M. Santamaria, L. Palmisano, V. Loddo, M. Bellardita, Efficient photocatalytic partial oxidation of aromatic alcohols by using $ZnIn_2S_4$ under green conditions, *ChemSusChem* 17 (22) (2024) e202400404. https://doi.org/10.1002/cssc.202400404

[317] (a) S. Malato, J. Blanco, A. Vidal, C. Richter, Photocatalysis with solar energy at a pilot-plant scale: an overview, Applied Catalysis B: Environmental 37 (1) (2002) 1–15. doi.org/10.1016/S0926-3373(01)00315-0

[317] (b) P. Kant, S. Liang, M. Rubin, G. A. Ozin, R. Dittmeyer, Low-cost photoreactors for highly photon/energy-efficient solar-driven synthesis, Joule 7 (6) (2023) 1347–1362. doi.org/10.1016/j.joule.2023.05.006.